Computational Frameworks for Microstructure-Driven Design, Degradation, and Optimisation Analysis of Ni-GDC SOFC Anodes Using Phase-Field Methods

Zur Erlangung des akademischen Grades eines
DOKTORS DER INGENIEURWISSENSCHAFTEN (Dr.-Ing.)

von der KIT-Fakultät für Maschinenbau des
Karlsruher Instituts für Technologie (KIT)
angenommene

DISSERTATION

von

M.Eng. Ravi Kumar Jeela

Tag der mündlichen Prüfung:	09.10.2026
Hauptreferentin:	Prof. Dr. rer. nat. Britta Nestler
Korreferent:	Priv.-Doz. Dr.-Ing. André Weber

Abstract

Despite their advantages, the widespread commercialization of solid oxide fuel cells (SOFCs) remains limited by challenges in long-term stability, cost, and performance. At the cell level, performance is strongly determined by electrode materials and porous microstructure, while degradation is strongly linked to microstructural evolution, particularly within the anode. Compared with the relatively stable zirconia phase in Nickel-Yttria-stabilized zirconia (Ni-YSZ), Nickel-Gadolinium-doped ceria (Ni-GDC) anodes exhibit notable GDC phase evolution, resulting in more complex microstructural dynamics. Understanding the degradation of SOFCs resulting from microstructural evolution is essential for predicting long-term cell performance and durability. In this work, a multiphase-field model (MPF) based on a grand-potential formulation is employed to simulate the microstructural evolution of Ni-GDC SOFC anodes under high-temperature operating conditions. An active learning framework combined with Bayesian optimization is employed to identify model parameters for simulating the aging of Ni-GDC anodes, using Focused ion beam-scanning electron microscopy (FIB-SEM) reconstructed experimental microstructures and phase-field aging simulations. Diffusion and interfacial parameters are identified using a weighted-sum scalarization-based multi-objective optimization approach, resulting in values that are consistent with the available literature data.

Following parameter identification, quantitative MPF simulations of Ni and GDC coarsening are performed employing the FIB-SEM reconstructed 3D microstructures. The influence of interfacial energies on degradation is further examined, indicating that lower Ni contact angles primarily mitigate Ni coarsening, while

lower GDC contact angles influence Ni's long-term stability. The structure generator workflow is extended to create a realistic digital twin of Ni-GDC anodes by incorporating a computationally efficient morphological coalescence step similar to sintering. The generated synthetic structure is validated against FIB-SEM reconstructed 3D Ni-GDC anode microstructures across several quantitative descriptors, demonstrating strong agreement and enabling subsequent microstructure-property analyses for electrode optimization.

Fifteen synthetic microstructures are systematically generated by varying Ni, GDC, and pore volume fractions to investigate microstructural degradation. Electrochemical performance-relevant descriptors as well as mechanical integrity-relevant descriptors such as elastic moduli and average von Mises stress are analyzed as functions of phase volume fractions in pristine structures and their temporal evolution during isothermal aging. The results identify microstructural configurations that achieve a favorable balance between high initial electrochemical activity and reduced degradation, with the performance determined by the interplay between triple-phase boundary density, Ni percolation, and the Mixed ionic-electronic conductor (MIEC) behavior of the GDC. Configurations with lower Ni content remain viable due to stable GDC transport pathways and sustained electrochemical activity. Microstructures with intermediate porosity (about 35 %) exhibit the most balanced mechanical behavior, while lower and higher porosities result in increased stress concentrations and reduced functional performance, respectively. Overall, the results highlight that optimal Ni-GDC SOFC anode design requires an integrated electrochemical-mechanical performance consideration based on multiple microstructural descriptors rather than single-metric optimization. The findings provide quantitative guidelines for selecting Ni and GDC volume fractions tailored to specific electrode designs, as well as for modeling at the cell and stack levels.

Kurzfassung

Trotz der Vorteile von Festoxidbrennstoffzellen (SOFC), ist deren breite Kommerzialisierung weiterhin durch Herausforderungen hinsichtlich Langzeitstabilität, Kosten und Leistungsfähigkeit begrenzt. Auf Zellebene wird die Leistung maßgeblich durch die Elektrodenmaterialien und die poröse Mikrostruktur bestimmt, während die Degradation eng mit der mikrostrukturellen Evolution, insbesondere innerhalb der Anode, verknüpft ist. Im Vergleich zur relativ stabilen Zirkonoxidphase in Ni-Yttriumoxid-stabilisiertes Zirkonoxid (Ni-YSZ), weisen Ni-Gadolinium-dotiertes Ceroxid (Ni-GDC) Anoden eine ausgeprägte Evolution der GDC-Phase auf, was zu einer komplexeren mikrostrukturellen Dynamik führt. Das Verständnis dieser durch mikrostrukturelle Evolution verursachten Degradationsprozesse ist entscheidend für die Vorhersage der Langzeitleistung und Lebensdauer von SOFCs. In dieser Arbeit wird ein Multiphasenfeldmodell (MPF) auf Basis einer großkanonischen Potentialformulierung eingesetzt, um die mikrostrukturelle Evolution von Ni-GDC Anoden unter Hochtemperatur-Betriebsbedingungen zu simulieren.

Zur Identifikation der Modellparameter für die Simulation der Alterung von Ni-GDC Anoden wird eine Methode des aktiven Lernens in Kombination mit Bayes'scher Optimierung verwendet, wobei FIB-SEM rekonstruierte experimentelle Mikrostrukturen und Phasenfeld-Alterungssimulationen herangezogen werden. Die Diffusions- und Grenzflächenparameter werden mittels eines auf gewichteter Summenskalarisierung basierenden Mehrzieloptimierungsansatzes identifiziert. Dabei zeigt sich, dass die resultierenden Werte mit verfügbaren Literaturdaten konsistent sind. Basierend auf den identifizierten Parametern wird die Vergröberung von Ni und GDC mithilfe quantitativer Phasenfeldsimulationen

mittels FIB-SEM rekonstruierten dreidimensionalen Mikrostrukturen untersucht. Die Validierung anhand ungealterter und vorgealterter Proben zeigt eine gute Übereinstimmung bei den zentralen mikrostrukturellen Kenngrößen, wobei die vorgealterten Strukturen genauer wiedergegeben werden. Der Einfluss der Grenzflächenenergien auf die Degradation wird untersucht. Dabei zeigt sich, dass niedrigere Ni-Kontaktwinkel die Ni-Vergröberung reduzieren, während niedrigere GDC-Kontaktwinkel die Langzeitstabilität des Ni beeinflussen. Darüber hinaus wird der Strukturgenerator um einen recheneffizienten, sinterähnlichen morphologischen Koaleszenzschritt erweitert, um realistische digitale Zwillinge von Ni-GDC Anoden zu erzeugen. Die generierten synthetischen Mikrostrukturen werden anhand mehrerer quantitativer Deskriptoren erfolgreich gegen FIB-SEM rekonstruierte Strukturen validiert und ermöglichen weiterführende Mikrostruktur-Eigenschafts Analysen zur Elektrodenoptimierung.

Zur Untersuchung der mikrostrukturellen Degradation werden fünfzehn synthetische Mikrostrukturen durch systematische Variation der Volumenanteile von Ni, GDC und Poren erzeugt. Sowohl elektrochemisch relevante Deskriptoren als auch mechanische Kenngrößen, wie Elastizitätsmodule und gemittelte von-Mises-Spannungen, werden als Funktion der Phasenvolumenanteile in den ungealterten Strukturen, sowie in ihrer zeitlichen Entwicklung während isothermer Alterung analysiert. Die Ergebnisse identifizieren mikrostrukturelle Konfigurationen, die ein günstiges Verhältnis zwischen hoher elektrochemischer Ausgangsaktivität und geringer Degradation ermöglichen. Das elektrochemische Leistungsverhalten wird dabei durch das Zusammenspiel von Dreiphasengrenzliniendichte (TPB-Dichte), Ni-Perkolation und dem gemischt ionisch-elektronisch leitenden Verhalten (MIEC-Verhalten) des GDC bestimmt. Konfigurationen mit geringerem Ni-Gehalt bleiben aufgrund stabiler GDC-Transportpfade und anhaltender elektrochemischer Aktivität funktionsfähig. Mikrostrukturen mit mittlerer Porosität (etwa 35 %) zeigen das ausgewogenste mechanische Verhalten, während geringere und höhere Porositäten zu erhöhten Spannungskonzentrationen beziehungsweise zu verminderter funktionaler Leistungsfähigkeit führen. Insgesamt verdeutlichen die Ergebnisse, dass ein optimales Design von Ni-GDC SOFC Anoden eine integrierte Betrachtung der elektrochemischen und mechanischen Leistungsfähigkeit

auf Basis mehrerer mikrostruktureller Deskriptoren erfordert, anstatt einer Optimierung anhand einer einzelnen Kenngröße. Die gewonnenen Erkenntnisse liefern quantitative Richtlinien für die Auswahl geeigneter mikrostruktureller Parameter für spezifische Ni-GDC Elektrodendesigns und bilden eine Grundlage für weiterführende Modellierungen auf Zell- und Stackebene.

Acknowledgements

I would like to express my sincere gratitude to all those who have supported and contributed to this work. This thesis was written at the Karlsruhe Institute of Technology (KIT) under the supervision of Prof. Dr. rer. nat. Britta Nestler. I am especially thankful to her for providing the opportunity to work in an environment characterized by scientific freedom and independence, as well as for her continuous trust and support. I would also like to thank PD Dr.-Ing. André Weber for serving as co-reviewer and for his openness and willingness to engage in discussions on topics related to fuel cell anodes and collaborative research.

Furthermore, this dissertation was carried out during my time as a research assistant at the Institute for Digital Materials Science (IDM) at Karlsruhe University of Applied Sciences. I gratefully acknowledge the financial support provided by the Federal Ministry of Education and Research (Bundesministerium für Bildung und Forschung) within the framework of the "WirLebenSOFC" project (funding code: 03SF0622D). I also acknowledge funding from the German Research Foundation (DFG) for the project "Ceria-based Cathodes for High Performance Electrolysis Cells" (project number: 467256728).

Special thanks to my team leader, Dr.-Ing. Daniel Schneider, for his continuous guidance, valuable discussions, and unwavering support throughout this work. His trust and encouragement have been essential to the successful completion of this research. I am grateful to my collaborators – Giovanna Tosato, Dr.-Ing. Arnd Koeppe, Ahmed Elmoghazy, Dr.-Ing. Andreas Prahs, and Dr.-Ing. Lukas Schöller – for their technical support and contributions across various projects. I also thank Dr. Matthias Wieler from Robert Bosch GmbH and Yanting Liu from IAM-ET at KIT for insightful discussions and collaborative work on fuel cell anodes. My

special thanks go to Dr. Momin Ahmad, Dr.-Ing. Nishant Prajapati, Dr. Sumanth Nani Enugala, Dr.-Ing. Paul Hoffrogge, Dr.-Ing. Simon Daubner, Dr.-Ing. Martin Reder, Akash Kumar, and Muhammad Umar for numerous stimulating discussions and their valuable guidance, from which I have gained immensely. I also thank Ahmed Elmoghazy and Dr.-Ing. Martin Reder for proofreading this thesis and providing constructive feedback. I especially thank our administrator, Christof Ratz, for his prompt and efficient support with computer technical matters and for sharing his extensive knowledge of Linux systems.

This work would not have been possible without the contributions of my colleagues. I sincerely thank my predecessors, especially Dr.-Ing. Paul Hoffrogge and Dr. Momin Ahmad, for their contributions to the codebase. I also extend my appreciation to all my colleagues at Steinbeis, whose support and camaraderie made the working environment both productive and enjoyable. I especially enjoyed the engaging conversations during coffee and lunch breaks, as well as the shared activities with my colleagues beyond work, and the weekends spent participating in various cricket tournaments with my club team, KK Challengers – all of which made my time in Karlsruhe a truly unforgettable experience.

Finally, I would like to thank my parents, my brother, my friends, and my wife Esumani for their unconditional love, encouragement, and constant support. Their presence has been a source of strength throughout this journey. I am also deeply grateful to my teachers and mentors, whose guidance has shaped my curiosity and passion for scientific inquiry.

Karlsruhe, July 2026 *Ravi Kumar Jeela*

List of symbols

Latin Symbols

A	Thermodynamic prefactor / Surface area
a_0	Gradient energy prefactor
B	Rate constant for surface diffusion
C_{ij}	Components of the stiffness matrix in normalised Voigt notation
c_i	Composition of i'th component
c_i^α	Phase-inherent composition of i'th component in phase α
$c_{i,\mathrm{eq}}^\alpha$	Equilibrium composition of i'th component in phase α
D	Diffusion coefficient (diffusivity)
$D_i^{\alpha\beta}$	Self-diffusivity of component i along the α/β interface
$D_{i,\mathrm{ex}}^{\alpha\beta}$	Excess diffusivity of component i along the α/β interface
d_{50}	Mean particle diameter
E	Young's modulus
E_{xx}, E_{yy}, E_{zz}	Elastic moduli
E_{Hill}	Hill average elastic modulus
F	Aggregated (scalarised) objective function
f	Free energy density / Objective function of the optimisation problem
f^α	Phase-inherent bulk free energy density of phase α
G	Shear modulus

g	Auxiliary function
g_v	Term enforcing volume preservation
h	Interpolation function
i	Index indicating a chemical component
I_g	Dimensionless prefactor
j	Scalar flux density
K	Bulk modulus
ℓ	Length scale of the Matérn kernel
l_c	Characteristic length associated with attachment kinetics
l_{TPB}	Triple-phase boundary density
M	Mass / Chemical mobility
$M_i^{\alpha\beta}$	Chemical mobility of component i along the α/β interface
m	Interface mobility
N	Number of phases
N_{c}	Number of chemical components
$\tilde{N}$	Local number of active phases
N_x, N_y	Number of cells of the simulation grid
N_{xyz}	Total number of voxels of the grid
n	Free integer or real / Indicating normal direction
P	Probability
p	Indexing a voxel
S_{ij}	Components of the effective compliance
T	Temperature
t	Time
u_E, u_l, u_t	Model-specific energy, length, time units
V	Volume of the considered domain
v_n	Normal velocity of interface

w	Weight of the scalarisation
x, y, z	First, second and third Cartesian coordinate
Δx, Δy, Δz	Spatial discretisation step size (voxel size)

Greek Symbols

α	Indicating phase α
α_θ	Isotropic coefficient of thermal expansion
β	Indicating phase β / Exploration–exploitation trade-off parameter / Index of the macroscopic load case
γ	Interfacial energy parameter
γ_α^c	Curvature control parameter
δ	Indicating phase δ / Diffuse interface width / Atomistic thickness
$\Delta\square$	Difference
$\Delta^{\alpha\beta}$	Bulk driving force between phases α and β
ϵ	Interface width parameter
ε	Infinitesimal strain
ε_0	Amplitude of the applied macroscopic strain
θ	Wetting (contact) angle / Temperature
κ	Total curvature (twice mean curvature)
λ	Lagrange multiplier
μ	Chemical potential / Mean function of the Gaussian process
ν	Poisson's ratio / Smoothness parameter of the Matérn kernel
σ	Standard deviation predicted by the Gaussian process
σ_{ij}	Components of Cauchy stress tensor
σ_{vM}	von Mises equivalent stress
$\sigma_{\mathrm{threshold}}$	Reference stress level for the critical volume fraction

ρ	Mass density
τ	Relaxation constant (inverse of interface mobility)
τ_α	Tortuosity of phase α
ϕ	Order parameter
ψ	Grand-potential density
ψ^α	Grand-potential density of phase α
Ω	Grand-potential functional

Bold Symbols

$\boldsymbol{c}$	Vector of composition variables
$\mathbb{C}$	Stiffness tensor
$\bar{\mathbb{C}}$	Effective stiffness tensor
$\boldsymbol{I}$	Second-order identity tensor
$\mathbb{I}^{\mathrm{S}}$	Fourth-order symmetric identity tensor
$\boldsymbol{j}$	Flux density
$\boldsymbol{n}$	Normal vector
$\mathbb{P}_1, \mathbb{P}_2$	Projection tensors of the isotropic stiffness
$\mathbf{u}$	Displacement vector
$\boldsymbol{x}$	Position vector / Vector of design variables
$\boldsymbol{\varepsilon}$	Infinitesimal strain tensor
$\boldsymbol{\varepsilon}^\alpha$	Phase-specific strain tensor of phase α
$\bar{\boldsymbol{\varepsilon}}^\beta$	Macroscopic strain vector
$\{\boldsymbol{\varepsilon}\}^{\alpha\delta}$	Strain jump across the diffuse interface between α and δ
$\boldsymbol{\mu}$	Vector of chemical potentials
$\boldsymbol{\sigma}$	Cauchy stress tensor
$\overline{\boldsymbol{\sigma}}$	Interpolated Cauchy stress tensor

$\boldsymbol{\sigma}^{\alpha}$	Phase-specific Cauchy stress tensor of phase α
$\boldsymbol{\phi}$	Vector of order parameters

Calligraphic Symbols

$\mathcal{D}$	Observed data set of the Bayesian optimisation
$\mathcal{F}$	Free energy functional
$\mathcal{G}$	Gibbs simplex
$\mathcal{X}$	Feasible search (design) space

Superscripts and Subscripts

$\square_{\alpha}$ / $\square^{\alpha}$	Related to phase α
$\square_{\alpha\beta}$ / $\square^{\alpha\beta}$	Related to the interface between phases α and β
$\square_{i}$	Related to the i'th chemical component
$\square_{ij}$	Related to interaction of components i and j
$\square_{\text{bulk}}$	Bulk contribution
$\square_{\text{eq}}$	Equilibrium quantity
$\square_{\text{ex}}$	Excess quantity
$\square_{s}$ / $\square^{s}$	Related to a surface
$\square^{b}$	Related to bulk
$\square_{m}$	Molar
$\square_{\text{ref}}$	Reference state
$\square^{\text{el}}$	Elastic contribution
$\square^{\theta}$	Thermal contribution
$\square_{\text{Voigt}}$, $\square_{\text{Reuss}}$	Voigt and Reuss estimates
$\square_{\text{Hill}}$	Hill estimate

Abbreviations

AL	Active Learning
BAL	Bayesian Active Learning
BO	Bayesian Optimization
CTE	Coefficient of thermal expansion
CV	Coefficient of variation
CVF	Critical volume fraction
DPB	Double-phase boundary
FIB-SEM	Focused ion beam-scanning electron microscopy
GDC	Gadolinium-doped ceria
GP	Gaussian process
MAPE	Mean absolute percentage error
MIEC	Mixed ionic-electronic conductor
ML	Machine learning
MPF	Multiphase-field (model)
Ni	Nickel
OCV	Open-circuit voltage
PF	Phase-field
PFM	Phase-field method
PSD	Particle size distribution
RMSE	Root mean square error
RVE	Representative volume element
SIMD	Single instruction, multiple data
SOC	Solid oxide cell
SOFC	Solid oxide fuel cell
SSA	Specific surface area
TLM	Transmission line model

TPB	Triple-phase boundary
YSZ	Yttria-stabilized zirconia

Contents

Abstract i

Kurzfassung iii

Acknowledgements vii

List of symbols ix

1 Introduction 1

1.1 Fuel cells . . . 3

1.1.1 Fuel cell types . . . 4

1.2 Working principle of solid oxide fuel cells . . . 6

1.2.1 SOFC components . . . 8

1.2.2 Classification of SOFC systems . . . 13

1.3 Modeling of SOFCs . . . 14

1.3.1 Microscale modeling . . . 17

1.3.2 Mesoscale modeling . . . 18

1.3.3 Macroscale modeling . . . 21

1.4 SOFC anode microstructures . . . 23

1.4.1 Relationship between microstructure and fuel cell performance . . . 25

1.4.2 Degradation of SOFC anodes . . . 28

1.5 Modeling of SOFC anode degradation . . . 29

1.5.1 Microstructural evolutions . . . 29

1.5.2 Mechanical degradation . . . 32

1.6 Research aim and objectives 33
1.7 Structure of the thesis 34

2 Frameworks for microstructural evolutions and quantification 37
2.1 Introduction to the phase-field method 37
2.1.1 Two-phase models 38
2.1.2 Multiphase-field models 40
2.2 Coupled modeling of diffusion and phase transformation 43
2.2.1 Interface and bulk diffusion 45
2.2.2 Governing laws 47
2.3 Numerical implementation 51
2.4 Grand-potential multiphase-field model for aging simulations . . 52
2.5 Extension of structure generator workflow 58
2.5.1 Framework for sintering-like morphological coalescence 58
2.6 Solid mechanics framework for mechanical response of anodes . 64
2.7 Microstructure quantification 65
2.7.1 Electrochemical performance-related descriptors 65
2.7.2 Mechanical related descriptors 66
2.8 Experimental Ni-GDC SOFC anode microstructures 68
2.8.1 Fabrication of the cells 68
2.8.2 Cell operating conditions 69
2.8.3 3D microstructure reconstruction of pristine and aged cells 69
2.9 RVE of Ni-GDC anode 70

3 Framework for physical parameters estimation 77
3.1 Bayesian Active Learning framework 78
3.2 Physical parameters and model parameterization 82
3.2.1 Nickel diffusion coefficients 82
3.2.2 Nickel surface energy 84
3.2.3 GDC diffusion coefficients and surface energy 85
3.2.4 Nickel/GDC interfacial energy 86
3.2.5 Interface mobilities and parabolic free energy 87

3.3 Validation of framework 87
3.4 Framework on 3D FIB-SEM reconstructed Ni-GDC anode microstructures 92
3.4.1 Single objective optimization 93
3.4.2 Multi-objective optimization: weighted sum scalarization approach 97
3.5 Interim conclusion 103

4 MPF aging simulations of the Ni-GDC anode: experimental validation and effects of interfacial energy 107
4.1 Model parameters 108
4.2 Microstructural evolution of 3D Ni-GDC anode: comparative analysis of simulation and experimental results . . . 111
4.2.1 Phase-field simulations of 1100h aging: employing a pristine Ni-GDC anode as input 114
4.2.2 Phase-field simulations of 860h aging: employing a pre-aged (240h) Ni-GDC anode as input 117
4.3 Large-scale aging simulations 120
4.4 Sensitivity analyses of physical parameters - influence of interfacial energies on anode stability 130
4.4.1 Effect of interfacial energies on morphological evolutions: 2D analysis 132
4.4.2 Effects of interfacial energies on morphological evolutions: 3D analysis of FIB-SEM reconstructed experimental Ni-GDC SOFC anode microstructures . . 135
4.5 Predictive capability and limitations 144
4.6 Interim conclusion 144

5 Digital twin of Ni-GDC anode microstructure 147
5.1 Synthetic microstructure generation 148
5.2 Experimental validation 151

6 Effect of anode volume fractions on microstructural degradation and mechanical integrity **157**
6.1 Analysis of thermal expansion mismatch in Ni-GDC anode . . . 159
6.2 Generation of synthetic structures for aging simulations 160
6.3 Influence of initial microstructural configurations on properties . 163
6.3.1 Microstructural descriptors of electrochemical performance 163
6.3.2 Effective properties of mechanical response 168
6.4 Evolution and degradation of properties during aging 170
6.4.1 Electrochemical performance-related microstructural properties degradation 174
6.4.2 Mechanical performance-related effective properties degradation 182
6.5 Interim conclusion 188

7 Conclusion **191**
7.1 Summary 191
7.2 Outlook 194

Bibliography **197**

List of the author's publications **227**

List of Figures **229**

List of Tables **239**

1 Introduction

The growing global energy demand, together with the need to significantly reduce greenhouse gas emissions, places the transition toward low- and zero-emission energy systems at the center of global climate action strategies. The 28th United Nations Climate Change Conference (COP28), held in Dubai in 2023, concluded the first Global Stocktake under the Paris Agreement and highlighted gaps between current mitigation efforts and long-term climate goals, calling for an accelerated transition away from fossil fuels toward net-zero energy systems by 2050 and for tripling global renewable energy capacity and doubling the rate of energy efficiency improvements by 2030 [1]. In light of global climate change, Germany's climate policy is based on the Federal Climate Change Act (Klimaschutzgesetz), which sets legally binding targets of $-65\,\%$ greenhouse gas emissions by 2030, $-88\,\%$ by 2040, and climate neutrality by 2045 compared to 1990 levels [2]. A transition to sustainable, low-carbon energy systems is essential to meet growing energy demand while reducing greenhouse gas emissions.

Among clean energy sources, hydrogen (H_2) has received considerable attention due to its versatility and environmental benefits. When used in fuel cells, hydrogen reacts with oxygen (O_2) to generate electricity, producing only water (H_2O) as a byproduct and thus avoiding direct emissions of greenhouse gases and pollutants. Due to its high energy density and flexibility, hydrogen also serves as an effective energy carrier and storage medium. In particular, it enables the storage of excess electricity from renewable sources such as solar and wind through water electrolysis, thereby supporting the integration of variable renewable energy into the energy system. Among the various fuel cell technologies, solid oxide fuel cells (SOFCs) have gained significant attention as a bridge towards sustainable energy

systems. Their high efficiency (typically 45 %–60 % in fuel cell mode [3] and up to 90 % in electrolysis mode [4]) enhances their technological and economic viability. Furthermore, the same cell can be operated both as a fuel cell and as an electrolysis cell (reversible SOCs), enabling flexible energy conversion. In addition to hydrogen, these systems can also utilize hydrocarbon-based fuels such as natural gas and methanol [5] from fossil and renewable sources, facilitating a gradual transition to a hydrogen-based energy infrastructure. Fuel cells are considered a promising technology for applications in transportation, stationary power generation, and portable systems. Even before the federal government adopted the national hydrogen strategy [6], German industry had already begun investing in hydrogen technologies, with companies such as Robert Bosch GmbH playing a leading role in the development of mobile and stationary fuel cells. To enable large-scale market penetration, current efforts are primarily focused on improving durability and reducing system costs.

Despite its advantages, widespread commercialization of SOFC technology remains inhibited by limitations in long-term stability, cost, and performance. Improving durability and performance requires optimized cell and stack design, as well as integrated system development. At the individual cell level, performance is largely determined by the material selection and microstructure of the porous electrodes, while long-term performance degradation is strongly linked to microstructural evolution, particularly within the anode and cathode, where microstructural changes reduce the density of electrochemical reaction sites and gradually degrade performance. A detailed understanding of these structure-performance relationships is therefore essential for further improvements. The characterization and comparative analysis of electrode microstructures, as well as the investigation of their evolution during operation, are crucial for performance optimization. However, they remain experimentally challenging and resource-intensive due to reactions occurring at solid-solid and solid-pore interfaces and the strong coupling between transport and electrochemical processes within complex porous microstructures. Although macroscopic electrochemical characterization can be performed with relative ease, the underlying microstructural degradation

mechanisms cannot be directly captured. To bridge this gap, physics-based simulation models are widely employed to predict microstructure evolution driven by underlying degradation processes and to assess their impact on long-term cell performance. These models also enable the identification of optimal microstructural configurations and deepen the understanding of structure-performance correlations.

1.1 Fuel cells

Fuel cell technology offers an alternative approach to electricity generation and is increasingly regarded as a key component in the transition toward a sustainable, low-emission energy infrastructure. The origins of the fuel cell concept date back to the early 19th century, with the foundational ideas attributed to Sir Humphry Davy. However, the first working demonstration came in 1839 by Sir William Grove through the successful operation of an electrochemical hydrogen-oxygen cell, which is widely regarded as the starting point of modern fuel cell development. In Grove's system, hydrogen and oxygen react to form water and generate electricity at the same time. Fuel cells are electrochemical devices that convert the chemical energy of a fuel directly into electrical energy, with heat generated as a byproduct. A typical fuel cell consists of two porous electrodes (anode and cathode) separated by an electrolyte, which may be solid or liquid and is impermeable to gases. During operation, the fuel is continuously supplied to the anode, while an oxygen source, typically air, is supplied to the cathode. The oxidation reaction is facilitated by ion conduction through the electrolyte. At the electrode interfaces, fuel and oxidizing gases diffuse along the porous surfaces and undergo electrochemical reactions at the triple-phase boundary that forms between the electrode, electrolyte, and pore. This configuration enables continuous power generation as long as reactants are supplied. Nevertheless, the practical lifespan of fuel cells is often limited by material degradation, component failures, and other operational constraints.

Fuel cells generate electricity through a direct electrochemical conversion process, differentiating them fundamentally from combustion-based power generation. In a conventional thermal power plant, chemical energy is first converted into thermal energy, then into mechanical work, and finally into electrical energy, resulting in cumulative efficiency losses at each stage. In contrast, fuel cells eliminate these intermediate steps, enabling a more efficient energy conversion pathway. Another key advantage of fuel cells lies in their design flexibility. They can be configured in modular designs and manufactured in a wide range of sizes, enabling adaptation to diverse applications and offering significant advantages over conventional power generation technologies. The operating principle of a fuel cell is similar to that of a battery; however, they differ in one key aspect. In batteries, the electrodes and the electrolyte participate directly in the energy conversion process, leading to the gradual depletion of the internal reactants. Consequently, batteries must be recharged or replaced once their stored energy is exhausted. In contrast, fuel cells operate with a continuous supply of external fuel, while reaction products are simultaneously removed.

1.1.1 Fuel cell types

Fuel cell technologies encompass a range of systems that differ in terms of electrolyte used, operating temperature, and applications. Table 1.1 provides an overview of the five major fuel cell types, including their achievable electrical efficiencies, operating temperature ranges, and the corresponding electrolyte and catalyst materials. Low-temperature systems, including alkaline fuel cells (AFC), polymer electrolyte membrane fuel cells (PEMFC), and phosphoric acid fuel cells (PAFC), typically operate with hydrated electrolytes and require noble metal catalysts such as platinum to facilitate electrochemical reactions. In contrast, high-temperature fuel cells such as molten carbonate fuel cells (MCFC) and solid oxide fuel cells (SOFC) operate at elevated temperatures and do not rely on precious metal catalysts, offering advantages in terms of catalytic cost. Among the various fuel cell technologies, PEMFCs and SOFCs are widely regarded as two of the most commercially mature and technologically advanced systems, dominating

different application domains within the fuel cell market [7]. PEMFCs are particularly well-suited for transportation applications due to their low operating temperature (typically around 80 °C), high power density, and rapid start-up capability. These attributes have enabled their deployment in fuel cell electric vehicles and other mobility platforms [8]. However, their reliance on platinum catalysts significantly increases system cost, and their sensitivity to impurities, particularly carbon monoxide, can lead to catalyst poisoning and performance degradation. Furthermore, PEMFCs generally require high-purity hydrogen, which presents challenges related to fuel production, storage, and distribution infrastructure [9]. Although PEMFC technology has reached a relatively advanced stage of development, its limited tolerance to alternative fuels such as hydrocarbons or ammonia constrains its operational flexibility [9].

In contrast, high-temperature fuel cells such as SOFCs and MCFCs are more suitable for stationary and grid-scale power generation applications. SOFCs are predominantly developed and commercialized for stationary and distributed power generation, where their high efficiency and inherent fuel flexibility can be effectively utilised [10, 11]. A key advantage of SOFC technology lies in its ability to operate on a wide range of fuels, including liquefied natural gas (LNG), liquefied petroleum gas (LPG), methanol, and ethanol. In addition, SOFCs exhibit a high tolerance to fuel impurities, thereby reducing or eliminating the need for extensive fuel purification processes, particularly those associated with hydrogen production, storage, and transport. However, their high operating temperatures, typically in the range of 600 °C–1000 °C, impose significant limitations on their deployment in transportation applications, primarily due to issues related to thermal cycling and prolonged start-up times [9, 12]. Consequently, reducing the operating temperature has become a central focus in the development of next-generation SOFC systems. In this context, metal-supported SOFCs (MS-SOFCs) have attracted considerable attention due to their ability to operate at intermediate temperatures while maintaining robust performance, rapid start-up capability, and high power density, thereby positioning them as a promising candidate for mobile applications [9]. Despite these advancements, the application of SOFC-based systems in transportation remains at an early stage of development.

Nevertheless, the compatibility of SOFCs with existing fuel infrastructures, such as gas pipelines and conventional refueling stations, enhances their practical relevance. Over the past decades, intensive research and development efforts have significantly improved the performance, durability, and cost-effectiveness of SOFC technologies, bringing them closer to large-scale commercial deployment, particularly in stationary power applications. However, despite this substantial progress, key technical and economic challenges remain, which continue to limit their widespread implementation.

Table 1.1: Comparison of major fuel cell technologies (based on ref [13]).

Fuel cell Type	Operating Temperature (°C)	Electrolyte	Catalyst	Electrical efficiency (%)
PEMFC	< 120	Perfluorosulfonic acid	Pt	40–60
AFC	< 100	KOH solution	Ni/Ag	up to 60
PAFC	150–200	Phosphoric acid	Pt	up to 40
MCFC	600–700	Molten alkali carbonates	Ni	up to 50
SOFC	500–1000	YSZ (zirconia)	Ceramic/Ni	up to 60

1.2 Working principle of solid oxide fuel cells

As with other fuel cell systems, an SOFC consists of three key components: a dense electrolyte positioned between two porous electrodes, specifically the oxygen electrode (cathode) and the fuel electrode (anode). The SOFC electrolyte is a gas-tight ceramic that conducts oxide ions (O^{2-}) while electronically isolating the electrodes, thus preventing direct combustion between the fuel and oxygen. During operation, oxygen is supplied to the cathode, where it is adsorbed onto the catalytic surface and reduced to oxide ions through the incorporation of electrons. These oxide ions migrate through the electrolyte via vacancy-mediated diffusion, driven by the large difference in the oxygen chemical potential between the cathode (high oxygen partial pressure) and the anode (low oxygen partial pressure). The

transported oxide ions react with the supplied fuel, typically hydrogen, at the interface of the electrolyte and the anode, producing water and releasing electrons. The electrons generated at the anode are repelled by the negatively charged anode and drawn towards the positively charged cathode. Since the electrolyte exhibits negligible electrical conductivity, these electrons cannot flow directly across the electrolyte and are therefore compelled to traverse the external circuit to reach the cathode. When an external load is incorporated into the circuit, the resulting flow of electrons performs electrical work. However, in the case of an open circuit, there is no pathway for the electrons to return to the cathode. As a result, charge accumulates at the electrodes, leading to the formation of an electric potential difference between them. The simplified operating principle and schematic structure of a solid oxide fuel cell are shown in Figure 1.1.

The following electrochemical reactions take place in a solid oxide fuel cell operating with hydrogen as the fuel. At the SOFC anode:

$$2\,H_2 + 2\,O^{2-} \longrightarrow 2\,H_2O + 4\,e^-, \tag{1.1}$$

at the SOFC cathode:

$$O_2 + 4\,e^- \longrightarrow 2\,O^{2-}. \tag{1.2}$$

Thus, the overall cell reaction is:

$$2\,H_2 + O_2 \longrightarrow 2\,H_2O. \tag{1.3}$$

The overall redox reaction (eq 1.3) is composed of two spatially separated electrochemical half-cell reactions that take place at the porous anode and cathode, which are isolated from each other by a dense electrolyte. During operation, hydrogen and oxygen are continuously supplied to the anode and cathode, respectively, to sustain the reaction. Since the voltage and power output of a single SOFC are relatively small, multiple cells are connected to form a stack to achieve the desired power output. The electrochemical reactions occur at the triple-phase boundary (TPB) of the anode, defined as the region where the electronically conductive phase, the ionically conductive phase, and the gaseous phase meet.

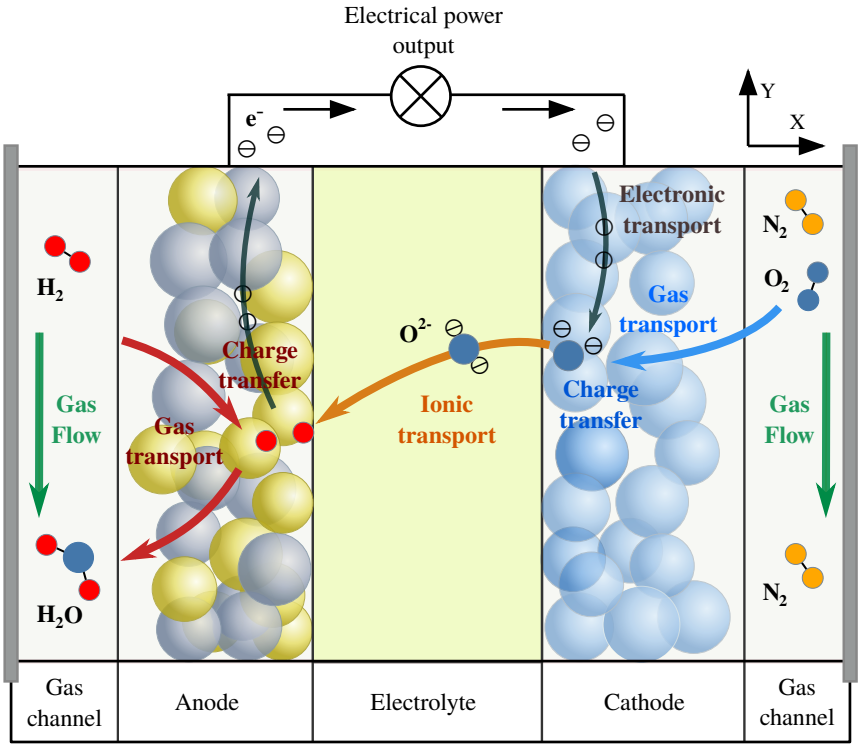


Figure 1.1: Schematic of an operating SOFC showing two porous electrodes (anode and cathode) separated by a dense electrolyte (adapted from ref [14]).

1.2.1 SOFC components

Each component of an SOFC serves multiple functions and needs to meet specific requirements, including the stability of its chemical composition, phase, morphology, and dimensions under oxidizing and/or reducing conditions at high temperatures, as well as chemical and thermomechanical compatibility with adjacent materials and adequate electronic and/or ionic conductivity. The electrolyte and the interconnect components are required to be dense to ensure effective separation of fuel and oxidant gases, while both the anode and the cathode must be

porous to enable gas transport to the electrochemical reaction sites. This Section briefly discusses the electrolyte and the cathode materials, with a greater emphasis on the anode.

Anode As a key component of the SOFC, the anode – where the fuel is electrochemically oxidized, releasing electrons – plays a critical role in determining electrochemical performance and must therefore provide and sustain optimal conditions for efficient fuel oxidation. The anode is required to meet the following specifications:

- Catalytic activity: High catalytic activity for the oxidation of fuels such as hydrogen and hydrocarbon gases.
- Stability: Chemical, morphological, and mechanical as well as dimensional stability under high-temperature operating conditions, including reducing and humid atmospheres, along with tolerance to redox cycling and to contaminants such as sulfur, as well as to carbon deposition (coking).
- Polarization resistance: Low polarization resistance to enable faster electrochemical kinetics and to minimize associated losses.
- Conductivity: High electronic conductivity to minimize ohmic losses, combined with adequate ionic conductivity (intrinsic or via a composite microstructure) to extend the triple-phase boundary into the electrode, thereby increasing electrochemical activity.
- Compatibility: Chemical, thermal, and mechanical compatibility with other cell components (e.g., electrolyte and interconnects) during fabrication and operation.
- Porosity: Optimal porosity to enable efficient gas transport while providing adequate mechanical strength.

The most commonly used and extensively studied anode material system is a Ni-based cermet, typically consisting of metallic nickel and yttria-stabilized zirconia

(YSZ), with 8 mol% YSZ (8YSZ) being the most widely employed composition. Nickel provides electronic conductivity and catalytic activity for hydrogen dissociation and subsequent electrochemical oxidation, enabling the transport of electrons through the external circuit. The YSZ phase facilitates the transport of oxygen ions from the electrolyte into the anode, where the electrochemical reactions occur. The porous microstructure further promotes gas diffusion and the removal of the reaction products. In addition to providing ion pathways, the ceramic phase improves thermal expansion compatibility with the electrolyte and suppresses nickel coarsening during operation. In conventional Ni-YSZ cermet anodes, the electrochemical reaction sites are limited to the TPBs. The TPB density and the connectivity of the electronic and ionic percolation networks are therefore critical factors for anode performance. The overall performance of the SOFC depends strongly on the microstructural parameters of the anode, including phase distribution, particle size, and volume fractions of nickel and YSZ, as well as porosity. In particular, a sufficient nickel content (approximately 30 vol.%) is required to ensure a continuous electron-conducting network [15], while the Ni/YSZ ratio critically determines the resulting transport properties and electrochemical activity [16].

Alternative anode materials Conventional Ni-YSZ cermet anodes have established the performance standard for SOFCs. Nevertheless, the large-scale commercialization of SOFCs is limited by cost constraints and long-term stability [17]. Lowering the operating temperature (<650 °C) is a key approach to enabling the use of more cost-effective materials while simultaneously improving durability. At lower temperatures, Ni-YSZ anodes exhibit performance limitations attributed to the relatively low ionic conductivity of YSZ, resulting in increased ohmic resistance [18, 19]. To address these limitations, alternative anode materials and designs are currently being actively researched. Among these, Ni/ceria-based anodes are emerging as promising alternatives, primarily due to the high ionic conductivity of gadolinium-doped ceria even at lower temperatures of 500 °C [19, 20]. In conventional Ni-YSZ systems, the electrochemical reaction sites are limited to the TPBs, where the electronic conductor, the ionic conductor, and the gaseous

fuel intersect. In contrast, Ni-GDC anodes benefit from the mixed ionic-electronic conductivity of GDC, which allows electrochemical reactions to occur both at TPBs and along the double-phase boundary (DPB) at the GDC/Pore interface [21–23]. Extending these reaction sites enhances the electrode's overall performance. Consequently, the distribution and long-term stability of these reaction sites play a crucial role in determining both the durability and efficiency of SOFC anodes under operating conditions.

An alternative to conventional cermet anode design is the employment of purely ceramic (metal-free) anodes capable of meeting all functional requirements of the anode. Such an approach aims to eliminate metallic components, which are often associated with instability and limited chemical tolerance under operating conditions. These materials, known as mixed ionic-electronic conductors (MIECs), simultaneously provide electronic conductivity, ionic conduction, and catalytic activity. Porous MIEC structures offer simplified electrode designs, enhanced chemical and structural stability, and reaction sites that extend beyond conventional triple-phase boundaries to the entire electrode surface. Currently, however, none of the ceramic materials meets the optimal balance of conductivity, catalytic activity, performance, and long-term stability required for metal-free anodes. Consequently, MIEC-based systems are typically combined with metallic phases to improve catalytic performance or conductivity, as well as overall electrochemical efficiency.

Electrolyte The dense electrolyte is a critical component in SOFC design, as it needs to be completely gas-tight to prevent direct contact between oxidizing and reducing gases. The electrolyte should exhibit higher ionic conductivity to enable efficient transport of oxide ions from the cathode-electrolyte interface to the electrolyte-anode interface, whilst simultaneously remaining electronically insulating to impede electrons released at the anode from flowing directly towards the cathode without passing through the external load. Furthermore, the electrolyte must be chemically stable in both oxidizing and reducing atmospheres and exhibit a coefficient of thermal expansion compatible with the adjacent electrode

materials to ensure mechanical integrity during operation and under thermal cycling. The most commonly used electrolyte in SOFCs is ZrO_2 doped with 8 mol% Y_2O_3 (8YSZ), a polycrystalline ceramic that exhibits excellent stability under both oxidizing and reducing conditions. Although 8YSZ provides high oxide ion conductivity, adequate transport of ions is generally achieved only at high operating temperatures (about 1000 °C), at which anion diffusion is thermally activated. In comparison, 3 mol% Y_2O_3 in ZrO_2 (3YSZ) offers improved mechanical properties, including higher fracture strength and elasticity, but its lower ionic conductivity limits its applicability to operation at intermediate or lower temperatures. Alternative ceria-based electrolytes are therefore being investigated for SOFCs in the intermediate and low-temperature ranges. With research moving increasingly toward low-temperature SOFCs, ohmic loss across the electrolyte becomes a performance bottleneck, and alternative solutions are required. One common strategy to mitigate this is to reduce the electrolyte thickness to about 5 µm, enabling operation at lower temperatures of 700 °C. At even lower temperatures, YSZ is not suitable, and materials such as GDC are considered more promising due to their higher ionic conductivity.

Cathode The durability and electrochemical performance of SOFCs are also influenced by the cathode. Conventional cathodes are typically ceramic materials without a metallic phase and must be operated under highly oxidizing conditions. Accordingly, cathode materials are required to exhibit chemical stability, good electronic and ionic conductivity, sufficient porosity for oxygen transport, and high catalytic activity for the oxygen reduction reaction. The choice of cathode materials closely depends on the electrolyte, requiring compatible thermal expansion behavior and chemical stability at the cathode-electrolyte interface to prevent undesirable reactions during operation. A widely utilized cathode material in SOFCs is strontium-doped lanthanum manganate (LSM), which offers high electronic conductivity, negligible ionic conductivity, and high catalytic activity for oxygen dissociation. Typically, the cathode is composed of a porous, sintered mixture of LSM and YSZ, allowing electrochemical reactions to occur at the TPBs whilst oxide ions are transported to the electrolyte through the YSZ

phase. Although LSM-YSZ cathodes perform well at high operating temperatures (1000 °C), their performance declines at lower temperatures (600 °C–800 °C). To address this limitation, alternative cathode materials are being actively investigated that exhibit higher catalytic activity at lower temperatures, are non-reactive with the electrolyte material, and offer high ionic and electronic conductivity. As SOFC developments progressively transition towards lower operating temperatures, researchers are considering MIEC materials as an alternative to mixed-ceramic cathodes. MIEC materials extend the active reaction zone beyond the TPB to the entire electrode surface; examples include lanthanum strontium cobalt ferrite (LSCF) and lanthanum strontium cobaltite (LSC). However, direct contact of these cathodes with zirconia-based electrolytes can lead to the formation of an insulating $SrZrO_3$ interlayer [24, 25]. This is usually mitigated by inserting a GDC interlayer between the LSCF cathode and the electrolyte [26].

1.2.2 Classification of SOFC systems

SOFCs are commonly classified according to operating temperature, cell/stack design, and support configuration. Based on temperature, they are generally divided into low-temperature SOFCs (500 °C–650 °C), intermediate-temperature SOFCs (650 °C–800 °C), and high-temperature SOFCs (800 °C–1000 °C). Higher operating temperatures reduce ohmic resistance and enhance electrode kinetics, thereby improving performance; however, higher operating temperatures also present challenges such as accelerated material degradation, weakened structural integrity, higher costs, and slower start-up and shut-down times. With regard to cell and stack designs, SOFCs are typically configured in tubular, planar, or segmented-in-series (integrated-planar) designs. Among these, planar and tubular designs are most widely adopted due to their scalability, with planar cells providing a higher packing density. In terms of mechanical support types, SOFCs can be electrolyte-, anode-, or cathode-supported. Electrolyte-supported cells are generally associated with high-temperature operation, while anode- and cathode-supported designs, enabled by thin electrolyte layers, are more suitable for intermediate and low-temperature operation. SOFCs may also be externally

supported, such as interconnect-supported, metal-supported, or porous substrate-supported configurations, the metal-supported variant being a particularly active area of recent development for low-temperature operation.

1.3 Modeling of SOFCs

Modeling and simulation provide a robust framework for advancing next-generation SOFCs by enabling a systematic evaluation of performance, degradation, and design optimization. A comprehensive understanding of the processes governing cell performance and lifetime, and of their dependence on materials, microstructure, cell design, and operating conditions, is essential for systematically improving overall performance and lifetime. While various experimental techniques can be employed to investigate the underlying physics of SOFC operation, numerical modeling provides a powerful, non-invasive approach to examining aspects of system dynamics that are challenging to assess experimentally. Optimization across the system, stack, cell, and electrode levels through experiments is often time-consuming, resource-intensive, and challenging, whereas numerical modeling enables rapid and cost-effective evaluation of design and operating parameters. Physical modeling is indispensable for a fundamental understanding of the causes and effects of the processes involved, as well as their interactions. Once validated, these models enable the efficient optimization of materials, microstructure, and operating conditions. In recent years, modeling has been widely employed to predict electrochemical performance, and its combination with experimental research remains central to improving efficiency and extending cell lifetime.

The complex interactions across different time and length scales, combined with the complexity of materials and structures, present a significant computational challenge in SOFC analysis. The performance of SOFCs is determined not solely by the macroscopic stack design, but also by the microstructure of the electrodes, depending on the morphology and composition of the constituent materials. As a result, optimization requires a holistic approach across all levels, from the

microstructure of the electrodes through individual cells to complete stack configurations. In the work of Grew and Chiu [27], a comprehensive overview of modeling and simulation techniques for SOFCs across the time and length scales is provided, summarizing key functional and degradation processes together with suitable modeling methods. As shown in Figure 1.2, these processes extend across a broad range of characteristic time and length scales, together with the corresponding modeling approaches capable of resolving them. Although the interactions underlying these phenomena originate at the atomic level in the atomic structure of individual atoms, these interactions reveal themselves in uniquely observable and measurable ways extending across a wide range of time and length scales, providing further insights. As modeling progresses from the system level toward reaction kinetics, model detailing increases while the corresponding length scale decreases. Accordingly, different modeling levels require specific formulations, governing equations, and parameter sets tailored to the respective scale and the phenomena under investigation. Based on the geometric representation, models are typically classified as zero-dimensional (0D), one-dimensional (1D), two-dimensional (2D), or three-dimensional (3D). Zero-dimensional models provide global outcomes, such as current-voltage characteristics, while higher-dimensional models progressively resolve spatial variations, with 3D models capturing the full distributions of transport fluxes within the cell. They can also be divided into white-box (physical) models, black-box (empirical) models, or gray-box (semi-empirical) models, reflecting the extent to which physical equations and experimental data are incorporated [28, 29]. In terms of length scale, SOFC models are categorized into microscopic, mesoscopic, and macroscopic models. Microscale models study atomic and molecular processes to determine intrinsic material properties and reaction kinetics. Mesoscale models focus on the microstructure of the electrodes and interfacial phenomena that govern transport and electrochemical activity. Macroscale models, which encompass analyses at the cell, stack, and system levels, are employed to predict overall performance and guide operating strategies. Across these scales, various numerical methods have been adopted to capture the relevant processes and their interactions.

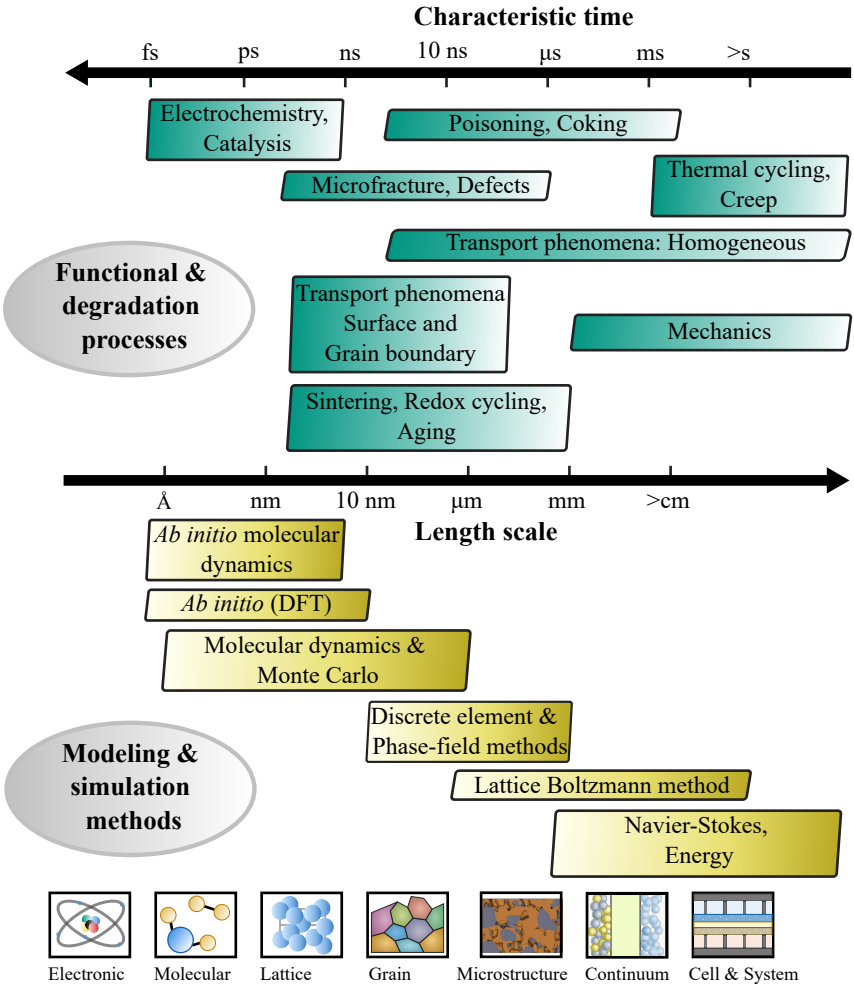


Figure 1.2: An overview of the characteristic time and length scales of functional and degradation processes in heterogeneous SOFC electrode structures, including common modeling and simulation approaches across these scales (adapted from ref [27]).

1.3.1 Microscale modeling

At the microscale, the analysis focuses on elementary reactions occurring at catalyst surfaces from an atomic and molecular standpoint, enabling a detailed understanding of the interaction mechanisms between reactants and catalyst materials. Microscale modeling in SOFCs captures the fundamental electronic and atomistic processes governing electrochemical phenomena and provides valuable insights into the development and optimization of the composition of catalyst materials. Among the most commonly employed computational approaches at this scale are density functional theory (DFT), kinetic Monte Carlo (KMC), and molecular dynamics (MD), which enable the investigation of reaction mechanisms and kinetics at the atomic level [30]. DFT is a quantum mechanical method used to investigate the structure and properties of multi-particle systems based on electron density. By solving the Schrödinger equation for a multi-particle system, the DFT method evaluates the ground-state structure and energy states of materials. DFT method is widely employed to study the electronic structure, chemical bonding, and surface phenomena, including adsorption, desorption, and elementary reaction steps on catalyst materials [31, 32]. It has also been applied to analyze catalytic and electrocatalytic reactions involving gaseous species in porous materials [33]. Furthermore, DFT modelling allows evaluation of reaction kinetics by calculating activation energies along different reaction pathways, thereby providing insights into the underlying mechanisms. MD is a physics-based modeling method used to study multi-body systems by employing classical Newton's laws of motion [34]. It is widely applied in the study of transport processes in materials, such as calculating diffusion coefficients using the Einstein equation [35]. MD modeling has been used, for example, to investigate oxygen diffusion in gadolinium-doped ceria (GDC) [36] as well as deformation mechanisms under mechanical loading [37]. It is also effective for predicting thermal properties; for instance, the thermal conductivity of ZrO_2 and YSZ was evaluated using MD simulations [38]. KMC is a stochastic modeling method used to simulate time-dependent processes, such as atomic diffusion in many-particle systems [39]. Unlike MD methods, the KMC method generates sequences of system states based on probabilistic event rates

rather than solving equations of motion, thereby permitting larger time steps [40]. Gunn et al. [41] used the KMC method to investigate oxygen and cation diffusion in 10 mol % GDC, while Krishnamurthy et al. [42] investigated oxygen diffusion in the YSZ system. In the latter study, activation energies obtained from DFT calculations were used as input parameters for the KMC simulations, and an optimal oxygen diffusivity was reported for yttria contents in the range of 8 %–12 %. Overall, microscale modeling methods enable the evaluation of fundamental physicochemical properties, including thermodynamics, reaction kinetics, electrical and thermal conductivity, and diffusion coefficients. It has become a powerful tool for the development of novel materials and the optimization of material structures at the atomic level. However, its applicability is limited by modeling time and length scales. Consequently, microscale modeling cannot directly capture larger-scale properties, such as the porous structure of electrodes and species transport within these structures.

1.3.2 Mesoscale modeling

Mesoscale modeling serves as a crucial bridge between atomistic simulations and continuum-scale models by capturing microstructural effects on intermediate length and time scales. It is particularly relevant in the analysis of degradation mechanisms and the optimization of electrode microstructures, since performance and durability are strongly dependent on the morphology, composition, and structural properties of the particles, which determine species transport and electrochemical activity. Using realistic electrode structures as computational domains, mesoscale models provide valuable insights for the design of high-performance cells and stacks. Commonly employed approaches at this scale include the Lattice Boltzmann method (LBM), the Discrete Element method (DEM), and the Phase-field method (PFM), which enable the investigation of interfacial dynamics, transport processes, and microstructural evolution. The LBM is a mesoscopic computational fluid dynamics modeling approach particularly well suited for simulating transport phenomena in porous media with complex geometries and multiphase flows [43]. In LBM, the computational domain is represented as a

discrete lattice in which particles move between positions by calculating the particle velocity distribution function. The Lattice Boltzmann method is commonly used to study internal flow behavior at the pore scale in the porous electrodes of SOFCs. LBM is often employed to model mass transport and electrochemical reaction processes within porous SOFC electrodes [44, 45]. The anode overpotential strongly influences SOFC performance [46], and its prediction provides insights into polarization behavior. LBM has been applied to simulate polarization resistance and overpotential in Ni-YSZ anodes, with the results validated against experimental impedance and electrochemical data [47, 48]. Furthermore, LBM enabled a three-dimensional analysis of the distributions of electrochemical potential and current density within the anode microstructures [47]. The DEM, first introduced by Cundall and Strack [49], is a well-established method for simulating packings of particles, particle flows, and fluid-particle interactions. It models the behavior of individual particles considering the forces of contact interactions, gravity, and friction [50]. Applications of DEM in SOFC research have been widely reported. DEM has been applied to generate realistic electrode microstructures, including partially sintered morphologies, to investigate packing behavior and evaluate effective electrical and ionic conductivity [51, 52]. DEM has also been employed to model the mechanical response of electrodes, including elastic and failure behavior [53].

PFM is a continuum-based approach that describes microstructural evolution using continuous field variables (order parameters) governed by thermodynamic and kinetic principles. It is well established for simulating processes such as phase transformations, grain growth, and particle coarsening in electrode materials [54–56]. In SOFCs, phase-field modeling can simulate the evolution of the three-phase microstructure (electrode, electrolyte, and pores), enabling the prediction of phenomena such as Ni coarsening in anodes and its impact on TPB distribution, electrochemical performance, and long-term degradation [54]. PFM predictions can be validated against experimental results obtained from imaging techniques such as scanning electron microscopy (SEM), transmission electron microscopy (TEM), and X-ray micro-computed tomography. PFM's ability to model such complex microstructural evolutions plays a key role in understanding

and mitigating degradation phenomena, which present a major bottleneck for the commercialization of fuel cell and electrolysis technologies [57, 58]. In this work, a phase-field method is employed to simulate the microstructural evolution of SOFC anodes under high-temperature operating conditions, in which pronounced morphological changes are observed during operation. Mesoscopic electrode models complement macroscopic cell and stack models by capturing phenomena that are difficult to resolve on larger scales, including Ni coarsening, carbon deposition, and the evolution of microstructural parameters. These models provide detailed insights into reaction mechanisms and structural changes within porous electrodes, thereby enabling more accurate prediction of electrode performance. Given that the overall performance of SOFCs is strongly determined by the electrode microstructure, achieving an optimal electrode configuration is essential for efficient and durable operation. Outputs from mesoscopic simulations, such as effective transport properties (e.g., ionic conductivity and gas diffusivity) and microstructural properties, can be incorporated as inputs into macroscopic continuum models to describe the performance of the entire cell or stack. In cell and stack models, microstructural parameters such as TPB, Ni and GDC specific surface area are often represented by averaged values, whereas their accurate characterization requires mesoscale electrode simulations. These parameters, particularly the TPB density, play a decisive role in electrochemical performance and can be fully understood at the micro- or mesoscale. Mesoscopic modeling thus provides detailed insights into reaction-transfer mechanisms, parameter estimation, and degradation processes that cannot be captured at the macroscopic level. The resulting effective properties and mechanistic descriptions can then be incorporated into cell and stack models, enabling more reliable large-scale simulations and facilitating the design and optimization of commercial SOFC systems. Figure 1.3 shows mesoscale modeling at the electrode microstructure level, demonstrating its role as a crucial bridge linking atomistic and continuum-scale approaches by capturing microstructural effects over intermediary length and time scales.

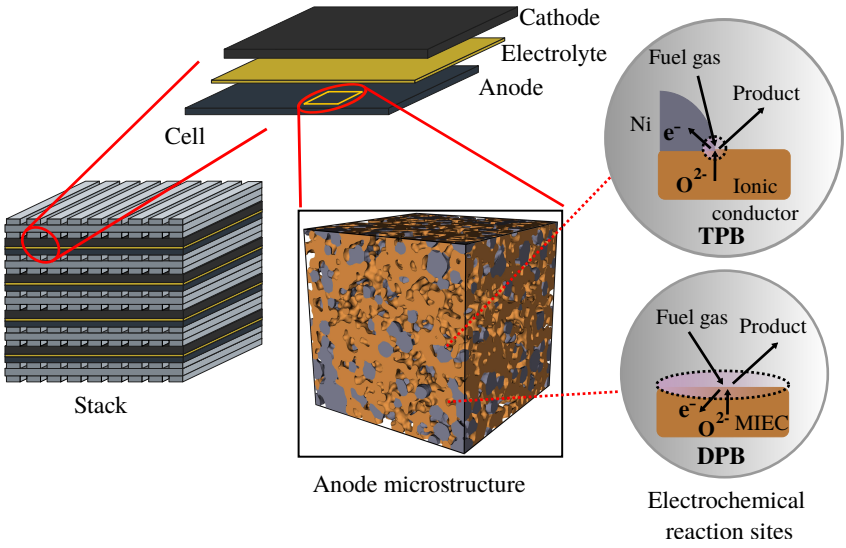


Figure 1.3: Different modeling levels for solid oxide fuel cells, spanning from stack-level to atomic-scale reaction kinetics.

1.3.3 Macroscale modeling

At the macroscopic level, the overall behavior of the SOFC is described by integrating smaller-scale information into continuum models for system-level analysis. Such models typically consist of coupled partial differential equations, including the Nernst-Planck, Poisson, and conservation equations, to simulate multiphysics transport processes. These frameworks enable the prediction of key parameters, including gas and temperature distributions, material concentrations, and current density [59–61]. Cell-level modeling simulates the operation of a single SOFC cell under controlled conditions, often employing inputs derived from mesoscale simulations. A continuum approach is commonly adopted, in which porous electrodes and the species therein are treated as a homogenized continuum [39]. Electrochemical response is modeled using formulations based

on the Nernst equation and polarization losses. SOFC cell/stack models are generally classified as steady-state or transient models. Steady-state models neglect time-dependent terms and are primarily employed to investigate transfer mechanisms, fuel flexibility, structural optimization, and stress distribution. In contrast, transient models capture dynamic behavior, including start-up, degradation, and other time-dependent aspects in SOFC operation. Although cell-level models provide detailed insights into the behavior of individual cells, practical applications require the integration of multiple cells into stacks. Nevertheless, the results from cell-level simulations serve as essential inputs for stack- and system-level modeling, thereby supporting the design and optimization of large-scale SOFC systems. Stack-level modeling describes the behavior of SOFC stacks consisting of multiple cells, interconnects, manifolds, seals, and support frames. These models provide a detailed description of stack operations and are commonly used to optimize performance through improvements in stack design and operating strategies. At this level, computational fluid dynamics (CFD) is typically used to analyze transport processes within the stack. These methods enable detailed predictions of physicochemical processes based on conservation equations for mass, momentum, and energy, along with electrodynamic reaction kinetics. System-level modeling considers the entire SOFC system, including the stacks and balance of plant (BoP) components such as pumps, heat exchangers, fuel processing units, and power conversion systems (Alternating Current/Direct Current converters). The primary objective is to enhance overall system efficiency by optimizing system design and operating strategies. This is typically achieved through thermodynamic analyses based on the first and second laws of thermodynamics. Additionally, system-level models provide boundary conditions for stack and cell-level models. At this level, modeling approaches are generally categorized into lumped parameter models (black-box models) and spatial distribution models [62]. The widely used lumped parameter models are based on the principles of mass and energy conservation and offer computational efficiency, although the detailed field distributions remain unaccounted for. In contrast, spatial distribution models capture the variation of key parameters within the system and provide deeper insights into spatial effects and system behavior [63–65]. Interestingly, modeling of SOFCs is often presented from a top-down paradigm, from the system down to the cell/stack and then to the

electrode, whereas practical development typically follows the reverse direction. High-performance systems are achieved by first designing and optimizing the electrodes, enabling the fabrication of high-performance cells and stacks, and ultimately leading to stable and efficient operation at the system level. The integration of SOFC modeling with artificial intelligence is emerging as a promising research direction. By linking microscale physical mechanisms with macroscale system behavior, machine learning (ML) techniques can enhance predictive accuracy while reducing computational cost, thereby accelerating the development and optimization of energy systems [66–69].

1.4 SOFC anode microstructures

The increasing requirements for the performance and durability of SOFCs underscore the importance of a detailed understanding of the 3D microstructure of the electrodes at the micrometer scale, as this structure affects both transport processes and reaction kinetics. The microstructural features directly influence key electrochemical properties, such as polarization resistance, effective conductivity, and power density [70]. Therefore, the precise characterization and correlation of the microstructure with electrochemical performance is imperative for optimizing electrode design. Electrode microstructure also plays a critical role in ensuring the proper functioning of all physical phenomena within an SOFC, and analyzing the geometry and evolution of the microstructure during operation provides insights into structure-performance correlations. Furthermore, three-dimensional digital representations of electrode microstructures enable the application of computational tools for the quantitative characterization of key morphological properties and physical simulations.

Currently, porous electrode microstructures are generated using both experimental reconstruction methods and numerical approaches. Experimental methods rely on high-resolution instruments (e.g., SEM) to obtain 2D slices, which are subsequently processed into 3D structures using image processing technologies. Common tomography methods include X-ray computed tomography (X-ray CT),

FIB-SEM, electron tomography, and atomic probe tomography, with increasing resolution provided at the expense of smaller reconstructed volumes. Among these methods, X-ray CT and FIB-SEM are most frequently employed in porous electrode reconstruction studies. Earlier work, dating back to about two decades ago, employed FIB-SEM to reconstruct the electrode microstructure of the SOFC anode and extract key parameters such as TPB density and tortuosity [71]. Although these techniques provide accurate representations of real structures, they are not predictive and depend on the availability of samples, image resolution, and post-processing, all of which can lead to uncertainties; FIB-SEM is a destructive technique, precluding repeated analyses of the same region, and is time-consuming, as reconstructions take hours to days [72]. As an alternative, numerical approaches, including statistical, physics-based, and Artificial Intelligence (AI)- driven methods, are being applied to generate synthetic microstructures. Stochastic methods generate 3D porous structures by imposing statistical constraints such as porosity and pore size distribution, while physics-based approaches generate the 3D microstructure by simulating its formation processes. These digitally generated 3D structures enable multiphysics simulations to investigate electrochemical, thermal, mechanical, and morphological behavior. In the microstructural analysis of heterogeneous SOFC electrodes, the representative volume element (RVE) is essential to ensure quantitative reliability. The RVE defines a sufficiently large volume that is statistically representative of the overall structure [73], meaning that the measured properties are independent of the chosen spatial location. Due to the intrinsic heterogeneity of electrode microstructures and limitations in the field of view with imaging techniques, careful selection of the RVE is necessary to capture key morphological properties for accurate prediction of transport and electrochemical behavior. The RVE size is a variable quantity and depends on several factors, such as the phase volume fraction and the characteristic particle size. Therefore, it must be chosen so that the RVE is neither undersized, which leads to statistical bias, nor excessively large, which unnecessarily increases computational resources.

While 3D experimental reconstructions and synthetic microstructures provide digital representations, their meaningful interpretation and application in predictive modeling require quantitative descriptors such as particle size distribution, specific

surface area, tortuosity, and TPB length. These parameters determine the electrochemical reaction sites and control the transport of electrons, ions, and gaseous species, thereby determining local reaction kinetics and overall electrochemical performance. Several methods can be applied to quantify the microstructure, with each descriptor capturing specific aspects of electrode behavior. Tortuosity, for example, characterizes the complexity of transport pathways and strongly influences the effective transport properties in porous electrodes. The TPBs represent the primary reaction site in conventional SOFC electrodes, and therefore their density is an important performance indicator. Furthermore, anodes composed of MIEC, such as Ni-GDC, have attracted increasing attention due to their improved electrochemical performance, resulting from the DPBs in addition to the conventional TPBs. Figure 1.4 shows the 3D SOFC anode's microstructure as well as key morphological and effective properties, including TPBs, DPBs, tortuosity, specific surface area, mean particle diameter, volume fraction, and elastic moduli, that can be extracted from the RVE. These descriptors are essential to establish correlations between microstructure, electrochemical performance, mechanical integrity, and degradation behavior during operation.

1.4.1 Relationship between microstructure and fuel cell performance

To evaluate SOFC performance, it is essential to understand the relationship between electrode and cell performance. Figure 1.5 shows a typical current-voltage curve (I-V curve) for an SOFC. The dashed line represents the ideal voltage resulting from the Nernst potential under standard conditions. At open circuit (zero current), deviations from standard conditions result in a lower measured voltage. As current flows, additional voltage losses arise due to finite reaction kinetics. These voltage losses, referred to as overpotentials or polarization losses, collectively reduce the operating voltage below its ideal value and determine the overall performance of the cell. The magnitude of the voltage drop increases with current density and depends on factors such as temperature, pressure, gas composition, and flow rate, as well as material properties. Total polarization is the

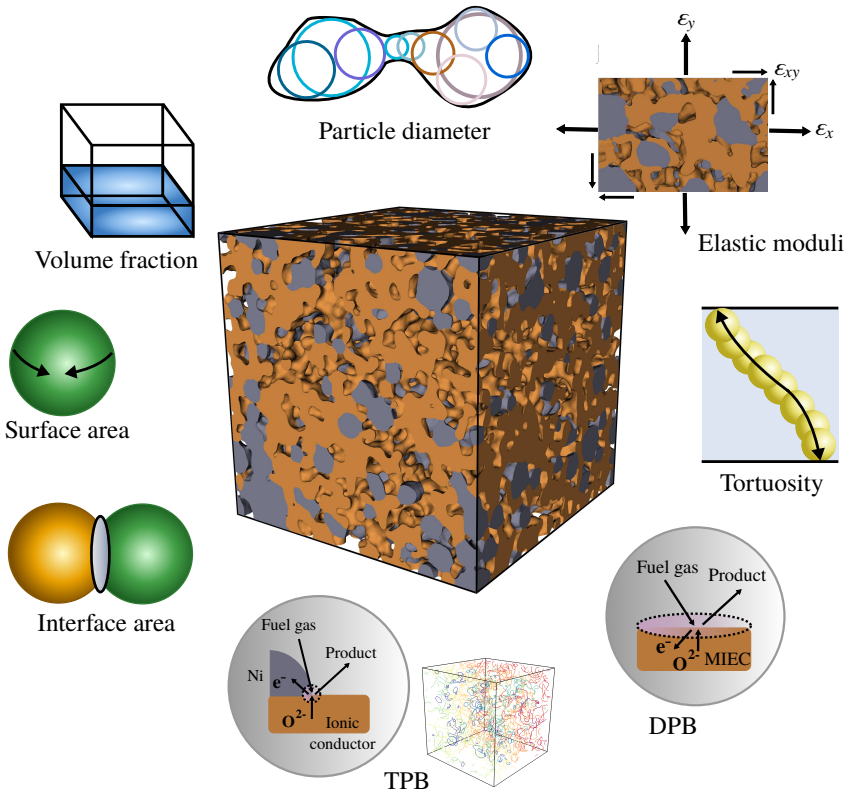


Figure 1.4: Representative Volume Element (RVE) of an SOFC anode microstructure, along with key microstructural characterization metrics related to structural features, electrochemical performance, and mechanical integrity.

sum of activation, ohmic, and concentration losses. Although these losses cannot be completely eliminated, they can be minimized through appropriate material selection and optimized cell design. At low current densities, the activation overpo-

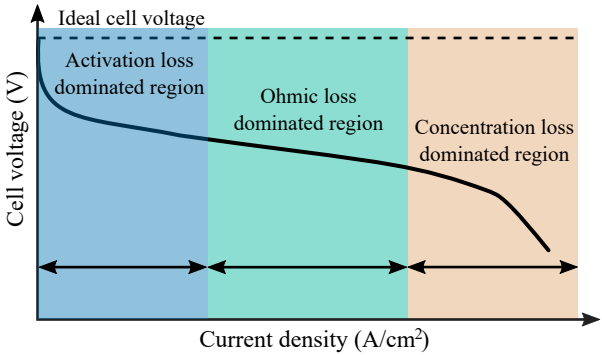


Figure 1.5: Schematic representation of the current-voltage characteristic curve of an SOFC, indicating three major losses contributing to the cell voltage drop: activation loss, ohmic loss, and concentration loss.

tential dominates and is governed by the kinetic processes of the electrochemical reactions within the electrode's microstructure. These reactions are required to overcome an intrinsic energy barrier, known as the activation energy, thereby resulting in activation or charge-transfer polarization. Since electrochemical reactions occur at both TPBs and DPBs in Ni-GDC anodes, increasing the density and distribution of TPBs and DPBs through microstructural optimization effectively reduces activation polarization and improves the overall performance of the cell. At intermediate current densities, cell performance is primarily limited by ohmic resistance. Ohmic polarization arises from the resistance of the conducting ions through the electrolyte, electrons through the electrodes and current collectors, and interfacial contact resistances between the cell components. These resistances are strongly influenced by microstructural properties, particularly tortuosity and constrictivity, which describe the complexity and narrowing of the transport paths for ions and electrons. Lower tortuosity values shorten the effective transport paths

and thereby reduce the ohmic resistance. Furthermore, the intrinsic electronic and ionic conductivities of the constituent materials also influence the magnitude of ohmic losses within the system. At high current densities, cell performance is primarily restricted by concentration overpotentials associated with limitations in mass transport. Concentration or diffusion polarization arises when electrochemical reactions are limited by the rate of reactant supply and/or product removal, such that diffusion to and from the electrochemically active sites is slower than that corresponding to the charging/discharging current. Under these conditions, assuming sufficient reaction sites and minimal restrictions on charge transport, the dominant losses arise from gas transport through the porous electrode structure. Reducing the mass transport resistance through optimized porous structure and tortuosity values enhances the gas diffusion pathways and thereby mitigates concentration losses.

1.4.2 Degradation of SOFC anodes[1]

»The degradation of Ni-based cermet anodes arises from several phenomena, including poisoning by fuel impurities [75], coking [76], redox cycling [77–79], and microstructural evolution [16]. In terms of microstructural degradation, the coarsening of nickel particles is found to be the primary degradation mechanism in the microstructure of SOFC anodes [80, 81]. Furthermore, polarization effects also influence Ni morphology, as demonstrated by Jiao et al. [82], observing Ni spreading along the YSZ surface near active TPBs in patterned Ni film anodes. Several studies investigated the morphological changes observed in commonly used anodes, with aging primarily caused by Ni coarsening, agglomeration, and depletion [83–85]. In contrast to the relatively stable zirconia matrix in Ni-YSZ systems, Ni-GDC anodes exhibit notable GDC phase evolution [83, 86]. Several experimental studies reported findings under electrochemically operated conditions [83, 87, 88], whereas some were performed under purely thermal/open-circuit voltage (OCV) conditions [86, 89]. In polarized conditions, Zekri et

[1] The content of this section has been taken directly from Jeela et al. [74] with minor linguistic changes.

al. [83] reported a significant GDC agglomeration after 20,000h, which reduced the Ni-Ni and Ni-GDC contacts, decreasing the TPB density and increasing the electronic resistance. Their work also reported the formation of a GDC coating on Ni surfaces after about 15,000h, which suppresses Ni coarsening but hinders mass transfer, further reducing TPB density and Ni percolation. Holzer et al. [86] reported similar Ni surface coverage after only 2,286 hours under humidified OCV conditions. Recently, Liu et al. [89], also under humidified OCV conditions, reported Ni coarsening associated with minor GDC growth, but found no evidence of nano-GDC particles or nanoscale changes in the GDC phase. In addition, operando studies highlighted Ni migration, spreading, and splitting at active TPB sites in both Ni-YSZ and Ni-GDC systems under polarization [87, 88]. This work employs reconstructed electrode microstructures from a cell aged purely under thermal, humidified open-circuit conditions for model validation. Understanding the relationship between these microstructural evolutions and the degradation of electrochemical performance is essential for improving SOFC durability and optimizing anode design.«

1.5 Modeling of SOFC anode degradation[2]

1.5.1 Microstructural evolutions

Ni-YSZ anodes »The coarsening of Ni in solid oxide cell (SOC) electrodes by phase-field modeling is extensively studied [54, 91–101]. Most models assume nickel self-diffusion, either in the volume or at the surface, driven by curvature effects. The early work by Chen et al. [91] used FIB-SEM reconstructed 3D microstructures with limited size and investigated the influence of wettability on microstructural evolution, a topic that was further explored in the work by Li et al. [54], Davis et al. [92], Jiao et al. [94], Lei et al. [97], and Sun et al. [100]. Ni

[2]The content of this section has been taken directly from Jeela et al. [74, 90] with minor linguistic changes.

coarsening in SOC electrodes is known to proceed significantly faster in a humid atmosphere, though the underlying mechanisms are not yet fully understood. Lei et al. [95, 97, 101] investigated Ni migration driven by $Ni(OH)_2$ diffusion and changes in Ni-YSZ wettability using a multiphysics model. They reported that the accelerated coarsening under humid conditions cannot be explained by the diffusion of $Ni(OH)_2$ alone. Instead, the electrochemical formation of $Ni(OH)_x$ at high overpotentials may enhance Ni transport in fuel cell mode.

Phase-field models of SOC coarsening were implemented with different mass transport mechanisms, ranging from predominant surface diffusion at Ni-pore interfaces [91, 93] to the combination of interfacial diffusion across multiple phase boundaries [92]. In the early models, the multiphase Cahn-Hilliard model [102] and the combination of Allen-Cahn and Cahn-Hilliard formulations [103, 104] were mostly employed. Lei et al. [105] advanced the Chen-Fan model [106] toward tunable interfacial energies and consistent interfacial thicknesses, allowing for a more accurate representation of wetting conditions in evolving microstructures. The phase-field model utilized in this work, developed by Choudhury and Nestler [107] and extended by Hoffrogge et al. [108], provides several key advantages. It allows the interfacial energies to be controlled independently for each binary interface while maintaining uniform and finite interface thicknesses. Furthermore, the model enables an accurate representation of interfacial diffusion, facilitating the direct incorporation of experimentally measured surface diffusivities and wetting angles into the simulations. Hoffrogge et al. [98] employed this model to investigate the coarsening in FIB-SEM reconstructed Ni-YSZ anodes and the role of Ni wettability on YSZ. Simulated results were used as inputs to an established transmission line model to predict performance degradation. Here, the YSZ phase was treated as stationary, and Ni transport along the Ni-YSZ interfaces was neglected due to a lack of experimental data. In their work, although the results presented were not validated directly against aged FIB-SEM 3D reconstructions of Ni-YSZ microstructures, the quantitative evolution of microstructural properties was reported and stated to be consistent with experimental observations and available literature.

Ni-GDC anodes It is noteworthy to mention that the above-mentioned phase-field studies were primarily focused on Ni-YSZ anodes, where microstructural evolution is dominated by Ni coarsening, while the YSZ phase remains largely stable. In contrast, phase-field investigations of Ni-GDC systems remain relatively unexplored due to their complexity, as the evolution of both the Ni and GDC phases results in a more complex microstructural evolution. Sun et al. [109] developed an integrated mesoscale model to predict the morphological and performance degradation of Ni-GDC over long-term operation. In their study, the phase-field model was utilized to simulate compositional changes, considering the interactions between Ni-GDC and wettability. In their work, synthetic microstructures were used, and the model results were validated against experimental data from the literature of Holzer et al. [86]. Previous work, while informative, relied on indirect validation involving only three microstructural properties (mean particle diameter of nickel, GDC, and TPBs) from literature data. Recently, Chang et al. [110] developed a multi-scale simulation framework combining discrete element modeling to generate initial Ni-GDC anode microstructures and a phase-field model to simulate the evolution of the Ni-GDC anode microstructure. In their work, validation of the generated microstructures was limited to a small set of descriptors, primarily TPB density and tortuosities of GDC and pore, and the simulation results were validated against experiments using primarily TPB density values from the literature. Due to computational limitations, the modeled electrode volume was restricted to $3.5 \times 3.5 \times 1.1$ μm^3, limiting the representativeness of the anode microstructure. In contrast, the validation strategy in this work incorporates both pristine and experimentally aged FIB-SEM 3D microstructures, allowing direct validation of all key descriptors – particle sizes, TPB densities, tortuosities, and specific surface areas – for a more comprehensive and quantitative assessment of model predictability. Furthermore, the current work also provides detailed insights into the sensitivity of surface and interfacial energies, their role in morphological evolution, and the resulting impact on anode performance with large-scale phase-field simulations.

1.5.2 Mechanical degradation

It is well established that SOFC anode microstructures profoundly influence macroscopic properties, including mechanical integrity and electrochemical performance. In particular, porosity has been shown to influence the elastic modulus and biaxial strength significantly [111–113]. Despite extensive studies on electrochemical behavior and microstructure evolution, direct and time-resolved investigations of mechanical property degradation under steady-state, isothermal aging conditions remain scarce. These studies are critical since the anode serves as a load-bearing component in many SOFC designs, such as anode-supported and metal-supported cells, where microstructural changes directly affect mechanical reliability [114]. Liu et al. [115] developed a deep learning-based homogenization framework that links porous Ni-YSZ anode microstructures to effective macroscopic properties, including elastic modulus, Poisson's ratio, shear modulus, and thermal expansion, and demonstrates their dependence on porosity and Ni content. However, their work was limited to Ni-YSZ anodes, and the effects of aging, as well as the influence of electrolyte volume fraction, were not investigated. More recently, Elmoghazy et al. [116] performed strain-controlled numerical homogenization to evaluate the evolution of effective elastic properties in Ni-GDC anodes during aging, but their analysis was confined to a single initial microstructural configuration. Thus, a systematic investigation of how variations in initial Ni-GDC microstructures, particularly phase volume fractions, affect effective mechanical properties and their degradation during aging is still lacking. To the best of our knowledge, this has not been comprehensively addressed in the literature. In multi-scale and multi-physics SOFC modeling, accurate macroscopic mechanical parameters are essential for stress analysis under thermal loading [117]. Since these properties are determined by the microstructure of the electrode, establishing quantitative correlations between microstructural features and macroscopic mechanical responses, together with electrochemically relevant metrics such as TPBs, DPBs, and tortuosities, is essential.«

1.6 Research aim and objectives

The overall aim of this dissertation is to develop a comprehensive computational framework for understanding, predicting, and optimizing the microstructural evolution and aging behavior of Ni-GDC SOFC anodes under long-term operating conditions. This work combines FIB-SEM reconstructed 3D microstructures, phase-field simulations, and machine learning approaches to establish quantitative correlations between microstructural features and key indicators of electrochemical performance and mechanical integrity. The main objectives of the thesis are as follows:

- Gain a comprehensive understanding of the microstructural processes occurring in Ni-GDC SOFC anodes during operation, together with key descriptors relevant to electrochemical performance and mechanical integrity, and the phase-field method.
- Develop a machine learning framework for identifying unknown physical parameters under given SOFC operating conditions by integrating pristine and aged FIB-SEM reconstructed 3D microstructures and phase-field simulations.
- Apply the phase-field model incorporating surface and interfacial diffusion along the Ni/GDC interface to perform quantitative 3D simulations of Ni and GDC coarsening in SOFC anodes, and validate the model's predictive capability under different initial conditions of the FIB-SEM reconstructed 3D microstructures.
- Perform large-scale aging simulations of Ni-GDC SOFC anodes to predict microstructural evolution and performance degradation over operational times of up to 60,000 hours.
- Extend the structure generator workflow to create realistic digital twins of Ni-GDC anode microstructures and validate them against FIB-SEM reconstructed 3D microstructures using a comprehensive set of quantitative

descriptors, including structural, geometric, electrochemically relevant, and mechanical properties.

- Investigate the mechanical behavior of Ni-GDC anodes, including elastic moduli and stress distributions resulting from the thermal expansion mismatch between Ni and GDC under steady-state isothermal aging conditions.
- Integrate synthetic microstructures with phase-field aging simulations to optimize the microstructural design of Ni-GDC anodes and provide insights into initial performance and durability, considering both electrochemical performance and mechanical integrity-related metrics.

1.7 Structure of the thesis

This dissertation begins with an introduction to the fundamental principles of fuel cells, with a particular focus on SOFCs, and then reviews state-of-the-art modeling approaches for SOFCs at scales ranging from atomistic-scale models of reaction kinetics to macroscopic system-level models, with a strong emphasis on phase-field methods at the mesoscale for describing microstructural evolution. The role of the anode microstructure in determining the electrochemical performance and durability of SOFCs is discussed, together with experimentally observed degradation mechanisms and current modeling approaches. From this introduction, the key research gaps are identified, and the research questions and objectives of this dissertation are formulated. The remainder of this dissertation is structured as follows. Chapter 2 details the methodological framework, comprising the grand-potential multiphase-field model employed for aging simulations, the extended structure generator workflow, the solid mechanics formulation for computing the mechanical response of the anode, and the procedures for statistically quantifying RVEs of the FIB-SEM reconstructed 3D anode microstructures. Chapter 3 introduces the Bayesian Active Learning framework, developed for identifying unknown physical parameters under given SOFC operating conditions. The framework is first presented, validated, and subsequently applied to FIB-SEM

reconstructed 3D anode microstructures to obtain the input parameters required for the multiphase-field model. Chapter 4 employs these determined parameters as inputs for multiphase-field aging simulations. Simulation results are then validated against experimental microstructures aged for 240h and 1,100h, respectively, using a comprehensive set of quantitative microstructural descriptors across distinct initial conditions. Subsequently, large-scale aging simulations of up to 60,000h are presented, and the influence of phenomena such as Ni and GDC wetting on the microstructural evolution of the anode, and thereby on its performance, is compared. Chapter 5 demonstrates the extended structure generator's ability to create a digital twin of the Ni-GDC SOFC anode. The generated structures are validated both qualitatively and quantitatively against experimental microstructures using an extensive set of structural, geometric, and mechanical properties, and the robustness of the generator in creating reliable synthetic microstructures is also demonstrated. Chapter 6 builds upon the validated predictive capability of the phase-field model and the structure generator. Fifteen synthetic Ni-GDC anode microstructures with different volume fractions are generated to investigate the influence of phase compositions on microstructural degradation and mechanical integrity, with the objective of optimizing the microstructural configuration of the SOFC anode for both initial performance and long-term durability. In addition to electrochemical performance metrics, this analysis also considers mechanically relevant properties as well as the stress distributions resulting from the thermal expansion mismatch between Ni and GDC under steady-state isothermal aging conditions. Finally, Chapter 7 summarizes the key findings of the dissertation and provides an outlook on future research directions.

2 Frameworks for microstructural evolutions and quantification

2.1 Introduction to the phase-field method

The evolution of the microstructure is driven by the minimization of total free energy, which may include chemical free energy, interfacial, elastic, magnetic, and electrostatic energies, as well as externally applied fields such as electric and magnetic fields. Due to the complexity and nonlinearity of these processes, numerical methods are often required. Traditional approaches to modeling microstructure evolution treat the regions separating compositional or structural domains as mathematically sharp interfaces and explicitly track their evolution; although such an interface-tracking approach can be successful in 1D systems, it proves impractical for complex 3D microstructures. The phase-field method represents microstructures using continuous field variables describing composition and/or structural domains. In contrast to sharp-interface models, in which properties change discontinuously across interfaces, phase-field methods allow smooth transitions, resulting in diffuse boundaries between phases. For this reason, phase-field models are also referred to as "diffuse boundary" models, whereas the corresponding moving boundary problems are referred to as "sharp-interface" theories. Diffuse boundary models eliminate the need for explicit interface tracking, thus simplifying numerical implementation, particularly for complex 3D systems. Due to this advantage, phase-field methods are widely used in materials science and engineering and are increasingly being applied in other fields such as earth sciences, biology, and medicine [118, 119]. The origins of the diffuse interface approach can be traced back to early work by van der Waals on gas condensation [120],

Landau and Ginzburg on phase transitions [121], and Cahn and Hilliard on the thermodynamics of heterogeneous systems [104]. These approaches introduce phase-field variables (order parameters) to represent material states and simulate phase transitions. A key distinction can be made between conserved (typically associated with composition) and non-conserved variables, which describe structural features such as crystal orientation. The Cahn-Hilliard nonlinear diffusion equation governs the evolution of conserved field variables [104, 122], while non-conserved field variables follow the Allen-Cahn relaxation equation [123, 124] or the time-dependent Ginzburg-Landau equation [125]. These two kinetic equations constitute the basic physics underlying many commonly used phase-field models in the literature.

2.1.1 Two-phase models

2.1.1.1 Energy functional

In the simplest case, a single scalar order parameter ϕ is utilized to distinguish between two coexisting phases. The construction of a phase-field model typically begins with the formulation of a free energy functional $\mathcal{F}$ expressed in terms of the order parameter over a system of volume V. In its most basic form, this functional can be written as follows:

$$\mathcal{F} = \int_V f(\phi) + a_0 |\boldsymbol{\nabla}\phi|^2 \, \mathrm{d}V. \tag{2.1}$$

Here, $f(\phi)$ denotes the energy density ($\mathrm{J\,m^{-3}}$) defining the model's potential energy landscape, and the second term is a gradient energy scaled by a constant factor a_0 ($\mathrm{J\,m^{-1}}$). The potential term defines stable bulk phases as energy minima, while the gradient term enforces a finite interface width by penalizing sharp transitions. Common choices for $f(\phi)$ include the double well potential $f(\phi) \propto \phi^2(1-\phi)^2$ and the obstacle potential $f(\phi) \propto \phi(1-\phi)$, both are formulated such that $\phi = 0$ and $\phi = 1$ represent stable bulk states. Depending on how the evolution

of the order parameter is postulated, phase-field models can be roughly divided into two main classes discussed below.

2.1.1.2 Allen-Cahn model

Materials can undergo phase transitions without changing their composition, but instead by altering their crystallographic structure. In such cases, a non-conserved order parameter describes the structural evolution. Consequently, the Cahn-Hilliard nonlinear diffusion equation, which governs the evolution of a conserved field (introduced below), is not applicable. Instead, the dynamics follows an Allen-Cahn type equation [103], also referred to as the time-dependent Ginzburg-Landau equation. Here, the evolution of the order parameter is proportional to the functional derivative of the free energy $\mathcal{F}$:

$$\epsilon \frac{\partial \phi(\boldsymbol{x},t)}{\partial t} = -m \frac{\delta \mathcal{F}}{\delta \phi} = -m \left(\frac{\partial f(\phi)}{\partial \phi} - 2a_0 \nabla^2 \phi \right). \tag{2.2}$$

Here, m denotes the mobility parameter with the unit $\mathrm{m^4\,J^{-1}\,s^{-1}}$, while $\epsilon > 0$ determines the characteristic interface thickness. Positive mobility is required for evolution to proceed locally toward minimizing free energy.

2.1.1.3 Cahn-Hilliard model

In phase-field models of Cahn-Hilliard type [104], the functional derivative of the free energy is interpreted as the chemical potential, $\mu = \frac{\delta \mathcal{F}}{\delta \phi}$, which has units of $\mathrm{J\,m^{-3}}$. Gradients in the chemical potential drive a flux directed against it according to $\boldsymbol{j} = -M \boldsymbol{\nabla} \mu$, where $M > 0$ denotes the proportionality constant. Based on this flux density, the order parameter is treated identically to a composition, assuming a constant molar volume. As a result, it is conserved, resulting in the corresponding continuity equation

$$\frac{\partial \phi(\boldsymbol{x},t)}{\partial t} = -\boldsymbol{\nabla} \cdot \boldsymbol{j} = \boldsymbol{\nabla} \cdot (M \boldsymbol{\nabla} \mu) = M \nabla^2 \mu \,. \tag{2.3}$$

2.1.2 Multiphase-field models

Multiphase-field models extend the phase-field approach by replacing a single order parameter with a set of variables represented by an N-tuple $\boldsymbol{\phi} = \{\phi_\alpha, \phi_\beta, \ldots, \phi_N\}$ to represent N different phases. First introduced by Steinbach et al. [126], this class of models imposes a constraint $\sum_{\alpha=1}^{N} \phi_\alpha = 1$ enabling the order parameter ϕ_α to be interpreted as the local volume fraction of the α phase. Accordingly, only $N-1$ variables are independent in a system with N phases. The total free energy functional, including the bulk contribution (f_{bulk}), can then be expressed as follows:

$$\mathcal{F} = \int_V f_{\text{pot}} + f_{\text{grad}} + f_{\text{bulk}} \, \mathrm{d}V \,, \tag{2.4}$$

where f_{pot} denotes the potential energy density and f_{grad} corresponds to the contribution of the gradient energy. In the multiphase-field framework, the potential energy is constructed by setting the phase variables ϕ_α and ϕ_β with those of ϕ and $1-\phi$ in the two-phase formulations. Using the double-obstacle and double-well potentials discussed in Section 2.1.1.1, the initial expressions for the potential energy can be written as follows:

$$f_{\text{pot}}^{\text{ob},a} = \frac{16}{\pi^2 \epsilon} \sum_{\alpha=1}^{N} \sum_{\beta=\alpha+1}^{N} \gamma_{\alpha\beta} \, \phi_\alpha \phi_\beta \,, \qquad f_{\text{pot}}^{\text{well},a} = \frac{9}{\epsilon} \sum_{\alpha=1}^{N} \sum_{\beta=\alpha+1}^{N} \gamma_{\alpha\beta} \, \phi_\alpha^2 \phi_\beta^2 \,. \tag{2.5}$$

Here, $\gamma_{\alpha\beta}$ denotes pairwise interfacial energy. However, these forms can introduce non-physical (spurious) phases, necessitating a reformulation consistent with the summation constraint on the phase fields. A detailed discussion of this topic can be found in the work of Daubner et al. [127]. The formulated multi-obstacle potential, in general, can be expressed as follows:

$$f_{\text{pot}}^{\text{ob}} = \frac{16}{\pi^2 \epsilon} \sum_{\alpha=1}^{N} \sum_{\beta=\alpha+1}^{N} \gamma_{\alpha\beta} \, \phi_\alpha \phi_\beta + \sum_{\alpha=1}^{N} \sum_{\beta=\alpha+1}^{N} \sum_{\delta=\beta+1}^{N} \gamma_{\alpha\beta\delta} \, \phi_\alpha \phi_\beta \phi_\delta \,, \tag{2.6}$$

The triplet term, scaled by the higher-order term $\gamma_{\alpha\beta\delta}$, suppresses the formation of spurious phases at triple and higher-order junctions. To ensure $0 \leq \phi_\alpha \leq 1 \quad \forall\, 1 \leq \alpha \leq N$, a Gibbs simplex function can be numerically integrated into the multi-obstacle potential, and is defined as

$$\mathcal{G} = \begin{cases} 1 & \sum_{\alpha=1}^{N} \phi_\alpha = 1 \cap \phi_\alpha \geq 0 \,\forall\, 1 \leq \alpha \leq N \\ \infty & \text{else}\,. \end{cases} \tag{2.7}$$

Similarly, the gradient energy in multiphase-field models can be obtained by extending the two-phase system $a_0|\boldsymbol{\nabla}\phi|^2$ to a system of multiple order parameters. In accordance with the formulations in refs [126, 128], it can be expressed as follows:

$$f_{\text{grad}} = \epsilon \sum_{\alpha=1}^{N} \sum_{\beta>\alpha}^{N} \gamma_{\alpha\beta} \left|\phi_\alpha \boldsymbol{\nabla}\phi_\beta - \phi_\beta \boldsymbol{\nabla}\phi_\alpha\right|^2, \tag{2.8}$$

while following the formulation in ref [129], the gradient energy may alternatively be expressed as:

$$f_{\text{grad}} = -\epsilon \sum_{\alpha=1}^{N} \sum_{\beta>\alpha}^{N} \gamma_{\alpha\beta}\, \nabla\phi_\alpha \cdot \nabla\phi_\beta \tag{2.9}$$

For a more detailed discussion of the differences and alternative formulations of gradient energy, as well as its coupling with various potential energy terms, the reader is referred to ref [127].

The bulk energy f_{bulk} is interpolated in terms of phase-inherent contributions f_α as:

$$f_{\text{bulk}} = \sum_{\alpha=1}^{N} h_\alpha(\boldsymbol{\phi}) f_\alpha\,, \tag{2.10}$$

where $h_\alpha(\boldsymbol{\phi})$ is an interpolation function satisfying the conditions

$$h_\alpha(\phi_\alpha = 1, \phi_{\beta\neq\alpha} = 0) = 1 \tag{2.11}$$

$$h_\alpha(\phi_\alpha = 0) = 0\,. \tag{2.12}$$

For further details on interpolation constructions and their properties, the reader is referred to ref [130].

The evolution equation for the N order parameters, following the notation of Nestler et al. [128], can be expressed as

$$\tau(\boldsymbol{\phi})\,\epsilon\,\frac{\partial \phi_\alpha(\boldsymbol{x},t)}{\partial t} = -\frac{\delta \mathcal{F}}{\delta \phi_\alpha} - \lambda\,, \tag{2.13}$$

where λ denotes a Lagrange multiplier enforcing the phase-field sum constraint. The time relaxation parameter $\tau(\boldsymbol{\phi})$, representing the inverse of mobility, is commonly arithmetically interpolated from relaxation times of the binary interfaces

$$\tau(\boldsymbol{\phi}) = \frac{\sum_{\alpha<\beta} \tau_{\alpha\beta}\,\phi_\alpha\,\phi_\beta}{\sum_{\alpha<\beta} \phi_\alpha\,\phi_\beta}. \tag{2.14}$$

The choice of interpolation scheme (e.g., arithmetic/harmonic) significantly affects model behavior. In particular, studies from Enugala [131] have shown that arithmetic interpolation can lead to interface pinning at multi-phase junctions in practical simulations when the interface relaxation parameter $\tau_{\alpha\beta}$ differs by orders of magnitude.

An alternative formulation proposed by Steinbach and Pezzolla [129] expresses the evolution equation as

$$\epsilon \frac{\partial \phi_\alpha(\boldsymbol{x},t)}{\partial t} = \frac{1}{\tilde{N}} \sum_{\beta=1}^{N} m_{\alpha\beta} \left(\frac{\delta \mathcal{F}}{\delta \phi_\beta} - \frac{\delta \mathcal{F}}{\delta \phi_\alpha} \right). \tag{2.15}$$

This formulation avoids any interpolation of mobilities or relaxation parameters by relying solely on pairwise mobilities $m_{\alpha\beta}$. It also implicitly ensures the phase-field sum constraint, eliminating the need for a Lagrange multiplier when the initial condition complies. Here, $\tilde{N}$ denotes the number of locally active phases, i.e., phases with non-zero values or gradients of ϕ. In the case of two phases ($N = 2$), both the above formulations reduce to the two-phase Allen-Cahn model (eq 2.2).

2.2 Coupled modeling of diffusion and phase transformation

Until now, the discussion has focused on phase-field formulations applicable either to binary (two-phase) systems or to general multiphase configurations. However, the simultaneous interplay of multiple mechanisms is involved in several physical phenomena, notably the coupling between the diffusion of species and the evolution of a non-conserved order parameter. To address such cases, various phase-field models were formulated, integrating both effects within a unified framework. These coupled effects are essential for accurately describing processes such as solidification, in which phase transformations and the diffusion of solutes occur concurrently, and sintering, in which grain growth and coarsening occur simultaneously. A highly desirable characteristic in phase-field modeling of multicomponent systems is the decoupling of interfacial energy and thickness. Early formulations either assumed equal compositions of both phases across the interface [132] or a constant partition coefficient [133]. In the model proposed by Wheeler et al. [132], the interfacial region is treated as a mixture of both phases with an equal composition. However, this approach results in a nonzero contribution of the chemical free energy in the interfacial region, which scales with the interfacial thickness. Consequently, the interfacial energy is intrinsically coupled to the interfacial thickness. This imposes an upper limit on the permissible interface thickness for a given material system and requires a simulation resolution sufficiently fine to resolve the interfacial region. As a result, the computational efficiency of these types of models is limited, particularly for large-scale simulations. To overcome these limitations, several alternative formulations have been proposed.

Kim et al. [134] introduced the first approach to addressing such problems, based on analogies between pure material and an alloy from sharp-interface laws. In this approach, the chemical potential is identified as an intensive property that is continuous across an interface, in contrast to composition, which exhibits a jump discontinuity. The Kim-Kim-Suzuki model describes the interface region in a

binary two-phase alloy system as a mixture of two phases with different phase compositions, but constrained to the same chemical potential

$$\mu = \frac{\partial f_\alpha(c_\alpha)}{\partial c_\alpha} = \frac{\partial f_\beta(c_\beta)}{\partial c_\beta}. \tag{2.16}$$

As a result, the chemical energy in the interfacial region does not contribute to the interfacial energy, thereby decoupling the interfacial thickness from the interfacial energy. This decoupling allows for a larger interface thickness and a coarser simulation resolution. However, the Kim-Kim-Suzuki model introduces additional variables of phase composition, leading to increased complexity in the numerical solving of the equations. A nearly identical model was later proposed by Eiken et al. [135], in which the Kim-Kim-Suzuki model was generalized to multiphase and multicomponent systems. In this model as well, the governing equations are derived from a free-energy functional that includes dependencies of the order parameters ϕ_α as well as the phase-specific compositions c_α.

Grand-potential model A phase-field model for alloy solidification using a grand-potential functional has been developed, which retains the advantage of decoupling interfacial energy with interface thickness whilst eliminating the requirement for phase concentration variables. This grand-potential model was independently derived by Plapp [136] and by Choudhury and Nestler [107], with minor differences. Plapp proposed a two-phase model for the non-conserved order parameter employing a double-well potential, whereas Choudhury et al. [107] proposed a multiphase framework with an obstacle potential. In the grand-potential framework, the governing equations are derived from a functional based on the grand-potential density, rather than the Helmholtz free-energy density commonly utilized in phase-field models. The primary dynamic variables of the grand-potential functional (Ω) are the phase-field ϕ and the chemical potential μ, where μ is a conjugate of the composition c and represents an intensive thermodynamic quantity, analogous to temperature. The transition from concentration-based to chemical potential-based representations is achieved through a Legendre transformation of the free-energy density. In this framework, the thermodynamic bulk

driving force is given by grand-potential densities ψ_α rather than free-energy densities f_α and can be graphically obtained via a common-tangent construction. Due to the grand-potential formulation, the chemical energy does not contribute to the interfacial energy across the phases, which simplifies the parameterization and allows the interfacial thickness to be decoupled from the interfacial energy. This decoupling allows relatively larger interfacial thicknesses and improved computational efficiency. Furthermore, the composition evolution equation is substituted by a chemical potential evolution equation, which simplifies the numerical treatment. It is noteworthy that, in its simplest form (a two-phase, single-component system with a well-potential), the grand potential model provides results similar to the Kim-Kim-Suzuki model.

2.2.1 Interface and bulk diffusion

In all of the formulations of the grand-potential framework discussed above, mass transport primarily occurs via bulk diffusion, and the composition evolution is often formulated to exclusively consider bulk diffusivities. However, such considerations overlook the physically significant contribution of atomic migration along the local tangential directions of the interface, i.e., surface diffusion. To overcome these limitations, Hoffrogge et al. [108] extended the existing grand-potential multiphase-field model of Choudhury et al. [107] by explicitly incorporating an interfacial flux term into the composition evolution equation. Their model not only captures surface diffusion mechanisms in a physically consistent manner but also remains generally applicable to a wide range of material systems. A comprehensive overview of earlier phase-field modeling approaches of surface diffusion, including fourth-order Cahn-Hilliard type models and coupled Allen-Cahn/Cahn-Hilliard formulations (both fourth- and second-order), can be found in the works of Hoffrogge et al. [108, 130]. In contrast to classical Cahn-Hilliard based approaches, which rely on fourth-order equations and encounter difficulties in limiting surface diffusion strictly to interfacial regions, their approach employs a coupling of two second-order equations. Specifically, an Allen-Cahn type evolution equation for the phase-field, supplemented with an obstacle-type potential,

is coupled to a conservative diffusion equation that describes the evolution of the chemical potential or composition. The proposed model effectively restricts surface diffusion to the interface while ensuring numerical efficiency, and was validated through thermal grooving simulations and demonstrated good agreement with analytical sharp-interface solutions. The key extension was introduced through a modified composition evolution equation, in which the total flux is decomposed into a bulk contribution and an additional interfacial contribution of species i, and is given as follows:

$$\frac{\partial c_i(\boldsymbol{x},t)}{\partial t} = -\boldsymbol{\nabla}\cdot\boldsymbol{j}_i\,, \tag{2.17}$$

$$\boldsymbol{j}_i \equiv \boldsymbol{j}_i^b + \boldsymbol{j}_i^s\,. \tag{2.18}$$

In accordance with the original formulations, the bulk flux density $\boldsymbol{j}_i^b$ was defined by interpolating the phase-inherent flux densities ($\boldsymbol{j}_i^\alpha$)

$$\boldsymbol{j}_i^b \equiv \sum_{\alpha=1}^{N} h_\alpha(\boldsymbol{\phi})\,\boldsymbol{j}_i^\alpha\,, \tag{2.19}$$

and the interface flux density was postulated as

$$\boldsymbol{j}_i^s \equiv -\frac{1}{\epsilon}\sum_{\alpha=1}^{N}\sum_{\beta=\alpha+1}^{N}\sum_{j=1}^{N_c-1} M_{ij}^{\alpha\beta}(\boldsymbol{\phi})\boldsymbol{\nabla}\mu_j\,, \tag{2.20}$$

$$M_{ij}^{\alpha\beta}(\boldsymbol{\phi}) \equiv \bar{M}_{ij}^{\alpha\beta}\, g_{\alpha\beta}(\boldsymbol{\phi})\,, \tag{2.21}$$

and based on the superposition of all pairwise interfacial contributions through the chemical mobilities at the interface $\bar{M}_{ij}^{\alpha\beta}$ ($\mathrm{m^6\,J^{-1}\,s^{-1}}$), which enables independent control over the transport rates of atoms along the phase boundary. To ensure that additional interface flux density vanishes in the bulk, the dimensionless function

($g_{\alpha\beta}$), as a generalization of existing two-phase formulations, was formulated as follows:

$$g_{\alpha\beta}(\boldsymbol{\phi}) \begin{cases} > 0 & \phi_\alpha > 0 \cap \phi_\beta > 0 \\ = 0 & \phi_\alpha = 0 \cup \phi_\beta = 0 \end{cases} . \tag{2.22}$$

A natural choice of dimensionless function ($g_{\alpha\beta}$) is

$$g_{\alpha\beta}(\boldsymbol{\phi}) = \phi_\alpha^n \phi_\beta^n \tag{2.23}$$

with exponent $n > 0$, where $n \in \mathbb{R}$.

2.2.2 Governing laws

Sharp-interface relations A sharp-interface description of surface diffusion in pure materials, as presented in [137], is based on the Gibbs-Thomson relation, which relates the chemical potential to interface curvature κ:

$$\mu = \mu_{\text{eq}} + V_m \gamma \kappa \,. \tag{2.24}$$

Here, μ_{eq} denotes the equilibrium chemical potential for a planar interface, V_m is the molar volume, and γ represents the interfacial energy. In accordance with Mullins's theory [137], surface diffusion results in tangential mass transport along the interface, described by the flux

$$\boldsymbol{j}_s = -\frac{D_s \rho_s}{RT} \boldsymbol{\nabla}_{\boldsymbol{s}} \mu \,. \tag{2.25}$$

Here, D_s ($\mathrm{m^2\,s^{-1}}$) denotes the surface diffusivity, ρ_s ($\mathrm{mol\,m^{-2}}$) the number of atoms per surface area is the proportionality factor for converting the volumetric quantity into a surface-excess property, and RT represents the Einstein relation, including the ideal gas constant R ($\approx 8.314\,\mathrm{J\,mol^{-1}\,K^{-1}}$) and the temperature T (K). The operator $\boldsymbol{\nabla}_{\boldsymbol{s}}$ denotes the surface gradient operator. The resulting surface flux has the units of $\mathrm{mol\,m^{-1}\,s^{-1}}$ and represents a surface excess flux, rather than

a conventional flux. The surface divergence $\boldsymbol{\nabla_s}\cdot$ of the surface excess flux governs the normal velocity v_n of the interface, leading to a displacement of the surface profile that can be expressed as

$$v_n = -V_m \boldsymbol{\nabla_s} \cdot \boldsymbol{j}_s = \frac{V_m D_s \rho_s}{RT} \nabla_s^2 \mu \,. \tag{2.26}$$

Here, ∇_s^2 represents the surface Laplace operator. By substituting eq (2.24), the above equation can be stated in terms of curvature, leading to the following equation

$$v_n = \frac{V_m^2 D_s \rho_s \gamma}{RT} \nabla_s^2 \kappa = B \nabla_s^2 \kappa \tag{2.27}$$

as the governing equation describing the change in the surface's shape. Accordingly, the rate of surface evolution is controlled by the proportionality constant B ($\mathrm{m^4\,s^{-1}}$), which is stated as follows:

$$B \equiv \frac{V_m^2 D_s \rho_s \gamma}{RT} \,. \tag{2.28}$$

In contrast to surface diffusion, in which atomic transport proceeds tangentially to the interface, thermally activated atomic jumps can generate a net flux normal to the interface, either toward or away from it. These processes result in a corresponding decrease or increase in the interfacial area. Such behavior arises when one phase is energetically favored, as described by rate-reaction theory [138]. In this framework, the normal velocity of the interface is proportional to a thermodynamic driving force Δf,

$$v_n = m \Delta f \tag{2.29}$$

where m is the interfacial mobility with units $\mathrm{m^4\,J^{-1}\,s^{-1}}$. The driving force, expressed in $\mathrm{J\,m^{-3}}$, represents an energy density or, equivalently, a pressure acting normally to the interface.

A unified description considering both tangential surface diffusion and atomic movement normal to the interface is presented by Cahn and Taylor [139]. Within this framework, the normal velocity is given by

$$v_n = -\nabla_s^2 \left(\frac{1}{m} \nabla_s^2 - \frac{\gamma}{B} \right)^{-1} \kappa\gamma \,. \tag{2.30}$$

Interestingly, the above equation introduces another length scale, giving two limiting cases: interface motion limited by attachment kinetics (rate-reaction theory) and motion governed purely by surface diffusion. The characteristic length scale

$$l_c \equiv \sqrt{\frac{B}{m\gamma}} \tag{2.31}$$

depends on the material parameters of the interface. For length scales that are significantly smaller than l_c, the attachment kinetics is the rate-limiting factor, whereas for length scales that greatly exceed l_c, diffusion along the tangential direction of the interface becomes the rate-limiting factor. An equivalent representation, as shown by Rätz et al. [140], expresses eq (2.30) as two coupled second-order equations:

$$v_n = \frac{B}{\gamma} \nabla_s^2 \mu \,, \tag{2.32}$$

$$\mu = \mu_{\text{eq}} + \kappa\gamma + \frac{v_n}{m} \,. \tag{2.33}$$

Therefore, finite attachment kinetics leads to a relaxed form of the Gibbs-Thomson relation through the introduction of an additional term proportional to the interface velocity.

Sharp-interface limiting behavior of the grand-potential MPF model

The consistency of phase-field models with sharp-interface counterparts is commonly demonstrated through asymptotic analysis [141–143]. The asymptotic approach is a mathematical technique, and the sharp-interface case can be approached as a limiting case. Asymptotic analysis systematically derives the

limiting behavior as the interface thickness approaches zero, thereby linking the diffuse-interface formulation to classical continuum descriptions with sharp boundaries. As a result, asymptotic analysis serves to demonstrate the model's ability to recover important physical aspects as the interface thickness tends toward zero. Beyond validation, asymptotic analysis provides a framework for relating model parameters to the underlying material properties, thereby enabling a quantitative interpretation of the simulation results. For the grand-potential MPF model employed in current research, asymptotic analyses were performed for cases involving pure bulk diffusion [107], surface diffusion [108], and combined surface and bulk diffusion [130]. Studies from Hoffrogge et al. [108] demonstrate that the resulting sharp-interface limit recovers a combined description of surface diffusion and finite attachment kinetics. Accordingly, relations between physical properties and model parameters were derived, thereby facilitating a quantitative interpretation of the simulation results.

To deduce an expression for the surface diffusion rate constant B, an asymptotic analysis is presented in the works of Hoffrogge et al. [108]. This approach gives a set of equations, valid for small deviations from equilibrium, corresponding to the sharp-interface formulations eqs (2.32) and (2.33), and describe the coupled motion by surface diffusion and attachment kinetics. From this analysis, the growth rate constant dominated by surface diffusion is obtained as

$$B = \frac{\bar{M} I_g \gamma_{\alpha\beta}}{(c^{\alpha}(\mu_{\mathrm{eq}}) - c^{\beta}(\mu_{\mathrm{eq}}))^2} \tag{2.34}$$

establishing the relation between the physical and model-specific time scales. Here, $\bar{M}$ is the chemical mobility, $c^{\alpha}(\mu_{\mathrm{eq}})$ and $c^{\beta}(\mu_{\mathrm{eq}})$ are the equilibrium compositions of phases α and β, I_g is a dimensionless prefactor representing a normal integral associated with the dimensionless surface diffusion mobility function $g_{\alpha\beta}$, and $\gamma_{\alpha\beta}$ denotes the interfacial energy parameter of the model. The characteristic length scale associated with the attachment kinetics, according to eq (2.31), is given by

$$l_c \equiv \sqrt{\frac{B}{m_{\alpha\beta}\gamma_{\alpha\beta}}}, \tag{2.35}$$

where $m_{\alpha\beta}$ is the interfacial mobility parameter of the model. To minimize the effect of the attachment kinetics, interfacial mobilities in the model are selected such that the attachment kinetics remain subdominant. This can be achieved by ensuring the length scale on which the attachment kinetics operate is significantly smaller than the interface width ($l_c \ll \pi^2\epsilon/4$). Using eqs (2.34) and (2.35), this length scale l_c can be calculated.

2.3 Numerical implementation

All simulations are performed using codes based on a finite-difference discretization method and an explicit Euler time-integration scheme. These simulations are conducted using the in-house developed software package Phase-field Algorithms for Computational Engineering in 3D (PACE3D) [144], developed at the Institute for Digital Materials Science (IDM) of the Karlsruhe University of Applied Sciences (HKA) and at the Institute for Applied Materials Science - Microstructure Modeling and Simulation (IAM-MMS) of the Karlsruhe Institute of Technology (KIT). This framework enables multiphysics simulations and allows for the investigation of microstructural evolution, incorporating phase transformations, diffusion, thermal effects, solid mechanics, fluid mechanics, and electromagnetic phenomena. The structure generator extension presented in Section 2.5 has been integrated as an additional component into the structure generator tool of the PACE3D framework and applied in conjunction with aging simulations of SOFC anodes for microstructure optimization. Parallelization was implemented in PACE3D via domain decomposition using the Message Passing Interface (MPI) [145], with each subdomain assigned to an individual MPI process, enabling massive parallelization and accelerating the computation. Given the long operating times relevant to SOFCs, computational efficiency is of critical importance. Therefore, the Grand-chem MPF solver has been optimized through vectorized floating-point operations, leveraging modern CPU architectures to speed up computing times [146]. Combined with extensive modeling features and

a scalable parallel implementation, code vectorization within PACE3D allows for large-scale simulations on high-performance computing systems.

2.4 Grand-potential multiphase-field model for aging simulations[1]

»This study employs a simplified modeling approach that captures the essential physical mechanisms of coarsening in Ni-GDC anodes while maintaining computational efficiency. The model is based on the following assumptions:

- Conservation of mass and volume: The mass and volume (phase fractions) of Ni and GDC are assumed to remain constant during the coarsening process. This assumption is justified by the negligible evaporation of Ni at typical operating temperatures of solid oxide cells (500 °C–1000 °C) [96, 147].
- Isotropic interfacial properties: The interfacial energy and diffusion coefficients are treated as isotropic and constant. This simplification allows for neglecting the effects of crystal orientation on the interfacial energies and diffusion coefficients of Ni and GDC.
- Mass transport mechanisms: Surface and interfacial diffusion are considered as the primary mass transport mechanisms, and contributions from bulk diffusion are neglected for both Ni and GDC. This assumption is based on the higher diffusion rates typically observed along surfaces and interfaces compared to bulk diffusion in materials at the temperatures considered here [148].
- Coarsening of both Ni and GDC as a degradation mechanism: Ni-GDC anodes exhibit significant GDC phase evolution in addition to Ni coarsening. Previous works reported pronounced GDC agglomeration after 20,000h

[1] The content of this section has been taken directly from Jeela et al. [74] with minor linguistic changes.

and GDC coating formation on Ni surfaces at around 15,000h [83]. Liu et al. [89] observed Ni coarsening and little GDC growth, with no evidence of nanoscale GDC features. In this study, the coarsening of Ni and GDC is assumed to be the main degradation mechanism, and the GDC coating-like formation is investigated by surface and interfacial energy sensitivity analysis in Ni-GDC systems.

These assumptions enable a focus on the main physical processes driving microstructural evolution in Ni-GDC anodes while maintaining a tractable model. Although these assumptions may introduce some limitations, they provide a reasonable balance between model accuracy and computational feasibility for the large-scale simulations of the coarsening behavior in SOFC anodes with larger domain sizes. The current work, therefore, focuses only on investigating the effects of the coarsening of Ni and GDC particles on the microstructural evolution of the anode and, thereby, on the SOFC performance in long-term operation.

Building upon the MPF model based on the free-energy functional presented in Section 2.1.2, the formulation is extended in this section using the grand-potential functional approach. MPF model based on the grand-potential functional developed by Choudhury and Nestler [107] and subsequently extended to incorporate surface self-diffusion effects [108] is employed in this work. This model enables the simulation of the coarsening dynamics of Ni and GDC phases. The formulation is essentially centered on the grand-potential functional, denoted as Ω (J), representing the energetic state of a system of volume V. This functional is expressed in terms of the order parameters $\boldsymbol{\phi} = \{\phi_\alpha, \phi_\beta, \ldots, \phi_N\}$ (dimensionless) for N distinct phases and the volumetric chemical potentials $\boldsymbol{\mu} = \{\mu_1, \mu_2, \ldots, \mu_{N_c-1}\}$ ($\mathrm{J\,m^{-3}}$) for N_c chemical components, as follows:

$$\Omega(\boldsymbol{\phi}, \boldsymbol{\nabla\phi}, \boldsymbol{\mu}) = \int_V f_{\mathrm{intf}}(\boldsymbol{\phi}, \boldsymbol{\nabla\phi}) + \psi(\boldsymbol{\phi}, \boldsymbol{\mu})\, \mathrm{d}V. \tag{2.36}$$

Here, $f_{\mathrm{intf}}(\boldsymbol{\phi}, \boldsymbol{\nabla\phi})$ and $\psi(\boldsymbol{\phi}, \boldsymbol{\mu})$ represent the interfacial and bulk energy contributions, respectively. To account for the interfacial energy and to stabilize the interface profile with a finite thickness, the combined potential and gradient terms

as given in ref [128] are incorporated. The potential term ensures the order parameters remain within a thin and defined diffuse interface thickness range and captures the interfacial energy contribution. In this study, we adopted an obstacle potential with the following formulation

$$f_{\text{pot}}(\boldsymbol{\phi}) = \begin{cases} \frac{16}{\epsilon\,\pi^2} \sum_{\substack{\alpha,\beta=1 \\ \alpha<\beta}}^{N,N} \gamma_{\alpha\beta}\phi_\alpha\phi_\beta, & \phi \in \mathcal{G} \\ \infty, & \phi \notin \mathcal{G}, \end{cases} \tag{2.37}$$

where $\gamma_{\alpha\beta}$ represents the interfacial energy between phases α and β. The parameter ϵ (m) determines the diffuse interface width, defined as $\delta = \epsilon\pi^2/4$. The Gibbs simplex $\mathcal{G}$ is defined as:

$$\mathcal{G} = \left\{ \sum_{\alpha=1}^{N} \phi_\alpha = 1 : \{\phi_\alpha \geq 0, \forall \alpha \in \{1,\ldots,N\}\} \right\}. \tag{2.38}$$

This ensures that the order parameters ϕ_α remain non-negative and their sum equals unity. In addition, the gradient term incorporates interfacial energy into the system and stabilizes the profile of diffuse interfaces with a finite thickness. Following the formulation in ref [129], the gradient term is given as

$$f_{\text{grad}}(\boldsymbol{\nabla\phi}) = -\epsilon \sum_{\substack{\alpha,\beta=1 \\ \alpha<\beta}}^{N,N} \gamma_{\alpha\beta} \boldsymbol{\nabla}\phi_\alpha \cdot \boldsymbol{\nabla}\phi_\beta\,, \tag{2.39}$$

where $\boldsymbol{\nabla}\phi_\alpha$ and $\boldsymbol{\nabla}\phi_\beta$ are the gradients of the order parameters. Hoffrogge et al. [149] demonstrated that the combination of eqs (2.39) and (2.37) correctly reflects Young's law up to negligible deviations. The bulk grand-potential density is expressed as an interpolation of the grand-potential densities of individual bulk phases. It is given by

$$\psi(\boldsymbol{\phi}, \boldsymbol{\mu}) = \sum_{\alpha=1}^{N} \psi^{\alpha}(\boldsymbol{\mu}) h_\alpha(\boldsymbol{\phi})\,, \tag{2.40}$$

where the grand-potential density for phase α is described as,

$$\psi^{\alpha}(\boldsymbol{\mu}) = f^{\alpha}\left(\boldsymbol{c}^{\alpha}(\boldsymbol{\mu})\right) - \sum_{i=1}^{N_c-1} \mu_i c_i^{\alpha}(\boldsymbol{\mu}), \forall \alpha \in \{1,\ldots,N\}. \tag{2.41}$$

The bulk free energy f^{α} corresponds to phase α, which depends on the phase-specific compositions $c^{\alpha} = \left\{c_1^{\alpha}, c_2^{\alpha}, \ldots, c_{N_c-1}^{\alpha}\right\}$. In this work, the interpolation function h_{α} is chosen to be $h_{\alpha}(\boldsymbol{\phi}) = \phi_{\alpha}$, ensuring the constraint $\sum_{\alpha=1}^{N} h_{\alpha}(\boldsymbol{\phi}) = 1$ is satisfied. A local quasi-equilibrium assumption is applied, ensuring that, at every spatial location, the condition

$$\mu_i = \frac{\partial f^{\alpha}\left(c^{\alpha}\right)}{\partial c_i^{\alpha}} = \frac{\partial f^{\beta}\left(c^{\beta}\right)}{\partial c_i^{\beta}} = \cdots = \frac{\partial f^{N}\left(c^{N}\right)}{\partial c_i^{N}} \tag{2.42}$$

is met for all $i \in \{1,\ldots,N_c-1\}$.

According to ref [129], the evolution equation of each phase-field ϕ_{α} is specified as

$$\epsilon \frac{\partial \phi_{\alpha}(\boldsymbol{x},t)}{\partial t} = \frac{1}{\tilde{N}} \sum_{\substack{\beta=1 \\ \beta\neq\alpha}}^{N} m_{\alpha\beta}\left(\frac{\delta\Omega}{\delta\phi_{\beta}} - \frac{\delta\Omega}{\delta\phi_{\alpha}}\right). \tag{2.43}$$

In this context, $\tilde{N}$ denotes the local number of phases, while $m_{\alpha\beta}$ (with units of $\mathrm{m^4\,J^{-1}\,s^{-1}}$) represents the mobility of the interface between α and β phases. The terms $\delta/(\delta\phi_{\alpha})$ and $\delta/\left(\delta\phi_{\beta}\right)$ refer to the variational derivatives with respect to ϕ_{α} and ϕ_{β} respectively. Ni and GDC are modeled as pure solids with nearly fixed compositions. Their free energies are introduced in the form $f^{\alpha}\left(\boldsymbol{c}^{\alpha}(\boldsymbol{\mu})\right) = \sum_{i=1}^{N_c-1} f_i^{\alpha}\left(c_i^{\alpha}\right)$, where each contribution is assumed to follow a simple parabolic form $f_i^{\alpha}\left(c_i^{\alpha}\right) = A_i\left(c_i^{\alpha}\left(\mu_i\right) - c_{i,\mathrm{eq}}^{\alpha}\right)^2$, for $i \in \{\mathrm{Ni}, \mathrm{GDC}\}$. The prefactor A_i characterizes the strength of immiscibility and is chosen to be sufficiently large to ensure volume conservation within each phase. $c_{i,\mathrm{eq}}^{\alpha}$ denotes the equilibrium concentration of species i in phase α.

The porous Ni-GDC system is described using three distinct order parameters $\boldsymbol{\phi} = \{\phi_{Ni}, \phi_{GDC}, \phi_{Pore}\}$, representing the metallic nickel phase, the GDC structure,

and the voids. For the transport of each substance, a set of two dimensionless composition variables, $\boldsymbol{c} = \{c_{\mathrm{Ni}}, c_{\mathrm{GDC}}\}$, representing the mole fractions of nickel and GDC, is employed. With $N_{\mathrm{c}} = 3$, the composition of the porous phase is expressed as $c_{\mathrm{Pore}} = 1 - c_{\mathrm{Ni}} - c_{\mathrm{GDC}}$. For a clear distinction between the phase symbols and the component notation, italicized symbols are used to represent the phases throughout the text. The dimensionless composition fields, $c_i = \sum_{\alpha=1}^{N} h_\alpha c_i^a$ (mole fractions), are conserved quantities within the system. Conservation laws govern their evolution, ensuring mass balance consistency across the phases. The equations account for the dynamic redistribution of the composition fields during the coarsening process and are expressed as follows

$$\frac{\partial c_i(\boldsymbol{x},t)}{\partial t} = -\boldsymbol{\nabla} \cdot \boldsymbol{j}_i \,. \tag{2.44}$$

Here, $\boldsymbol{j}_i$ represents the flux of species i, measured in units of $\mathrm{m\,s^{-1}}$. The evolution of the chemical potential can be expressed using Einstein's notation as

$$\frac{\partial \mu_i(\boldsymbol{x},t)}{\partial t} = \left[\sum_{\alpha=1}^{N} h_\alpha(\boldsymbol{\phi}) \frac{\partial c_j^\alpha(\boldsymbol{\mu})}{\partial \mu_i}\right]^{-1} \left[\frac{\partial c_j(\boldsymbol{x},t)}{\partial t} - \sum_{\alpha=1}^{N} c_j^\alpha(\boldsymbol{\mu}) \frac{\partial h_\alpha(\boldsymbol{\phi}(\boldsymbol{x},t))}{\partial t}\right]. \tag{2.45}$$

In SOFC anodes, surface diffusion is assumed as the dominant mechanism for mass transfer within the typical operating temperature range. In contrast to Ni-YSZ anodes, Ni-GDC anodes demonstrate coarsening behavior for both Ni and GDC over time [83]. This model extends the analysis by incorporating both surface diffusion and diffusion along the interface between nickel and GDC. The inclusion of the additional diffusion pathways provides a more comprehensive representation of the mass transfer processes within Ni-GDC anodes. Consequently, the flux density of nickel is derived as follows:

$$\boldsymbol{j}_{\mathrm{Ni}} = -\frac{32}{\pi^2 \epsilon} \nabla \mu_{\mathrm{Ni}} (M_{\mathrm{Ni}}^{NiPore}\, \phi_{Ni}\phi_{Pore} + M_{\mathrm{Ni}}^{NiGDC} \phi_{Ni}\phi_{GDC}) \,. \tag{2.46}$$

The diffusion of nickel along the tangential direction of the free nickel surface and the Ni-GDC interface is determined by the mobilities M_{Ni}^{NiPore} and M_{Ni}^{NiGDC}

with the units of $m^6\,J^{-1}\,s^{-1}$. These mobilities are directly related to the surface self-diffusivity D_{Ni}^{NiPore} and the interfacial self-diffusivity D_{Ni}^{NiGDC} by an Einstein-like relationship as described in (cf. [[108], eq (99) ff.]), which is expressed as follows:

$$M_{\mathrm{Ni}}^{NiPore} = \frac{D_{\mathrm{Ni}}^{NiPore}\,\delta_s V_m \left(\Delta c_{\mathrm{Ni},eq}^{Ni\text{-}Pore}\right)^2}{RT}, \tag{2.47}$$

$$M_{\mathrm{Ni}}^{NiGDC} = \frac{D_{\mathrm{Ni}}^{NiGDC}\delta_I V_m \left(\Delta c_{\mathrm{Ni},eq}^{Ni\text{-}GDC}\right)^2}{RT}. \tag{2.48}$$

The atomistic thicknesses of the surface (δ_s) and the interface (δ_I) are approximately 0.1 nm. Nickel's molar volume (V_m) is included in the formulation, along with the ideal gas constant (R) and temperature (T). To simplify the model and avoid arbitrary assumptions about interface thicknesses, the term excess interface diffusivity is defined. These are expressed as $D_{\mathrm{Ni,ex}}^{NiPore} \equiv D_{\mathrm{Ni}}^{NiPore}\delta_s$ and $D_{\mathrm{Ni,ex}}^{NiGDC} \equiv D_{\mathrm{Ni}}^{NiGDC}\delta_I$, respectively, both measured in $m^3\,s^{-1}$. The model-specific composition difference $\Delta c_{\mathrm{Ni},eq}^{Ni\text{-}Pore}$ and $\Delta c_{\mathrm{Ni},eq}^{Ni\text{-}GDC}$ are specified as $\Delta c_{\mathrm{Ni},eq}^{Ni\text{-}Pore} \equiv c_{\mathrm{Ni,eq}}^{Ni} - c_{\mathrm{Ni,eq}}^{Pore} = 0.8$ and $\Delta c_{\mathrm{Ni},eq}^{Ni\text{-}GDC} \equiv c_{\mathrm{Ni,eq}}^{Ni} - c_{\mathrm{Ni,eq}}^{GDC} = 0.8$, respectively. Similarly, the flux density of GDC and the corresponding mobilities are expressed as

$$\boldsymbol{j}_{\mathrm{GDC}} = -\frac{32}{\pi^2\epsilon}\nabla\mu_{\mathrm{GDC}}\left(M_{\mathrm{GDC}}^{GDCPore}\phi_{GDC}\phi_{Pore} + M_{\mathrm{GDC}}^{NiGDC}\phi_{GDC}\phi_{Ni}\right), \tag{2.49}$$

$$M_{\mathrm{GDC}}^{GDCPore} = \frac{D_{\mathrm{GDC}}^{GDCPore}\delta_s V_m \left(\Delta c_{\mathrm{GDC},eq}^{GDC\text{-}Pore}\right)^2}{RT}, \tag{2.50}$$

$$M_{\mathrm{GDC}}^{NiGDC} = \frac{D_{\mathrm{GDC}}^{NiGDC}\delta_I V_m \left(\Delta c_{\mathrm{GDC},eq}^{Ni\text{-}GDC}\right)^2}{RT}. \tag{2.51}$$

At the domain boundaries, zero-flux boundary conditions are enforced, treating them as isolating (i.e., $\boldsymbol{j_i}\cdot\boldsymbol{n} = 0 \forall i, x \in \mathrm{d}V$), where $\boldsymbol{n}$ denotes the normal to the domain boundary, which means there is no net flux across the boundary. In addition, a perpendicular contact condition for the order parameter is assumed ($\boldsymbol{\nabla}\phi_\alpha\cdot\boldsymbol{n} = 0$), which ensures the gradient of the order parameter is normal to the boundary. In this work, a SIMD (Single Instruction, Multiple Data) vectorized

solver is used, the implementation of which is described in detail in [[146], Section 4.2]. The interested reader is referred to refs [108] and [98] for model validation. To establish a stable and physically consistent initial condition for our phase-field simulations, we employ a preconditioning algorithm that generates a diffuse interface profile. This step aims to generate a sinusoidal and sufficiently diffuse interface at the boundaries between the phases. Following the approach described in ref [150], this is achieved by omitting the curvature term in the evolution equation and in the absence of any chemical driving force. Preconditioning is performed over a sufficient number of iterations to ensure a stable profile characterized by a constant interface width.«

2.5 Extension of structure generator workflow

2.5.1 Framework for sintering-like morphological coalescence[2]

»In the work of Schöller et al. [151], synthetic microstructures were generated in a four-step process as shown in the schematic workflow (original workflow) in Figure 2.1: (i) dense packing of hard spheres using a discrete element method, enforcing prescribed particle size distributions for different material phases; (ii) identification of contact points via a neighbor graph connecting all spheres based on a minimum spanning tree (MST); (iii) generation of individual particle geometries using spherical harmonics with specified angular energy spectra, incorporating the previously identified contact points; (iv) the resulting parameterized microstructure was then voxelized and converted into a diffuse-interface representation using a multiphase-field method. Further details on the original framework can be found in ref [151]. Validation of the virtual structure generator was performed by comparison with experimentally reconstructed electrode microstructures in previous work [151]. A comparison of key microstructural descriptors, such

[2]The content of this section has been taken directly from Jeela et al. [90] with minor linguistic changes.

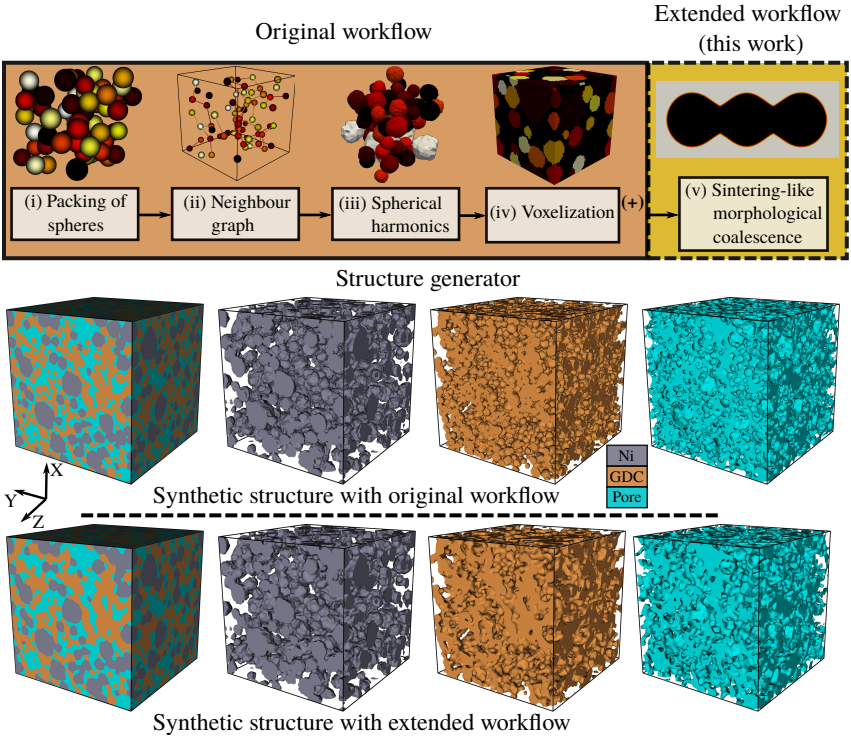


Figure 2.1: Schematic representation of the extended microstructure generation workflow, emphasizing the extended sintering-like morphological coalescence step and resulting enhancements to synthetic SOFC Ni-GDC anode microstructures. The figure has been adjusted to the format of this dissertation.

as phase volume fractions, specific surface areas, and tortuosities, as well as a qualitative visual comparison, showed that the reported deviations were limited to a few percentage points. The generator relies on several input parameters, such as particle size distributions and angular power spectra; their influence on the resulting morphology is not known a priori. A multi-objective Bayesian optimization was employed to systematically calibrate the generator by minimizing the discrepancy between the morphological metrics of the generated and experimental microstructures across multiple objectives.

Although the original structure generator workflow provides a reasonably close representation of the experimental SOFC anode microstructures and agrees well with several quantitative descriptors, the workflow lacks the ability to generate microstructures more realistic to the experimental structures. In particular, key quantitative metrics such as TPB density and mean particle diameter are not validated against experimental structures. The current work extends the original workflow to further improve synthetic SOFC anode microstructures in comparison to experimental structures. One significant limitation of the original generator is the missing particle coalescence, which results from the sintering stage in the experimental fabrication process. To address this, a sintering-like morphological coalescence step is integrated as an extension of the original workflow. The aim of this extension is not to simulate the physical mechanisms governing sintering, as this would require detailed governing equations, extensive parameterization, and substantial computational resources, as well as time for large 3D domains. Instead, the focus is on efficiently replicating sintering-like morphological features, particularly the formation of sintering necks and particle coalescence, in a computationally tractable manner suitable for synthetic microstructure generation. Figure 2.1 shows a qualitative comparison between the synthetic microstructures obtained using the original and extended Workflows.

The primary objective of the structure generator workflow extension in this work is to generate synthetic SOFC anode microstructures that are visually and quantitatively representative of the experimental structures across a large set of microstructural descriptors. To achieve sintering-like morphological coalescence

in the synthetic structures, a multiphase-field method is employed. The MPF method is well established for simulating the evolution of complex microstructures across micro- and mesoscopic length scales. The model utilized in this study is based on the multiphase-field formulation of Steinbach et al. [129] and Nestler et al. [128] and incorporates a targeted modification of the Allen-Cahn equation to simulate sintering-like coalescence while preserving phase volumes. Although the classical Allen-Cahn equation [103] is not inherently volume-conserving, this property can be enforced by means of an extra artificial bulk driving force for volume preservation of specific phases [152]. In addition, an obstacle potential is used together with a corrective term that suppresses the curvature minimization dynamics intrinsic to the Allen-Cahn equation. This curvature minimization behavior, resulting from the Laplace term $\Delta\boldsymbol{\phi}$ in eq (2.58), leads to changes in both phase shape and phase volume. Following the approach proposed by Sun et al. [150], this dynamics can be partially or fully eliminated, enabling controlled morphological coalescence.

In a system with N phases, the microstructure is represented by a set of order parameters $\boldsymbol{\phi} = \{\phi_1, \phi_2, \ldots, \phi_N\}$, whereby each order parameter or phase field variable $\phi_\alpha(\boldsymbol{x}, t)$ represents the presence of phase α at position $\boldsymbol{x}$ and time t. Values $\phi_\alpha = 1$ and $\phi_\alpha = 0$ correspond to the presence or absence of phase α. Diffuse interfaces with finite thickness are employed in place of sharp phase boundaries, where ϕ_α smoothly varies between 0 and 1. The phase field variable ϕ_α can therefore be interpreted as the local volume fraction of phase α. The total free energy $\mathcal{F}$ of a multi-phase heterogeneous material containing N solid phases is represented as the volume integral of the free energy density f over domain V

$$\mathcal{F}[\boldsymbol{\phi}, \boldsymbol{\nabla\phi}] = \mathcal{F}_{\text{intf}}[\boldsymbol{\phi}, \boldsymbol{\nabla\phi}] + \mathcal{F}_{\text{bulk}}[\boldsymbol{\phi}] = \int_V \underbrace{f_{\text{grad}}(\boldsymbol{\nabla\phi}) + f_{\text{pot}}(\boldsymbol{\phi})}_{f_{\text{intf}}(\boldsymbol{\phi}, \boldsymbol{\nabla\phi})} + \underbrace{f(\boldsymbol{\phi}) + g_v(\boldsymbol{\phi})}_{f_{\text{bulk}}(\boldsymbol{\phi})} \, \mathrm{d}V. \tag{2.52}$$

Following the notation of Nestler et al. [128], the combined potential f_{pot} and the gradient term f_{grad} together account for the interfacial energy and ensure a diffuse

interface with finite thickness. The term $f(\boldsymbol{\phi})$ represents the phase-inherent bulk energy of the phases and acts as the driving force for phase transformation. An additional positive contribution, $g_v(\boldsymbol{\phi})$, enforces the volume preservation of the phases. For more details, interested readers are referred to Nestler et al. [152]. The gradient [129] and potential terms are as follows:

$$f_{\text{grad}}(\boldsymbol{\nabla\phi}) = -\epsilon \sum_{\alpha,\beta>\alpha} \gamma_{\alpha\beta} \boldsymbol{\nabla}\phi_\alpha \cdot \boldsymbol{\nabla}\phi_\beta \,, \tag{2.53}$$

$$f_{\text{pot}}(\boldsymbol{\phi}) = \begin{cases} \dfrac{16}{\epsilon\pi^2} \displaystyle\sum_{\alpha,\beta>\alpha} \gamma_{\alpha\beta}\, \phi_\alpha \phi_\beta + \frac{1}{\epsilon} \sum_{\alpha,\beta>\alpha,\delta>\beta} \gamma_{\alpha\beta\delta}\, \phi_\alpha \phi_\beta \phi_\delta, & \text{if } \boldsymbol{\phi} \in \mathcal{G}\,, \\ \infty, & \text{otherwise}\,. \end{cases} \tag{2.54}$$

Here, $\gamma_{\alpha\beta}$ represents the interfacial energy of the α and β phases, and ϵ controls the diffuse interfacial width. The second term in eq (2.54) prevents the growth of unwanted interfacial contributions at binary interfaces. The order parameter ϕ_α evolution follows an Allen-Cahn type equation, driving the system towards minimal energy. The evolution equation reads as follows:

$$\begin{aligned} \frac{\partial \phi_\alpha(\boldsymbol{x},t)}{\partial t} = -\frac{1}{\tilde{N}\epsilon} \sum_{\beta\neq\alpha}^{\tilde{N}} \Bigg[m_{\alpha\beta} \Bigg(& \frac{\delta \mathcal{F}_{\text{intf}}}{\delta \phi_\alpha} + \epsilon \hat{a}(\phi_\alpha, \boldsymbol{\nabla}\phi_\alpha) \\ & - \frac{\delta \mathcal{F}_{\text{intf}}}{\delta \phi_\beta} - \epsilon \hat{a}(\phi_\beta, \boldsymbol{\nabla}\phi_\beta) - \frac{8\sqrt{\phi_\alpha \phi_\beta}}{\pi} \Delta^{\alpha\beta} \Bigg) \Bigg], \end{aligned} \tag{2.55}$$

where $m_{\alpha\beta}$ represents the mobility, $\tilde{N}$ refers to the number of locally active phases, and the variational derivative

$$\frac{\delta \mathcal{F}}{\delta \phi_\alpha} = \frac{\partial f}{\partial \phi_\alpha} - \boldsymbol{\nabla} \cdot \frac{\partial f}{\partial \boldsymbol{\nabla}\phi_\alpha} \,. \tag{2.56}$$

Meanwhile, $\Delta^{\alpha\beta}$ is given as:

$$\Delta^{\alpha\beta} = \left(\frac{\delta}{\delta\phi_\alpha} - \frac{\delta}{\delta\phi_\beta} \right) \mathcal{F}_{\text{bulk}}, \tag{2.57}$$

where f_{bulk} denotes the phase-inherent bulk energy of the phases and an additional positive contribution that enforces volume preservation. As demonstrated by Schoof et al. [153] in the multiphase-field context, the addition of an extra isotropic gradient energy density term, $\epsilon\hat{a}(\phi_\alpha, \boldsymbol{\nabla}\phi_\alpha)$, to the phase-field evolution is specified as follows:

$$\epsilon\hat{a}(\phi_\alpha, \boldsymbol{\nabla}\phi_\alpha) = -\epsilon\gamma_\alpha^c \left(\Delta\phi_\alpha - |\boldsymbol{\nabla}\phi_\alpha| \, \boldsymbol{\nabla} \cdot \left(\frac{\boldsymbol{\nabla}\phi_\alpha}{|\boldsymbol{\nabla}\phi_\alpha|} \right) \right). \tag{2.58}$$

This term enables the calibration of the curvature-driven interface evolution by a surface energy-like parameter γ_α^c, which does not contribute to curvature minimization. The parameter γ_α^c can be understood as a numerical factor for calibrating the strength of the artificially constructed interface. The combined contribution of the interfacial free energy density and this additional isotropic gradient term, as discussed in refs [153, 154], provides a means of controlling the curvature minimization dynamics determined by $\gamma_{\alpha\beta}$. In the present work, these formulations are used as a numerical means of controlling curvature minimization. The extended workflow's ability to generate synthetic microstructures representative of experimental SOFC anode microstructures is validated in this work using an extensive set of quantitative descriptors.«

2.6 Solid mechanics framework for mechanical response of anodes[3]

»The effective elastic properties during aging are determined by load simulations of the aged microstructures within the PACE3D multiphysics framework [144]. A quasi-static solid mechanics formulation is adopted for determining the locally resolved stress and strain fields within the microstructure, assuming negligible body forces and small deformations. Under these assumptions, the momentum balance is given by

$$\nabla \cdot \overline{\boldsymbol{\sigma}} = \mathbf{0}, \qquad \overline{\boldsymbol{\sigma}} = \sum_{\alpha=1}^{N} \phi_\alpha \boldsymbol{\sigma}^\alpha, \tag{2.59}$$

cf. [155], where $\overline{\boldsymbol{\sigma}}$ refers to the interpolated Cauchy stress calculated from phase-specific stresses $\boldsymbol{\sigma}^\alpha$, and ϕ_α represents the order parameter of the α phase. The infinitesimal strain tensor is interpolated analogously as $\boldsymbol{\varepsilon} = \sum_{\alpha=1}^{N} \phi_\alpha \boldsymbol{\varepsilon}^\alpha$. In accordance with the jump condition approach [156–158], the local phase strain $\boldsymbol{\varepsilon}^\alpha$ is expressed as

$$\boldsymbol{\varepsilon}^\alpha = \boldsymbol{\varepsilon} + \sum_{\delta=1,\,\delta\neq\alpha}^{N} \phi_\delta \{\boldsymbol{\varepsilon}\}^{\alpha\delta}, \tag{2.60}$$

whereby $\{\boldsymbol{\varepsilon}\}^{\alpha\delta}$ indicates the strain jump over diffuse interfaces between phases α and δ defined by $\{\boldsymbol{\varepsilon}\}^{\alpha\delta} = \boldsymbol{\varepsilon}^\alpha - \boldsymbol{\varepsilon}^\delta$. The phase-specific strain $\boldsymbol{\varepsilon}^\alpha$ is additively decomposed as $\boldsymbol{\varepsilon}^\alpha = \boldsymbol{\varepsilon}^{\mathrm{el},\alpha} + \boldsymbol{\varepsilon}^{\theta,\alpha}$ with $\boldsymbol{\varepsilon}^{\mathrm{el},\alpha}$ denoting the elastic contribution and $\boldsymbol{\varepsilon}^{\theta,\alpha}$ the thermal contribution. In this regard, $\boldsymbol{\varepsilon}^{\theta,\alpha} = \alpha_\theta^\alpha \Delta\theta \boldsymbol{I}$ is considered, wherein α_θ^α is the isotropic thermal expansion coefficient of the phase α, $\Delta\theta = \theta - \theta_{\mathrm{ref}}^\alpha$ is the temperature difference relative to the reference temperature, and $\boldsymbol{I}$ is the identity tensor of second order.

According to Hooke's law, the corresponding phase-specific stresses in each phase are given by $\boldsymbol{\sigma}^\alpha = \mathbb{C}^\alpha \left[\boldsymbol{\varepsilon}^{\mathrm{el},\alpha}\right] = \mathbb{C}^\alpha \left[\boldsymbol{\varepsilon}^\alpha - \boldsymbol{\varepsilon}^{\theta,\alpha}\right]$, with $\mathbb{C}^\alpha$ indicating the phase-specific stiffness tensor. Under the assumption of isotropic elasticity, the stiffness

[3] The content of this section has been taken directly from Jeela et al. [90] with minor linguistic changes.

of phase α is given by $\mathbb{C}^\alpha = 3K^\alpha \mathbb{P}_1 + 2G^\alpha \mathbb{P}_2$, where K^α and G^α denote the compression and shear moduli, respectively. The projection tensors are given by $\mathbb{P}_1 = \frac{1}{3} \boldsymbol{I} \otimes \boldsymbol{I}$ and $\mathbb{P}_2 = \mathbb{I}^{\mathrm{S}} - \mathbb{P}_1$, whereby $\mathbb{I}^{\mathrm{S}}$ refers to the fourth-order symmetric identity.«

2.7 Microstructure quantification[4]

2.7.1 Electrochemical performance-related descriptors

»The microstructural features of the 3D Ni-GDC porous anode, including mean particle diameters derived from continuous particle size distributions, phase volume fractions, specific surface areas, tortuosity, and TPB lengths, were accurately characterized using established analytical techniques. Particle coarsening analysis employs continuous particle size distributions as described by Münch and Holzer [159]. The mean particle size (d_{50}), representing the midpoint of the cumulative distribution, is a key metric in this analysis. Tortuosity (τ_α) of a phase, a dimensionless measure of transport pathway complexity, is calculated as the ratio of the ideal current to the actual current in a given phase, offering a scale-invariant representation of transport efficiency [160]. The mean tortuosity of a phase is computed as

$$\tau_\alpha \equiv \frac{1}{3} \left(\tau_{\alpha,x} + \tau_{\alpha,y} + \tau_{\alpha,z} \right) \tag{2.61}$$

to capture the phases' overall transport properties. The TPB length, a crucial parameter influencing electrochemical reactions, is determined using a skeletonization algorithm [161]. Specific surface areas (A_α) for each phase are calculated by integrating the magnitude of the phase order parameter gradient:

$$A_\alpha = \frac{1}{V} \int_V |\boldsymbol{\nabla} \phi_\alpha| \, \mathrm{d}V, \tag{2.62}$$

[4]The content of this section has been taken directly from Jeela et al. [74, 90] with minor linguistic changes.

with individual interface areas ($A_{\alpha/\beta}$) obtained through a system of linear equations

$$A_{Ni} = A_{Ni/Pore} + A_{Ni/GDC}\,, \tag{2.63}$$

$$A_{GDC} = A_{Ni/GDC} + A_{GDC/Pore}\,, \tag{2.64}$$

$$A_{Pore} = A_{Ni/Pore} + A_{GDC/Pore}\,. \tag{2.65}$$

GDC's mixed ionic and electronic conductivity highlights the significance of the GDC/Pore interface, which forms the double-phase boundary and plays a pivotal role in electrochemical reactions. All methodologies mentioned above were implemented in-house within the PACE3D Framework and validated through established test cases [98]. All these properties are critical in determining the anode's structural and functional efficiency, as they directly impact electrochemical performance, ion and gas transport, and overall cell performance.

2.7.2 Mechanical related descriptors

The effective elastic properties of the 3D SOFC anode microstructure are determined using numerical homogenization. In this regard, the effective stiffness tensor $\bar{\mathbb{C}}$ is determined using six independent strain-controlled macroscopic load cases. For each load case $\beta = 1, \ldots, 6$, a defined macroscopic strain vector $\bar{\boldsymbol{\varepsilon}}^{\beta}$ is applied, such that $\mathbf{u} = \boldsymbol{\varepsilon}_0(\boldsymbol{x}) \in \delta V$ holds true. For example, $\beta = 1$ corresponds to the macroscopic strain $\bar{\boldsymbol{\varepsilon}}^1 = \varepsilon_0\, \mathbf{e}_1 \otimes \mathbf{e}_1$. The solution to the resulting linear elastic boundary value problem yields the local stress field $\boldsymbol{\sigma}^{\beta}(\boldsymbol{x})$, from which the volume-averaged macroscopic stress response can be determined as

$$\langle \boldsymbol{\sigma}^{\beta} \rangle = \frac{1}{V} \int_V \boldsymbol{\sigma}^{\beta}(\boldsymbol{x})\, \mathrm{d}V. \tag{2.66}$$

The macroscopic stress-strain relation from the numerical homogenization scheme is described as follows: $\langle \boldsymbol{\sigma}^{\beta} \rangle = \bar{\mathbb{C}} \bar{\boldsymbol{\varepsilon}}^{\beta}$. The stiffness contribution for each load case is determined by

$$\underline{\underline{\bar{C}}}^{\beta} = \frac{\langle \sigma^{\beta} \rangle \, (\bar{\varepsilon}^{\beta})^{T}}{(\bar{\varepsilon}^{\beta})^{T} \, (\bar{\varepsilon}^{\beta})}, \tag{2.67}$$

where $\underline{\underline{\bar{C}}}$ denotes the matrix representation of the stiffness tensor $\mathbb{C}$ in normed Voigt notation and $\underline{\underline{\bar{C}}}^{\beta}$ refers to the matrix representation of the βth column of $\underline{\underline{\bar{C}}}$. Each load case results in a column of the effective stiffness tensor. For example, a uniaxial strain $\bar{\boldsymbol{\varepsilon}}^{1} = \varepsilon_0 \, \mathbf{e}_1 \otimes \mathbf{e}_1$ with the Voigt representation $\underline{\bar{\boldsymbol{\varepsilon}}}^{1} = [\varepsilon_0, 0, 0, 0, 0, 0]^{T}$ determines the first column of $\bar{\mathbb{C}}$, while shear load cases provide the corresponding shear columns using the standard $\sqrt{2}$ Voigt normalization [162]. Since mechanical model used for extracting the effective stiffness is fully linear elastic, the homogenized stiffness tensor is independent of the amplitude of ε_0.

The effective stiffness tensor is constructed by superimposing the contributions of all six independent load cases: $\underline{\underline{\bar{C}}} = \sum_{\beta=1}^{6} \underline{\underline{\bar{C}}}^{\beta}$. The methodology presented in Böhlke and Brüggemann [163] is used to calculate and plot the elastic modulus body. The directional elastic moduli (E_{xx}, E_{yy}, and E_{zz}) can be directly extracted from the elastic modulus body as detailed in ref [163]. Beyond the directional moduli, an effective isotropic modulus is obtained by projecting the anisotropic tensor onto its isotropic Voigt and Reuss bounds and combining these using the Hill average [164]. The Voigt estimates of the bulk and shear moduli are then evaluated accordingly

$$K_{\text{Voigt}} = \frac{C_{11} + C_{22} + C_{33} + 2(C_{12} + C_{13} + C_{23})}{9}, \tag{2.68}$$

$$G_{\text{Voigt}} = \frac{C_{11} + C_{22} + C_{33} - (C_{12} + C_{13} + C_{23}) + 3(C_{44} + C_{55} + C_{66})}{15}. \tag{2.69}$$

Whereas the Reuss bounds result from the compliance tensor according to

$$\frac{1}{K_{\text{Reuss}}} = S_{11} + S_{22} + S_{33} + 2(S_{12} + S_{13} + S_{23}), \tag{2.70}$$

$$\frac{1}{G_{\text{Reuss}}} = \frac{4}{15}\left(S_{11} + S_{22} + S_{33} - S_{12} - S_{13} - S_{23}\right) + \frac{3}{15}\left(S_{44} + S_{55} + S_{66}\right). \quad (2.71)$$

This gives the Hill average values $K_{\text{Hill}} = \frac{1}{2}(K_{\text{Voigt}} + K_{\text{Reuss}})$, $G_{\text{Hill}} = \frac{1}{2}(G_{\text{Voigt}} + G_{\text{Reuss}})$, whereas the effective isotropic modulus of elasticity is given by

$$E_{\text{Hill}} = \frac{9K_{\text{Hill}}G_{\text{Hill}}}{3K_{\text{Hill}} + G_{\text{Hill}}}. \quad (2.72)$$

We emphasize that the Voigt-Reuss-Hill estimates give an isotropic projection of the generally anisotropic effective stiffness tensor and should therefore solely be used as scalar measures for comparing the overall stiffness evolution across different aging states.«

2.8 Experimental Ni-GDC SOFC anode microstructures

2.8.1 Fabrication of the cells

Electrolyte-supported symmetric cells containing Ni-GDC electrodes (1 cm^2) were fabricated at Forschungszentrum Jülich GmbH (FZJ). The GDC powder ($Gd_{0.1}Ce_{0.9}O_{1.95}$) was processed into a screen-printable paste using *α-terpineol* as a dispersing agent and *ethylcellulose* as a transporting medium. Similarly, the NiO-GDC functional layer was produced by mixing equal weights of GDC and NiO powders (50:50). Subsequently, a NiO contact layer was deposited by screen printing and dried overnight at 80 °C. The final design of the electrolyte-supported symmetrical cell consists of an 8 mol % YSZ electrolyte (thickness: 200 µm, Kerafol GmbH, Eschenbach, Germany), two porous GDC interlayers (5 µm each), two Ni-GDC anode layers (8 µm each), and two Ni current collector layers (4 µm each).

2.8.2 Cell operating conditions

The cells discussed in Section 2.8.1 were heated to 800 °C at a rate of $3\,\mathrm{K\,min^{-1}}$ under a nitrogen atmosphere and then gradually reduced using hydrogen/nitrogen gas mixtures at the Karlsruhe Institute of Technology (KIT). Subsequently, the gas composition was adjusted to a hydrogen flow rate of $0.5\,\mathrm{L\,min^{-1}}$ and an oxygen flow rate of $0.125\,\mathrm{L\,min^{-1}}$, thereby generating a H_2/H_2O mixture with a 1:1 ratio using an upstream burner [165]. Afterwards, electrochemical impedance spectroscopy (EIS) measurements were performed at 800 °C, 650 °C, and 600 °C. Following the initial characterization, the furnace temperature was increased to 900 °C to perform aging tests. Cell performance was continuously monitored via impedance measurements at open-circuit voltage to ensure electrochemical symmetry between the electrodes. Three cells produced from the same batch were investigated: Cell A (pristine) was subjected to reduction but not aged; Cell B was aged for 240h at 900 °C; and Cell C was aged for 1100h under identical conditions. Following the operation, all cells were cooled to room temperature under a reducing atmosphere ($H_2/N_2 = 0.05 : 0.95$).

2.8.3 3D microstructure reconstruction of pristine and aged cells

The experimental 3D microstructures utilized in this work were reconstructed by using Ni-GDC anode samples produced at FZJ as described in Section 2.8.1, and subsequently aged at KIT as described in Section 2.8.2. Although the samples originate from the same production batch and were tested under the same conditions, they differ from the samples presented in the work of Liu et al. [89]. Sample preparation consisted of infiltrating the pore space with a conductive epoxy resin, followed by metallographic sectioning and micro-preparation using a focused ion beam. Subsequently, a plasma-FIB system was applied to acquire serial cross-sections, thereby generating a stack of SEM images. The grayscale image stack underwent denoising with a Split-Bregman optimization approach and was segmented using a watershed algorithm. To ensure effective Watershed

seeding, threshold values were extracted from the grayscale histogram by applying a tailored procedure, and markers near high-gradient areas and ridge-like features were eliminated using a Meijering filter.

2.9 RVE of Ni-GDC anode[5]

»The size of a representative volume element (RVE) for Ni-GDC anodes is crucial for performing phase-field simulations, especially for ML-based iterations in Chapter 3. To analyze the RVE size, subdomains representing $^1/_4$th, $^1/_9$th, and $^1/_{16}$th of the real domain volume were extracted and evaluated. Specifically, subdomain sizes of $14.0 \times 18.5 \times 6.4$ µm^3 ($^1/_4$th of the real domain volume), $9.4 \times 12.4 \times 6.4$ µm^3 ($^1/_9$th of the real domain volume), and $7.0 \times 9.2 \times 6.4$ µm^3 ($^1/_{16}$th of the real domain volume) were extracted from the real Ni-GDC anode microstructure ($28.2 \times 37.0 \times 6.4$ µm^3). These subdomains were analyzed and compared based on their microstructural properties to determine the optimal domain size for phase-field simulations. This analysis helps in determining the optimal 3D Ni-GDC domain size to conduct numerous ML-driven phase-field simulations on the initial microstructure in Chapter 3, exploring a wide range of thermophysical parameters from the literature to identify the appropriate and missing physical parameters of the Ni-GDC anode under given operating conditions. Although simulating significantly larger volumes could provide comprehensive insights, the requirement for computing resources and simulation times increases greatly. Therefore, the study focuses on finding a balance between computational feasibility and the accuracy of microstructural representation. Figure 2.2 illustrates the positions of the subdomains derived from the digital representation of the real microstructure domain and their morphology.

[5] The content of this section has been taken directly from Jeela et al. [166] with minor linguistic changes. The publication has shared first authorship between the author and G. Tosato. The author's contribution to this work includes conceptualisation of the study, contributions to methodology, software development, visualization, validation, drafting the original manuscript, and review and editing.

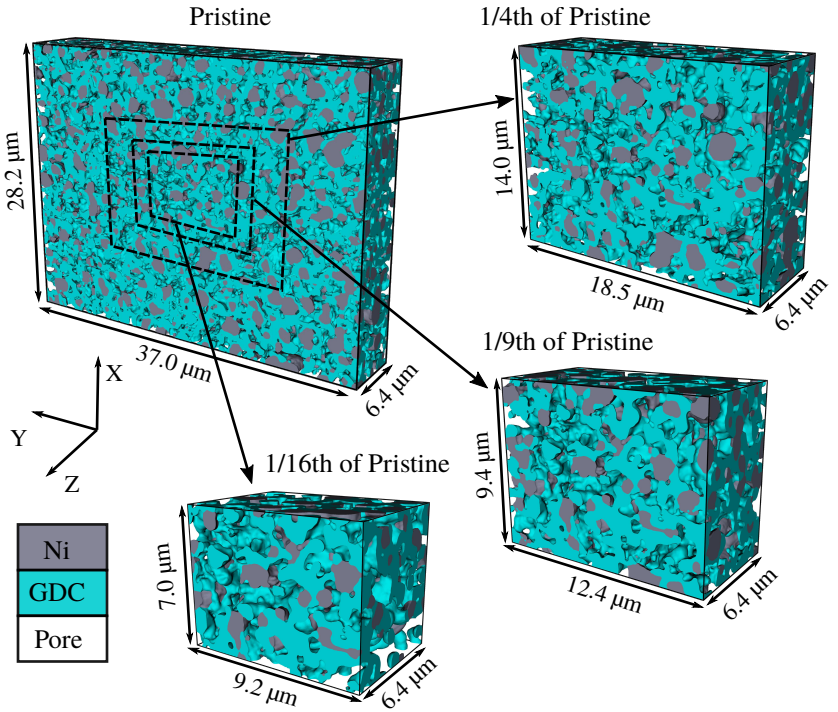


Figure 2.2: Sub-regions extracted from a pristine FIB-SEM reconstructed 3D real microstructure. Sub-regions representing $^1/_4$th, $^1/_9$th, and $^1/_{16}$th of the total volume were extracted from the Central region of the real microstructure. Given that the microstructure's thickness in the z-direction is only 6.4 µm, it was kept consistent for all sub-regions, with only the x- and y-dimensions being reduced accordingly. The figure has been adjusted to the format of this dissertation.

Table 2.1: Microstructural characteristic properties of pristine and subdomains of various volumes.

Parameter	real domain	1/4th of real domain	1/9th of real domain	1/16th of real domain
Ni vol.%	22.44	22.60	21.92	22.00
GDC vol.%	41.38	40.73	41.57	42.06
Pore vol.%	36.18	36.67	36.51	35.94
Ni/Pore Specific Area (μm^{-1})	0.37	0.37	0.36	0.34
GDC/Pore Specific Area (μm^{-1})	1.50	1.49	1.51	1.52
Ni/GDC Specific Area (μm^{-1})	0.67	0.67	0.67	0.67
GDC Tortuosity (−)	2.57	2.56	2.51	2.46
Pore Tortuosity (−)	2.57	2.57	2.68	2.74
Total TPB density (μm^{-2})	1.82	1.81	1.80	1.73
Nickel Mean Particle Diameter (µm)	0.91	0.92	0.93	0.93
GDC Mean Particle Diameter (µm)	0.59	0.58	0.58	0.58
Pore Mean Particle Diameter (µm)	0.60	0.62	0.62	0.61
Total volume (μm^3)	6666	1664	743	417
Voxel size (µm)	0.05	0.05	0.05	0.05

Table 2.1 presents the microstructural characteristic properties of the real domain and various subdomains (1/4th, 1/9th, and 1/16th of the real domain volume) for the Ni-GDC anode. The table shows that the volume percentages of Ni, GDC, and pore phases exhibit minimal variation across all subdomains, indicating that the chosen subdomains adequately represent the bulk properties. Specific surface areas for Ni/Pore and GDC/Pore show relatively higher deviations in the 1/16th subdomain compared to the other subdomains. In contrast, the Ni/GDC interface remains consistent across all subdomains. Tortuosity values vary with smaller subdomains, with relatively high deviations suggesting that tortuosity is a more localized property and transport paths are not uniformly homogeneous across the structure. The total TPB density also shows a significant deviation from the real domain in the 1/16th subdomain. However, the mean particle diameters for Ni, GDC, and pores remain consistent across all subdomains, further validating the representativeness of these smaller volumes.

Selecting the subdomain with 1/9th of the real domain volume emerges as an optimal choice, balancing computational efficiency and accurately representing

the real domain's microstructural properties. This subdomain size retains the essential characteristics of the real domain while significantly reducing computational demands compared to the larger 1/4th subdomain. Consequently, the 1/9th subdomain size is ideal for performing efficient phase-field simulations without compromising the fidelity of the microstructural representation. In contrast, the 1/16th subdomain, while further reducing computational load, may not be as suitable. The larger deviation in TPB density and the increasing tortuosity deviations indicate that the smallest subdomain may not capture the complex microstructural details as accurately as the larger subdomains. Therefore, the 1/16th subdomain could potentially lead to less reliable simulation results, making it a less optimal choice for accurate phase-field simulations.

To assess the effects of statistical fluctuations and verify the representativeness of the selected subdomain, we performed a quantitative error analysis based on variations in microstructural properties in nine non-overlapping subdomains, each comprising 1/9 of the total volume. For each subdomain, the microstructural properties are calculated, and their statistical variability is assessed in relation to the values of the original domain. The results, summarized in Table 2.2 and illustrated in Figure 2.3(a), show that the coefficient of variation (CV) for all nine microstructural properties is in the range of 1 %–5 %, with a mean CV of about 3 %, indicating low variability. Furthermore, based on the law of large numbers and assuming statistical independence of the subdomains, the statistical uncertainty of the properties of the total volume is only approximately $\sqrt{1/9} = 1/3$ of the observed scatter of the subdomains. Thus, the expected CV for the total volume for all properties is less than 2 %. In comparison, the aged microstructure exhibits property changes of up to 20 % compared to the pristine state, with a mean deviation of about 11 %.

Although the pristine and aged microstructures were reconstructed from distinct regions, both originate from relatively central areas of the anode, minimizing edge effects and spatial heterogeneity. This is supported by a statistical analysis of four non-overlapping 1/2 subdomains of the original microstructure, which shows CV values between 0 and 2 % across all properties, indicating negligible spatial

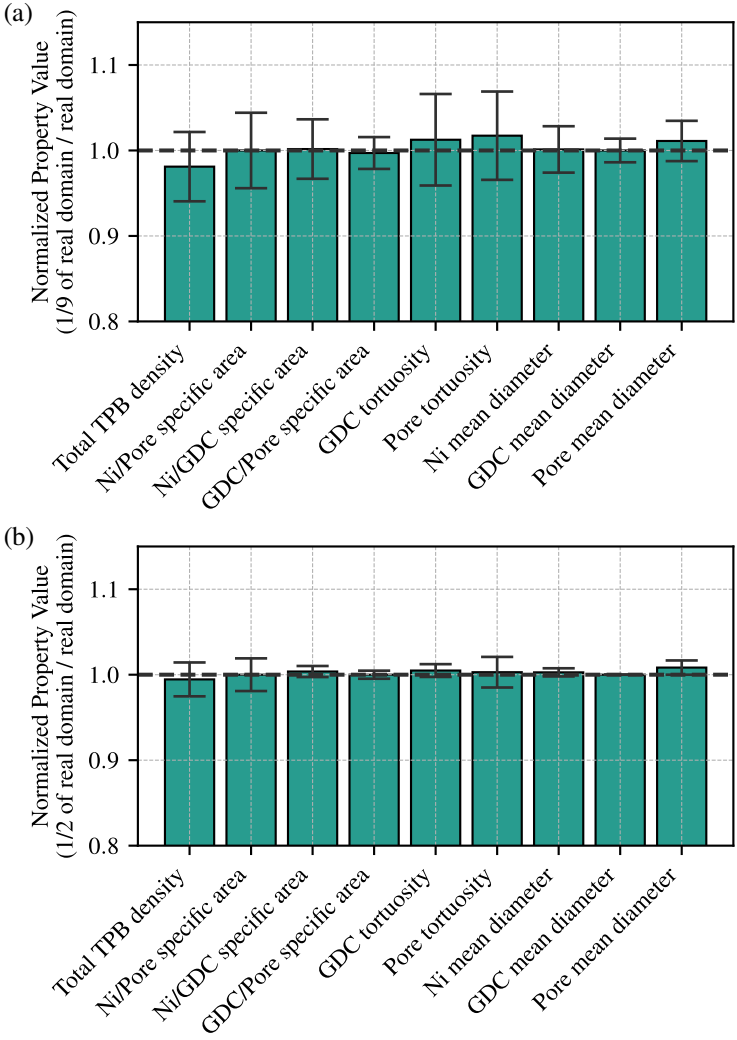


Figure 2.3: Comparison of normalized microstructural properties variations over different subdomain sizes against the real domain. (a) Normalised property values and error bars for the nine subdomains of size 1/9. (b) Normalised property values and error bars for the four subdomains of size 1/2. Each bar represents the mean value across the subdomains, with the error bars indicating the standard deviation. The values of the real domain are used as a normalisation reference. The figure has been adjusted to the format of this dissertation.

Table 2.2: Evaluation of statistical fluctuations in microstructural properties over 1/9th of real domains.

Parameter	Mean	Standard Deviation	Coefficient of Variation (%)
Total TPB density (μm^{-2})	1.79	0.074	4.13
Ni/Pore Specific Area (μm^{-1})	0.37	0.016	4.41
Ni/GDC Specific Area (μm^{-1})	0.67	0.023	3.47
GDC/Pore Specific Area (μm^{-1})	1.50	0.028	1.87
GDC Tortuosity (−)	2.60	0.138	5.29
Pore Tortuosity (−)	2.61	0.133	5.08
Nickel Mean Particle Diameter (µm)	0.91	0.0247	2.71
GDC Mean Particle Diameter (µm)	0.59	0.008	1.38
Pore Mean Particle Diameter (µm)	0.60	0.014	2.33

variations (see Table 2.3 and Figure 2.3(b)). Furthermore, the volume of the

Table 2.3: Evaluation of statistical fluctuations in microstructural properties over 1/2 of real domains.

Parameter	Mean	Standard Deviation	Coefficient of Variation (%)
Total TPB density (μm^{-2})	1.810	0.036	1.99
Ni/Pore Specific Area (μm^{-1})	0.370	0.007	1.91
Ni/GDC Specific Area (μm^{-1})	0.673	0.004	0.64
GDC/Pore Specific Area (μm^{-1})	1.50	0.007	0.47
GDC Tortuosity (−)	2.583	0.019	0.74
Pore Tortuosity (−)	2.578	0.046	1.79
Nickel Mean Particle Diameter (µm)	0.913	0.004	0.47
GDC Mean Particle Diameter (µm)	0.590	0.000	0.00
Pore Mean Particle Diameter (µm)	0.605	0.005	0.83

original microstructure exceeds the threshold for the RVE of 10^3 particles, where most properties converge to stable values, as concluded by Joos et al. [167].«

3 Framework for physical parameters estimation[1]

»Ensuring the sustainable operation of solid-oxide fuel cells (SOFCs) requires an understanding of the components' lifespan. Multiphase-field simulation studies play a major role in understanding the underlying microstructural changes and the resulting property alterations in SOFCs over time. The primary challenge in such simulations lies in identifying a suitable model and defining its parametrization. This Chapter presents an Active Learning framework combined with Bayesian Optimization to identify optimal model parameters to simulate the aging of nickel-gadolinium doped ceria (Ni-GDC) anodes. The investigations performed in this work overcome the incompleteness and inconsistency of literature data and navigate the complex, high-dimensional parameter space by leveraging experimental microstructure data and the power of the AL framework. The successful parameter search enables simulation studies of Ni-GDC anode aging and performance during long-term SOFC operation. This approach improves the accuracy of phase-field simulations and offers a versatile tool for broader applications in SOFC development, predicting material behavior under various operational conditions.

Predicting the long-term degradation of anodes in a quantitative manner requires reliable material parameters under realistic operating conditions, including interface energies and diffusion coefficients. These parameters have a critical role in

[1] The content of this chapter is based on Jeela et al. [166]. The publication has shared first authorship between the author and G. Tosato. The author's contribution to this work includes conceptualisation of the study, contributions to methodology, software development, visualization, validation, drafting the original manuscript, and review and editing. Sections that are taken directly from the publication, with minor linguistic changes, have been marked.

simulating the coarsening of the Ni-GDC anode. In Section 3.2, a comprehensive review of the literature data for Ni and GDC interface energies and diffusion coefficients is given, highlighting both the scarcity of data and the lack of reliability and accuracy in the reported values, which are required for phase-field simulations. In the work of Hoffrogge et al. [98], the model is parameterized to describe the coarsening of nickel in Ni-YSZ SOFC anodes at a temperature of 750 °C. The physical parameters were derived from thermal grooving experiments and density functional theory (DFT) calculations [168, 169]. Experimentally determining these physical parameters for Ni-GDC anodes at given operating conditions is challenging due to the time-intensive nature of the processes, the significant resources required, the complexity of the measurements, and the associated costs.

This chapter aims to enhance SOFC numerical investigations with Bayesian Active Learning (BAL). Active Learning (AL) [170] is a systematic machine-learning approach to explore vast parameter spaces while minimizing resource expenditures, which, coupled with Bayesian Optimization (BO) [171], has emerged as a valuable tool for materials design [172, 173].«

3.1 Bayesian Active Learning framework

Virtual research environment The current research was performed within the framework of the Kadi4Mat infrastructure [174], which enables FAIR-compliant scientific data and process management and modeling. A core element of the Kadi ecosystem is the visual workflow provided via KadiStudio [175], a standalone desktop application that allows users to design and execute scientific workflows using interconnected function nodes. These workflows enable structured data processing, visualization, and seamless communication with the KadiWeb platform. The AL framework employed in this work is implemented in KadiAI, Kadi4Mat's interface for Machine Learning and Artificial Intelligence, and is available as a set of workflow nodes. The integration of established libraries such as TensorFlow-Keras [176] and scikit-learn [177] ensures compliance with widely adopted standards along with robust performance.

Bayesian Optimization Bayesian optimization (BO) refers to a sequential, surrogate-based methodology to optimize expensive-to-evaluate black-box functions, similar to those encountered, for example, in the modeling of microstructure evolution in SOFC anodes. The optimization problem can generally be formulated as follows

$$\min_{x \in \mathcal{X}} f(x), \quad \mathcal{X} \subseteq \mathbb{R}^n . \tag{3.1}$$

Here, f is a derivative-free, potentially non-convex, and noisy objective function with computationally intensive evaluations. In this work, f quantifies the discrepancy between simulated and experimentally observed microstructural characteristics of the Ni-GDC anode (see Section 3.4). To efficiently explore the search space, BO constructs a probabilistic surrogate model, typically the Gaussian process (GP), over f. This model gets updated iteratively based on the observed data and guides the selection of new evaluation points. Founded on Bayes' theorem, it integrates the *priori* knowledge regarding the space of possible objective functions with the *likelihood* associated with the observed data $\mathcal{D}$ to generate a *posteriori* distribution

$$P(f|\mathcal{D}) \propto P(\mathcal{D}|f)P(f), \tag{3.2}$$

this constitutes the updated estimate of f, considering the observed data $\mathcal{D}$. A common technique to address this problem entails treating it as a Gaussian process regression model. A GP refers to an extended version of a multivariate Gaussian distribution applicable to a stochastic process, which constructs a joint Gaussian distribution across all finite samples of function values [178]. For a more comprehensive discussion and additional details, the reader is referred to [166].

Scientific workflow implementation The AL framework is implemented as a modular workflow consisting of specific nodes for each processing step (see Figure 3.1). The workflow is structured into (c) preprocessing, (d) simulation execution and cluster communication, (e) postprocessing, as well as two AL-specific components: (b) the Bayesian optimization oracle and (f) the scorer. The BO oracle serves as the central decision-making unit and progressively suggests new parameter configurations to refine the model's performance. It

retrieves the information required for the search from KadiWeb (Umbrella Record), including the optimization objective, the tunable parameters, and the defined boundaries, and applies BO to efficiently explore the high-dimensional parameter space and suggest the next parameter configuration. A GP regression model is employed through the scikit-learn implementation using a Matérn-5/2 kernel (smoothness parameter $\nu = 2.5$ and length scale $\ell = 1.0$), providing a balance between smoothness and model flexibility [178–180]. The acquisition function is defined by the upper confidence bound (UCB):

$$UCB(\boldsymbol{x}, \beta) = \mu(\boldsymbol{x}) + \beta\sigma(\boldsymbol{x}), \tag{3.3}$$

where μ and σ denote the predicted mean and the uncertainty of the GP, respectively. The parameter β regulates the trade-off between exploration and exploitation, with larger values promoting the exploration of unknown regions and smaller values favoring the exploitation of high-performance regions. A key aspect of the optimization framework is the evaluation of each simulation trial against the defined objective. This is achieved through a scoring mechanism implemented by the "scorer", the second key component of the AL framework. The scorer, or objective function, gives a quantitative measure of agreement between the trials' results and the target values; this metric is computed at each iteration, thereby guiding the oracle in navigating the parameter space. Iterative optimization proceeds until either a predefined maximum number of iterations is reached or a specified convergence criterion is met. In this study, the objective function is formulated as the deviation between the experimentally observed and the simulated microstructural evolution of the SOFC anode. To facilitate implementation, this deviation is estimated on the basis of a set of nine key parameters that characterize the microstructure. The resulting score indicates the distance between the trials and the target values, and the optimization is therefore posed as a minimization problem. Lower scores indicate improved agreement and, consequently, more accurate replication of the target experimental microstructure.

Figure 3.1: Visualization of the KadiStudio workflow for automated parameter identification of Ni-GDC anode aging in SOFCs. The workflow consists of: (a) user input nodes for configuring environment settings, working directories, and KadiWeb communication tokens; (b) a Bayesian Optimization Oracle node; (c) preprocessing nodes that convert the Oracle outputs into input data for PACE3D simulations; (d) nodes for job submission and monitoring on the computing cluster; (e) postprocessing nodes for analyzing the simulation results; and (f) a Scorer node that evaluates each simulation output against the defined objective. All nodes continuously update the corresponding records in Kadi4Mat, thereby ensuring synchronized data management across the entire workflow (based on joint work presented in [166]).

3.2 Physical parameters and model parameterization

»This Section explains the method for determining the physical parameters for coarsening in the Ni-GDC anode. For the current work, the temperature 900 °C is chosen, corresponding to the experimental conditions for Ni-GDC anode annealing. Determining the parameters in physical modeling simulations corresponding to experimental conditions is pivotal to quantitatively reproducing the microstructural aging of the Ni-GDC anode as observed in experiments. Figure 3.2 demonstrates the importance of identifying these parameters for predicting the long-term performance of the anode under specific operating conditions. For the sake of simplicity, the phase-field model parameters are expressed in a model-specific unit system, with u_l, u_E and u_t representing the model's units for length, energy, and time, respectively. The length unit u_l is defined based on the resolution of the initial microstructure (Δx) in the numerical grid of discretization $\Delta x = \Delta y = \Delta z$. The energy and time units are related through the Nickel surface energy γ_{NiPore}, Nickel surface diffusivity D_{Ni}^{NiPore}, and temperature T (refer to eq (2.47)). Table 3.1 presents the model's parameterization.

3.2.1 Nickel diffusion coefficients

The mechanisms of volume self-diffusion are well-established, and the corresponding Arrhenius parameters are known with high precision. In contrast, surface diffusion is less extensively studied and exhibits a considerable degree of measurement uncertainty, often varying by one to two orders of magnitude. This variability is evident in the literature, where reported values for surface and grain boundary self-diffusion are highly inconsistent [148, 181–183]. Anisotropy, annealing atmosphere, and material purity significantly influence measured diffusivities. The annealing atmosphere has a particularly pronounced effect on surface diffusion, as the mobility of surface atoms is highly sensitive to the adsorption of gas molecules and impurities. For nickel, the partial pressure of oxygen in

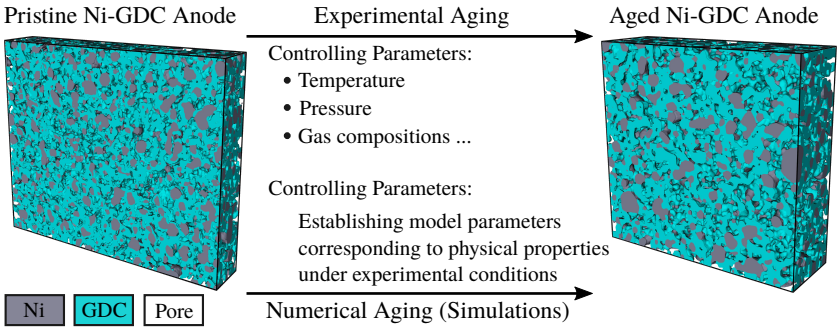


Figure 3.2: Microstructural evolution in Ni-GDC anodes. Experimental conditions (temperature, environment) drive microstructure changes, while precise parameter settings in physical modeling simulations aim to reproduce these outcomes accurately. This precision is crucial for quantitatively simulating microstructural aging. Note: Size variations between pristine and aged samples reflect different FIB-SEM volume segments, not aging effects. The figure has been adjusted to the format of this dissertation.

the annealing environment notably impacts surface diffusion rates. The current literature on nickel surface and grain boundary diffusion lacks the necessary precision for reliable phase-field simulations. Haremski et al. [169] recently performed thermal grooving experiments on nickel bicrystals to determine the surface diffusion coefficient with high accuracy. These studies, conducted at a temperature of 750 °C, report values that align with those found by Blakely et al. [148] when extrapolating the Arrhenius lines for the {100} and {111} surfaces to lower temperatures. Based on this correlation, the excess surface diffusion coefficient ($D_{\mathrm{Ni,ex}}^{NiPore}$) for pure and impure nickel at 900 °C was evaluated using the Arrhenius equation fitted to Blakely et al.'s experimental data [148], resulting in a range of 1.74×10^{-21} m^3 s^{-1}–2.1×10^{-20} m^3 s^{-1}. Hoffrogge et al. [98] assumed, following the results of Haremski et al. [169], that diffusion along the slow {100} surface orientation is rate-limiting and estimated an excess surface diffusion coefficient from an average of four data points near {100} as 3.75×10^{-22} m^3 s^{-1} at 750 °C. Given the considerable variation in reported surface diffusion values in the literature, excess surface diffusion coefficient with a range of 4.0×10^{-22} m^3 s^{-1}–4.0×10^{-20} m^3 s^{-1} is considered. The diffusion values range considered in the

current work accounts for inherent uncertainties and encompasses both faster and slower diffusion rates along different surface orientations. This approach ensures a comprehensive evaluation of diffusion behavior across various conditions. Due to the scarcity of literature data, the excess diffusion coefficient of nickel along the nickel/GDC interface ($D_{\mathrm{Ni,ex}}^{NiGDC}$) is assumed to range from $4.0 \times 10^{-22}\,\mathrm{m^3\,s^{-1}}$–$4.0 \times 10^{-27}\,\mathrm{m^3\,s^{-1}}$. This range is consistent with the general theory that surface diffusion is the fastest, followed by interface diffusion, and bulk diffusion is the slowest.

3.2.2 Nickel surface energy

The literature reports experimentally determined mean surface energies of nickel ranging from $1.6\,\mathrm{J\,m^{-2}}$–$2.5\,\mathrm{J\,m^{-2}}$, varying with method, temperature, and atmospheric conditions, providing an initial indication of their magnitude [181, 184–188]. Complementary to these experimental findings, atomistic simulations can determine the anisotropy of surface energy, typically calculated at $T = 0\,\mathrm{K}$. It is observed that surface energy decreases with increasing temperature, with a difference of approximately 10 % between values at $T = 0\,\mathrm{K}$ and the melting temperature. These simulations have provided weighted mean surface energy values for nickel of $2.04\,\mathrm{J\,m^{-2}}$ [189] and $2.54\,\mathrm{J\,m^{-2}}$ [190], respectively. However, the experimental conditions differ significantly from those within an SOFC anode. Furthermore, the influence of humidity on these parameters has not been extensively studied. It is known that oxygen adsorption can reduce surface energy, and impurities adsorbed on the surface can similarly affect surface energy.

Haremski et al. [168] conducted thermal grooving experiments on Ni polycrystals and Ni-YSZ anode microstructures under SOFC anode operating conditions at 750 °C in both dry and humid forming gas using atomic force microscopy. The carrier gas used was forming gas (95 % N_2/5 % H_2), and a maximum humid atmosphere (29 vol.% H_2O and 71 vol.% forming gas) was chosen, without annealing in an oxidizing environment. The measured oxygen partial pressure was $P_{O_2} = 1 \times 10^{-25}$ atm in dry forming gas and $P_{O_2} = 1 \times 10^{-19}$ atm in humid forming

gas. They concluded that these values are still low and not forming an oxidizing atmosphere, thus avoiding the adsorption of oxygen on the surface, which could reduce the surface energy.

In the current study, the SOFC operating conditions are at a temperature of 900 °C with a gas composition of 50 % H_2/50 % H_2O, and the material system is Ni-GDC. Under these conditions, the oxygen partial pressure could potentially impact the surface energy values. It was shown in the study by Fujimatsu et al. [191] that the oxygen partial pressure in SOFCs can vary significantly depending on current density, flow rate, and operating temperature and can range up to $P_{O_2} = 1 \times 10^{-15}$ atm. Also, investigations on the effects of oxygen partial pressure on surface energies indicate that the surface energy decreases with increasing oxygen partial pressure [192, 193]. As a result, rather than employing a fixed surface energy value, this study considers the surface energy of nickel as a variable, spanning a range from 1.5 $J\,m^{-2}$–2.5 $J\,m^{-2}$, to account for possible variations.

3.2.3 GDC diffusion coefficients and surface energy

Experimental studies of grain-boundary grooving on polished surfaces of Ceria (CeO_2) annealed in an argon atmosphere were conducted over a temperature range of 1473 K–1773 K. From Arrhenius plots of the surface diffusion coefficient, the value at 900 °C was estimated to be $7.2 \times 10^{-18}\,m^2\,s^{-1}$, and the corresponding excess surface diffusion coefficient was $2.4 \times 10^{-27}\,m^3\,s^{-1}$ [194]. Another study examined polycrystalline CeO_2 by developing thermal grain boundary grooves at different temperatures 1473 K–1663 K in air, using atomic force microscopy (AFM). The surface diffusion coefficient of CeO_2 was calculated from Arrhenius plots at 900 °C, yielding values ranging from $1 \times 10^{-18}\,m^2\,s^{-1}$–$1 \times 10^{-20}\,m^2\,s^{-1}$ [195]. As a result, GDC excess surface diffusion coefficient ($D_{\mathrm{GDC,ex}}^{GDCPore}$) for the AL Bayesian framework is given in the range of $2.4 \times 10^{-25}\,m^3\,s^{-1}$ to $2.4 \times 10^{-28}\,m^3\,s^{-1}$. Given the lack of experimental data, the excess diffusion coefficient of GDC at the nickel/GDC interface ($D_{\mathrm{GDC,ex}}^{NiGDC}$) is assumed to fall within the range of $2.4 \times 10^{-27}\,m^3\,s^{-1}$ to $2.4 \times 10^{-33}\,m^3\,s^{-1}$.

From the literature, it was found that the surface energies of CeO_2 from simulation studies are reported for the {100}, {110}, and {111} surfaces with values of (1.44 $J\,m^{-2}$, 1.06 $J\,m^{-2}$ and 0.71 $J\,m^{-2}$), (1.4 $J\,m^{-2}$, 1.0 $J\,m^{-2}$ and 0.7 $J\,m^{-2}$), and (1.41 $J\,m^{-2}$, 1.04 $J\,m^{-2}$ and 0.69 $J\,m^{-2}$), respectively [196–198]. The GDC surface energy for the {100}, {110}, and {111} surfaces was given as 1.46 $J\,m^{-2}$, 0.90 $J\,m^{-2}$ and 0.74 $J\,m^{-2}$, respectively [196]. Experimental studies using the multiphase equilibration technique estimated the surface energy of CeO_2 in an argon atmosphere at 900 °C by extrapolation to be 1.80 $J\,m^{-2}$ [194]. Considering all the above findings, the GDC surface energy for the AL Bayesian framework is assigned in the range of 0.7 $J\,m^{-2}$–2.0 $J\,m^{-2}$.

3.2.4 Nickel/GDC interfacial energy

To the best of our knowledge, no literature data are available for the interface energies for the Ni/GDC or Ni/CeO_2 systems. However, a study using the multiphase equilibration technique to determine the interface energy of the CeO_2/Cu system in an argon atmosphere at temperatures ranging from 1473 K–1773 K reports interface energy of 2.88 $J\,m^{-2}$ at 900 °C, based on linear temperature extrapolation [194]. Additionally, various experimental and computational methods have determined the interfacial energy values for the Ni/YSZ interface. Using Transmission Electron Microscopy (TEM) and Winterbottom analysis, a study measured the interfacial energy for Ni/YSZ(111) in the range of 1.8 $J\,m^{-2}$–2.1 $J\,m^{-2}$, depending on the specific configuration of the interface, for Ni/YSZ(001) as around 2.5 $J\,m^{-2}$ at 1350 °C in an $Ar + H_2$ (99 %) atmosphere with a $P_{O_2} = 1 \times 10^{-20}$ atm [199, 200]. By considering these similar systems and to account for different scenarios of wetting to dewetting, a range of 1.0 $J\,m^{-2}$–3.0 $J\,m^{-2}$ as Ni/GDC interfacial energy is considered appropriate for this study.

3.2.5 Interface mobilities and parabolic free energy

A comprehensive investigation of surface diffusion-driven thermal grooving was conducted by Hoffrogge et al. [108] to validate the model employed in the present work against established theories. Their results showed good agreement with analytical solutions of sharp interfaces, confirming model accuracy. In addition, the surface diffusion-controlled kinetics can be correctly quantified using the growth rate constant (B) of the model obtained from the asymptotic analysis. The value of B is evaluated in the present study according to (cf. [[108], eq (99) ff.]). In order to minimize the effects of attachment kinetics, the interface mobilities ($m_{\alpha\beta}$) are chosen in this work such that attachment kinetics remain subdominant. It is ensured by the characteristic length scale associated with the attachment kinetics, defined as ($l_c = \sqrt{B/(\gamma_{\alpha\beta} m_{\alpha\beta})}$) being much smaller than the diffuse interface width, i.e., ($l_c \ll \pi^2\epsilon/4$) [108].

The minima of the parabolic free energy $c^{\alpha}_{i,\,\mathrm{eq}}$ are specifically chosen values of 0.1 and 0.9, with an emphasis on maintaining adequately distinct values to enable differentiation, for instance, between Ni-rich and Ni-poor phases. The parabolic free energy function's chosen prefactor A_i ensures consistent volume preservation. To establish the model's energy and time scales, we consider the maximum values of nickel's surface diffusion and surface energy. Subsequently, all other model parameters and their respective ranges are aligned with this scaling system. Parameters such as interface mobilities, stable time steps, and simulation time are selected by our AL Bayesian Oracle for each simulation trial. This optimization ensures efficient resource utilization while maintaining a consistent physical time across all simulations.

3.3 Validation of framework

The initial AL framework validation study demonstrates the reliability and effectiveness of our method. For the validation run, we conduct a single-parameter optimization, focusing on the interfacial energy between nickel and GDC γ_{NiGDC},

Table 3.1: Phase-field parameters used in simulations of Ni-GDC anode ($u_l = 50\,\mathrm{nm}, u_E = 6.25 \times 10^{-15}\,\mathrm{J}, u_t = 1.45 \times 10^{-2}\,\mathrm{s}$).

Parameter (symbol)	Value (model units)	Value (physical units)
Ni-surf. chem. mobility (M_{Ni}^{NiPore})	$(10^{-1} \ldots 10^{-3})\, u_l^6/(u_E u_t)$	$(1.73 \times 10^{-29} \ldots 1.73 \times 10^{-31})\, \frac{\mathrm{m}^6}{\mathrm{Js}}$
Ni-nickel/GDC interf. chem. mobility (M_{Ni}^{NiGDC})	$(10^{-3} \ldots 10^{-8})\, u_l^6/(u_E u_t)$	$(1.73 \times 10^{-31} \ldots 1.73 \times 10^{-36})\, \frac{\mathrm{m}^6}{\mathrm{Js}}$
GDC-surf. chem. mobility ($M_{\mathrm{GDC}}^{GDCPore}$)	$(2.11 \times 10^{-6} \ldots 2.11 \times 10^{-9})\, u_l^6/(u_E u_t)$	$(3.65 \times 10^{-34} \ldots 3.65 \times 10^{-37})\, \frac{\mathrm{m}^6}{\mathrm{Js}}$
GDC-nickel/GDC interf. chem. mobility (M_{GDC}^{NiGDC})	$(2.11 \times 10^{-8} \ldots 2.11 \times 10^{-14})\, u_l^6/(u_E u_t)$	$(3.65 \times 10^{-36} \ldots 3.65 \times 10^{-42})\, \frac{\mathrm{m}^6}{\mathrm{Js}}$
Interfacial energy Ni/Pore (γ_{NiPore})	$1.0 \ldots 0.6\, u_E/u_l^2$	$2.5 \ldots 1.5\, \frac{\mathrm{J}}{\mathrm{m}^2}$
Interfacial energy Ni/GDC (γ_{NiGDC})	$1.2 \ldots 0.4\, u_E/u_l^2$	$3.0 \ldots 1.0\, \frac{\mathrm{J}}{\mathrm{m}^2}$
Interfacial energy GDC/Pore ($\gamma_{GDCPore}$)	$0.8 \ldots 0.28\, u_E/u_l^2$	$2.0 \ldots 0.7\, \frac{\mathrm{J}}{\mathrm{m}^2}$
Interface mobility Ni/Pore (m_{NiPore})	$(10^{-1} \ldots 10^{-3})\, u_l^4/(u_E u_t)$	$(6.92 \times 10^{-15} \ldots 6.92 \times 10^{-17})\, \frac{\mathrm{m}^4}{\mathrm{Js}}$
Interface mobility Ni/GDC (m_{NiGDC})	$(10^{-1} \ldots 10^{-3})\, u_l^4/(u_E u_t)$	$(6.92 \times 10^{-15} \ldots 6.92 \times 10^{-17})\, \frac{\mathrm{m}^4}{\mathrm{Js}}$
Interface mobility GDC/Pore ($m_{GDCPore}$)	$(10^{-1} \ldots 10^{-3})\, u_l^4/(u_E u_t)$	$(6.92 \times 10^{-15} \ldots 6.92 \times 10^{-17})\, \frac{\mathrm{m}^4}{\mathrm{Js}}$
Interface width parameter (ϵ)	$2.0\, u_l$	100 nm
Voxel-size ($\Delta x = \Delta y = \Delta z$)	$1.0\, u_l$	50 nm
Thermodynamic prefactor Nickel (A_{Ni})	$5\, u_E/u_l^3$	$2.5 \times 10^8\, \frac{\mathrm{J}}{\mathrm{m}^3}$
Thermodynamic prefactor GDC (A_{GDC})	$50\, u_E/u_l^3$	$2.5 \times 10^9\, \frac{\mathrm{J}}{\mathrm{m}^3}$
Equil.-comp. Ni-Ni ($c_{\mathrm{Ni,eq}}^{Ni}$)	0.9	90 mol%
Equil.-comp. Ni-GDC ($c_{\mathrm{Ni,eq}}^{GDC}$)	0.1	10 mol%
Equil.-comp. Ni-Pore ($c_{\mathrm{Ni,eq}}^{Pore}$)	0.1	10 mol%
Equil.-comp. GDC-Ni ($c_{\mathrm{GDC,eq}}^{Ni}$)	0.1	10 mol%
Equil.-comp. GDC-GDC ($c_{\mathrm{GDC,eq}}^{GDC}$)	0.9	90 mol%
Equil.-comp. GDC-Pore ($c_{\mathrm{GDC,eq}}^{Pore}$)	0.1	10 mol%

while keeping the other parameters fixed. A 2D reference structure was generated by initially creating a Voronoi structure consisting of nickel, GDC, and pore phases, and then by applying phase coarsening through phase-field simulations. Interface energy between nickel and GDC (γ_{NiGDC}) of 0.577 (in model scale units) was used in the model parameters. All parameters are expressed in model scale, as the focus of this validation was on testing the framework against provided model parameters rather than directly correlating with aged experimental microstructures or physical properties. The AL framework was then employed to tune the parameter γ_{NiGDC} within a physically meaningful range (0.4–1.2). The Oracle initiates the Bayesian search by performing three iterations of random search, providing initial seeds to construct the probabilistic model of the objective function. Each parameter value selected by the Oracle for γ_{NiGDC} is automatically passed to the phase-field simulations, executed with the in-house developed framework PACE3D [145]. Upon completion, simulation results are evaluated and scored, providing valuable information for strategic navigation of the search space. Throughout our study, the score represents a quantitative measure of deviation from the target microstructure. In PACE3D, the microstructure is stored in a 2D/3D grid, with each voxel assigned to one of the phases ϕ_{Ni}, ϕ_{GDC}, and ϕ_{Pore}. For the validation phase of the study, we chose a voxel-wise frame-difference score, calculated as follows:

$$\text{score} = \sum_{p=1}^{N_{xyz}} |\phi_i^{\text{sim}}(p) - \phi_i^{\text{reference}}(p)| \qquad i \in \{\text{Ni, GDC, Pore}\}, \tag{3.4}$$

where p represents each voxel of the grid, and N_{xyz} the total number of voxels. These computations are enclosed within a PACE3D post-processing tool called *framedifference*, which facilitates streamlined assessment of microstructure deviations.

Minimizing the deviation is a successful validation step, which leads to the identification of the correct model parameters. Our AL framework converged at iteration 6 (see Figure 3.3), yielding results that closely aligned with the target parameters and successfully validated the 1D problem. The best value found for

the parameter γ_{NiGDC} was 0.57715, with a target value of 0.57700 and an accepted threshold of 0.02.

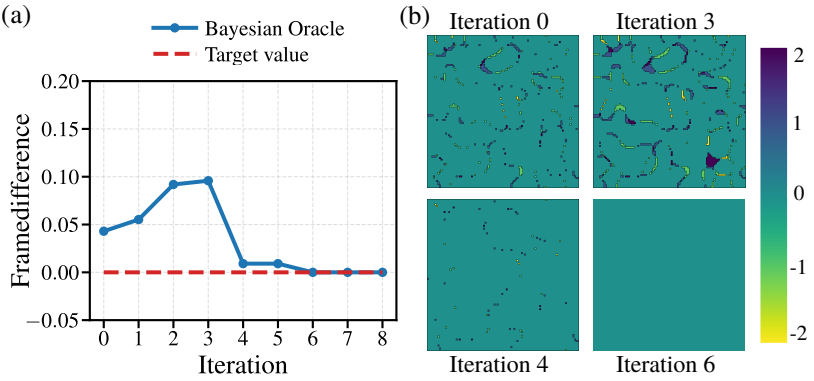


Figure 3.3: AL framework validation for a 1D, single-objective optimization problem. Tuned parameter: γ_{NiGDC}. The figure shows (a) an overview of the search and (b) a visualization of the error at four different iteration steps. The error is measured as a voxel-by-voxel difference between the resulting and target microstructure (*framedifference*). The first 3 data points are randomly sampled to produce a sufficient baseline for the BO Oracle search. The figure has been adjusted to the format of this dissertation.

To address the complexity of the SOFC's microstructural evolution, we moved to a more advanced multidimensional validation phase, optimizing six parameters simultaneously. The chosen parameters (discussed in detail in Section 3.2), together with their ranges of validity, and the best results obtained after 25 iterations of our framework, can be seen in Table 3.2. For this second validation phase, the scoring mechanism remained unchanged, i.e., as in eq (3.4), for each iteration of the method, we measured the deviation of the resulting microstructures from the reference. A shorter simulation time was considered to save computational resources and time, as the purpose here was still pure validation, giving no meaningful scientific results. Consequently, while the results obtained by the framework for some parameters may not appear optimal at first, there are a few factors to take into consideration. The terms in the model that are related to the

Table 3.2: Overview of the values chosen by the Bayesian Oracle at iteration 22, which gave the best result. The oracle explored the parameter space within predefined constraints, alongside the specified ranges of validity. For the interface energy parameters (γ_{NiGDC}, $\gamma_{GDCPore}$), values were sampled as floats with 0.01 increment. For the diffusion coefficients related parameters (M_{Ni}^{NiPore}, M_{Ni}^{NiGDC}, $M_{\mathrm{GDC}}^{GDCPore}$, M_{GDC}^{NiGDC}), where only changes in the order of magnitude have significant impact on the outcome, the oracle selected integer values for the exponent, effectively adjusting the parameters by powers of ten. The comprehensive error, used as a score for the oracle, was computed with *framedifference* according to eq (3.4) and gave a result of 0.0097.

Model parameters	Given range	Reference value	Predicted value
γ_{NiGDC}	0.45–1.49	1.20	1.19
$\gamma_{GDCPore}$	0.29–0.57	0.4	0.32
M_{Ni}^{NiPore}	0.1–1.0	0.6	0.54
M_{Ni}^{NiGDC}	3.52×10^{-5}–3.52×10^{-2}	10^{-3}	10^{-5}
$M_{\mathrm{GDC}}^{GDCPore}$	3.52×10^{-9}–3.52×10^{-4}	3.52×10^{-6}	3.52×10^{-7}
M_{GDC}^{NiGDC}	3.52×10^{-11}–3.52×10^{-5}	3.52×10^{-7}	3.52×10^{-4}

interface energy and nickel's surface diffusion coefficient (first three in Table 3.2), have a greater influence on the microstructure at smaller time frames, while the other terms in the model related to diffusion coefficients (last three in Table 3.2), only cause notable changes in the microstructure over an extended simulation period, due to their low magnitude of values. It is therefore logical for the firsts to approximately reach the reference value, while for the lasts, a closer alignment with the reference value is expected in longer simulation times. It is important to note that the diffusion values were restricted to variations by orders of magnitude, leading to the reference and predicted values aligning precisely with the same coefficient values. Furthermore, as the dimensionality of the problem increases, the volume of the search space expands exponentially, and so does the number of evaluations needed to ensure thorough exploration. Figure 3.4 shows an overview of the search.

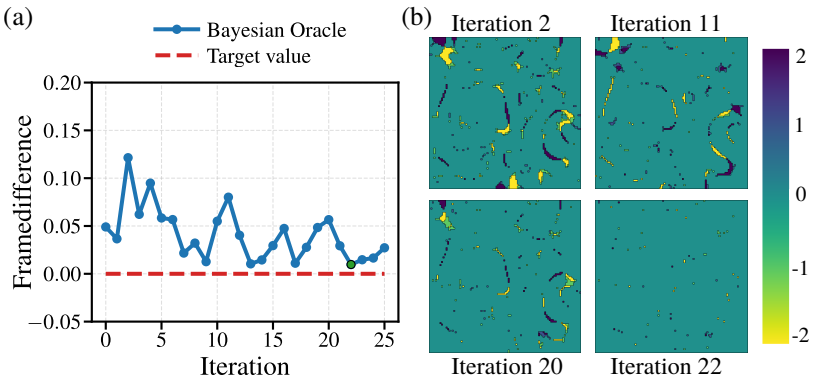


Figure 3.4: Framework validation for a 6-dimensional, single-objective optimization problem. The figure shows the overview of the search (a) and a visualization of the error at four different iteration steps (b). The error is measured as a voxel-by-voxel difference between the resulting and target microstructure (*framedifference*). The best result is found at iteration 22, with a *framedifference* error of 0.0097. The figure has been adjusted to the format of this dissertation.

3.4 Framework on 3D FIB-SEM reconstructed Ni-GDC anode microstructures

The developed AL framework was exploited to optimize a wide set of parameters for phase-field simulations of coarsening in the Ni-GDC anode under specific operating conditions. A proof of concept, demonstrating our method's potential for efficient parameter optimization in both single- and multi-dimensional problems, is detailed in Section 3.3. Following validation, the framework was applied to 3D FIB-SEM reconstructed Ni-GDC anode microstructures. In this Section, we present the results of both single- and multi-objective formulations of the considered optimization problem. The FIB-SEM reconstructed experimental microstructures of the Ni-GDC anode, both in pristine condition and after 240 hours of aging under the given operating conditions, are now used as a reference in the AL framework. At this stage, the goal is to identify an optimal set of input parameters that most accurately replicate the target microstructure properties

Table 3.3: Microstructural characteristic properties of pristine and 240h aged Ni-GDC anodes.

Parameter	Symbol	Pristine	240h aged
Ni vol.%	V_{Ni}	22.44	22.43
GDC vol.%	V_{GDC}	41.38	39.84
Pore vol.%	V_{Pore}	36.18	37.74
Ni/Pore Specific Area (μm^{-1})	$A_{Ni/Pore}$	0.37	0.33
GDC/Pore Specific Area (μm^{-1})	$A_{GDC/Pore}$	1.50	1.38
Ni/GDC Specific Area (μm^{-1})	$A_{Ni/GDC}$	0.67	0.61
GDC Tortuosity (−)	τ_{GDC}	2.57	3.07
Pore Tortuosity (−)	τ_{Pore}	2.57	2.40
Total TPB density (μm^{-2})	l_{TPB}	1.82	1.55
Nickel Mean Particle Diameter (µm)	d_{Ni}	0.91	1.04
GDC Mean Particle Diameter (µm)	d_{GDC}	0.59	0.62
Pore Mean Particle Diameter (µm)	d_{Pore}	0.60	0.68
Total volume (μm^3)	V	6666	4800
Voxel size (µm)	$\Delta x = \Delta y = \Delta z$	0.05	0.05

observed in the FIB-SEM experimental data. The key microstructural properties of these experimental microstructures are shown in Table 3.3. These parameters collectively define the anode's structural and functional efficiency, significantly influencing its electrochemical activity, as well as ion and gas transport, and ultimately impacting the overall cell performance.

3.4.1 Single objective optimization

Building on the successful validation of our approach, we apply the AL framework to address the core scientific objective of this study: identifying an optimal parameterization for a Ni-GDC anode coarsening model under given operating conditions. Using the Kadi4Mat Research Data Management (RDM) environment,

which integrates our entire data workflow, a seamless transition from the validation phase to the subsequent stages was straightforward.

As explained in Section 2.9, subdomains of real microstructures were employed, since repeatedly simulating the entire microstructure within the framework is computationally prohibitive. A subdomain with $9.4 \times 12.4 \times 6.4\ \mu m^3$ of volume was selected as the initial structure for the multiphase-field simulations. Given the inherently destructive nature of FIB-SEM techniques, the pristine and aged experimental microstructures originate from different regions within the Ni-GDC anode rather than from a consistent, singular location. This variability limits direct comparisons of aging between simulated and experimental structural morphologies. As a result, we focus our benchmark on the total density of the TPB, an important microstructural parameter that reflects the phenomena of the aging process. This approach provides a more reliable benchmark for comparing the aging of simulated and experimental microstructures, circumventing the limitations of localized structural variations.

As design variables for our AL Bayesian study, we considered the parameters γ_{NiGDC}, $\gamma_{GDCPore}$, $M_{\mathrm{GDC}}^{GDCPore}$, M_{GDC}^{NiGDC}, M_{Ni}^{NiGDC}, resulting in a 5D search space. For each of these parameters, we defined a range of plausible values based on available literature data and physical constraints (see Table 3.1). Although the values for nickel's surface energy and surface diffusion coefficient show considerable variation across different sources, they remain well-documented in the literature and are better established than those for GDC. For this study, we used fixed values of $2.26\,\mathrm{J\,m^{-2}}$ for the surface energy [168] and $5.48 \times 10^{-22}\ \mathrm{m^3\,s^{-1}}$ for the surface diffusion coefficient, towards lower end of the value range and approximately one-third of minimum value from Blakely et al. [148] under the given operating temperature of 900 °C. Using these fixed values across all simulations reduces the dimensionality of the search space, ensures a consistent scaling system of the model, and simplifies the calculation of other parameters.

The framework structure established during the validation stage (see Section 3.3), along with the KadiStudio workflow automating the whole process (see Figure 3.1), remains fundamentally unchanged, aside from a few adjustments. Due to

the significant increase in computational resources required by the simulations, we have included in our data stream a component that handles the automated communication with an HPC cluster. Each simulation was run on the idm-hpc03 high-performance computing cluster, which consists of eight computing nodes, each equipped with 64 cores. This cluster is part of the network infrastructure of the Institute for Digital Materials Science (IDM), and all computational tasks were managed using the SLURM workload manager. For this study, five nodes of the cluster were employed to perform the computations. At each iteration of the framework, the Bayesian Oracle provides its prediction of the most informative data point in the form of a complete parameter configuration. The oracle's output is subsequently input into a job file designed to initiate PACE3D simulations with the specified values. The job is then submitted to a computing cluster using SLURM and constantly monitored until completion, at which point the results are retrieved for post-processing and scoring. The framework was furthermore modified to incorporate a new scoring metric based on the total triple-phase boundary (TPB) density, a primary parameter characterizing the resulting microstructure. This new metric quantifies the deviation of the simulated TPB density from the experimentally measured value of the target microstructure. In other words, the objective of the Bayesian Oracle at this phase is to mimic the total TPB density of the target microstructure, assessing whether this replication suffices for a comprehensive comparison of the entire microstructure. Figure 3.5(a) shows an overview of the 5D optimization search, finding the target value of 1.55 at iteration 11, and definitively converging at iteration 14. The model successfully minimized the deviation for the single objective parameter, demonstrating its capability in a focused optimization scenario. However, analyzing Figure 3.5(b), we can conclude that a perfect match of a single considered property or descriptive parameter is insufficient to fully capture the morphology of the entire Ni-GDC anode microstructure, as significant deviations are observed when evaluating other critical descriptive parameters. To address this limitation, it is essential to adopt a more comprehensive approach, ensuring that all key characteristics are effectively considered and represented in the optimization process.

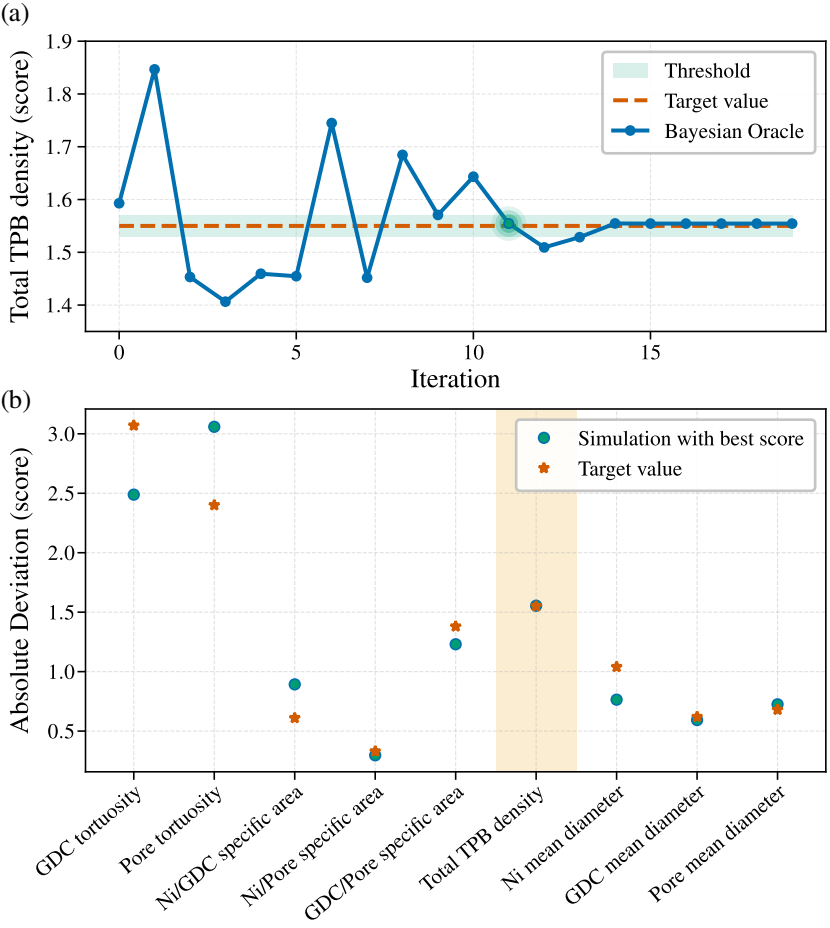


Figure 3.5: (a) Search overview of a 5D, single objective optimization, with total TPB density used as scoring value. Target value for total TPB density found at iteration 11. (b) A comparison is presented between the target values for the nine considered microstructure properties and those obtained from the Oracle-guided simulation at iteration 11. The plot demonstrates that the parameter considered for scoring closely matches the target, while others mostly deviate from their respective target values. The figure has been adjusted to the format of this dissertation.

3.4.2 Multi-objective optimization: weighted sum scalarization approach

As demonstrated in the previous Section, it is crucial to consider multiple aspects of the microstructure of Ni-GDC anodes to achieve a comprehensive representation that can effectively guide the optimization process. Ideally, we aim to closely replicate the nine most critical microstructure properties of the reference microstructure: GDC Tortuosity, Pore Tortuosity, Ni/GDC Specific Area, Ni/Pore Specific Area, GDC/Pore Specific Area, Total TPB density, Nickel Mean Particle Diameter, GDC Mean Particle Diameter, Pore Mean Particle Diameter (for more details, refer to Section 2.7 and Table 3.3).

Multi-objective optimization techniques facilitate the simultaneous optimization of multiple criteria by considering different objective functions. The goal for these problems is to find a set of solutions that represent the best trade-offs among the objectives. This set of solutions is known as the Pareto optimal set or Pareto front when referring to the image of the Pareto Set in the objective space (refs [201] and [202]). Each solution in this set is non-dominated, meaning that it is not possible to improve one objective without worsening at least one other. Building on this concept, for the final improved configuration of our AL framework, we define an objective function for each of the mentioned key properties, thereby integrating all of them into the optimization process. As we are working with subdomains of the entire microstructure, in our view, aiming for equal precision in replicating all the properties is not an effective approach. Therefore, as a score metric, we employ a weighted sum scalarization approach (see e.g., refs [203] and [204]), a method widely used to convert a multi-objective problem into a single-objective. This is achieved by forming an aggregate objective function using a linear combination of all objective functions, i.e., solving a problem of the form:

$$\min_x F(x) = w_1 f_1(x) + w_2 f_2(x) + \cdots + w_n f_n(x)\,, \tag{3.5}$$

where f_i are the different objective functions, and w_i the respectively assigned weights, typically normalized according to $0 \leq w_i \leq 1, \sum w_i = 1$, which leaves the

parameter space with $n-1$ degrees of freedom. Adjusting the weights results in different trade-offs between the objectives, thereby emphasizing certain properties over others and leading to different optimal solutions. The strength of the weighted sum scalarization method lies in its flexibility and conceptual transparency, which allow seamless incorporation of user or domain preferences. We exploited this property to reflect tortuosity's high sensitivity to local microstructural variations (as outlined in Section 2.9). Specifically, tortuosity parameters were assigned lower weights (half those of the other seven parameters). The primary purpose of the AL Bayesian framework is to efficiently explore the physical parameter space. This approach is particularly valuable for incorporating parameters with incomplete or inconsistent literature data, as well as those influenced by varying operating conditions (refer to Section 3.2 for the details). Hence, we extend the set of design variables in order to provide the Oracle with greater flexibility in exploring a now 7D parameter space. In addition to the five key input parameters discussed in the previous Section 3.4.1, this comprehensive approach involves tuning the model parameters related to nickel's surface diffusion coefficient M_{Ni}^{NiPore} and surface energy γ_{NiPore}. The specifically selected ranges of validity are outlined in Table 3.1. These include three interfacial energies and four excess interface diffusivities. The interfacial energies ranges are as follows: γ_{NiGDC} from $3.0\,\mathrm{J\,m^{-2}}$ to $1.0\,\mathrm{J\,m^{-2}}$, $\gamma_{GDCPore}$ from $2.0\,\mathrm{J\,m^{-2}}$ to $0.7\,\mathrm{J\,m^{-2}}$, and γ_{NiPore} from $2.5\,\mathrm{J\,m^{-2}}$ to $1.5\,\mathrm{J\,m^{-2}}$. The excess interface diffusivities are considered within the following ranges: $D_{\mathrm{GDC,ex}}^{GDCPore}$ from $2.4\times10^{-25}\,\mathrm{m^3\,s^{-1}}$ to $2.4\times10^{-28}\,\mathrm{m^3\,s^{-1}}$, $D_{\mathrm{GDC,ex}}^{NiGDC}$ from $2.4\times10^{-27}\,\mathrm{m^3\,s^{-1}}$ to $2.4\times10^{-33}\,\mathrm{m^3\,s^{-1}}$, $D_{\mathrm{Ni,ex}}^{NiGDC}$ from $4.0\times10^{-22}\,\mathrm{m^3\,s^{-1}}$ to $4.0\times10^{-27}\,\mathrm{m^3\,s^{-1}}$, and $D_{\mathrm{Ni,ex}}^{NiPore}$ from $4.0\times10^{-22}\,\mathrm{m^3\,s^{-1}}$ to $4.0\times10^{-20}\,\mathrm{m^3\,s^{-1}}$. The chosen upper bounds of these parameter ranges are used to establish the model's time and energy scales across all simulation runs. Given that nickel's surface diffusion coefficient can vary by up to two orders of magnitude, it is crucial to adjust the related model parameters accordingly, such as stable time step, interface mobilities, and total simulation time. This ensures efficient usage of computational resources while maintaining a consistent representation of the physical aging of microstructures. To achieve this, the above-mentioned model parameters are fine-tuned for each simulation run based on the specific surface

diffusion values for nickel selected by the Bayesian Oracle (for more details, refer to Section 3.2).

The increased dimensionality of the parameter space offers the potential for better exploration but at the price of higher computational and time demands. An explicit time integration method is used in our phase-field model, resulting in limitations on the permissible stable time step. As a result, when simulating the same physical aging time with higher values of nickel's surface diffusion coefficients, the stable time step is further limited. This results in a longer simulation time and a longer utilization of computing resources. Therefore, higher values of the surface diffusion coefficients of nickel substantially increase the computational resource requirements. As the Bayesian Oracle now navigates a more complex and challenging landscape, it is expected to require additional initial information and an overall greater number of iterations to reach optimal solutions. This translates into a preset higher number of initial random points (seven), and results in an extended timeframe to achieve satisfactory accuracy. Figure 3.6 provides an overview of the framework executed with the aforementioned setting. The entire execution of 43 iterations using the Bayesian AL framework took approximately 7 days and 18 hours on the idm-hpc03 high-performance computing cluster employing 315 cores.

Since in multi-objective optimization the goal is typically to find a set of solutions rather than a single optimum data point, we consider the five best results with an overall 7 %–8 % error, obtained at iterations 19, 27, 31, 37, and 38. Table 3.4 details the values suggested by the Oracle for each one of these iterations, along with the associated errors for each microstructure parameter. The five iterations yield a total score between 0.07 and 0.08, requiring a closer analysis of the physical parameters associated with each result. The excess surface diffusivity of nickel was consistently found to be $4.0 \times 10^{-22}\,\mathrm{m^3\,s^{-1}}$ across all five iterations with the best scores. The value estimated from the Bayesian AL framework, $4.0 \times 10^{-22}\,\mathrm{m^3\,s^{-1}}$, is approximately four times lower than the $1.74 \times 10^{-21}\,\mathrm{m^3\,s^{-1}}$ calculated for the $\{100\}$ surface at 900 °C using the Arrhenius relation from the experimental data of Blakely et al. [148]. Nevertheless, considering experimental measurement

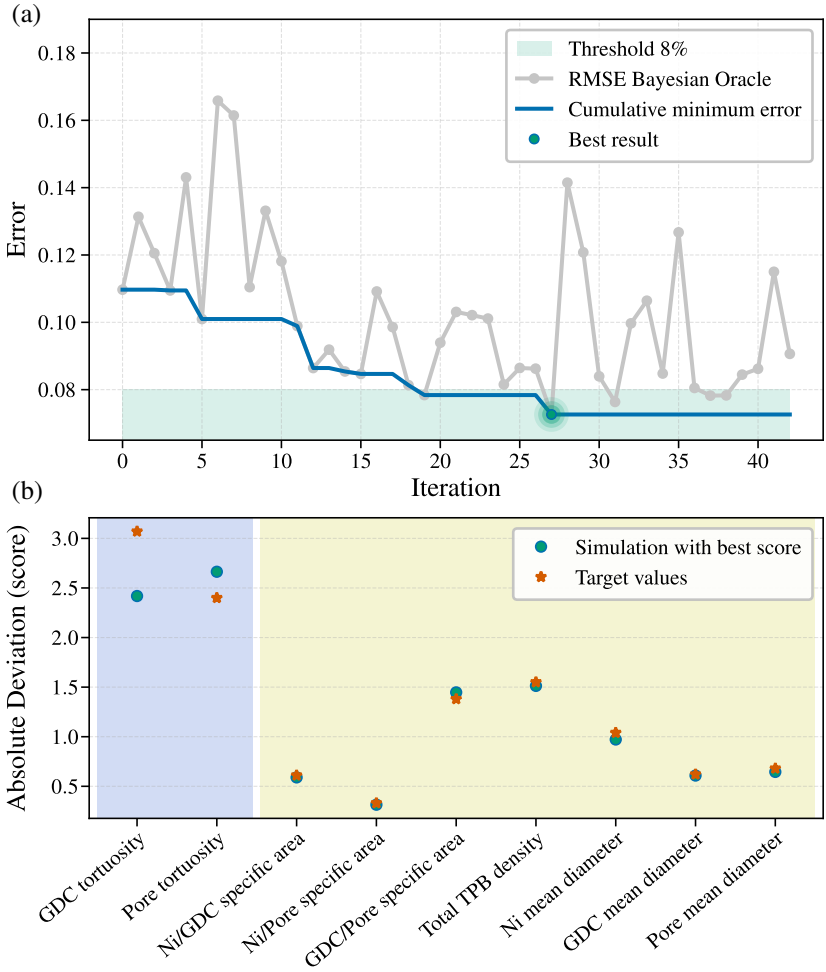


Figure 3.6: (a) Optimization convergence over time: The blue line shows the cumulative minimum error at each iteration, reflecting continual improvement in solution quality and evidence of plateauing around iteration 27. The grey line displays the RMSE for each iteration, providing insight into the overall search dynamics. (b) Agreement with target microstructural properties: Comparison of nine key descriptors – highlighting the Oracle-guided simulation at iteration 27, which delivered the best fit at 7 % total error. The two tortuosity metrics (left) were assigned a lower weight during scalarization, while the remaining seven parameters (right) received higher weights to guide the optimization. The figure has been adjusted to the format of this dissertation.

uncertainties ranging from one to two orders of magnitude, the estimated value is reasonable and aligns well with Hoffrogge et al.'s [98] assumption that diffusion along the slow {100} surface orientation is the rate-limiting factor. Furthermore, several factors need to be considered to account for the observed discrepancy: variations in experimental conditions and material purity, assumptions of isotropy and homogeneity, coarsening as the primary degradation mechanism in the model, and the inherent limitations of the Bayesian multi-objective optimization framework using the scalarization approach. Nickel diffusion coefficients reported by Blakely were measured on pure nickel surfaces under high vacuum conditions ($\sim 10^{-5}$ mm Hg), whereas the present study involves a Ni-GDC composite anode operating in an atmosphere of 50 % H_2/50 % H_2O. Blakely et al. [148] reported that impurities tend to adsorb preferentially on specific crystallographic planes, particularly the {100} planes, thereby obstructing diffusion pathways and significantly reducing surface diffusion rates. As a result, surface diffusion is highly sensitive to the annealing atmosphere, as adsorbed species can significantly affect atomic mobility. The operating conditions of SOFCs can influence Ni diffusivity at the surface due to oxygen partial pressure, impurities, adsorption of gas species, and interface interactions with GDC. Jiao et al. [205] reported that the wettability of Ni on YSZ improves during SOFC operation. This behavior is attributed to the adsorption of oxygen species on the Ni surface. Considering the above factors, it can be expected that the surface diffusion coefficient for Ni in the SOFC Ni-GDC system to be lower than the value reported by Blakely et al. [148]. Scalarization reduces multiple objectives to a single scalar objective, potentially oversimplifying the problem and failing to capture the full range of trade-offs between competing objectives. This simplification can lead to suboptimal solutions or an incomplete representation of variability in the diffusivity estimates.

The excess surface diffusivity of GDC was found to be in the range of $1 \times 10^{-26}\,\mathrm{m^3\,s^{-1}}$ to $1 \times 10^{-27}\,\mathrm{m^3\,s^{-1}}$ across all five iterations. Notably, the values from iteration 37 and iteration 38, $2.16 \times 10^{-27}\,\mathrm{m^3\,s^{-1}}$ and $4.96 \times 10^{-27}\,\mathrm{m^3\,s^{-1}}$, closely match the literature value for the surface diffusion coefficient at 900 °C, estimated as $2.4 \times 10^{-27}\,\mathrm{m^3\,s^{-1}}$ [194]. The excess interface diffusivity of nickel along the Ni-GDC interface was 3 to 5 orders of magnitude lower than that of the

excess surface diffusivity. Although no direct literature is available for validation, this aligns with the general understanding that interface or grain boundary diffusion is typically lower than surface diffusion. A similar trend is observed in the excess interface diffusivity of GDC along the Ni-GDC interface.

While the absolute values of surface and interfacial energies appear to vary across the five best iterations, their ratios – a key factor in driving the system towards thermodynamic equilibrium – show a clear consistency. The values for the surface energy of nickel at iterations 19 and 37, obtained as $2.50\,\mathrm{J\,m^{-2}}$, appear to disagree with values commonly reported in the literature [168, 181, 184–189]. Similarly, a value of $1.50\,\mathrm{J\,m^{-2}}$ from iteration 27 is significantly lower than most literature findings. However, the surface energies of $1.85\,\mathrm{J\,m^{-2}}$ and $2.10\,\mathrm{J\,m^{-2}}$, obtained in iterations 31 and 38, are more in line with the reported data. For GDC, surface energies of $1.28\,\mathrm{J\,m^{-2}}$, $1.43\,\mathrm{J\,m^{-2}}$, and $1.53\,\mathrm{J\,m^{-2}}$ in iterations 37, 38, and 19 respectively, are consistent with experimental studies using the multiphase equilibration technique, which estimate the surface energy of CeO_2 in an argon atmosphere at 900 °C to be approximately $1.80\,\mathrm{J\,m^{-2}}$ [194].

Considering all physical parameters and their comparison with the available literature, the values derived from iteration 38 proved to be consistent and representative values for aging simulations of the Ni-GDC anode at the given operating conditions. Figure 3.7 shows the evolution of the initial 3D microstructure and its 2D cross-sectional view through distinct iterations of the AL framework. Iteration 6 produces a microstructure with an overall 16.6 % error in microstructural parameters compared to experimental results, while iteration 38 reduces this error to 7.8 %. The morphological differences between the aged microstructures from these two iterations are also evident in Figure 3.7. The optimized input physical parameter values obtained from our AL Bayesian framework in iteration 38 yield interfacial energies for γ_{NiGDC}, $\gamma_{GDCPore}$, and γ_{NiPore} as $2.43\,\mathrm{J\,m^{-2}}$, $1.43\,\mathrm{J\,m^{-2}}$ and $2.10\,\mathrm{J\,m^{-2}}$, respectively. These values align well with the available literature on the surface energies of nickel and ceria, as discussed in Section 3.2. The excess surface and interface diffusivities of nickel and GDC are $D^{NiPore}_{\mathrm{Ni,ex}}$, $D^{NiGDC}_{\mathrm{Ni,ex}}$, $D^{GDCPore}_{\mathrm{GDC,ex}}$, and $D^{NiGDC}_{\mathrm{GDC,ex}}$, with values of $4.0\times10^{-22}\,\mathrm{m^3\,s^{-1}}$, $4.0\times10^{-27}\,\mathrm{m^3\,s^{-1}}$,

$4.96 \times 10^{-27}\,\mathrm{m^3\,s^{-1}}$ and $1.14 \times 10^{-33}\,\mathrm{m^3\,s^{-1}}$, respectively, under the operating conditions of Ni-GDC at a temperature of 900 °C with a gas composition of 50 % H_2/50 % H_2O.

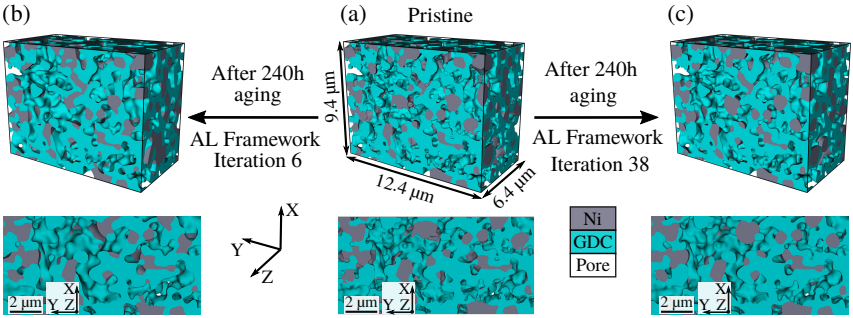


Figure 3.7: The figure shows the evolution of the 3D microstructure and its 2D cross-section at distinct iterations of the AL framework. (a) Initial 3D microstructure for simulation and a 2D cross-sectional view of it, (b) 240h evolved 3D microstructure and 2D cross-section obtained from the AL framework at iteration 6 with a poor overall error percentage of 16.6, and (c) 240h evolved 3D microstructure and 2D cross-section obtained from the AL framework at iteration 38 with a best overall error percentage of 7.8. The figure has been adjusted to the format of this dissertation.

3.5 Interim conclusion

To accurately simulate the aging of Ni-GDC anodes and predict their long-term behavior under operational conditions, precise parameterization of the phase-field model is essential. However, this task is made challenging by incomplete or inconsistent literature data, especially regarding key parameters like surface diffusivities and interface energies. In this Chapter, we have presented an AL framework combined with Bayesian optimization, designed to efficiently explore the high-dimensional parameter space and identify the optimal model parameters for simulating the aging of Ni-GDC anodes.

Table 3.4: Overview of the 5 iterations with the best score. The top part of the table shows the values suggested by the Bayesian Oracle for each of the 7 input parameters that we asked to tune (for ranges of validity, refer to Table 3.1). The bottom part of the table shows the error obtained for each of the 9 considered microstructure properties in relation to the reference microstructure and the overall score.

Physical parameters	iter 19	iter 27	iter 31	iter 37	iter 38
γ_{NiGDC} ($\mathrm{J\,m^{-2}}$)	2.98	1.70	1.78	2.68	2.43
$\gamma_{GDCPore}$ ($\mathrm{J\,m^{-2}}$)	1.53	0.70	0.70	1.28	1.43
γ_{NiPore} ($\mathrm{J\,m^{-2}}$)	2.50	1.50	1.85	2.50	2.10
$D^{GDCPore}_{\mathrm{GDC,ex}}$ ($\mathrm{m^3\,s^{-1}}$)	2.16×10^{-26}	1.72×10^{-26}	2.07×10^{-26}	2.16×10^{-27}	4.96×10^{-27}
$D^{NiGDC}_{\mathrm{GDC,ex}}$ ($\mathrm{m^3\,s^{-1}}$)	1.14×10^{-33}	1.72×10^{-31}	1.14×10^{-33}	1.14×10^{-33}	1.14×10^{-33}
$D^{NiGDC}_{\mathrm{Ni,ex}}$ ($\mathrm{m^3\,s^{-1}}$)	4.0×10^{-27}	1.15×10^{-24}	5.40×10^{-26}	1.91×10^{-25}	4.0×10^{-27}
$D^{NiPore}_{\mathrm{Ni,ex}}$ ($\mathrm{m^3\,s^{-1}}$)	4.0×10^{-22}	4.0×10^{-22}	4.0×10^{-22}	4.0×10^{-22}	4.0×10^{-22}
GDC Tortuosity err	3.2e-3	2.8e-3	2.9e-3	2.4e-3	2.7e-3
Pore Tortuosity err	9.8e-4	7.5e-4	8.7e-4	5.4e-4	9.6e-4
Ni/GDC Specific Area err	7.9e-5	1.4e-4	6.0e-6	2.1e-5	4.2e-5
Ni/Pore Specific Area err	7.5e-4	2.9e-4	7.4e-4	1.0e-3	9.6e-4
GDC/Pore Specific Area err	3.3e-5	2.9e-4	1.6e-4	8.1e-4	2.3e-4
Total TPB Density err	5.2e-4	7.3e-5	2.6e-4	1.2e-4	1.8e-4
Ni Mean Particle Diameter err	6.0e-4	5.4e-4	6.8e-4	6.2e-4	8.0e-4
GDC Mean Particle Diameter err	1.5e-7	4.4e-5	3.8e-5	1.3e-4	7.8e-5
Pore Mean Particle Diameter err	2.5e-5	3.3e-4	1.6e-4	3.9e-4	1.8e-4
final score	0.078	0.073	0.076	0.078	0.078

While single-objective optimization can simplify the design process and might be sufficiently effective in enhancing a particular material property, in the context of Ni-GDC SOFC anodes, it does not adequately capture the full range of physical characteristics of the microstructure of interest. This approach can lead to significant deviations in other critical, descriptive parameters that are not considered, resulting in possibly suboptimal material performance. Given these limitations, we transitioned to a multi-objective optimization approach to better address the complexity of our problem. This shift allows for the simultaneous consideration of multiple critical microstructure properties, ensuring overall improved solutions. By employing a scalarization approach, precisely a weighted sum method, we can aggregate different objective functions into a single objective, thereby balancing competing criteria and achieving a more comprehensive representation of the desired microstructure. In the context of SOFCs, we identified a promising set of solutions with an overall error on the order of 10^{-2} (specifically, between 0.07 and 0.08), indicating a good balance between competing objectives. Moreover, within this set, we identified results that align with the limited literature data available, further validating our approach.

In conclusion, the AL Bayesian framework has demonstrated strong performance, providing good practice for intelligent data selection and model optimization. Beyond its success in finding physical parameters for Ni-GDC anode microstructure under given operating conditions, our framework's generic implementation ensures its applicability across various other applications. This approach proves particularly valuable in scenarios where missing parameters need to be inferred or manual trial-and-error tuning is challenging, extending its utility well beyond the specific context of this study. Although this work focuses on the Ni-GDC anode system, the framework can be readily transferable to other SOFC material systems, such as the widely used Ni-YSZ anodes. For this, FIB-SEM-reconstructed experimental microstructures of Ni-YSZ in both pristine and aged states, together with appropriate adaptation of material-specific parameter ranges, such as interface energies and diffusion coefficients, are required for optimization.«

4 MPF aging simulations of the Ni-GDC anode: experimental validation and effects of interfacial energy[1]

»The long-term durability of SOFCs requires a comprehensive understanding of electrode degradation mechanisms. Performance degradation of Ni-GDC electrodes, however, is not yet thoroughly understood, limiting their effective design and advancement. MPF simulation studies provide an effective method to understand the underlying microstructural changes and the resulting electrochemical property alterations in SOFCs over time. In this Chapter, quantitative simulations of nickel and GDC coarsening in SOFC anodes employing an MPF model utilizing FIB-SEM reconstructed experimental 3D microstructures and reliable thermophysical parameters, derived in Chapter 3 through a Bayesian active learning framework, are presented. The model is initialized with experimentally reconstructed pristine and pre-aged Ni-GDC microstructures and validated against aged experimental microstructures after 240 and 1100 operating hours. Key microstructural properties, mean particle size, TPB density, tortuosity, and specific surface areas, are evaluated to assess degradation. Furthermore, large-scale aging simulations of up to 60,000 aging hours are being investigated, as well as the influence of interfacial energies on long-term degradation by considering distinct

[1] The content of this chapter has been taken directly from Jeela et al. [74] with minor linguistic changes. Additional content concerning large-scale aging simulations over the operational lifetime of the solid oxide fuel cell is considered. The figures have been adjusted to the format of this dissertation.

thermodynamic equilibrium contact angle scenarios at the triple junction and the formation of layers around particles in Ni-GDC systems.

4.1 Model parameters

Accurately simulating the aging process in Ni-GDC anodes and reliably predicting their long-term behavior under operating conditions requires accurate parameterization of the phase-field model. However, the scarcity and inconsistency of literature data render this task considerably more challenging, especially for critical parameters such as surface diffusivities and interfacial energies for the Ni-GDC system. Although data for similar systems, such as Ni-YSZ, can be obtained from the literature, these details are not available for Ni-GDC, which presents a significant challenge. To address these limitations, an active learning (AL) framework with integrated Bayesian optimization was implemented as shown in Chapter 3. This approach was specifically designed to efficiently navigate the high-dimensional parameter space and enable the identification of optimal model parameters for simulating the aging behavior of Ni-GDC anodes. With the help of this framework, a promising set of parameter values that not only optimize the model but also match the existing literature's data was identified. From the parameter optimization of the AL-Bayesian framework, interfacial energy values of γ_{NiGDC}, $\gamma_{GDCPore}$, and γ_{NiPore} as $2.43\,\mathrm{J\,m^{-2}}$, $1.43\,\mathrm{J\,m^{-2}}$ and $2.10\,\mathrm{J\,m^{-2}}$, respectively, were obtained. These values are consistent with literature-reported surface energies. For nickel, surface energies are reported in the range of $1.6\,\mathrm{J\,m^{-2}}$–$2.5\,\mathrm{J\,m^{-2}}$ [181, 185, 187, 206]. Similarly, the surface energies of GDC for the {100}, {110}, and {111} orientations are $1.46\,\mathrm{J\,m^{-2}}$, $0.90\,\mathrm{J\,m^{-2}}$ and $0.74\,\mathrm{J\,m^{-2}}$ respectively, as reported in ref [196]. Experimental studies employing the multiphase equilibration technique estimated the surface energy of CeO_2 in an argon atmosphere at 900 °C to be approximately $1.80\,\mathrm{J\,m^{-2}}$ through extrapolation [194]. Additionally, the optimized excess surface and interface diffusivities for the Ni-GDC system were determined as follows: $D^{NiPore}_{\mathrm{Ni,ex}}$, $D^{NiGDC}_{\mathrm{Ni,ex}}$, $D^{GDCPore}_{\mathrm{GDC,ex}}$, and $D^{NiGDC}_{\mathrm{GDC,ex}}$, with values of $4.0\times10^{-22}\,\mathrm{m^3\,s^{-1}}$, $4.0\times10^{-27}\,\mathrm{m^3\,s^{-1}}$, $4.96\times10^{-27}\,\mathrm{m^3\,s^{-1}}$ and

$1.14 \times 10^{-33}\,\mathrm{m^3\,s^{-1}}$, respectively, from AL Bayesian framework. These values correspond to operating conditions for Ni-GDC anodes at a temperature of 900 °C with a gas composition of 50 % H_2/50 % H_2O in the SOFC mode.

For simplification of the analysis, the parameters of the phase-field model are represented in a model-specific system of units, where u_l, u_E, and u_t denote the characteristic units of length, energy, and time, respectively. The length unit u_l is determined by the resolution of the original microstructure (Δx). The units of energy and time are linked by the surface energy of the nickel, γ_{NiPore}, the surface diffusivity of the nickel, $D^{NiPore}_{\mathrm{Ni,ex}}$, and the operating temperature, T (refer to eq (2.47)). A detailed parameterization of the model can be found in Table 4.1. The interfacial mobilities, $m_{\alpha\beta}$, are selected to remain sufficiently low to ensure that the system operates in the surface diffusion-controlled regime (cf. [[108], eq (99) ff]), thus preventing these mobilities from becoming the dominant rate-limiting factors. Equilibrium compositions $c^{\alpha}_{i,\,\mathrm{eq}}$, which correspond to the minima of the parabolic free energy function, are assigned distinct values of 0.1 and 0.9, allowing a clear distinction between the phases, such as Ni-rich and Ni-poor regions. The pre-factor A_i in the parabolic free energy formulation, which characterizes the strength of immiscibility, is chosen to ensure consistent volume conservation throughout the simulation.

For the investigation of the influence of different scenarios of contact angles, the following selection strategy is considered. Since both the Ni and GDC phases evolve over time in these systems, scenarios in which Ni transitions from dewetting to wetting and a similar transition for GDC are investigated independently. Sufficient differences in contact angles are chosen between the simulation cases to ensure that any trends observed in the results draw reliable conclusions about variations in contact angle. While smaller contact angles, such as 60° or 75°, may not be achievable experimentally without particular additives or preparation, this study provides valuable insight into whether improved wetting characteristics could contribute to mitigating anode-side degradation. It should be noted that experimental findings of Ni-GDC in the literature reported on the formation of a GDC layer around the nickel [83, 86], and the present investigation may provide

Table 4.1: The phase-field model parameters employed in the coarsening simulations of the Ni-GDC anode. These parameters are derived from the physical properties of the material system and represented in a model-specific system of units. The model units are stated as $u_l = 50\,\mathrm{nm}, u_E = 5.25 \times 10^{-15}\,\mathrm{J}, u_t = 1.72\,\mathrm{s}$. Physical parameter values for both surface and interfacial diffusion coefficients and energies at a temperature of 900 °C with a gas composition of 50 % H_2/50 % H_2O were adopted from earlier Chapter 3 and converted into the corresponding model parameters.

Parameter (symbol)	Value (model units)	Value (physical units)
Ni-surf. chem. mobility (M_{Ni}^{NiPore})	$0.1\ u_l^6/(u_E u_t)$	$1.73 \times 10^{-31}\,\frac{\mathrm{m}^6}{\mathrm{Js}}$
Ni-nickel/GDC interf. chem. mobility (M_{Ni}^{NiGDC})	$1.0 \times 10^{-6}\ u_l^6/(u_E u_t)$	$1.73 \times 10^{-36}\,\frac{\mathrm{m}^6}{\mathrm{Js}}$
GDC-surf. chem. mobility ($M_{\mathrm{GDC}}^{GDCPore}$)	$4.37 \times 10^{-6}\ u_l^6/(u_E u_t)$	$7.55 \times 10^{-36}\,\frac{\mathrm{m}^6}{\mathrm{Js}}$
GDC-nickel/GDC interf. chem. mobility (M_{GDC}^{NiGDC})	$1.0 \times 10^{-12}\ u_l^6/(u_E u_t)$	$1.73 \times 10^{-42}\,\frac{\mathrm{m}^6}{\mathrm{Js}}$
Interfacial energy Ni-Pore (γ_{NiPore})	$1.0\ u_E/u_l^2$	$2.1\,\frac{\mathrm{J}}{\mathrm{m}^2}$
Interfacial energy Ni-GDC (γ_{NiGDC})	$1.16 \ldots 0.47\ u_E/u_l^2$	$2.43 \ldots 0.98\,\frac{\mathrm{J}}{\mathrm{m}^2}$
Interfacial energy GDC-Pore ($\gamma_{GDCPore}$)	$0.68 \ldots 1.87\ u_E/u_l^2$	$1.43 \ldots 3.92\,\frac{\mathrm{J}}{\mathrm{m}^2}$
Interface mobility Ni-Pore (m_{NiPore})	$0.1\ u_l^4/(u_E u_t)$	$6.92 \times 10^{-17}\,\frac{\mathrm{m}^4}{\mathrm{Js}}$
Interface mobility Ni-GDC (m_{NiGDC})	$0.1\ u_l^4/(u_E u_t)$	$6.92 \times 10^{-17}\,\frac{\mathrm{m}^4}{\mathrm{Js}}$
Interface mobility GDC-Pore ($m_{GDCPore}$)	$0.1\ u_l^4/(u_E u_t)$	$6.92 \times 10^{-17}\,\frac{\mathrm{m}^4}{\mathrm{Js}}$
Interface width parameter (ϵ)	$2.0\ u_l$	100 nm
Voxel-size ($\Delta x = \Delta y = \Delta z$)	$1.0\ u_l$	50 nm
Thermodynamic prefactor Nickel (A_{Ni})	$5\ u_E/u_l^3$	$2.1 \times 10^8\,\frac{\mathrm{J}}{\mathrm{m}^3}$
Thermodynamic prefactor GDC (A_{GDC})	$50\ u_E/u_l^3$	$2.1 \times 10^9\,\frac{\mathrm{J}}{\mathrm{m}^3}$

additional insight into such dynamics. Nevertheless, it is important to note that exploring the practical feasibility of improving the wetting properties of nickel or GDC in Ni-GDC systems is beyond the scope of this work.

4.2 Microstructural evolution of 3D Ni-GDC anode: comparative analysis of simulation and experimental results

In this Section, we present an analysis of microstructural evolution in Ni-GDC anodes using multiphase-field coarsening simulations and experimental results. Our approach couples 3D FIB-SEM reconstructions of experimental microstructures with phase-field modeling to predict and gain insights into the aging process of Ni-GDC anodes under high temperatures of 900 °C in a reducing atmosphere of 50 % H_2/50 % H_2O, without including electrochemical charge-transfer processes. Here, we employ two experimental microstructures as inputs for the phase-field simulations: a pristine Ni-GDC anode microstructure and an anode after 240 hours of experimental aging. Thereafter, we perform the phase-field simulations on two distinct initial microstructures: 1100 hours on the pristine microstructure (corresponding to the first validation scenario) and 860 hours on the pre-aged microstructure (extending the predictions to two distinctive initial microstructures). With this approach, we compare the simulation results with those of experimentally aged microstructures after 240 and 1100 hours. By employing pristine and pre-aged reference microstructures, the predictability of the model under different initial conditions is evaluated, as well as the influence of local microstructural inhomogeneities on the aging behaviour. This multi-faceted approach enables the robust validation of our phase-field results and provides a deeper understanding of the complex microstructural evolution in Ni-GDC anodes, which is essential for predicting and optimizing the long-term performance of SOFCs.

Three experimental cells at different stages of aging were subjected to FIB-SEM 3D reconstructions: pristine, after 240 hours of operation, and after 1100 hours of operation (see Figure 4.1). In all three reconstructed cells, a similar composition is observed (see Table 4.2). The differences in phase volume fractions among the pristine and aged experimental microstructures in Table 4.2 most probably result from slight inhomogeneities across the anode samples from the same batch. Holzer et al. [86] observed standard deviations of about 2 % in the average volume

Table 4.2: Structural properties of pristine, 240h aged, and 1100h aged FIB-SEM 3D reconstructed experimental microstructures of the Ni-GDC anode.

Parameter	Symbol	Pristine Exp.	240h aged Exp.	1100h aged Exp.
Ni vol.%	V_{Ni}	22.44	22.43	21.87
GDC vol.%	V_{GDC}	41.38	39.84	40.81
Pore vol.%	V_{Pore}	36.18	37.73	37.32
Total volume (μm^3)	V	6666	4800	5104
Voxel size (μm)	$\Delta x = \Delta y = \Delta z$	0.05	0.05	0.05

fractions of all three phases in four nominally identical samples and attributed these discrepancies to sample production variations and possible preparation effects. Similar variations could thus be observed in the samples utilized for the aging experiments in this work. Liu et al. [89] also reported from experimental observations that pristine and aged cells showed fairly similar overall compositions, further indicating that these observed variations are due to minor sample-to-sample differences. These reconstructions enabled the quantification of key microstructural characteristics of the Ni-GDC anode, as shown in Table 4.3, and provided insight into microstructural evolution over time. The density of the TPB lines, representing electrochemically active sites, decreased from an initial value of $1.82\,\mu m^{-2}$ in the pristine anode to $1.55\,\mu m^{-2}$ after 240 hours of operation, a reduction of 14.8 %. This decrease continued during prolonged aging, with the TPB density decreasing further to $1.41\,\mu m^{-2}$ after 1100 hours, corresponding to an overall reduction of 22.5 % compared to the initial state. Similarly, the density of the DPB area – another key parameter representing electrochemically active sites in Ni-GDC anodes – also showed a decrease in value. The DPB density decreased from an initial value of $1.50\,\mu m^{-1}$ to $1.38\,\mu m^{-1}$ after 240 hours, corresponding to an 8 % reduction, and further decreased to $1.31\,\mu m^{-1}$ after 1100 hours, corresponding to an overall reduction of 12.7 %.

Experimental studies showed that higher DPB density increases the electrochemical activity in Ni-GDC anodes. Nakamura et al. [207] reported an extension of

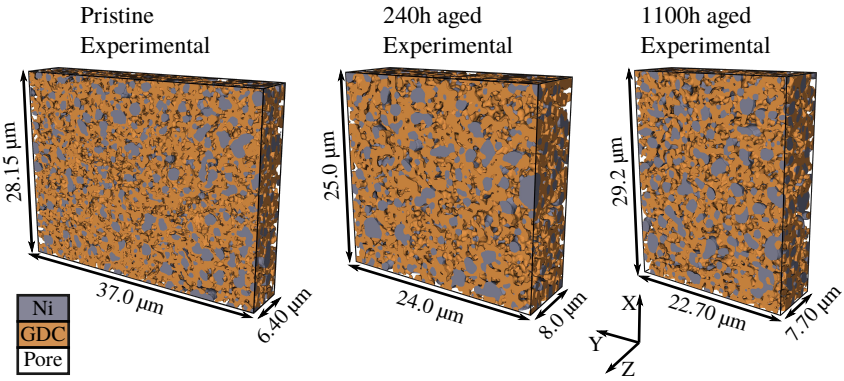


Figure 4.1: FIB-SEM 3D reconstructed pristine Ni-GDC anode microstructure alongside experimentally aged samples from the same batch after 240 and 1100 hours.

the active reaction zone beyond the TPB to the GDC/gas interface in ceria-based anodes, with an increased GDC surface area improving performance. Consistent with this, Chueh et al. [22], utilizing well-defined ceria metal structures, demonstrated that H_2 oxidation at equilibrium occurs predominantly via electrocatalysis at the oxide/gas interface, with limited contribution from conventional TPBs. These results highlight the crucial role of DPBs (GDC/pore interfaces) in lowering the activation overpotentials for hydrogen oxidation. These observed reductions in both TPB and DPB density over aging suggest a deterioration in the overall electrochemical performance of the Ni-GDC. Although the pristine and aged microstructures were reconstructed from different domains, both microstructures correspond to the central regions of the anode, thereby minimizing edge effects and spatial heterogeneity. Statistical analysis of four non-overlapping $1/2$ subdomains of the original microstructure in Section 2.9 revealed coefficients of variation (CV) between 0 %–2 % for all properties, suggesting negligible spatial variations. In addition, the original microstructure volume exceeds the representative volume element (RVE) threshold of 10^3 particles, above which most properties converge to stable values as reported by Joos [167].

Table 4.3: Microstructural characteristic properties of pristine and aged Ni-GDC anodes: comparative analysis of experimental aging with simulations

Parameter	Pristine Exp.	240h Sim. Input: pristine	240h Exp.	1100h Sim. Input: pristine	1100h Sim. Input: pre-aged	1100h Exp.
Ni/Pore SSA (μm^{-1})	0.37	0.31	0.33	0.29	0.29	0.31
GDC/Pore SSA (μm^{-1})	1.50	1.44	1.38	1.39	1.32	1.31
Ni/GDC SSA (μm^{-1})	0.67	0.62	0.61	0.61	0.56	0.60
GDC tortuosity (−)	2.57	2.50	3.09	2.42	2.68	3.08
Pore tortuosity (−)	2.57	2.55	2.36	2.59	2.37	2.38
Total TPB density (μm^{-2})	1.82	1.52	1.55	1.40	1.31	1.41
Nickel mean dia. (µm)	0.91	0.955	1.04	0.966	1.08	1.111
GDC mean dia. (µm)	0.59	0.60	0.62	0.62	0.64	0.663
Pore mean dia. (µm)	0.60	0.63	0.68	0.66	0.71	0.723

4.2.1 Phase-field simulations of 1100h aging: employing a pristine Ni-GDC anode as input

As described in the previous subsection, a pristine FIB-SEM reconstructed experimental microstructure of the Ni-GDC anode was employed as the initial reference for phase-field simulations. Aging simulations were performed for up to 1100h, and the microstructural properties at 240h and 1100h were compared to experimentally aged counterparts (see Table 4.3). A comprehensive understanding of Ni-GDC anode degradation requires the analysis of several interrelated microstructural properties. To ensure accurate validation of experimental and simulated microstructural evolutions, replication of key features of the microstructure is essential. Therefore, we considered nine critical parameters: specific interface areas (Ni/Pore, GDC/Pore, and Ni/GDC), tortuosity of GDC and pore phases, TPB density, and mean particle diameters of Ni, GDC, and Pores.

Comparison of experimental and simulated results after 240h of aging

The evolution of specific surface areas in the simulations aligns well with experimental data, with deviations of 6 % for Ni/Pore and 2 % for Ni/GDC interfaces.

The GDC/Pore interface, which presents DPBs essential for electrochemical reactions, shows a 4 % deviation. The tortuosity values show larger discrepancies, with deviations of 19 % for GDC and 8 % for pores. These differences might be due to their more localized property nature (high sensitivity against local microstructural changes) and not uniformly homogeneous transport paths across the structure. The tortuosity values for the Ni phase are not specified in Table 4.3 as the phase is non-percolating. As a result of isolated and poorly connected Ni particles, the nickel phase remains too disconnected to determine a finite tortuosity value. In the literature, such instances are often stated as undefined or infinite tortuosity. The total TPB density, a key parameter for electrochemical activity, differs by about 2 %, demonstrating close agreement between the phase-field simulation and experimental aging results. Experimentally, the morphological evolution of Ni and GDC during aging is observed [83, 86, 89], indicated also by the increase in the mean particle diameter. The deviations in the mean particle size are 8 % for Ni, 3 % for GDC, and 7 % for pores. Thus, except for the tortuosity of GDC, all the microstructural characteristics predicted by the phase-field simulations remain within 8 % deviation from the experimental values over the aging, demonstrating the predictive capability of our phase-field model on the microstructural evolution of Ni-GDC anodes. To further illustrate the microstructural evolution, the 3D morphological microstructure evolution and a 2D cross-section of it are shown over the aging times of 0, 240, and 1100h in Figure 4.2.

Comparison of experimental and simulated results after 1100h of aging The deviations in the microstructural properties of simulations and experiments observed after 1100h of aging are consistent with those observed after 240h. Interestingly, a notable discrepancy is observed in the evolution of the mean nickel particle diameter. In simulations, the mean nickel diameter remains nearly unaltered, increasing slightly from 0.955 µm at 240h to 0.966 µm at 1100h. On the contrary, the experimental results show a clear increase from 1.04 µm to 1.11 µm in the same period (see Table 4.3). Multiple factors might contribute to this discrepancy. Nickel particles are coarser than GDC particles (0.91 µm compared to 0.59 µm in the pristine state), and the non-percolating nickel phase

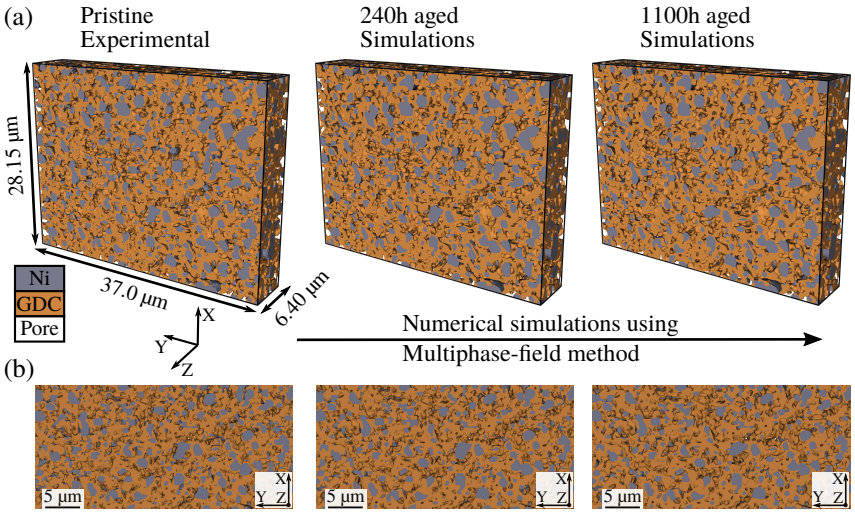


Figure 4.2: Phase-field simulation of the (a) 3D microstructure and (b) 2D cross sections at different aging times of 0h, 240h, and 1100h using the pristine microstructure as initial input.

accounts for only 22.4 % of the total domain volume, compared to 41.4 % for GDC and 36.2 % for pores. This limited connectivity may hinder coarsening mechanisms, as isolated Ni particles present fewer possibilities for coarsening through particle interactions. Furthermore, slight inhomogeneities in the nickel particle distribution across the cell may amplify the deviations between the simulated and experimental microstructures, given the lower volume fractions of nickel. Additionally, the 3D reconstruction and segmentation methods, as well as the diffusivity and energy parameters derived from the Bayesian multi-objective optimization approach, may also introduce some possible associated errors.

4.2.2 Phase-field simulations of 860h aging: employing a pre-aged (240h) Ni-GDC anode as input

To further investigate the predictive capability of our phase-field model for simulating the microstructural evolution of Ni-GDC anodes and to examine the influence of local microstructural inhomogeneities on the aging behavior, phase-field simulations are performed using a pre-aged (240h) experimental FIB-SEM reconstructed 3D Ni-GDC anode microstructure as the initial condition. Simulations are performed for an aging duration of 860h on a pre-aged (240h) Ni-GDC anode, effectively resulting in a 1100h aged microstructure. The resulting microstructural properties are then compared to the experimentally aged microstructure of 1100h (see Table 4.3). As shown in Table 4.3, all microstructural properties show similarities in their evolution behavior between simulations and experiments. In particular, the mean nickel particle diameter increased from 1.04 µm to 1.08 µm in simulations, compared to an increase from 1.04 µm to 1.11 µm in experiments. This corresponds to a deviation of about 3 %, a significant improvement in accuracy compared to simulations with a pristine microstructure as an initial condition. In conclusion, these results demonstrate that the initial morphological configuration of the Ni particles – and the associated inhomogeneities in the cell – play a role in attaining agreement between experimental and simulated results, in addition to the model's predictive capability. Further quantitative analyses show that the GDC/Pore-specific surface area deviates just about 1 %, while the total density of the TPBs deviates by 7 %. Except for GDC tortuosity deviating about 13 %, all other microstructural property deviations remain below 7 %, which shows a further better agreement with experimental data compared to phase-field simulations initiated with the pristine microstructure. The 3D morphological evolution and a corresponding 2D cross-section of the microstructure over the aging periods of 240h, 670h, and 1100h are shown in Figure 4.3.

All simulated microstructural parameters indicate qualitative agreement and good quantitative accuracy with the experimental results, except for the GDC tortuosity.

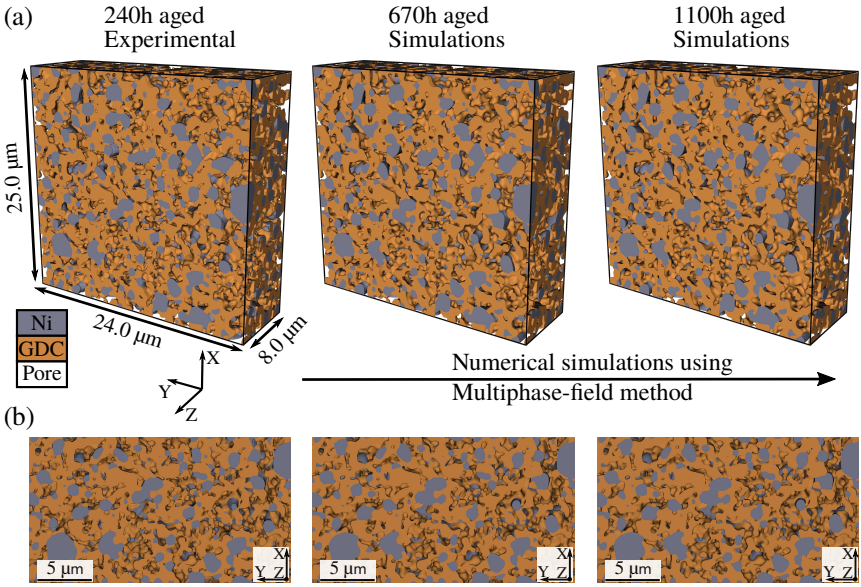


Figure 4.3: Phase-field simulation of the (a) 3D microstructure and (b) 2D cross sections at different aging times of 240h, 670h, and 1100h using the pre-aged (240h) microstructure as initial input.

- Evolution of degradation kinetics: In experiments, local GDC diffusion values resulting from spatial P_{O_2} gradients may deviate from the global value. Furthermore, this work considers and assumes a uniform Ni/GDC wettability over the entire domain due to a lack of experimental findings or data. However, inclusion of a spatially dependent wettability could provide an improved representation of the local GDC redistribution. Additionally, as tortuosity is highly sensitive to local variations in particle connectivity or isolation, as opposed to the volume properties (which are less affected by such local events), minor particle isolation or changes in percolation can alter values significantly.

- Holzer et al. [86] and Sciazko et al. [208] reported that in the early stages, coarsening dominates, while in the later stages, an interplay between Ni

coarsening and GDC layer formation leads to more complex microstructural evolution. In the current work, a static Ni/GDC wettability is assumed from the initial stage, while the wettability in experiments may evolve dynamically with the local conditions, microstructure redistribution, and over longer aging times.

- Statistical representativeness of the simulated sample volume: Variations in tortuosity may partly result from sample-to-sample differences or segmentation inaccuracies. However, the FIB-SEM reconstructions in this study were systematically performed at central anode regions where microstructural homogeneity is highest, thereby minimizing spatial heterogeneity. In Section 2.9, statistical analysis of four non-overlapping half-volume subdomains showed coefficients of variation of only 0 %–2 % for key characteristics, confirming very low variability. As microstructural changes of this magnitude are within the methodological standard deviation reported by Holzer et al. [86], domain representativeness is unlikely to contribute significantly to the observed discrepancies between GDC tortuosity trends in simulations and experiments.
- Accuracy of the model parameters: The present work employs Ni-GDC parameters derived through an Active Learning framework with Bayesian optimization utilizing experimental microstructures operated at high temperatures of 900 °C in a reducing atmosphere of 50 % H_2/50 % H_2O under OCV conditions (see Chapter 3). While this approach provided an optimized parameter set consistent with the available literature, further refinement through multi-objective approaches (e.g., evolutionary algorithms) could improve the accuracy of the parameters. Simulations demonstrate a slower GDC coarsening rate than experiments, as reflected in the slower evolution of the mean particle diameter, suggesting a lower GDC diffusion coefficient used in the model.

The observed discrepancy between simulations and experimental results could be attributed to several factors, as outlined above.«

4.3 Large-scale aging simulations

This Section presents findings from a multiphase-field simulation analyzing microstructural coarsening over a period of 60,000 hours under operating conditions of 900 °C with a gas composition of 50 % H_2/50 % H_2O. SOFCs are required to operate for more than 40,000h (approximately 4.6 years) to be considered commercially viable, with a potential lifetime extending up to 80,000h [209]. However, conducting experimental aging tests over such a long duration, particularly to capture microstructural evolutions and extract FIB-SEM reconstructions at several time intervals for quantitative analysis, is extremely resource-intensive and time-consuming. In this work, phase-field simulations, validated against experimental FIB-SEM reconstructed 3D microstructure of SOFC anodes up to 1,100 hours, are further extended to predict microstructural evolution over several thousand hours. Employing an optimized, vectorized solver capable of performing large-scale computations, simulations are conducted for aging durations of 60,000h to analyze time-dependent microstructural and property changes. These simulations employ a FIB-SEM reconstructed pristine 3D microstructure as the initial condition. Large-scale simulations are performed on the BwUniCluster high-performance computing system using 1,656 cores over approximately 10 days, resulting in an aging period corresponding to 60,000h for the Ni-GDC anode microstructure. The resulting morphological evolutions of the Ni-GDC anode microstructure at 30,000h and 60,000h are shown in Figure 4.4. To comprehensively evaluate anode aging, this analysis focuses on the temporal evolution of key microstructural and electrochemically relevant properties, including the mean particle diameters of Ni, GDC, and pores, as well as TPBs, DPBs, and phase tortuosities. These microstructural properties were evaluated at intervals of 500h to quantify and describe the evolution. The objective here is to evaluate the degradation of these key parameters over the operational lifetime of the SOFC anode.

Evolution of microstructure and particle size Figure 4.5 shows the evolution of the 3D microstructure along with the corresponding 2D cross-sections

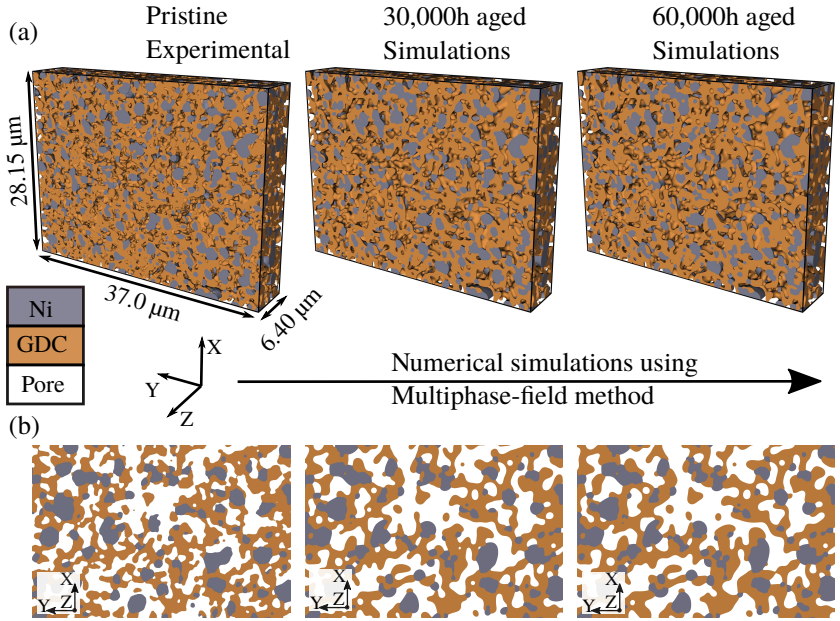


Figure 4.4: Phase-field simulation of the (a) 3D Ni-GDC SOFC anode microstructure and (b) 2D cross sections at different aging times of 0h, 30,000h, and 60,000h using the pristine microstructure as initial input.

of the nickel phase at aging times of 0h, 30,000h, and 60,000h. Due to the relatively low volume fraction of nickel (around 22 %) and the presence of largely isolated, non-percolating Ni particles in this specific configuration, only limited morphological changes can be observed over the simulated duration. The continuous particle size distributions of the nickel phase at selected aging times (0h, 500h, 30,000h, and 60,000h) are shown in Figure 4.6(a). The cumulative distributions exhibit a nearly symmetrical sigmoidal shape with minimal variations over time. The mean particle diameter was determined by initially deriving particle size distributions from the cumulative distributions and then fitting them to a log-normal distribution. All three phases were consistently well represented by a log-normal distribution throughout the aging process, as the coefficient of

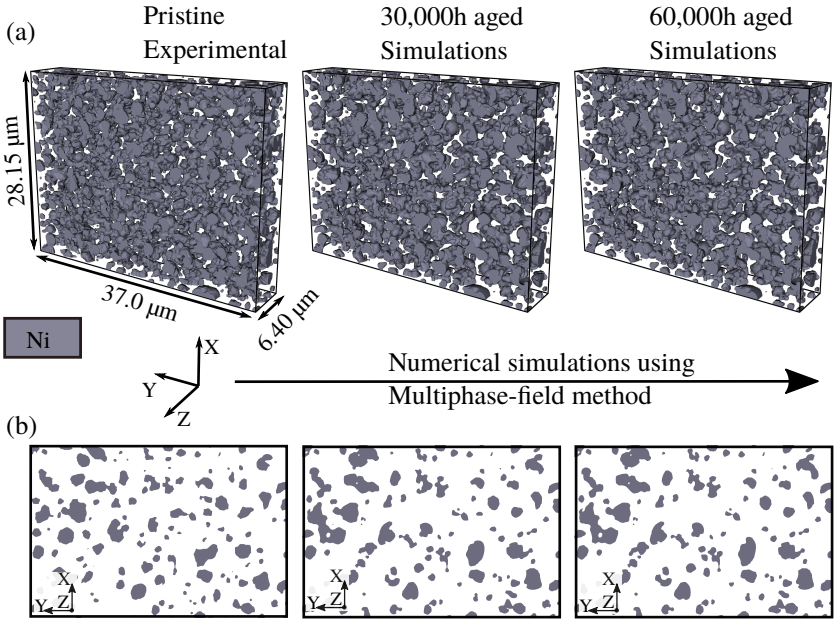


Figure 4.5: Phase-field simulation of the (a) Ni phase 3D morphology and (b) 2D cross sections at different aging times of 0h, 30,000h, and 60,000h using the pristine microstructure as initial input.

determination (R-squared) values were in the range of 0.94–0.99 in all cases. As shown in Figure 4.6(b), the nickel phase shows a relatively rapid initial increase of 4.1 % within the first 1,000h (0.91 µm–0.947 µm), followed by a pronounced plateau during which the mean diameter increases further by only 1.5 % over the remaining 59,000h, reaching a value of 0.961 µm at 60,000h. The coefficient of variation (CV), which quantifies the relative (size-normalized) spread of each distribution, decreases for the nickel phase from 0.396 to 0.390 over 60,000h, corresponding to a negligible change of 1.4 %. These values are consistent with nickel's coarsening being effectively hindered after the initial hours, so that its distribution shape, as well as its mean size, becomes stable relatively quickly and subsequently changes marginally. These results indicate that microstructural

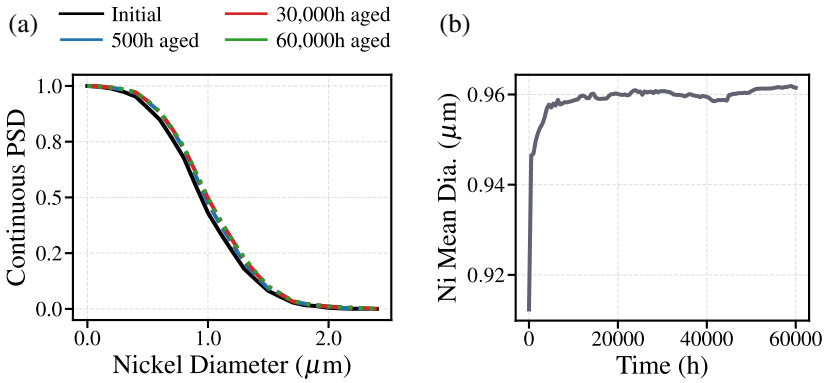


Figure 4.6: (a) Continuous particle size distributions of the nickel phase at selected aging times up to 60,000h; (b) Evolution of the mean nickel particle diameter over the same duration.

configurations with a lower nickel volume fraction, characterized by predominantly isolated particles, exhibit comparatively higher morphological stability of the nickel phase, even over extended operating periods of up to 60,000 hours.

Figure 4.7 shows the evolution of the 3D microstructure along with the corresponding 2D cross-sections of the GDC phase at aging times of 0h, 30,000h, and 60,000h. Despite the comparatively high volume fraction of GDC (approximately 41 %) and lower initial mean particle diameter of about 0.6 µm compared to the nickel phase (0.91 µm), the morphological evolution in the GDC phase proceeds slowly due to its much lower diffusivity values (by about four to five orders of magnitude). Nevertheless, significant changes in morphology can be observed over the simulation period of 60,000h, as illustrated by the 2D cross-sections at 30,000h and 60,000h (see Figure 4.7(b)).

The continuous particle size distributions of the GDC phase at selected aging time periods (0h, 500h, 30,000h, and 60,000h) are shown in Figure 4.8(a). Over time, these distributions shift toward larger particle sizes, indicating continuous coarsening. The coefficient of variation decreases from 0.301 to 0.281, corresponding to a moderate narrowed range of about 6.6 %. In contrast to the nickel

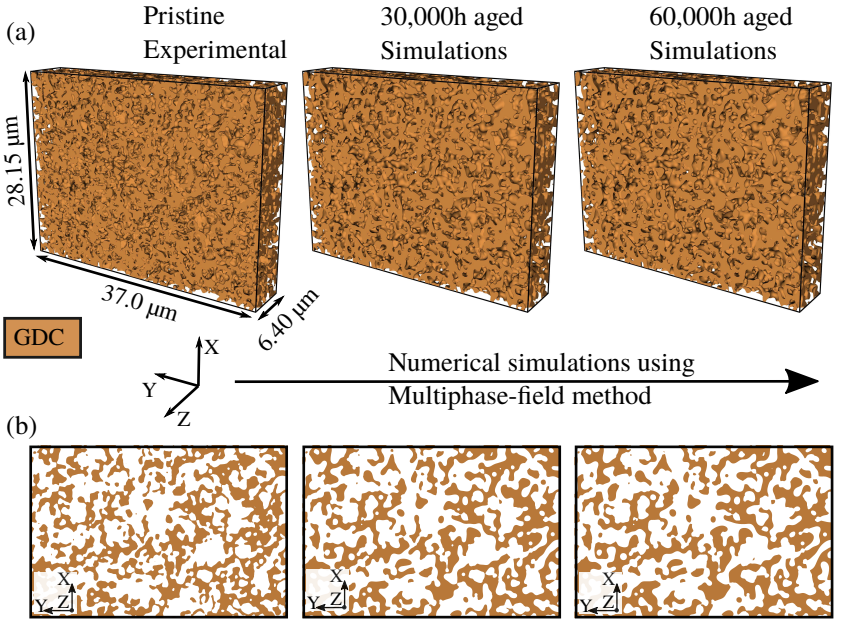


Figure 4.7: Phase-field simulation of the (a) GDC phase 3D morphology and (b) 2D cross sections at different aging times of 0h, 30,000h, and 60,000h using the pristine microstructure as initial input.

phase, the GDC phase exhibits sustained, unsaturated growth throughout the entire aging period. The mean particle diameter increases by 26.4 % from 0.605 µm to 0.765 µm (see Figure 4.8(b)). During the first 30,000 hours, the diameter increases to about 0.72 µm, followed by a slower but sustained growth to 0.765 µm over the next 30,000 hours. These results show that the GDC phase, unlike conventional Ni-YSZ anodes, in which the ceramic phase is often considered stable, undergoes significant evolution over the course of long-term operation. Although nickel coarsening becomes negligible in this specific configuration after the first thousand hours, it is expected that the continued evolution of the GDC phase influences the microstructural properties and may affect the TPB and DPB densities over longer operating times.

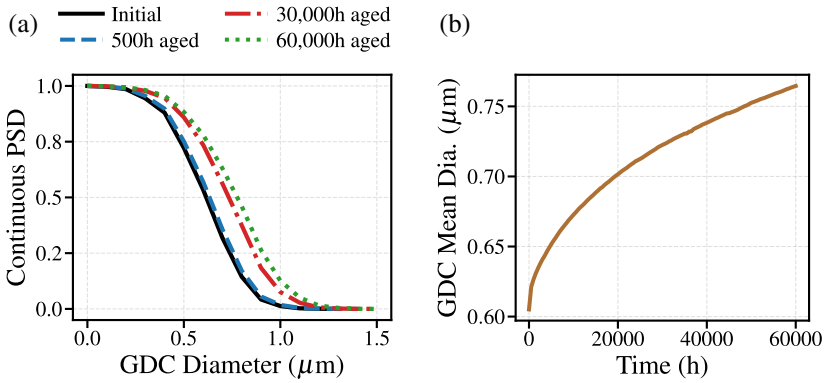


Figure 4.8: (a) Continuous particle size distributions of the GDC phase at selected aging times up to 60,000h; (b) Evolution of the GDC particle diameter over the same duration.

Figure 4.9 displays the evolution of porosity resulting from the combined morphological changes in the nickel and GDC phases within the Ni-GDC microstructure, along with the corresponding 2D cross-sections at aging times of 0h, 30,000h, and 60,000h. Over the simulation period of 60,000h, significant changes in the pore structure can be observed, as indicated from the coarsening and redistribution of the pores in the 2D cross-sections at 30,000h and 60,000h (see Figure 4.9(b)).

The continuous PSD of the pore phase at selected aging time points of 0h, 500h, 30,000h, and 60,000h is shown in Figure 4.10(a). Similar to the GDC phase, the distributions shift progressively toward larger pore sizes, indicating continuous coarsening. However, the rate of this shift decreases at later aging stages. The coefficient of variation decreases from 0.416 to 0.303, which corresponds to a considerable relative reduction of about 27 % and indicates a significant narrowing of the pore size distribution. During the entire duration of the simulation, the pore phase exhibits continuous growth in mean pore size, which increases by 48.6 % from 0.592 µm to 0.880 µm (see Figure 4.10(b)). This increase in pore size over longer operating times could contribute to improved gas transport within the

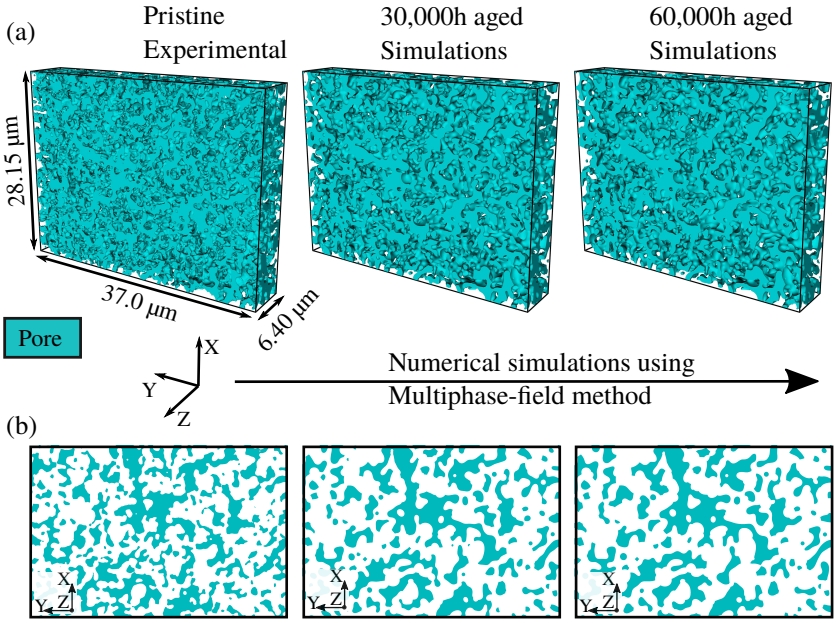


Figure 4.9: Phase-field simulation of the (a) Pore phase 3D morphology and (b) 2D cross sections at different aging times of 0h, 30,000h, and 60,000h using the pristine microstructure as initial input.

Ni-GDC microstructure and potentially enhance the effective supply of reactants to the electrochemical reaction sites.

TPBs and DPBs evolution Figure 4.11 shows the spatial distribution of the TPBs within the 3D microstructure of the Ni-GDC anode in its initial state and after 60,000h of aging. The TPB distributions clearly indicate a significant decrease in density over longer periods of operation. The evolution of the total TPB density over an aging period of 60,000h is shown in Figure 4.12(a). Consistent with the initial rapid coarsening of the nickel phase, the TPB density shows a sharp decline in the early stages of aging, followed by a slower decrease as aging progresses. In the later stages, the continued coarsening of the GDC phase

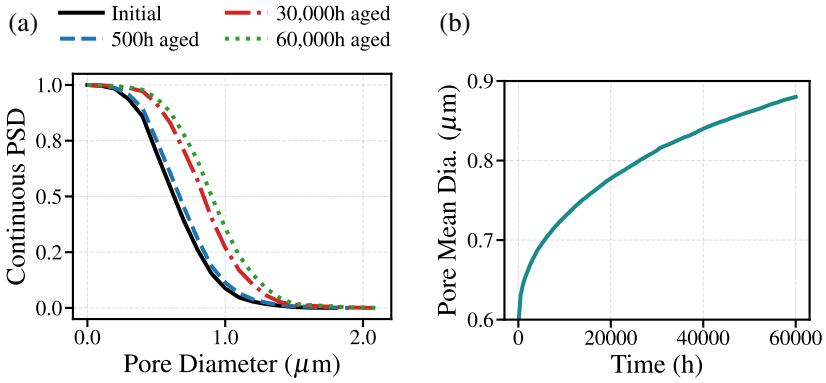


Figure 4.10: (a) Continuous PSD of the Pore phase at selected aging times up to 60,000h; (b) Evolution of the mean Pore diameter over the same duration.

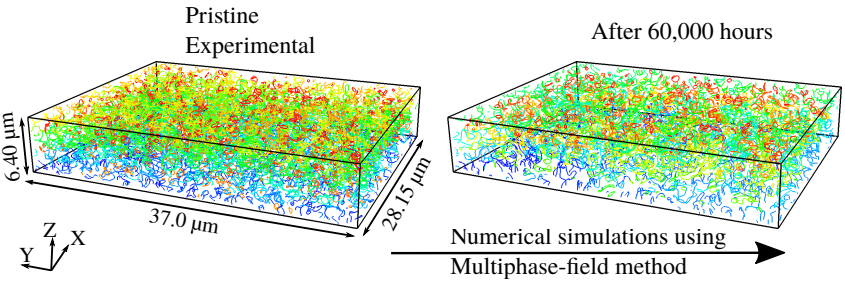


Figure 4.11: Distribution of TPBs within the 3D Ni-GDC anode microstructure at the pristine state and after 60,000h of aging, obtained from MPF simulations, with color-coded TPB segments.

contributes to a further, gradual decrease in TPB density. Overall, the evolution of TPB density shows an inverse correlation with the increase in the mean particle diameters of both the Ni and GDC phases. After 60,000 operating hours, the TPB density decreases by about 40 % relative to its initial value, indicating a significant loss of electrochemical reaction sites and a corresponding degradation in cell performance. Notably, around 36 % of this decline occurs within the first 30,000h, while another 4 % decline is observed in the following 30,000h. This trend aligns with the temporal evolution of the GDC particle size, which shows higher growth rates during the first 30,000h, followed by slower coarsening over the subsequent 30,000h. The overall microstructural evolution is determined by the combined effects of nickel and GDC coarsening, coupled with interfacial phenomena such as dewetting at Ni/GDC interfaces, which further contribute to the complexity of TPB density degradation.

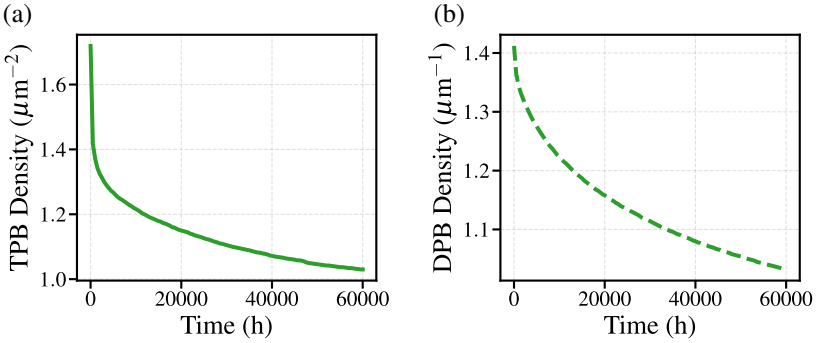


Figure 4.12: Evolution of (a) TPB density and (b) DPB density in Ni-GDC SOFC anode microstructure over an aging period of 60,000h, estimated using MPF simulations.

The evolution of the DPB density over an aging period of 60,000h is shown in Figure 4.12(b). In the Ni-GDC SOFC anode, DPBs provide additional electrochemical reaction sites due to the mixed ionic and electronic conductivity of GDC. Over the 60,000h aging duration, the DPB density exhibits a monotonic decline

with a total reduction of about 27 %. As with the TPB evolution, this decline in DPB density is expected to contribute to a degradation in cell performance. The reduction in DPB density could be primarily attributable to the coarsening of the GDC phase, which leads to a decrease in the total GDC surface area and a corresponding reduction in the interfacial areas between the GDC and the pores.

Tortuosities evolution The temporal evolution of phase tortuosity, used to quantify the effective transport pathways for electrons, ions, and gas, is shown in Figure 4.13. In Ni-GDC anodes, the GDC phase also exhibits electronic conductivity that is one to two orders of magnitude higher than its ionic conductivity, thereby reducing the likelihood of electron transport being the limiting step in the electrochemical reactions [210]. Consequently, the tortuosity of the nickel is less critical in Ni-GDC systems with non-percolating nickel, such as in this configuration; the effective electronic conductivity is largely determined by the GDC phase. The evolution of GDC mean tortuosity over 60,000h (See Figure 4.13(a)) shows only a slight decline, suggesting that both the ionic and electronic transport pathways remain largely stable. Although some local coalescence of the GDC particles occurs, the high volume fraction, the smaller initial mean particle size, and the low diffusivity of GDC seem to favor the formation of smoother, more continuous networks, thereby maintaining long-range connectivity over time. In contrast, the pore tortuosity (See Figure 4.13(b)) exhibits a discontinuous, non-monotonic, and weakly correlated behavior with the evolution of pore size. These findings reflect the complex microstructural evolution of both nickel and GDC coarsening, as well as interfacial dynamics, making direct correlations with morphological evolution and pore tortuosity less straightforward. Overall, pore tortuosity remains relatively unchanged over 60,000 hours, indicating that the gas transport pathways remain largely stable throughout the aging period.

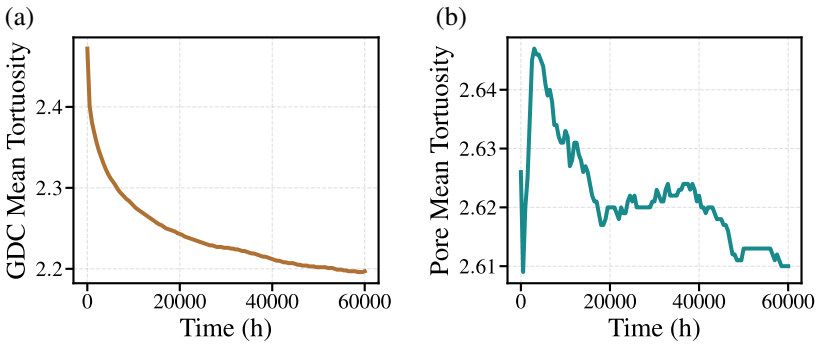


Figure 4.13: Evolution of the mean tortuosities of (a) GDC and (b) Pore in the microstructure of the Ni-GDC SOFC anode over an aging period of 60,000h, estimated using MPF simulations.

4.4 Sensitivity analyses of physical parameters - influence of interfacial energies on anode stability

»Investigations into the sensitivity of parameters such as the surface and interfacial energies of the system on long-term stabilities and durabilities of Ni-GDC SOFC anode microstructure are carried out. Three different thermodynamic equilibrium scenarios are incorporated into the simulation studies through sets of surface and interfacial energy values. The contact angles at the triple point are indirectly controlled via the interfacial energies $\gamma_{\alpha\beta}$ in the current model. The wettability between Ni and YSZ is directly related to the aggregation and coarsening behavior of the Ni particles and affects the long-term stability of SOFCs [82, 94, 98]. While phase-field studies exist on the influence of the contact angle between Ni and YSZ on microstructural evolution and thereby properties [91, 92, 94, 98], systematic phase-field studies of microstructural evolution for the Ni-GDC system, where two phases simultaneously evolve, are lacking. To investigate these effects, two additional phase-field simulations with the changes in the surface energies of GDC and the interfacial energy of Ni-GDC are carried out, with changes

to surface and interfacial energy parameters obtained from an ML Bayesian active learning framework. In the literature, both coarsening of Nickel and GDC, as well as a smoothing layer of GDC around nickel phenomena, are observed for Ni-GDC systems [83, 86, 89]. However, the mechanisms responsible for such phenomena are not yet fully understood. Analysis of these morphological evolutions provides additional insight into the underlying mechanisms and the impact on microstructural properties.

Ni wettability on YSZ is known to significantly influence the stability of the TPB active sites and phase contiguity in Ni-YSZ fuel electrode cell anode materials [92, 98]. The durability of conventional Ni-YSZ composite electrodes can, therefore, be improved by controlling the Ni wettability on the YSZ surface. Jiao et al. [82, 94, 205] systematically investigated the effects of polarization on the morphological evolution of Ni in both SOFC and Solid Oxide Electrolysis Cell (SOEC) modes using a patterned Ni film electrode. From their results, it was found that the wettability of Ni on YSZ significantly improves during SOFC operation. This behavior was attributed to the adsorption of oxygen species on the Ni surface, influencing both the surface energy of Ni and the adhesion work at the Ni-YSZ interface. The activity of oxygen adsorbed on the Ni surface was correlated with the equivalent partial pressure of H_2O and equated to an atomic percentage (at. %). With H_2O partial pressure in the range of 0.8 atm to 0.994 atm, and just before Ni oxidation occurs, the Ni contact angle is predicted to decrease sharply from about 110° to below 30°. These experimental results, together with previous studies on Ni-YSZ systems, provide a basis for investigating the influence of the wetting behavior of Ni on the microstructural evolution of Ni-GDC. Since both Ni and GDC undergo morphological changes during operation, understanding their wetting interactions is essential to the optimization of Ni-GDC anodes and the improvement of their long-term performance.

Here, a contact angle $\theta_\alpha < 90°$ indicates a wetting behavior, while $\theta_\alpha > 90°$ indicates dewetting. The relationships at the triple junction in equilibrium can be expressed as follows:

$$\gamma_{NiGDC} + \gamma_{NiPore}\cos(\theta_{Ni}) + \gamma_{GDCPore}\cos(\theta_{GDC}) = 0, \tag{4.1}$$

$$\gamma_{GDCPore} \sin(\theta_{GDC}) = \gamma_{NiPore} \sin(\theta_{Ni}). \tag{4.2}$$

Here, γ_{NiPore}, $\gamma_{GDCPore}$, and γ_{NiGDC} denote surface energies of Ni and GDC with the pore phase and the interfacial energy between Ni and GDC, respectively. θ_{Ni} and θ_{GDC} represent the contact angles of the nickel and GDC phases, respectively. Surface and interfacial energies obtained from Bayesian active learning studies are γ_{NiGDC}, γ_{NiPore} and $\gamma_{GDCPore}$ as: $2.43\,\mathrm{J\,m^{-2}}$, $2.10\,\mathrm{J\,m^{-2}}$ and $1.43\,\mathrm{J\,m^{-2}}$ respectively (see Chapter 3), and the computed equilibrium contact angles for Ni, GDC, and the pore phase in this configuration are $\theta_{Ni} - \theta_{GDC} - \theta_{Pore}$ as $144° - 121° - 95°$ respectively. We selected the other two contact angle configurations based on two main criteria. Firstly, the variation in the angles studied needs to be sufficiently large to ensure that observed trends in the simulations could be attributed to changes in the relevant contact angle configurations. Secondly, both scenarios of Ni and GDC wetting in the Ni-GDC system needed to be covered. A lower bound of 60° is selected for nickel contact angle θ_{Ni}, consistent with reported experimental values in Ni-YSZ systems under polarization [82]. The other two configurations of contact angles are as follows: $\theta_{Ni} - \theta_{GDC} - \theta_{Pore}$ as $60° - 152° - 148°$ and $144° - 60° - 156°$. The presented simulation studies provide meaningful insights into the potential for mitigating anode degradation through optimized contact angles. Investigations into the practical feasibility of such contact angle configurations within the Ni-GDC system, however, are beyond the scope of the current work. Based on eqs (4.1) and (4.2), the calculated equivalent contact angles of Ni, GDC, and Pore based on the given surface and interfacial energies in the Ni-GDC system are summarized in Table 4.4. A sum of all three phase angles of 360° was ensured in the calculations.

4.4.1 Effect of interfacial energies on morphological evolutions: 2D analysis

The complexity of the 3D Ni-GDC anode microstructure and its evolution presents a difficulty in gaining a clear understanding of the role of interfacial energies and associated morphological evolutions. Therefore, for a mechanistic understanding

Table 4.4: Equilibrium contact angles at triple junctions corresponding to three different sets of specified interfacial energies. The values in the first row γ_{NiGDC}, γ_{NiPore} and $\gamma_{GDCPore}$ ($2.43\,\mathrm{J\,m^{-2}}$, $2.10\,\mathrm{J\,m^{-2}}$ and $1.43\,\mathrm{J\,m^{-2}}$) correspond to the results of previous Chapter 3, whereas second- and third-row values represent the assumed and modified surface energy of GDC and interfacial energy of Ni/GDC to obtain a target contact angle of 60° for both Ni and GDC.

γ_{NiGDC} ($\mathrm{J\,m^{-2}}$)	γ_{NiPore} ($\mathrm{J\,m^{-2}}$)	$\gamma_{GDCPore}$ ($\mathrm{J\,m^{-2}}$)	θ_{Ni} (°)	θ_{GDC} (°)	θ_{Pore} (°)
2.43	2.1	1.43	144	121	95
2.43	2.1	3.92	60	152	148
0.98	2.1	1.43	144	60	156

of the influence of interfacial energies, an analysis is conducted using a simplified 2D two-particle system consisting of Ni and GDC particles. Phase-field simulations are performed using three triple junction equilibrium contact angle scenarios (as presented in Table 4.4), representing distinct surface and interfacial energy conditions. Encompassing dewetting to wetting interactions of both nickel and GDC, these scenarios provide a detailed understanding of interfacial energies governing the morphological evolution of Ni and GDC.

The initial system consists of two equal-sized, adjacent rectangular nickel and GDC particles in contact at a common interface and aligned at right angles. To ensure general applicability, all quantities are expressed in an arbitrary unit system. The energy unit is defined as $u_E \equiv \lambda_E\,\mathrm{J}$, where λ_E is a dimensionless prefactor and J denotes joules. Similarly, units of length and time are defined as $u_l \equiv \lambda_l\,\mathrm{m}$ and $u_t \equiv \lambda_t\,\mathrm{s}$, respectively, where the dimensionless prefactors λ_l and λ_t correspond to their SI equivalents. The simulation domain consists of a grid with a width of $N_x = 200$ cells and a height of $N_y = 200$ cells. Zero flux boundary conditions are applied at the domain boundaries, which are treated as insulating. The spatial discretization is set to $\Delta x = \Delta y = 1\ u_l$. Both nickel and GDC components are assumed to have the same diffusivity along their surfaces and at their mutual interfaces. This assumption of assigning equal diffusivity values to the nickel and GDC components allows for faster convergence to the thermodynamic equilibrium state. Here, the primary objective is to study the final morphological configuration

of the system at equilibrium. Consequently, equal chemical surface and interface mobilities of $M_{\mathrm{Ni}}^{NiPore} = M_{\mathrm{Ni}}^{NiGDC} = M_{\mathrm{GDC}}^{GDCPore} = M_{\mathrm{GDC}}^{NiGDC} = 0.1\, u_l^6/(u_E\, u_t)$ are assigned, whereby equal rates of mass transport via surface diffusion of nickel and GDC and interface diffusion between nickel and GDC are ensured. The interfacial energy values corresponding to the three contact angle configurations considered in the model are given as follows: $(\gamma_{NiGDC}, \gamma_{NiPore}, \gamma_{GDCPore}) = (1.15,\ 1.0,\ 0.68)$, $(1.15,\ 1.0,\ 1.87)$, and $(0.47,\ 1.0,\ 0.68)$. These values define the relative energetics that drive morphological evolution in each scenario. Simulations are performed for a sufficiently long time to ensure that only negligible changes are observed in later phases, corresponding to an equilibrated system.

Figure 4.14(a) shows the initial configuration of Ni and GDC, two solid particles in contact with each other. Figure 4.14(b-d) depict morphological evolution at equilibrium under different interfacial energy conditions, simulated by the phase-field model. In Figure 4.14(b), the contact angles for nickel, GDC, and the pore phase are 144°, 121°, and 95°, respectively. Due to a higher interfacial energy, the system evolves by minimizing the Ni/GDC interface, thereby evolving in a thermodynamically consistent manner to reduce the total energy of the system. Consequently, this configuration represents a dewetting scenario, where Ni and GDC display limited chemical affinity for each other. As shown in Figure 4.14(c), the contact angles are 60°, 152°, and 148° for nickel, GDC, and the pore phases, respectively. Here, the system primarily reduces the surface area of GDC, as this is energetically unfavorable. This results in a wetting configuration in which Ni tends to spread around the GDC particle. In Figure 4.14(d), the contact angles for nickel, GDC, and the pore phase are 144°, 60°, and 156°, respectively, indicating that the system minimizes the surface of nickel due to its relatively high surface energy. This results in a wetting configuration of GDC around the Ni particle. Simulated contact angles are in good agreement with the values of the interfacial energy and the corresponding contact angle calculations given in Table 4.4. Thus, the phase-field simulations accurately incorporate the prescribed interfacial energy and effectively capture the morphological evolution driven by the minimization of the interfacial energy.

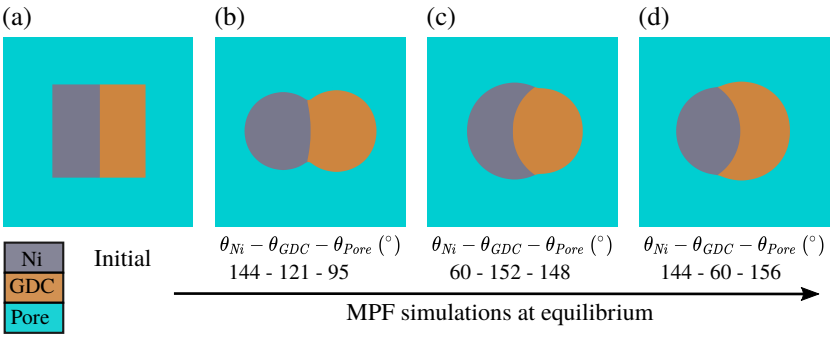


Figure 4.14: Morphological evolution of (a) the initial two adjoining nickel and GDC particles contacting a common interface at right angles. (b–d) Morphological evolution at equilibrium by the phase-field simulations using the same kinetic coefficients and paths, but with different sets of thermodynamic equilibrium contact angles $\theta_{Ni} - \theta_{GDC} - \theta_{Pore}$ as $144° - 121° - 95°$, $60° - 152° - 148°$, and $144° - 60° - 156°$ respectively.

4.4.2 Effects of interfacial energies on morphological evolutions: 3D analysis of FIB-SEM reconstructed experimental Ni-GDC SOFC anode microstructures

Phase-field aging simulations are conducted on the FIB-SEM reconstructed pristine 3D Ni-GDC anode microstructure, incorporating three different contact angle scenarios. These simulations aim to analyze the influence of different contact angle configurations on the degradation of microstructural properties. The characteristic microstructural properties of these simulations for aging times of 0h, 200h, and 2000h are presented in Table 4.5. It can be seen that the contact angle relations significantly affect the kinetics of particle growth, structural tortuosity, and interfacial properties. Furthermore, contact angles also influence the density of the total TPBs. Microstructural changes are directly related to the electrochemical performance and gas transport mechanisms, and thus to the long-term stability of SOFC anodes. A detailed analysis of the correlations between contact angles and microstructural properties allows for a targeted optimization of operating conditions and interface energies, whereby both the durability and the efficiency of SOFCs

Table 4.5: Microstructural characteristic properties over the aging of three simulations with distinct configurations of contact angles.

$\theta_{Ni}-\theta_{GDC}-\theta_{Pore}$ (°)	t (h)	τ_{GDC} (−)	τ_{Pore} (−)	d_{Ni} (µm)	d_{GDC} (µm)	d_{Pore} (µm)	l_{TPB} (µm^{-2})	$A_{Ni/Pore}$ (µm^{-1})	$A_{GDC/Pore}$ (µm^{-1})	$A_{Ni/GDC}$ (µm^{-1})
144−121−95	0	2.57	2.57	0.91	0.59	0.60	1.82	0.37	1.50	0.67
144−121−95	200	2.52	2.57	0.96	0.60	0.63	1.53	0.31	1.45	0.62
144−121−95	2000	2.39	2.60	0.97	0.62	0.68	1.36	0.28	1.37	0.60
60−152−148	0	2.57	2.57	0.91	0.59	0.60	1.82	0.37	1.50	0.67
60−152−148	200	2.52	2.89	0.72	0.60	0.75	1.67	0.34	1.12	0.94
60−152−148	2000	2.37	3.39	0.67	0.62	0.86	1.43	0.29	1.00	0.98
144−60−156	0	2.57	2.57	0.91	0.59	0.60	1.82	0.37	1.50	0.67
144−60−156	200	2.52	2.68	0.87	0.60	0.68	1.53	0.30	1.33	0.75
144−60−156	2000	2.36	2.83	0.86	0.61	0.74	1.33	0.26	1.24	0.78

can be effectively improved. The morphological evolution of the 3D Ni-GDC anode microstructure and its phases from the initial microstructures after an aging time of 2000h for the three scenarios of contact angle are shown in Figure 4.15. For clarity and ease of reference, we categorize the three configurations as follows: high contact angle configuration: $\theta_{Ni}-\theta_{GDC}-\theta_{Pore} = 144°-121°-95°$; low Ni contact angle configuration: $\theta_{Ni}-\theta_{GDC}-\theta_{Pore} = 60°-152°-148°$; low GDC contact angle configuration: $\theta_{Ni}-\theta_{GDC}-\theta_{Pore} = 144°-60°-156°$.

Figure 4.16(a) shows the evolution of the nickel mean particle diameter for three different contact angle configurations. Among these, the high contact angle configuration exhibits an increase in mean diameter of about 6 % over an aging period of 2000h. In contrast, the low Ni contact angle configuration results in a significant decrease of the mean diameter by 27 %. Lastly, the low GDC contact angle configuration also shows a decrease in mean diameter, though more moderate at about 6 %. A similar decline in nickel mean particle diameter is also reported in phase-field studies by Davis et al. [92] at lower contact angles of nickel. Despite these quantitative differences, all three configurations display a similar qualitative trend of an initial period of accelerated growth or decline in mean

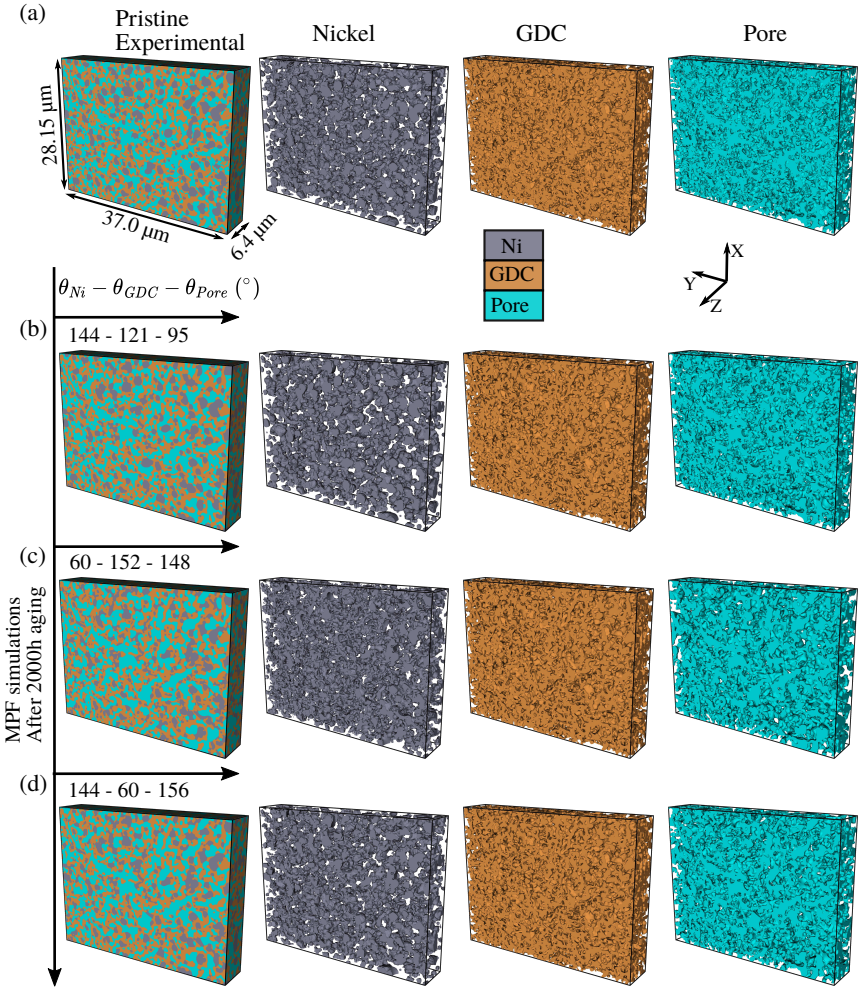


Figure 4.15: Morphological evolution of the (a) initial pristine 3D Ni-GDC anode microstructure and constituent phases over 2000h of aging, simulated for (b-d) three distinct contact angle configurations using the MPF method.

particle diameter for nickel, consistent with previous phase-field studies on Ni-YSZ systems [98]. From these results, it can be seen that interfacial energies and, respectively, contact angle conditions strongly control the coarsening behavior. Low contact angle configurations, indicative of improved wetting, promote a coating-like microstructure (as illustrated in Figure 4.15(c) for nickel), which contrasts with the morphology observed at high contact angle configurations. The significant reduction in mean nickel diameter for the low Ni contact angle configuration is a result of the increased Ni/GDC interfacial area due to the nickel coating around the GDC particles. Such evolution is evident from the increase in Ni/GDC interface area density from $0.672\,\mu m^{-1}$–$0.978\,\mu m^{-1}$ (see Table 4.5), thereby resulting in lower total energy of the system. Furthermore, this wetting behavior contributes to a further reduction in the GDC surface area density, associated with a higher energy, from $1.5\,\mu m^{-1}$–$1.002\,\mu m^{-1}$, along with a coarsening mechanism of the GDC particles to minimize surface area. In the utilized morphology of the 3D Ni-GDC anode for the contact angle sensitivity studies, where volume fractions of nickel are 22.44 % and the nickel particles are non-percolated, the coating of nickel around GDC particles at nickel/GDC interfaces predominated over the coarsening of nickel particle interactions. This results in a pronounced decrease in the mean particle diameter of nickel from the initial configuration over aging for smaller contact angles. The complex interplay between the mechanisms of Ni wettability enhancement at Ni-GDC interfaces and the coarsening of Ni particles ultimately determines the morphological evolution of nickel as observed in this configuration. The low GDC contact angle configuration exhibits a moderate decrease in the mean Ni particle diameter, while including a Ni contact angle of 144°. Here, the low GDC contact angle (60°) promotes the formation of a continuous GDC layer around Ni, suppressing Ni coarsening. Also in this configuration, the Ni/GDC interfacial energy ($0.98\,J\,m^{-2}$) is lower than the surface energies of Ni ($2.1\,J\,m^{-2}$) and GDC ($1.43\,J\,m^{-2}$), which favors an increase of the Ni/GDC interfacial area leading to a reduction of the total energy of the system. Thus, the observed moderate decrease in the mean Ni particle diameter is not solely due to the Ni contact angle, but rather to the coupled evolution of the Ni and GDC phases, with wetting by GDC strongly influencing Ni stability and particle growth. Holzer et al. [86] reported similar observations of enhanced GDC

wetting in humid environments covering Ni grains, suppressed growth over the long run, and even negative growth.

As shown in Figure 4.16(b), the evolution of the mean particle diameter (d_{50}) of GDC exhibits distinct growth patterns across the three contact angle configurations. As expected, the high contact angle configuration resulted in more pronounced GDC particle growth than configurations with low contact angles of Ni and GDC. Among the low contact angle configurations, the low GDC contact angle configuration suppressed GDC particle growth more. This can be attributed to the higher volume fraction of GDC (41.38 %) compared to nickel (22.44 %) and the smaller mean diameter of GDC particles (0.59 µm against 0.91 µm in nickel) in the initial microstructure. The morphological evolution of nickel can be observed rather quickly compared to GDC owing to the significantly higher diffusivities of nickel compared to GDC (about five orders of magnitude). As reported by Zekri et al. [83], the formation of a GDC coating around nickel can be observed only after longer operating hours.

To analyze the distribution of the total three-phase boundary sites, the evolution of TPB density over the 2000h aging period is presented in Figure 4.16(c). Across all contact angle configurations, TPB density undergoes substantial degradation, decreasing from an initial value of approximately $1.82\,\mu m^{-2}$ to a range of $1.33\,\mu m^{-2}$–$1.43\,\mu m^{-2}$, corresponding to an overall reduction of 21 %–27 %. This decline indicates a significant loss of electrochemically active sites, directly affecting cell performance. Among the tested configurations, the low Ni contact angle configuration exhibits the most favorable TPB retention, with the smallest overall reduction over the 2000h aging period. The observed results can be attributed to the stronger suppression of nickel coarsening and the rapid formation of a nickel layer around GDC particles due to its higher diffusivity. This layer inhibits GDC evolution, thereby preserving interfacial pores more effectively than in other configurations [205], ultimately leading to higher TPB densities. Conversely, the high contact angle configuration initially exhibits a similar TPB degradation rate to the configuration with a low GDC contact angle. However, at longer aging times, the reduction in TPB density is less severe than in the low

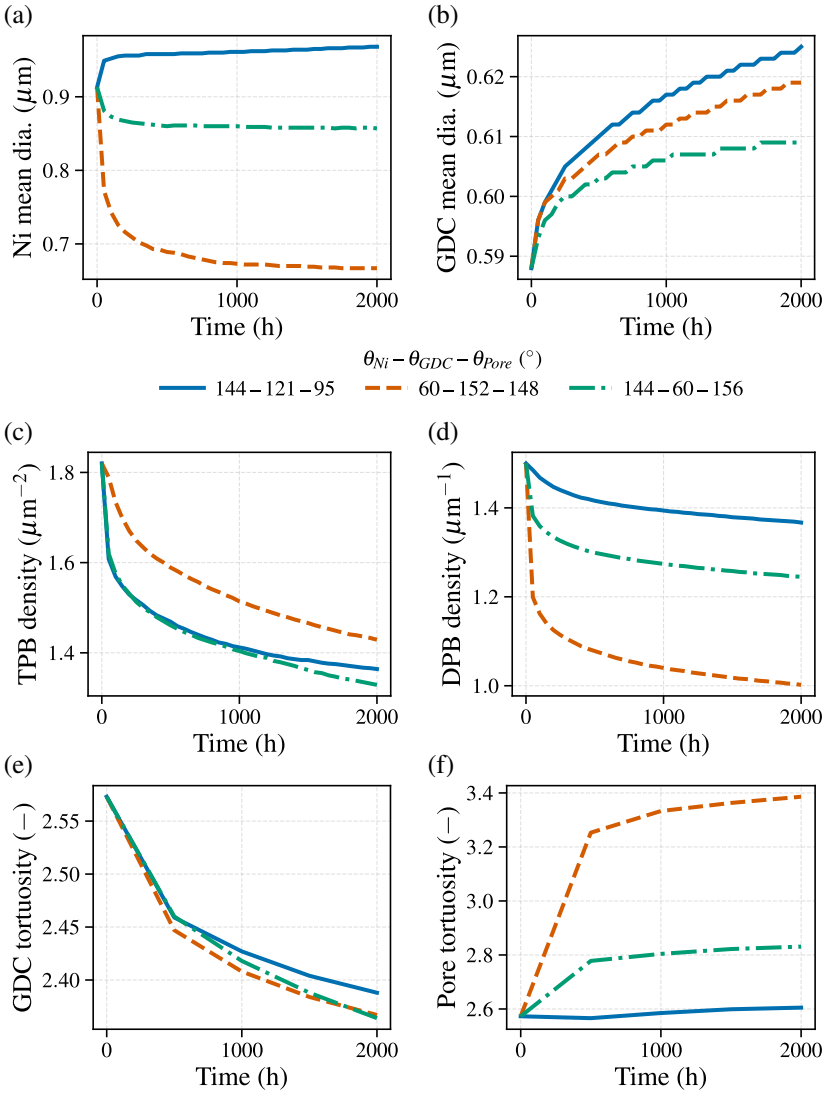


Figure 4.16: Microstructural properties evolution over the aging period of 2000h for three distinct configurations of contact angles in the MPF simulations: (a,b) mean diameter of nickel and GDC, (c) Total TPB density, (d) DPB density, (e,f) mean tortuosities of GDC and pore.

GDC contact angle configuration. This trend aligns with previous findings by Davis et al. [92], which suggest that high-contact-angle systems, characterized by lower wettability, promote the formation of closed-loop TPBs, stabilizing the TPB density over time. The most pronounced TPB degradation is observed in the low GDC contact angle configuration, which experiences a sharp decline within the first 250h, followed by a more gradual reduction. Theoretical considerations by Jiao et al. [205] indicate that systems with initially high TPB density, such as Ni-YSZ composites, undergo rapid TPB degradation at early stages due to the elimination of interfacial pores via coalescence. Similarly, in the Ni-GDC system, the wetting behavior of GDC at Ni/GDC interfaces gradually reduces interfacial pores over longer aging times owing to the slower diffusion coefficients of GDC, thereby decreasing TPB density. While GDC layer formation might suppress nickel coarsening, it is unlikely to prevent early-stage degradation due to comparatively lower diffusivity values of GDC. However, at extended operating times, this coating effect could mitigate further coarsening of nickel and stabilize the TPB densities.

These findings underscore the critical role of interfacial energies in shaping individual phase morphologies and the stability of three-phase junctions, which are essential for electrochemical activity and performance. Notably, a low Ni contact angle configuration contributes to enhanced microstructural stability by preserving TPB density over long-term operation of 2000h. Nevertheless, the overall variation in TPB degradation across the tested configurations remains relatively small – ranging from approximately 2 %–6 % at 2000h – compared to the initial degradation of 21 %–27 %. The competing mechanisms of Ni and GDC coarsening, coupled with wetting and dewetting conditions at Ni/GDC interfaces, add complexity to morphological evolution. Further quantitative investigations into large-scale simulations of dewetting and wetting behavior, Ni and GDC coating-like formation around particles, and their impact on microstructural properties are necessary to improve composite SOC electrodes for enhanced durability and performance.

Figure 4.16(d) shows the evolution of the DPB density over the 2000h aging period to estimate the distribution of total double-phase boundaries. In Ni-GDC systems, DPBs provide additional electrochemical reaction sites owing to the mixed ionic and electronic conductivities of GDC. Over the aging period, the DPB density shows a monotonic decline across all contact angle configurations, decreasing from an initial value of about $1.5\,\mu m^{-1}$ to a range of $1.0\,\mu m^{-1}$–$1.37\,\mu m^{-1}$, corresponding to an overall reduction of 9 %–33 %. Among the configurations investigated, the high contact angle configuration exhibits the highest stability of the DPB distribution, with the least overall reduction in GDC/Pore interface density over the aging period. Here, the coarsening mechanism of the GDC particles mainly contributes to the reduction in the total GDC surface area. In contrast, the low Ni contact angle configuration experiences the most significant degradation, attributed to the formation of a Ni layer around the GDC particles. This layer effectively reduces the exposed GDC surface area, leading to a more pronounced decrease in DPB density. The low GDC contact angle configuration shows a moderate decrease in DPBs among the three configurations.

Figure 4.16(e) shows the evolution of GDC tortuosity across contact angle configurations. The tortuosity of the GDC phase is a key factor influencing oxygen ion and electron transport within the anode, as higher tortuosity values indicate more restricted conduction pathways. Elevated tortuosity values are also associated with an increased likelihood of phase discontinuities due to the formation of islands, thus rendering these values a potential stability indicator for anode operation. Over the aging period, GDC tortuosity changes remain relatively minor, with values decreasing across all configurations from approximately 2.57 to 2.36. This modest decline suggests that ion and electron transport pathways remain largely stable over aging. However, for the low GDC contact angle configuration, the initial tortuosity value decreases relatively more, suggesting GDC wettability can improve electron and ion conduction over long-term operation. In Ni-YSZ systems, phase-field simulations by Hoffrogge et al. [98] reported improved nickel tortuosity values at lower contact angles of nickel. Pore tortuosity is a critical parameter for gas transport within the anode microstructure, with larger values indicating more convoluted diffusion pathways and potentially limiting the availability of reactants

at electrochemically active sites. The evolution of pore tortuosity, averaged over three orthogonal directions for 2000h of aging, is shown in Figure 4.16(f). Among the tested configurations, the high contact angle configuration exhibits the most stable behavior, with negligible changes in pore tortuosity during aging. This observation is consistent with phase-field studies by Chen et al. [91], indicating that prolonged coarsening in Ni-YSZ systems can have a positive effect on gas transport in the pore phase. Given the moderate coarsening in the microstructures studied, the observed trend in tortuosity is consistent with these previous findings. Conversely, the low Ni contact angle configuration shows a pronounced increase in pore tortuosity, elevating from 2.57 to 3.39 – a 32 % increase. This deterioration can be attributed to the formation of a continuous nickel layer obstructing and altering the pore phase pathways. Similarly, the low GDC contact angle configuration exhibits a moderate increase in tortuosity. Overall, high contact angles appear to mitigate pore constriction and suppress tortuosity value growth, thereby enhancing reactant diffusivity.

The high contact angle configuration exhibits the most severe degradation, characterized by significant nickel and GDC coarsening and substantial loss of TPB sites, while DPB density remains relatively stable. In contrast, the low Ni contact angle configuration inhibits nickel coarsening and allows moderate GDC growth, resulting in lower TPB density degradation at the expense of higher DPB density degradation. The low GDC contact angle configuration stabilizes the GDC particle size but exhibits pronounced TPBs degradation and moderate loss of DPBs, with the low diffusion coefficients of GDC playing a dominant role in degradation over longer operating hours. Each configuration is characterized by tradeoffs between TPBs, DPBs, and tortuosity, complicating the determination of optimal contact angle conditions. The microstructural properties obtained from phase-field simulations, such as tortuosity, TPB, and DPB densities, can be integrated into transmission line models (TLM) for Ni-GDC anodes to predict the temporal evolution of polarization resistance and determine the optimal contact angle configuration.

4.5 Predictive capability and limitations

The current model is primarily applicable to Ni-GDC or Ni-YSZ anodes subjected to high-temperature, open-circuit thermal aging conditions, where the microstructural evolutions are dominated by coarsening mechanisms. In the current work, model validity is demonstrated by employing reconstructed electrode microstructures from a cell aged under purely thermal, humidified OCV conditions in a symmetrical configuration. The model explicitly incorporates interfacial energies and diffusion coefficients along surfaces and interfaces and thus accounts for mass transport along grain boundaries, surfaces, and interfaces. Anisotropic interfacial energies and diffusion coefficients can certainly be included in the current model, but their inclusion is limited by the high computational cost associated with large-scale simulations of larger domains. In thick anodes, p_{O_2} gradients can lead to non-uniform wettability along the thickness, as reported in the literature for Ni-YSZ systems [211]. Such effects could also be relevant for Ni-GDC systems. The present work assumes uniform wettability across the entire domain due to the lack of experimental findings or data on wetting angle distribution in Ni-GDC anodes. However, the model can incorporate spatially dependent wettability upon the availability of such results or data, allowing for a more comprehensive understanding of Ni-GDC redistribution and degradation. While the model can easily be extended to include additional contributions from volume diffusion, additional degradation mechanisms such as evaporation-condensation processes and GDC migration under polarization are not yet included in the model. All these additional contributions require experimentally measured input parameters under operating conditions and precise calibration. Further research is needed to uncover the mechanisms that drive these morphological changes.

4.6 Interim conclusion

In this Chapter, the coarsening behavior of Ni and GDC in FIB-SEM reconstructed 3D Ni-GDC SOFC anodes was simulated using a multiphase-field model under

operating conditions of Ni-GDC at a temperature of 900 °C with a gas composition of 50 % H_2/50 % H_2O. Both surface diffusion of nickel and GDC components, as well as their interfacial diffusion along the Ni/GDC interface, were included in the model. By using both pristine and pre-aged microstructures, the model's predictive capability under various initial conditions was evaluated. Validation results included the evolution of mean particle size, TPB density, tortuosity, and specific surface areas. Validation with both pristine and pre-aged microstructures showed good agreement with experimental results for all microstructural properties, except for GDC tortuosity, with pre-aged microstructures showing further improved accuracy. Several factors potentially contributing to discrepancies between simulation and experimental results, particularly GDC tortuosity, are discussed. The influence of surface and interfacial energies on the degradation of Ni-GDC anodes, considering three thermodynamic equilibrium scenarios defined by a set of interfacial energies, highlighted wettability as a key factor in the microstructural degradation pathways in Ni-GDC anodes. Initial 2D simulations demonstrated the role of interfacial energies in governing the morphological evolution of Ni and GDC. Subsequent 3D phase-field simulations on pristine Ni-GDC microstructures over 2000h of aging revealed that the wettability of Ni and GDC significantly influences the balance between TPB and DPB evolutions. A low Ni contact angle primarily mitigates Ni coarsening, whereas a low GDC contact angle influences Ni long-term stability. Each investigated configuration revealed trade-offs between key microstructural properties such as TPBs, DPBs, and tortuosity, complicating the identification of an optimal contact angle condition. With the predictive capability of our phase-field model for Ni-GDC anode degradation validated, the following Chapters will focus on integrating phase-field simulations and synthetic microstructures with tailored volume fractions and particle sizes of Ni and GDC. This combined approach intends to optimize the microstructural design for improved performance and durability of Ni-GDC anodes.«

5 Digital twin of Ni-GDC anode microstructure[1]

»The electrochemical performance of Ni-GDC SOFC anodes strongly depends on microstructural properties such as TPB and DPB densities, defining the available sites for electrochemical reactions, as well as the tortuosity of the Ni, GDC, and pore phases, controlling the electron, ion, and gas transport through the porous network. The initial phase volume fractions and particle sizes of the microstructure strongly influence these properties, enabling microstructure optimization through tailored electrode compositions and particle sizes to enhance performance. In experimental optimization studies, however, the number of microstructures being investigated is inherently limited, as the fabrication of Ni-GDC samples, 3D microstructure characterization using advanced imaging techniques such as Focused Ion Beam-Scanning Electron Microscopy (FIB-SEM), and the large-scale aging studies to assess degradation are time-consuming, resource-intensive, and costly. As an alternative, numerical modeling approaches have been widely used to overcome these limitations, as they enable the rapid generation and systematic evaluation of a large number of microstructures [212–214]. Despite advances in modeling synthetic microstructures, accurately reproducing the complex microstructures of SOFC anodes, formed by the sintering of multi-component particles, remains a challenge. Sintering-induced particle overlap was implemented by simply enlarging the particle sizes [215]. A similar dilatation-based method was also employed by Zheng et al. [216] to reproduce sintering effects. Furthermore, key geometric

[1] The content of this chapter has been taken directly from Jeela et al. [90] with minor linguistic changes. The figures have been adjusted to the format of this dissertation.

and statistical descriptors, such as phase volume fractions and particle size distributions, are not always controllable in modeling approaches. Since the systematic optimization of the microstructure is based on these descriptors, the possibility of controlling these is crucial during the creation of structures in generator models. In this Chapter, we employ the extended structure generator workflow (see Section 2.5) to create a realistic digital twin of Ni-GDC anode microstructure. The extended workflow introduces a computationally efficient, sintering-like morphological coalescence step based on a modified Allen-Cahn formulation with volume preservation [152] and a correction term controlling curvature minimization [153] to replicate the sintering process in experimentally fabricated anodes without explicitly simulating physical mechanisms. The generated digital twin is rigorously validated against FIB-SEM reconstructed 3D Ni-GDC anode microstructures by incorporating seventeen quantitative structural, geometrical, electrochemical, and mechanically relevant descriptors.

5.1 Synthetic microstructure generation

The performance of the extended structure generator, introduced in Section 2.5, in replicating the experimental microstructural features of the SOFC anode was evaluated by generating a synthetic SOFC anode microstructure using particle size distributions and phase volume fractions derived from a 3D FIB-SEM reconstructed experimental microstructure (detailed in Section 2.9) as input for the generator. The generated structure was subsequently validated against the experimental reference through a combination of visual assessment and comprehensive quantitative metrics. Since the multi-stage structure generator workflow depends on several input parameters, such as phase volume fractions, particle size distributions, angular power spectra, and dilation factors, whose effects on the resulting morphology are not known a priori, a multi-objective Bayesian optimization (BO) approach is used for systematic calibration. A total of 200 trials were performed to minimize the global deviation from an experimental reference microstructure, with emphasis on key metrics such as phase volume fractions, tortuosities, and

specific surface densities of the Ni, GDC, and pore phases. The resulting database was analyzed to refine the parameter search space and identify suitable fixed input parameters.

Following the BO calibration, a limited number of manual tuning iterations were performed to adjust the simulation time and tuning parameters for curvature minimization that control the sintering-like morphological evolution, aiming to achieve TPB densities closer to the experimental values as well as to achieve particle coalescence in an efficient manner. The model parameters were determined through an iterative manual tuning procedure, in which the curvature control parameter and the interfacial energy configurations were adjusted to achieve closer agreement between simulated and experimental microstructural descriptors (e.g., TPB density, DPB density, and surface area densities). This was achieved by controlling the curvature-driven evolution to obtain realistic morphologies within a limited number of iterations, followed by a minor refinement of the interfacial energies to enhance the agreement with the target values. Without this sintering-like morphological step, the generated structures exhibit much higher TPB densities than the experimental reference structure, as the generated structures consist of isolated, nearly spherical particles resembling green body configurations. All other generator parameters were defined based on a combination of BO calibration and manual fine-tuning to ensure consistency across all generated structures, without necessitating repeated experimental validation for each structure. The optimization and validation approach thus establishes a robust set of parameters to be employed consistently across the generation of all synthetic microstructures. The Bayesian optimization was performed on a reduced but statistically representative domain (see Section 2.9), keeping the experimental voxel resolution, to reduce computational effort. For a more detailed description of the original structure generator, parameter sensitivities, and BO framework, the reader is referred to Schöller et al. [151]. The optimized input parameters given to the structure generator for creating a synthetic microstructure are summarized in Table 5.1. The mean particle diameter and standard deviation listed in Table 5.1 define the lognormal particle size distribution employed as input for the synthetic structure generation procedure to generate particle size distributions from a given distribution.

Table 5.1: Input parameters given to the structure generator for creating a synthetic microstructure.

Phase	Volume fraction (%)	Mean particle diameter (µm)	Standard deviation (µm)	Angular spectrum amplitude ($\mathrm{W\,nm^{-1}}$)	Dilation iterations
Ni	17.59	0.886	0.352	$10^{-1.8}$	1
GDC	29.21	0.494	0.070	$10^{-2.5}$	1

The extended workflow incorporates a sintering-like morphological coalescence step based on a modified Allen-Cahn phase-field equation that preserves the volume [152], as well as a correction term controlling curvature minimization [153], as described in Section 2.5. All parameters are expressed in a consistent arbitrary unit system. To accelerate morphological evolution, equal interfacial mobilities were assigned across all phase pairs, with $m_{NiPore} = m_{NiGDC} = m_{GDCPore} = 1\,u_l^4/(u_E\,u_t)$. The interfacial energies were set to $(\gamma_{NiGDC},\ \gamma_{NiPore},\ \gamma_{GDCPore}) = (1.43,\ 1.2,\ 2.43)$, while the curvature control parameter is chosen as $\gamma_\alpha^c = 9\,u_E/u_l^2$. A higher-order term $\gamma_{\alpha\beta\delta} = 50\,u_E/u_l^2$ is included to suppress the formation of spurious phase formation. The simulations were performed using an interfacial width parameter ϵ as 2.0 u_l, number of time steps as 100, and a total simulation time of 2.5 u_t. It is emphasized that this morphological evolution does not represent a physical sintering process. Instead, the phase-field simulations are employed as a numerical tool to generate sintering-like morphologies through particle coalescence rapidly. Accordingly, the simulation time represents a pseudo-time, and the parameters for mobility and surface energy are treated as numerical controls governing the rate and extent of morphological evolution.

The representativeness of the synthetic microstructure was evaluated by systematically comparing a comprehensive set of geometric, statistical, and microstructural descriptors, relevant to both electrochemical performance and mechanical behavior, with an experimental reference structure (see Table 5.2). The employed experimental 3D microstructure was reconstructed from Ni-GDC SOFC anode samples produced at Forschungszentrum Jülich and FIB-SEM tomography at KIT, as described in Section 2.8. The statistical representativeness of the experimental domain and its subvolumes was demonstrated in Section 2.9.

Table 5.2: Comparison of microstructural and mechanical properties: Digital Twin vs. Experimental.

Property	Unit	Phase	Experimental	Synthetic	Relative error (%)
Volume fraction	(%)	Ni	21.92	21.33	-2.69
		GDC	41.57	41.25	-0.77
Mean diameter	(µm)	Ni	0.91	0.91	0
		GDC	0.57	0.57	0
		Pore	0.57	0.55	-3.51
Surface area density	(μm^{-1})	Ni	1.03	1.00	-2.91
		GDC	2.19	1.90	-13.24
		Pore	1.87	2.00	6.95
Mean tortuosity	(−)	Ni	inf	inf	–
		GDC	2.51	2.21	-11.95
		Pore	2.68	3.02	12.69
TPB density	(μm^{-2})	–	1.80	1.95	8.33
DPB density	(μm^{-1})	–	1.51	1.45	-3.97
Elastic moduli	(GPa)	E_{xx}	59.16	62.78	6.11
		E_{yy}	58.47	59.45	1.68
		E_{zz}	63.94	62.52	-2.22
		E_{Hill}	60.40	61.38	1.62

5.2 Experimental validation

The 3D experimental and synthetic microstructures are shown in Figure 5.1. A visual inspection reveals a high degree of morphological resemblance at both the electrode and phase levels, including particle shapes, phase connectivity, and spatial distribution. A quantitative assessment, as shown in Table 5.2, validates this agreement across an extensive set of 17 quantitative metrics. Most relative errors remain below 5 %, with larger discrepancies of 11 %–13 % observed for GDC surface area density and the tortuosities. The generator precisely replicates the phase volume fractions and particle sizes of Ni, GDC, and pores, while showing high agreement in the specific surface areas for Ni and pore phases; the GDC surface area shows a higher underestimation of around 13 %. TPB and

DPB densities, important descriptors for electrochemical activity, are reproduced with errors of about 8 % and 4 %, respectively. The inclusion of a sintering-like coalescence step proves essential in achieving TPB values closer to those observed in experiments. The tortuosity values show larger deviations of about 12 % for GDC and pore phases. These values are highly sensitive to local microstructural changes. The tortuosity of nickel is not reported, as the Ni phase is not percolating in both experimental and synthetic structures. The directional and effective elastic moduli are also well captured and largely agree with the experimental values.

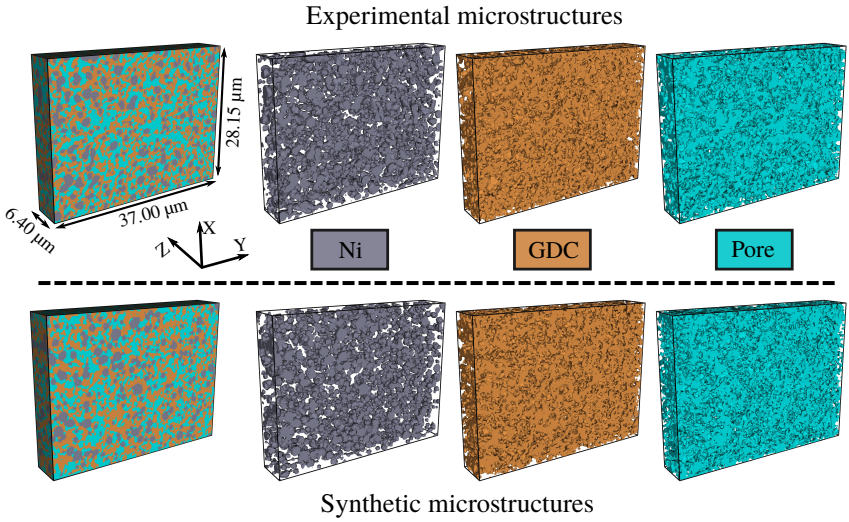


Figure 5.1: Comparison of the FIB-SEM reconstructed 3D SOFC anode microstructure and the individual phase morphologies with a digital twin created by a structure generator.

In order to quantify the overall accuracy of the synthetic microstructure, a global error metric is calculated, defined as the mean absolute percentage error (MAPE) in all metrics considered, which yields a value of 4.92 %, calculated from 16 parameters. One parameter with an infinite reference value is excluded, as the percentage error is undefined in this case. This single scalar metric demonstrates

the generator's ability to accurately reproduce across a wide range of geometric, transport-related, and mechanical properties. The strong agreement in both morphology and quantitative descriptors confirms the synthetic structure as a digital twin of the real SOFC anode and enables subsequent sensitivity analyses, correlations between microstructure and properties, to guide optimization of the electrodes in the following Chapter. The current work employs the continuous particle size distribution method of Münch and Holzer [159], which is particularly useful for porous networks as it avoids artificial segmentation into discrete particles. The method determines the fraction of the phase volume that can be occupied by overlapping spheres of a certain diameter and, in principle, results in a complementary cumulative distribution that decreases monotonically from unity to zero. For the validation of the generated synthetic microstructure, the continuous particle size distributions of the nickel, GDC, and pore phases are compared with those obtained from 3D FIB-SEM reconstruction (see Figure 5.2). The close agreement across all phases, as shown in Figure 5.2, further supports the validation of the generated structure in comparison to the experimental microstructure. Furthermore, a statistical analysis of 10 independently generated

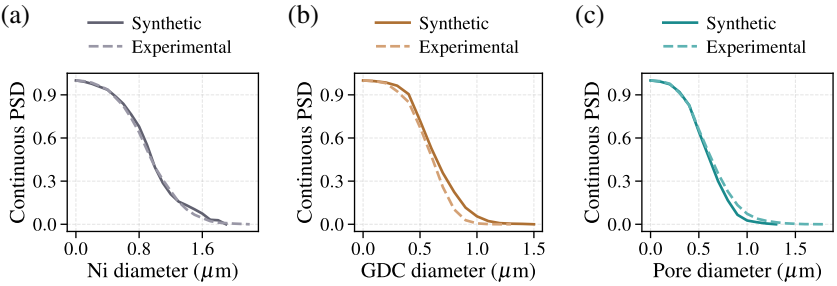


Figure 5.2: Comparison of continuous particle size distributions for the synthetic microstructure and the FIB-SEM reconstruction for (a) nickel phase, (b) GDC phase, and (c) pore phase.

microstructures under identical conditions (as in the validation case) is performed, and the resulting variability in key microstructural properties is summarized in Table 5.3.

Table 5.3: Evaluation of statistical variations in microstructural properties across 10 synthetic structures (S1 to S10 samples) generated independently under identical conditions from the structure generator.

Property	S1	S2	S3	S4	S5	S6	S7	S8	S9	S10	Mean	Standard deviation	Coefficient of Variation (%)
TPB density (μm^{-2})	1.90	1.92	1.88	1.86	1.96	1.86	1.86	1.87	1.95	1.89	1.89	0.03528	1.86
DPB density (μm^{-1})	1.46	1.46	1.48	1.44	1.43	1.47	1.46	1.47	1.45	1.45	1.46	0.01418	0.97
Ni SA density (μm^{-1})	0.95	0.96	0.95	0.96	0.99	0.95	0.96	0.95	0.98	0.97	0.96	0.01327	1.38
GDC SA density (μm^{-1})	1.90	1.89	1.90	1.87	1.89	1.89	1.90	1.89	1.89	1.89	1.89	0.00831	0.44
Pore SA density (μm^{-1})	1.98	1.98	2.01	1.97	1.95	1.99	1.98	1.99	2.00	1.99	1.98	0.01562	0.79
GDC Mean tortuosity (−)	2.19	2.20	2.17	2.26	2.26	2.22	2.18	2.19	2.18	2.21	2.21	0.03040	1.38
Pore Mean tortuosity (−)	2.93	3.13	2.86	3.01	3.12	2.97	3.13	2.98	3.10	2.99	3.02	0.08908	2.95
Ni Mean diameter (µm)	0.93	0.94	0.94	0.88	0.91	0.93	0.95	0.90	0.93	0.94	0.92	0.02062	2.23
GDC Mean diameter (µm)	0.57	0.57	0.58	0.59	0.58	0.58	0.58	0.58	0.58	0.57	0.58	0.00600	1.04
Pore Mean diameter (µm)	0.56	0.56	0.55	0.55	0.56	0.55	0.56	0.56	0.56	0.56	0.56	0.00458	0.82
E_{xx} (GPa)	59.57	61.04	61.81	59.72	61.86	60.51	60.18	59.48	61.34	61.38	60.69	0.87160	1.44
E_{yy} (GPa)	60.69	61.14	59.35	60.11	59.97	61.40	60.50	59.51	59.99	59.75	60.24	0.64370	1.07
E_{zz} (GPa)	60.59	61.74	59.71	61.80	61.17	60.93	60.61	61.04	61.92	61.03	61.05	0.63450	1.04
E_{Hill} (GPa)	60.18	61.26	60.00	60.07	60.72	60.78	60.39	60.00	60.83	60.38	60.46	0.40150	0.66

The low variance observed across a wide range of properties, with coefficients of variation of about 1 % for the majority of properties and 2 %–3 % for two other properties, confirms the robustness and reproducibility of the structure generation method. This further substantiates the reliability of the 15 synthetic structures generated and their comparative evaluation for the optimal configuration of the Ni-GDC SOFC anode presented in the subsequent chapter.«

6 Effect of anode volume fractions on microstructural degradation and mechanical integrity[1]

»Enhancing the performance and durability of SOFCs requires concurrent improvements in electrochemical activity and mechanical integrity, both strongly dependent on the initial anode microstructure and its degradation over long-term operation. This Chapter presents a comprehensive degradation investigation for Ni-GDC SOFC anode microstructures, combining the generation of realistic synthetic microstructures and large-scale aging simulations. Representative synthetic microstructures are generated with systematically varying phase volume fractions and subjected to long-term (2000h) aging using a validated multiphase-field model. Electrochemical performance descriptors, including triple-phase boundary (TPB), double-phase boundary (DPB) densities, phase tortuosities, and mechanical properties, such as elastic moduli and stress distributions resulting from thermal expansion coefficient mismatch between Ni and GDC, are collectively analyzed. The results provide detailed insights into the design of anode microstructures by highlighting trade-offs between initial and degradation-induced electrochemical and mechanical performance.

The microstructures of SOFC electrodes are defined by several independent parameters, such as phase volume fractions and particle sizes, which influence both

[1] The content of this chapter has been taken directly from Jeela et al. [90] with minor linguistic changes. The figures have been adjusted to the format of this dissertation.

initial performance and long-term degradation. Optimizing for the slowest degradation may not necessarily result in optimal initial performance, highlighting the complexity of microstructure design. Timurkutluk et al. [217] systematically examined TPB density as a function of particle size and phase volume fractions in synthetic SOFC electrode microstructures by generating a large number of virtual microstructures and evaluating performance based solely on TPB density. Prioux et al. [218] proposed a multiscale modeling framework for optimizing Ni-YSZ hydrogen electrode microstructures, utilizing experimentally measured electrochemical data at the cell level and 3D electrode reconstructions as references, and coupling synthetic microstructures with electrochemical models on the cell and electrode levels. Mütter et al. [219] applied an artificial neural network for optimizing process parameters. Despite attempts to optimize microstructure in SOFC research, this domain is still evolving, mainly as a result of limited understanding of microstructure evolution phenomena. Peng et al. [220] highlighted this research gap in a comprehensive review study. Optimizing electrode microstructures in such a high-dimensional parameter space requires extensive modeling efforts combined with a systematic investigation of independent parameters affecting performance in pristine structures as well as over long-term operation, both of which we have presented in this Chapter.

The mechanical response of Ni-GDC anode microstructures is evaluated using a quasi-static solid mechanics formulation with strain-controlled homogenization to estimate effective elastic moduli and the stack boundary conditions method, enabling coupled evolution of stress and strain resulting from thermal expansion and mechanical confinement [116]. Electrochemical performance-relevant descriptors such as TPBs, DPBs, and phase tortuosities, as well as mechanical integrity-relevant descriptors such as elastic moduli, average von Mises stress, and critical volume fractions (CVF), are analyzed as functions of phase volume fractions in pristine structures and their temporal evolution during isothermal aging, providing comprehensive insights into the design and degradation of Ni-GDC SOFC anodes.

6.1 Analysis of thermal expansion mismatch in Ni-GDC anode

Average von Mises stress In order to approximate the mechanical constraints imposed on the anode in an SOFC stack, a boundary condition setup was employed, similar to the approach used in the work of Elmoghazy et al. [116]. The interface between the anode and electrolyte was fully fixed $(u_x, u_y, u_z) = (0, 0, 0)$, the interface between the anode and interconnect was constrained only in the normal direction ($u_z = 0$), while the lateral surfaces were constrained in their normal displacement ($u_n = 0$) to account for the confinement by neighboring cells. Contrary to the strain-controlled homogenization framework employed to estimate the effective elastic moduli (see Section 2.7.2), the stack-level boundary condition setup enables the coupled evolution of stress and strain resulting from thermal expansion and mechanical confinement, thereby providing a more physically representative evaluation of the internal mechanical response. The average von Mises stress is defined as $\langle \sigma_{\mathrm{vM}} \rangle = \frac{1}{V} \int_V \sigma_{\mathrm{vM}}(\boldsymbol{x})\, \mathrm{d}V$. The von Mises stress is utilized here as an equivalent scalar measure of the multiaxial thermomechanical stress state, thereby enabling a quantitative comparison of stress levels and their spatial distribution across different microstructures and aging states. It is used solely as an indicator of the overall stress state and is not intended to predict fractures, failure, or damage. Material properties used for this analysis are listed in Table 6.1. As the material properties considered here refer to room temperature conditions, this could result in an overestimation of the predicted absolute values of effective stiffness at the operating temperatures of SOFCs. However, the relative differences in effective stiffness between the microstructures remain unchanged, since all microstructures were evaluated under the same constitutive assumptions.

A common degradation mechanism in SOFCs is delamination at the electrode-electrolyte interface, which compromises cell integrity and leads to performance degradation. This damage is primarily caused by thermomechanical stresses arising from different thermal expansion coefficients of the electrode components and the electrolyte; consequently, the composition of the anode has a strong influence

Table 6.1: Properties of the materials used in the mechanical simulations.

Phase	Elastic modulus E (GPa)	Poisson's ratio ν	Thermal expansion coefficient α_θ (K^{-1})
Ni	200 [221]	0.31 [221]	16.00×10^{-6} [222]
GDC	120 [223]	0.33 [223]	12.96×10^{-6} [224]

on the resulting stress distribution. In addition, partial performance degradation during operation is often associated with some partial breakup of Ni/YSZ or Ni/GDC interfaces, which disrupts ionic and electronic transport pathways and reduces the density of triple-phase boundaries. The critical volume fraction (CVF), employed in this work, was defined as $\mathrm{CVF} = \frac{1}{V_{\mathrm{tot}}} \int_{V(\sigma_{\mathrm{vM}} > \sigma_{\mathrm{threshold}})} \mathrm{d}V$, where the threshold value $\sigma_{\mathrm{threshold}}$ was taken as the average von Mises stress of the pristine state of the corresponding configuration. This microstructure-specific normalization accounts for intrinsic differences in stiffness, phase connectivity, and constraint among microstructures, enabling the CVF to reflect aging-induced stress localization with respect to the threshold of each configuration, rather than an absolute stress threshold applied uniformly to all structures. From a mechanical standpoint, the CVF quantifies the fraction of the microstructure exposed to stresses exceeding a threshold level.

6.2 Generation of synthetic structures for aging simulations

The influence of initial phase volume fractions on microstructural attributes that govern electrochemical performance and mechanical behavior initially and during aging was investigated by generating a series of synthetic microstructures through variation of phase volume fractions. Fifteen synthetic microstructures were created by varying the volume fractions of Ni, GDC, and pore phases while maintaining constant particle sizes. The targeted parameters for analysis and their values in the generated synthetic structures are summarized in Table 6.2. Three pore volume

fractions were considered: 25 % (group A), 35 % (group B), and 45 % (group C). Within each group, five configurations were generated by varying the Ni/GDC solid phase ratio in 10 % increments from 30/70 to 70/30. These parameter ranges comprise widely reported experimental and investigated compositions and enable a systematic evaluation of the effects resulting from the volume fractions of the three phases. To isolate the influence of particle sizes, the mean particle sizes of Ni and GDC were kept constant in all configurations. Mean particle diameters of 0.75 µm for Ni and 0.5 µm for GDC were chosen, corresponding largely to the experimental values for conventional screen-printed anodes. The resulting particle sizes in all generated microstructures remained close to these target values, as shown in Table 6.2.

Some representative examples of generated synthetic microstructures are shown in the first row of Figure 6.3. The statistical representativeness of the microstructures is ensured by the appropriate domain size, voxel resolution, and number of particles. All synthetic microstructures comprise a cubic domain of 10^3 µm^3 and a voxel size of 35 nm, providing sufficient resolution while maintaining computational tractability for long-term aging simulations. The volume of the domain is well above the representative volume element (RVE) threshold of 10^3 particles, where most properties converge to stable values, as found by Joos [167]. In Section 2.9, statistical error analysis of a FIB-SEM reconstructed domain ($9.4 \times 12.4 \times 6.4$ µm^3) demonstrated low variability in microstructural properties, with coefficients of variation (CV) ranging from 1 %–5 % (mean CV of about 3 %), confirming negligible spatial heterogeneity. Here, the simulation domain of $10.0 \times 10.0 \times 10.0$ µm^3 with a total volume of 1000 µm^3 is comparable to and slightly larger than the previously validated representative volume, ensuring statistical representativeness. Accordingly, any microstructural inhomogeneities are expected to be minimal, with no significant influence on the computed properties. Structure generator enables direct and flexible control over phase volume fractions and particle sizes. By modifying the parameters of the particle size distribution, microstructures with finer or coarser particle sizes can be systematically generated.

Table 6.2: Microstructural parameters of the generated synthetic structures. The bold values denote the target (reference) parameters used in the design of the fifteen synthetic microstructures, while the remaining values represent the corresponding realized parameters obtained from the generated structures.

Synthetic structures	Pore vol. frac. (%)	Ni		GDC		Ni mean dia. (µm)		GDC mean dia. (µm)	
		Target (solid vol. %)	Synthetic (vol. %)	Target (solid vol. %)	Synthetic (vol. %)	Target	Synthetic	Target	Synthetic
A1	**25**	**30**	22.51	**70**	52.57		0.757		0.508
A2		**40**	29.77	**60**	45.33		0.737		0.495
A3		**50**	37.60	**50**	37.99	**0.75**	0.740	**0.50**	0.493
A4		**60**	45.00	**40**	30.52		0.749		0.514
A5		**70**	52.71	**30**	22.87		0.755		0.499
B1	**35**	**30**	19.67	**70**	45.28		0.748		0.502
B2		**40**	25.71	**60**	39.13		0.761		0.498
B3		**50**	32.66	**50**	32.37	**0.75**	0.756	**0.50**	0.502
B4		**60**	38.91	**40**	26.10		0.758		0.502
B5		**70**	45.26	**30**	19.34		0.762		0.506
C1	**45**	**30**	16.78	**70**	38.34		0.753		0.497
C2		**40**	22.08	**60**	32.94		0.742		0.510
C3		**50**	27.58	**50**	27.34	**0.75**	0.750	**0.50**	0.504
C4		**60**	32.85	**40**	21.96		0.753		0.497
C5		**70**	38.60	**30**	16.50		0.748		0.499

6.3 Influence of initial microstructural configurations on properties

This Section systematically investigates the influence of the volume fractions of nickel, GDC, and pore phases in synthetic microstructures on the initial performance of Ni-GDC SOFC anodes. First, the influence on microstructural properties relevant to electrochemical performance, such as TPB and DPB densities, along with the tortuosity of the phases determining ion, electron, and gas transport, is analyzed in the pristine state, followed by the corresponding effects on effective mechanical properties and response.

6.3.1 Microstructural descriptors of electrochemical performance

Effect of composition on TPB and DPB densities TPBs represent the electrochemical reaction sites in both Ni-YSZ and Ni-GDC SOFC anodes. Figure 6.1(a) compares the influence of phase volume fractions on the total TPB density across all investigated synthetic microstructures. As expected, the TPB density shows a strong dependence on the phase volume fractions. For each porosity group, the TPB density initially increases, reaches a maximum at nearly equal Ni/GDC solid volume fractions, and then decreases thereafter. The TPB density values are highest at the equivalent Ni/GDC solid volume fraction (50/50) for the structures, except for the group with 45 % porosity. Furthermore, the TPB densities for Ni/GDC compositions of 50/50 and 60/40 show only minimal differences. Overall, the maximum TPB densities among the groups are observed in structures A3, B3, and C4, at 4.98 μm^{-2}, 4.04 μm^{-2} and 3.22 μm^{-2}, respectively. The highest TPB density can be seen in a group with 25 % porosity, as expected from the higher volume fractions of nickel and GDC. These results are consistent with the percolation-based analyses reported in the literature [225–227]. With comparable particle radii of the two solid phases, the TPB density increases with the solid phase fraction, reaches a maximum at the equivalent phase composition,

and is followed by a decrease. In the current work, the highest TPB density occurs in the A3 configuration, where nickel and GDC represent around 37.5 vol.% respectively, and the pore is 25 vol.%.

DPBs also contribute to the electrochemical activity in Ni-GDC SOFC anodes due to the mixed ionic and electronic conductivity of GDC, making the GDC/Pore interface an additional electrochemically active reaction site alongside the TPBs. As depicted in Figure 6.1(b), the DPB density decreases with decreasing GDC solid volume fraction for all porosity groups A, B, and C from $1.80\,\mu m^{-1}$–$2.02\,\mu m^{-1}$ to $0.86\,\mu m^{-1}$–$0.96\,\mu m^{-1}$. Within each group, a higher GDC content (solid volume fraction) leads to an increased DPB density as a result of the increased available GDC surface area. Across different porosities (A, B, C groups), however, a distinctive trend can be observed: Structures with a porosity of 25 % consistently exhibit lower DPB densities, while those with a porosity of 35 % and 45 % exhibit higher and nearly identical values, suggesting saturation. This behavior emphasizes that DPB density depends on both the GDC volume fraction and the pore phase, as well as connectivity. At lower porosity (25 %), the pore phase is poorly percolated, as reflected in high pore tortuosity values (in the range of 5.5–10; Figure 6.1(e)), limiting contact between GDC and pores, and rendering a significant fraction of the GDC surface confined within the solid network. Increasing the porosity to 35 % significantly improves pore connectivity (tortuosity in the range of 2.7–3.4; Figure 6.1(e)), uncovering more GDC surface area and increasing the DPB density. A further increase in porosity to 45 % leads to no further enhancement in DPB density, indicating a saturation stage in which nearly all accessible GDC surfaces are already in contact with the pore phase. Overall, systems with a porosity of 35 % (group B) deliver better results with regard to DPB densities.

Effect of composition on tortuosity TPB and DPB densities are not the sole determining factors for the electrochemical performance of Ni-GDC SOFC anodes; the efficient transport of fuel gas, electrons, and oxide ions is equally essential. The transport of gas is determined by pore phase contiguity, while

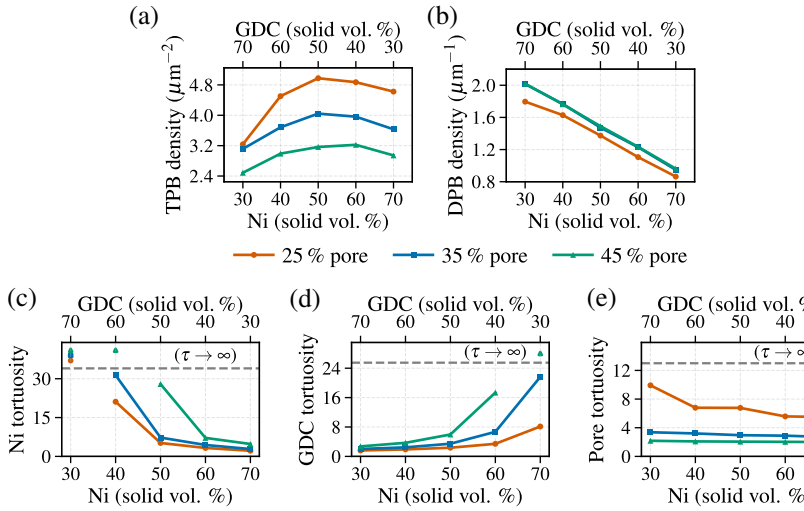


Figure 6.1: Variations in microstructural properties depending on porosity and solid volume fractions of Ni/GDC phases. (a) total TPB density, (b) DPB density, and mean tortuosities of (c) nickel, (d) GDC, and (e) pore.

continuous Ni and GDC pathways enable electronic and ionic conduction. Microstructure's influence on these transport processes can be quantified by tortuosity: higher values indicate poorly connected phases with long and convoluted paths that impede transport, while lower values correspond to well-connected, short, and relatively straight paths that enable efficient transport. Infinite tortuosity values indicate a non-percolating phase for which effective transport is not possible. Figure 6.1(c-e) shows the volume-dependent tortuosity of the Ni, GDC, and pore phases, averaged over the three principal directions.

Across all porosity groups, Ni tortuosity decreases with increasing Ni volume fraction, reflecting improved phase connectivity, a general trend reported for porous multiphase systems (Figure 6.1(c)). Structures with Ni volume fractions of 16.78 % (C1), 19.67 % (B1), 22.08 % (C2), and 22.51 % (A1) exhibit non-percolating Ni and thus infinite tortuosity, while the closest percolating case of B2 (25.71 % Ni) exhibits connectivity yet with a high tortuosity value of 31.36.

These trends align with the experimental Ni-GDC microstructure analyzed in this work (see Table 5.2) where a Ni volume fraction of 21.92 % results in a non-percolating Ni structure, even though the mean particle size (0.91 µm) is larger than in the synthetic structures (0.75 µm), but the particle size ratios are comparable (Ni/GDC is 1.59 in the experimental structure and 1.50 in the synthetic structure). In contrast, Ni volume fractions between 37.60 % and 52.71 % result in well-connected pathways, with tortuosity decreasing from 5.18 to 2.18. Although GDC offers mixed ionic and electronic conductivity, its electronic conductivity is several orders of magnitude lower than that of nickel [228]. Consequently, anodes with low or non-percolating Ni fraction may still be viable if GDC and pore phases are well connected, subject to design considerations, such as the thickness of the anode functional layer, and the dominant rate-limiting transport mechanism. Thus, the present results provide quantitative insight into the selection of Ni and GDC volume fractions tailored to specific cell designs, and the extracted microstructural parameters provide needed input for transmission line modeling of Ni-GDC SOFC anodes for cell performance as a function of microstructural composition.

The tortuosity of the GDC phase primarily determines the transport of oxide ions and primary or auxiliary electrons in SOFC anodes. As shown in Figure 6.1(d), GDC tortuosity decreases with increasing GDC volume fraction across all porosity groups, showing a similar trend to the Ni phase. However, GDC percolation is achieved at lower volume fractions: only a single structure (C5, 16.50 % GDC) is non-percolating, while the closest percolating case (B5, 19.34 % GDC) exhibits a connected structure, with a high tortuosity (21.63). The experimental Ni-GDC microstructure analyzed in this work (see Table 5.2), with a GDC volume fraction of 41.57 %, resulted in a mean tortuosity of 2.51, whereas the synthetic structure B2 (39.13 % GDC) with a tortuosity of 2.46 comes close to these results. Overall, GDC volume fractions in the range of 30.52 %–52.57 % result in well-connected transport pathways, with tortuosity decreasing from 3.69 to 1.61. GDC exhibits a lower percolation threshold and a lower tortuosity compared to Ni at equivalent phase volume fractions, indicating that transport connectivity is governed not only by volume fraction and particle size, but also possibly by phase interactions and microstructural evolution during fabrication of the anode. Due to their larger

size, Ni particles form fewer Ni-Ni contacts and can be disrupted more easily by surrounding GDC phases; consequently, Ni connectivity could be interrupted, leading to higher tortuosity and a higher percolation threshold. In contrast, the smaller GDC particles exhibit higher coordination and denser packing, enabling percolation at lower volume fractions and resulting in lower tortuosity. In the three-phase Ni-GDC-pore system, phase connectivity is furthermore explained by sintering-induced coalescence driven by particle size ratios, initial contact statistics, and interfacial thermodynamics. While Ni coalesces at a faster rate due to higher diffusivity and surface energy, these factors do not necessarily enhance long-distance connectivity. GDC with slower coalescence and lower surface energy instead develops smoother and more continuous networks, eventually leading to long-distance connectivity.

Pore tortuosity is another important indicator for gas transport in the anode, with higher values indicating more convoluted diffusion paths and reduced accessibility of reactants to sites of electrochemical reactions. As shown in Figure 6.1(e), pore tortuosity decreases with increasing porosity, as expected: Group A (25 % porosity) shows the highest values, while Group C (45 % porosity) shows the lowest values, reflecting improved pore connectivity. A pronounced decrease in tortuosity can be observed between 25 % and 35 % porosity, while small changes are observed between 35 % and 45 %, suggesting saturation once a well-connected pore network is established. At a fixed porosity, pore tortuosity is additionally influenced by the ratio of Ni/GDC solid volume fractions due to the differing particle sizes. Across all porosity groups, an increase in the Ni fraction resulted in lower pore tortuosity. Specifically, pore tortuosity decreases from 9.92 to 5.49 in group A, from 3.37 to 2.69 in group B, and from 2.18 to 2.00 in group C as the Ni/GDC ratio changes from 30/70 to 70/30. The influence of the solid phase composition is most prominent at low porosity (group A) and is negligible at high porosity (group C), which is consistent with the saturation of the pore network. This behavior reflects the interaction between particle size, solid volume fractions, and porosity: at constant porosity, a higher proportion of larger Ni particles tends to result in coarser pore channels, while a higher proportion of smaller GDC particles narrows the pore necks and increases the complexity of the pathways.

The experimental Ni-GDC anode microstructure with a pore volume fraction of 36.51 % features a mean pore tortuosity of 2.68 (see Table 5.2), corresponding well with the synthetic structures in group B (35 % porosity), where values range between 3.37 and 2.69 depending on the Ni/GDC ratio.

6.3.2 Effective properties of mechanical response

Elastic modulus As described in detail in Section 2.7.2, this work employs a homogenization method in which the heterogeneous anode microstructure is replaced by an equivalent homogeneous continuum, enabling a systematic evaluation of the effective mechanical properties and their evolution during aging as a function of the initial microstructural configuration. Effective mechanical properties of porous Ni-GDC anodes, comprising directional elastic moduli and Hill's average, were extracted from the initial synthetic microstructures of groups A, B, and C to establish structure-property correlations. The directional elastic moduli (E_{xx}, E_{yy}, and E_{zz}) for groups A, B, and C are shown in Figure 6.2(a-c). For groups A and B, the directional moduli for a given composition are clustered closely, indicating a nearly isotropic elastic response. In contrast, group C (45 % porosity) exhibits pronounced elastic anisotropy (Figure 6.2(c)). As shown in Figure 6.2(d), the Hill average modulus (E_{Hill}) decreases linearly with increasing porosity, declining from 84.23 GPa–105.41 GPa for group A (25 % porosity) to 41.51 GPa–48.19 GPa for group C (45 % porosity). This tendency is consistent with computational studies on reconstructed Ni-YSZ anodes and porous media models, which reported a reduction in the elastic modulus with increasing porosity, in accordance with Gibson-Ashby's scaling laws [229–231]. At fixed porosity, E_{Hill} increases with increasing Ni solid volume fraction in all groups. Specifically, E_{Hill} increases from 84.23 GPa to 105.41 GPa in group A, from 62.66 GPa to 72.72 GPa in group B, and from 41.5 GPa to 48.19 GPa in group C as the Ni/GDC solid volume fraction changes from 30/70 to 70/30. This behavior results from the higher elastic modulus of Ni (200 GPa) in comparison to GDC (120 GPa), as shown in Table 6.1.

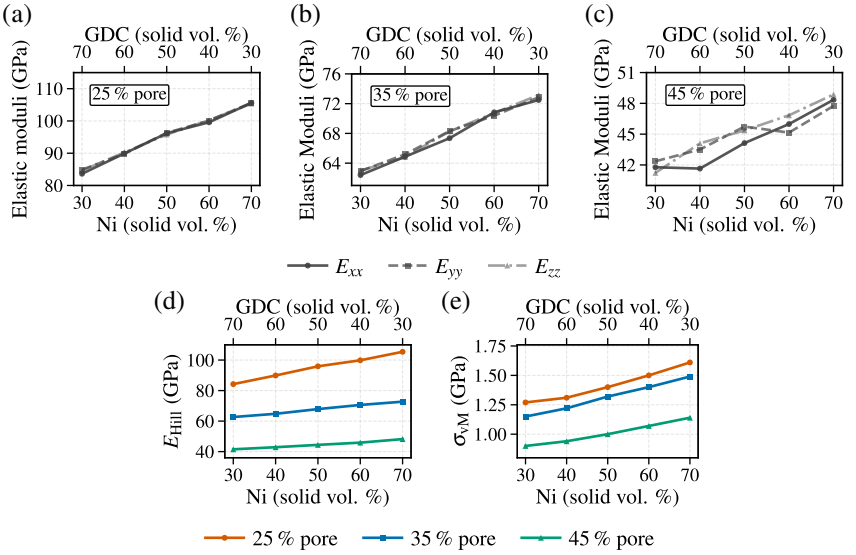


Figure 6.2: Effect of porosity and Ni/GDC solid volume fractions on effective mechanical properties and stresses: directional elastic moduli (E_{xx}, E_{yy}, E_{zz}) for pore volume fractions of (a) 25 %, (b) 35 %, and (c) 45 %, (d) Hill average elastic modulus (E_{Hill}), and (e) average von Mises stress.

Average von Mises stress Figure 6.2(e) shows the average von Mises stress under the applied stack boundary conditions and thermal expansion, for different porosities and Ni/GDC solid volume fractions. Overall, the average von Mises stress decreases with increasing porosity, declining from a maximum of 1.61 GPa for group A (25 % porosity) to 0.90 GPa for group C (45 % porosity). At fixed porosity, the average von Mises stress increases with Ni content in all groups: from 1.27 GPa–1.61 GPa in group A, from 1.15 GPa–1.49 GPa in group B, and from 0.90 GPa–1.14 GPa in group C, with the Ni/GDC ratio changing from 30/70 to 70/30. As expected, these trends largely correspond to those of the Hill average elastic modulus. The relatively high stress values predicted in this work are attributed to the purely elastic material model assumption. In practice, part of the stress would be relaxed by inelastic deformation or damage mechanisms.

Therefore, the present stress values should primarily be interpreted comparatively when evaluating differences between microstructures. It is observed that, on account of the similar evolution of E_{Hill} and the average von Mises stress, i.e., increase with Ni content and decrease with porosity, it can be approximated that the thermal eigenstrain remains nearly constant across all configurations. This insensitivity can be largely attributed to the relatively small differences in the thermal expansion coefficients of Ni and GDC (Table 6.1), thereby reducing the influence of solid volume fraction variations on the overall thermal eigenstrain.

6.4 Evolution and degradation of properties during aging

This Section presents the multiphase-field simulation results investigating the coarsening behavior in various initial synthetic microstructures under thermal operating conditions of 900 °C with a gas composition of 50 % H_2/50 % H_2O. Firstly, we examine the evolution of the microstructure over time with an analysis of the particle diameters. Subsequently, we explain the influence of aging on the microstructural properties relevant to electrochemical performance, followed by the effective mechanical properties.

Evolution of microstructure and particle size All pristine synthetic Ni-GDC microstructures were employed as inputs for multiphase-field aging simulations performed for 2000 hours, with properties evaluated at 50-hour intervals. To comprehensively characterize the anode degradation, the analysis focused on the temporal evolution of the mean particle diameters of Ni, GDC, and pores; electrochemically relevant metrics such as TPB and DPB densities as well as phase tortuosities; and effective mechanical properties like directional elastic moduli, Hill average elastic modulus, and critical volume fraction. The objective here is to quantify the influence of different initial configurations on the degradation of these key properties. A detailed analysis of the correlations between the

initial configurations of the microstructure and the degradation of its properties enables the targeted optimization of the initial microstructures, ultimately leading to improved durability and efficiency of SOFCs. Figure 6.3 shows the 3D microstructure evolution of selected configurations (A1, A5, B1, B5, C1, C5) after aging times of 1000h and 2000h. Microstructural evolution directly affects the electrochemical reaction sites, the transport of ions, electrons, and gases, and thus the long-term stability of the anode. Experimentally, aging-induced coarsening of Ni and GDC has been widely reported and is reflected by an increase in the mean particle size [83, 86, 89].

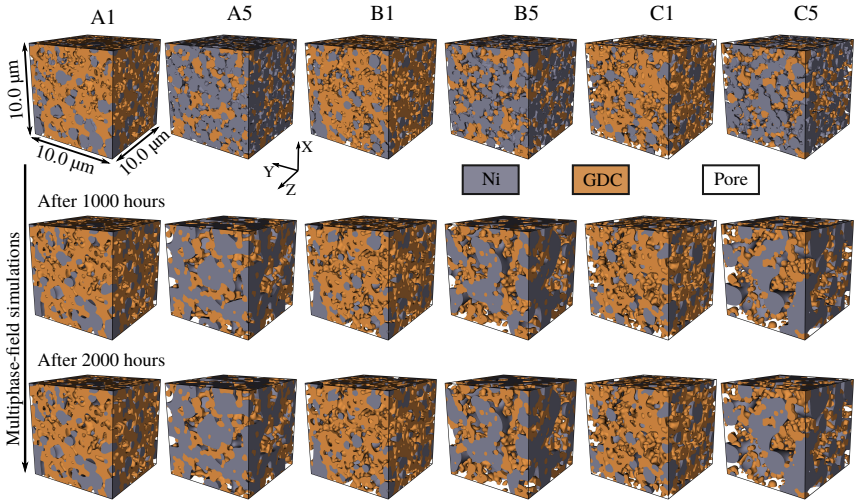


Figure 6.3: Morphological evolution of the pristine synthetic 3D Ni-GDC anode microstructures after 1000 and 2000 hours of aging for selected initial configurations (A1, A5, B1, B5, C1, C5) predicted from multiphase-field simulations.

Figure 6.4(a-c) depicts the evolution of the mean Ni particle diameter for porosity groups A, B, and C. In all microstructural configurations, Ni coarsening is most pronounced during the early stages of aging and slows considerably at later stages,

in agreement with experimental observations [86] and simulations [74, 98]. For all porosity groups, the relative increase in the mean Ni particle diameter, as expected, increases with increasing Ni solid volume fraction. The largest particle growth after 2000 aging hours is observed in A5 at 46.6 % (0.755 µm–1.117 µm), B5 at 54.8 % (0.762 µm–1.189 µm), and C5 at 56.7 % (0.748 µm–1.172 µm) with Ni volume fractions of 52.71 %, 45.26 %, and 38.60 %, respectively. It is noteworthy that the highest relative growth occurs in configuration C5, despite its lower Ni volume fraction. This behavior can largely be attributed to the combined effect of higher pore content (44.9 vol.%) and lower inhibition by the GDC network (16.5 vol.%) in conjunction with the significantly faster surface diffusivity of Ni in comparison to interfacial diffusivity (five orders of magnitude [166]), promoting rapid particle coalescence among the nickel particles and thus a higher increase in the mean particle diameter.

Figure 6.4(d-f) shows the evolution of the mean GDC particle diameter for porosity groups A, B, and C. In contrast to Ni, GDC exhibits a much slower and more gradual coarsening behavior over time, reflecting its significantly lower diffusivity, about five orders of magnitude lower than that of Ni [166]. Across all porosity groups, the relative increase in the mean GDC particle diameter increases with increasing GDC solid volume fraction, similar to the trend observed for Ni. Minor differences among the curves at different solid volume fractions within a given group arise from slightly different initial GDC particle sizes of those respective configurations. After 2000 aging hours, the largest particle growth is observed for A1 at 17.3 % (0.508 µm–0.603 µm), B1 at 8.9 % (0.502 µm–0.550 µm), and C1 at 5.6 % (0.497 µm–0.531 µm), with GDC volume fractions of 52.57 %, 45.28 %, and 38.34 %, respectively. The largest relative growth in GDC is observed in configuration A1, which has the highest GDC volume fraction. Given the smaller particle size, strong percolation, and relatively low diffusivity of GDC, particle coarsening is primarily dependent on the volume fraction in the investigated 2000h aging time, rather than the porosity and inhibition by the nickel network.

Figure 6.4(g-i) displays the evolution of the mean pore diameter across A, B, and C porosity groups. Porosity evolves in accordance with the rearrangement and

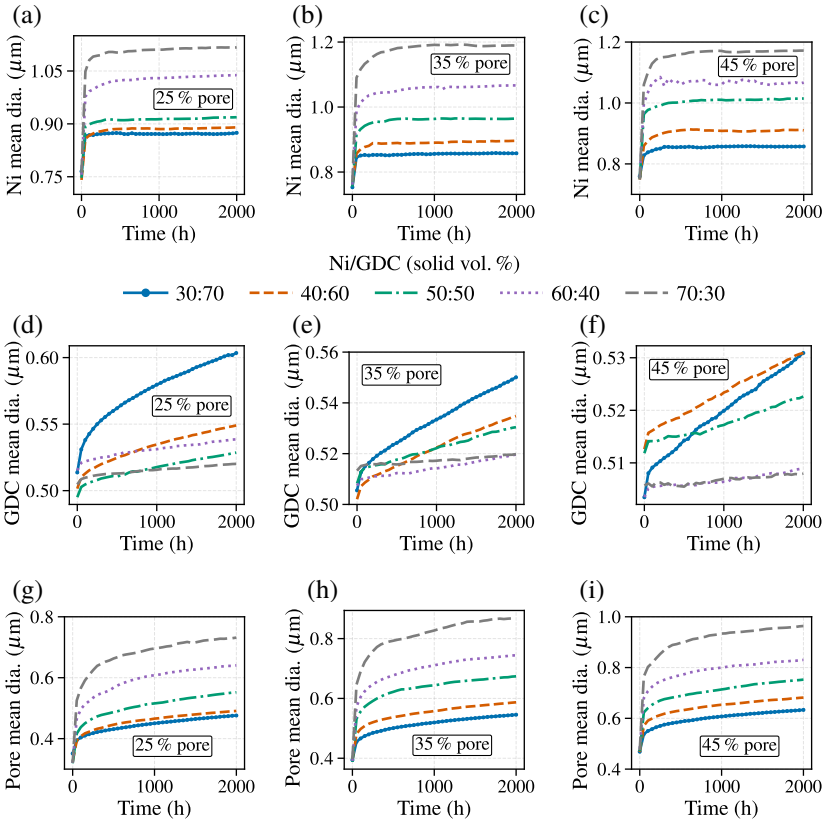


Figure 6.4: Evolution of the mean diameter over 2000 hours of aging from multiphase-field simulations. (a-c) nickel, (d-f) GDC, and (g-i) pore phases at porosity groups of 25 %, 35 %, and 45 %, respectively, across solid volume fractions (solid vol.%) of Ni/GDC.

coalescence of solid particles in the structure. As particle coalescence progresses, the pore network becomes increasingly connected – also reflected in the decreasing pore tortuosity as shown in Figure 6.7(g-i) – resulting in an increasing mean pore size over time. During early aging, pore evolution follows Ni coarsening closely, due to the rapid growth of Ni. In later stages, the continuing, but slower, coarsening of GDC determines the further pore evolution. The largest growth in pore size after 2000 aging hours is observed in A5 at 128.8 % (0.320 µm–0.732 µm), B5 at 119 % (0.397 µm–0.870 µm), and C5 at 102.7 % (0.475 µm–0.963 µm), with pore volume fractions of approximately 25 %, 35 %, and 45 %, respectively. As the porosity varies between groups A, B, and C, their initial pore size distributions also differ correspondingly. As a result, group C, with higher porosity displays the largest absolute pore diameters, while group A of lower porosity exhibits the largest relative pore growth, reflecting substantial enlargement of initially smaller and more restricted pores despite smaller final absolute sizes.

6.4.1 Electrochemical performance-related microstructural properties degradation

TPBs and DPBs evolution The evolution of the total TPB density for porosity groups A, B, and C is shown in Figure 6.5(a-c). In accordance with the rapid coarsening of Ni during early aging, the TPB density decreases sharply at the initial stage and slows down considerably over longer durations. Overall, it can be seen that the TPB evolution shows a qualitatively inverse correlation to the mean Ni and GDC particle diameter evolution. After 2000h of aging, the TPB density decreases by 43.8 %–69.4 % relative to the respective initial values, indicating a significant loss of electrochemical reaction sites and a corresponding degradation in cell performance. At a fixed porosity, a higher Ni solid volume fraction leads to relatively greater TPB degradation and lower absolute TPB densities after aging. Across all porosity groups, the structures with high porosity (group C) exhibit the lowest TPB densities after 2000h of aging, while the structures with low porosity (group A) display comparatively higher values. Considering both the initial TPB density and long-term stability, configurations A2 (29.77 vol.% Ni, 45.33 vol.%

GDC) and A3 (37.60 vol.% Ni, 37.99 vol.% GDC) show the best properties, with TPB densities decreasing from initial values of 4.5 μm^{-2} and 4.98 μm^{-2} to values of 1.87 μm^{-2} and 1.85 μm^{-2}, respectively, after 2000 aging hours. Competing mechanisms of Ni and GDC coarsening in conjunction with wettability or dewetting behavior at Ni/GDC interfaces enhance the complexity of morphological evolution. As demonstrated in Section 4.4.2, interfacial energy configurations in the Ni-GDC-Pore system with wetting behavior can mitigate TPB loss and enhance microstructural stability during long-term operation. Figure 6.6 shows the evolution of the total triple-phase boundary from the initial state to 2000h of aging for selected configurations (A3, B3, C3).

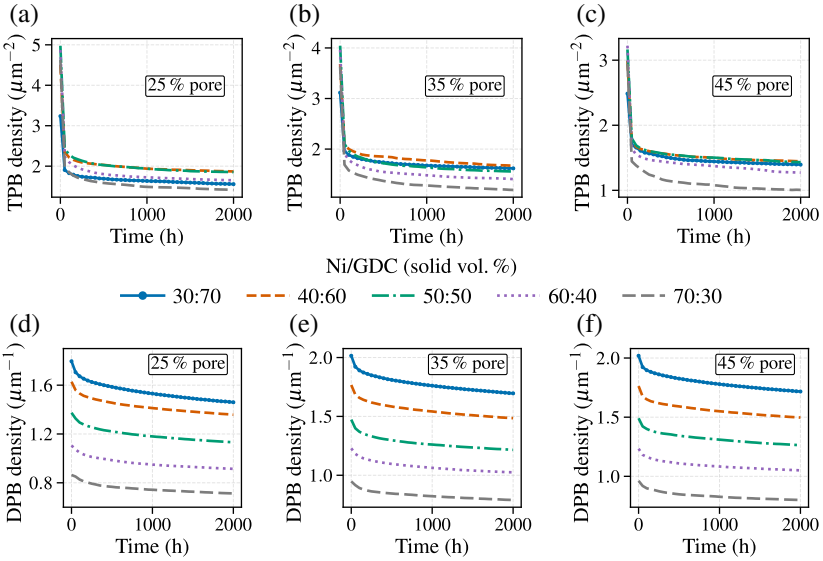


Figure 6.5: Evolution of electrochemical reaction sites over 2000 hours of aging from multiphase-field simulations. (a-c) Total TPB density, (d-f) DPB density at porosity groups of 25 %, 35 %, and 45 %, respectively, across solid volume fractions (solid vol.%) of Ni/GDC.

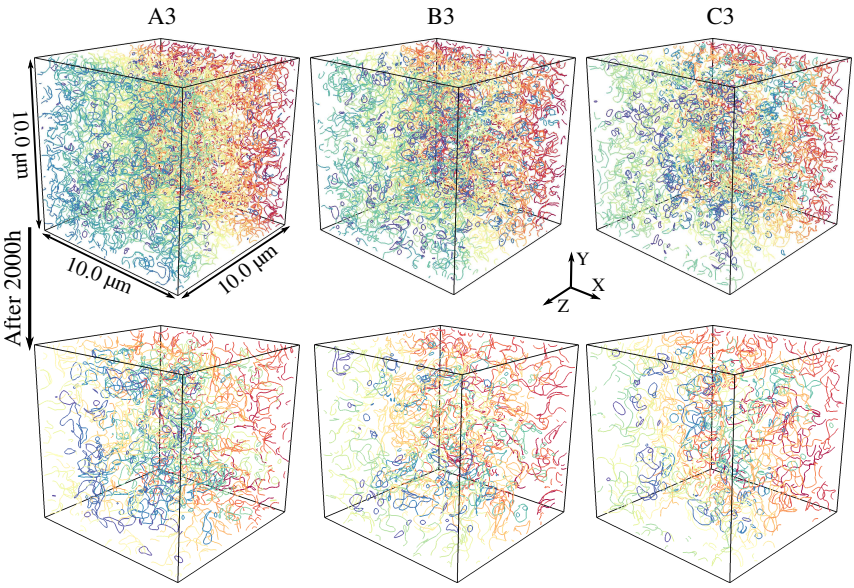


Figure 6.6: Total triple-phase boundary in the initial state and after 2000h of aging for porosity groups of 25 % (A3), 35 % (B3), and 45 % (C3), respectively, from multiphase-field simulations, with color-coded TPB segments.

Figure 6.5(d-f) illustrates the DPB density evolution for porosity groups A, B, and C. Across all configurations, DPB density decreases monotonically with aging, resulting in an overall reduction of 14.6 % to 18.9 % from the initial values after 2000h of aging. Porosity groups B (35 %) and C (45 %) maintain higher and nearly identical DPB densities over the entire aging period, in line with the higher initial values. Within each porosity group, a higher GDC solid fraction is also associated with higher DPB densities after long-term aging. Kishimoto et al. [232] have demonstrated through sensitivity analyses at 700 °C that the electrochemical reaction at the DPB is the rate-limiting step in ceria-based electrodes, indicating that increasing the DPB density is more effective for improving performance than increasing species transport. In accordance with these results, configurations B1 and C1 exhibit the highest DPBs both in their pristine state (2.02 μm^{-1} and

$2.02\,\mu m^{-1}$) and after 2000h of aging ($1.70\,\mu m^{-1}$ and $1.72\,\mu m^{-1}$), implying their preference in terms of both initial performance and long-term stability.

Tortuosities evolution To quantify effective electronic, ionic, and gas transport pathways, the time evolution of the mean tortuosity of the Ni, GDC, and pore phases is presented in Figure 6.7. The evolution of nickel mean tortuosity for porosity groups A, B, and C is shown in Figure 6.7(a-c). Multiple configurations (A1, B1, C1, C2) were not included, as nickel is non-percolating in the initial structures. Configuration C3 (27.58 vol.% Ni, 27.34 vol.% GDC) was initially percolated, with a mean nickel tortuosity of 27.94; however, it becomes non-percolating over aging due to a very high initial directional tortuosity value of 54 in the x-direction. Although percolation persists in the y- and z-directions, the loss of connectivity in the x-direction results in a non-percolated mean value. These results indicate that microstructures with high initial tortuosity values are prone to forming nickel islands, particularly at low nickel volume fractions. Configuration A2 (29.77 vol.% Ni, 45.33 vol.% GDC) exhibits a significant increase in nickel tortuosity from 21.12 to 29.93 after 2000h. In configurations with low Ni and high GDC volume fractions, nickel coarsening can lead to encapsulation of Ni particles by the GDC network in some areas, restricting further coalescence, but forming isolated Ni regions. This significantly increases tortuosity, as electron transport paths must circumnavigate the high density of GDC networks. Such microstructural configurations are highly sensitive to local morphological changes, where minor connectivity losses can cause large tortuosity variations. Increased tortuosity, resulting in an increased isolated Ni volume fraction, is reported in the literature [233]. The increase in tortuosity is most pronounced during early aging, consistent with rapid nickel coarsening, but shows various discontinuities (absent in particle size evolution). It could be due to tortuosity being highly sensitive to local variations in particle connectivity or isolation, unlike volume properties (which are less affected by such local events), where local particle isolation or percolation changes can significantly alter the values.

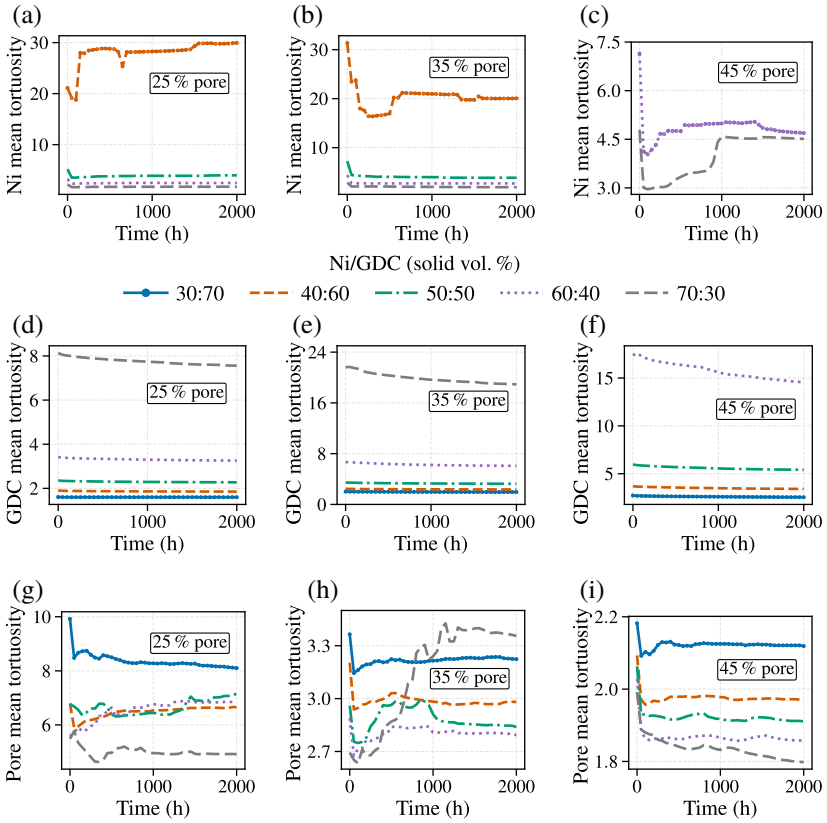


Figure 6.7: Evolution of mean tortuosity over 2000 hours of aging from multiphase-field simulations. (a-c) nickel, (d-f) GDC, and (g-i) pore phases at porosity groups of 25 %, 35 %, and 45 %, respectively, across solid volume fractions (solid vol.%) of Ni/GDC.

Configurations B2 (25.71 vol.% Ni, 39.13 vol.% GDC) and C4 (32.85 vol.% Ni, 21.96 vol.% GDC) show an initial decrease followed by a gradual increase and eventual stabilization of tortuosity. Despite lower nickel content in the B2 structure than in A2, reduced GDC network and higher porosity promote better connectivity initially as particle coalescence starts, but over time, the reduction in particle number and formation of nickel islands could result in increasing tortuosity values. Despite containing a similar nickel content to A2, the C4 structure, with its higher porosity of 45 %, exhibits better initial properties and a similar evolution to the B2 structure. These results demonstrate that nickel tortuosity depends not only on Ni content, but also on GDC fraction and porosity, consistent with prior studies stating that both solid fraction and porosity control percolation thresholds [234]. At higher nickel contents, the correlation is noticeably weaker, and an increasing particle size of Ni does not necessarily result in increased tortuosity of nickel over time. Consistent with previous studies that investigated structures with nickel contents of 20 %, 25 %, and 33 % for the Ni-YSZ system, the high nickel content of 33 % resulted in a tortuosity value that remained nearly invariant over time [130].

Electron transport is often not the rate-limiting process in SOFC anodes and may therefore make Ni tortuosity values seem less critical. In Ni-GDC anodes, the GDC phase also exhibits electronic conductivity, which is one to two orders of magnitude higher than its ionic conductivity, further reducing the likelihood of electron transport limiting electrochemical reactions. Consequently, the distribution of electrochemical activity is primarily determined by ionic conduction rather than electronic transport [210]. From this standpoint, nickel tortuosity may not be a primary design focus in Ni-GDC anodes. In cases where the nickel network becomes non-percolating, the effective electronic conductivity is predominantly controlled by the GDC phase. Nevertheless, the assumption that the entire DPB is electrochemically active remains subject to debate; instead, reactions may be localized around TPB regions. This effect can become more pronounced at lower operating temperatures due to the lower electronic conductivity in the GDC phase. Consequently, higher TPB and DPB densities, together with lower tortuosity of the Ni and GDC phases, may remain desirable in certain cell designs

and operating conditions. Therefore, the sensitivity of electrode performance to all microstructural properties in terms of initial configurations and degradation remains important, as it determines the parameters that need to be prioritized for microstructural optimization. Findings and insights gained from this study are likely to be useful in future efforts to enhance the microstructure of electrodes, as well as in cell-level modeling and TLM for electrochemical performance.

The evolution of GDC tortuosity for porosity groups A, B, and C is depicted in Figure 6.7(d-f). Configuration C5 was excluded due to the initial non-percolating GDC phase. For all other configurations, GDC tortuosity displays only a slight decrease over the aging period, indicating that the ionic and electronic transport pathways remain largely stable with respect to their initial states. Such behavior correlates with the slow coarsening kinetics of GDC, as reflected in only minor increases in the mean particle diameter. While local coalescence of GDC particles occurs, the degree of coalescence remains insufficient to result in particle isolation or loss of percolation. Instead, the low diffusivity and surface energy of GDC promote the formation of smoother, more continuous networks, thereby preserving long-range connectivity over time. Kishimoto et al. [232] investigated the sensitivity of electrode area-specific resistance (ASR) to key microstructural parameters, including DPB density, GDC tortuosity, and mean pore size. Their analysis concluded that ASR is most sensitive to DPB density, with variations spanning nearly two orders of magnitude, while changes in GDC tortuosity and pore size resulted in comparatively small ASR variations within the same order of magnitude. Furthermore, increased DPB density remains the most effective strategy for improving performance, with a 10 % increase in DPB density resulting in a 10 % reduction in ASR. Finally, the increase in GDC tortuosity needs to be limited to prevent an increase in ohmic losses associated with ion conduction.

Based on the aforementioned results, several conclusions could be drawn. In the initial microstructures, GDC volume fractions between 30.52 % and 52.57 % resulted in well-percolated transport networks, with GDC tortuosity dropping from 3.69 to 1.61. Given the role of GDC in electrochemical reactions, as well as ionic and electronic transport pathways, configurations with non-percolating

or low Ni content might still be viable depending on the cell design. In this regard, configurations B1 (19.67 vol.% Ni, 45.28 vol.% GDC), B2 (25.71 vol.% Ni, 39.13 vol.% GDC), and C1 (16.78 vol.% Ni, 38.34 vol.% GDC) prove to be favourable, as they exhibit high initial DPB densities and modest aging degradation (B1: 2.02 to 1.70 μm^{-1}, B2: 1.77 to 1.49 μm^{-1}, C1: 2.02 to 1.72 μm^{-1}) along with low and stable GDC tortuosity (B1: 2.02 to 1.95, B2: 2.46 to 2.36, C1: 2.72 to 2.55). Previous studies have shown that ceria-based electrodes hold the potential to operate as SOFC anodes without a secondary electronic phase. Chueh et al. [22] demonstrated this for single-phase ceria, and Nakamura et al. [207, 235] showed the same for micrometer-sized pure GDC. In addition to DPB density and GDC tortuosity, if Ni-related metrics are prioritized, such as TPB density and Ni tortuosity, configuration B2 may be preferable. Compared to B1 (3.12 to 1.62 μm^{-2}) and C1 (2.49 to 1.40 μm^{-2}), configuration B2 exhibits higher TPB density and lower degradation (3.68 to 1.67 μm^{-2}) in addition to being the only configuration among the three with a percolated Ni network. Nevertheless, simultaneous maximization of both the electrochemical reaction sites (TPBs and DPBs) and minimization of the tortuosity of the Ni and GDC transport networks is difficult, as these microstructural properties are inherently coupled and often compete with each other. Increasing and balancing solid volume fractions of Ni and GDC tends to increase TPB density but is likely to decrease DPB density. Conversely, high GDC volume fractions do not necessarily lead to the highest DPB densities, as limited pore volume could constrain DPB formation. Furthermore, efficient transport generally favors higher volume fractions of each phase, which further competes with the need for substantial interfacial reaction sites.

Figure 6.7(g-i) shows the evolution of pore tortuosity for porosity groups A, B, and C. Group C (45 % porosity), with an already low initial pore tortuosity, shows a moderate but overall decreasing pore tortuosity across all Ni/GDC solid volume fractions with aging. Pore tortuosity correlates well with initial pore size and its evolution, with larger pores promoting improved connectivity and lower tortuosity. These findings are consistent with the phase-field studies by Chen et al. [91], reporting that prolonged coarsening in Ni-YSZ systems can enhance gas transport through the pore phase. In contrast, groups A and B across different

Ni/GDC compositions show rather discontinuous and non-monotonic trends in pore tortuosity. In these systems with lower porosity, the correlation between pore size and tortuosity is noticeably weaker, and an increase in pore size does not necessarily correspond to a reduction in tortuosity over time. This behavior reflects the complex microstructural evolutions of Ni and GDC coarsening and interfacial dynamics, thus making direct correlations between morphological evolution and pore tortuosity less straightforward. Furthermore, microstructures with lower porosity are more sensitive to local particle redistributions occurring during aging than highly porous systems. Overall, pore tortuosity, similar to GDC tortuosity, shows no significant changes during aging across all configurations (except for configuration A1), indicating that gas diffusion pathways remain largely stable compared to their initial state.

6.4.2 Mechanical performance-related effective properties degradation

Evolution of elastic modulus Evolution of elastic properties for porosity groups A, B, and C is shown in Figure 6.8(a-l). All configurations show an overall reduction in elastic properties over aging. An increase in pore size and shape change generally results in a degradation of mechanical strength and a reduction in stiffness. For example, in configuration A1, the effective directional moduli E_{xx}, E_{yy}, and E_{zz} decrease from 83.63, 84.89, and 84.62 GPa to 78.77, 80.27, and 80.39 GPa, respectively, while Hill average elastic modulus E_{Hill} decreases from 84.23 to 79.77 GPa as the mean pore diameter increased from 0.351 to 0.476 µm over 2000h of aging. Figure 6.8(a-c) depicts the evolution of the Hill average elastic modulus E_{Hill} for porosity groups A, B, and C. For all configurations, E_{Hill} shows a pronounced initial decline, corresponding to rapid Ni coarsening in the early stages, followed by a gradual decline or a nearly constant value at longer aging times. The overall reduction in E_{Hill} ranges from 5.30 % to 14.48 %, with the highest deterioration observed in the high porosity group C and the lowest in group A.

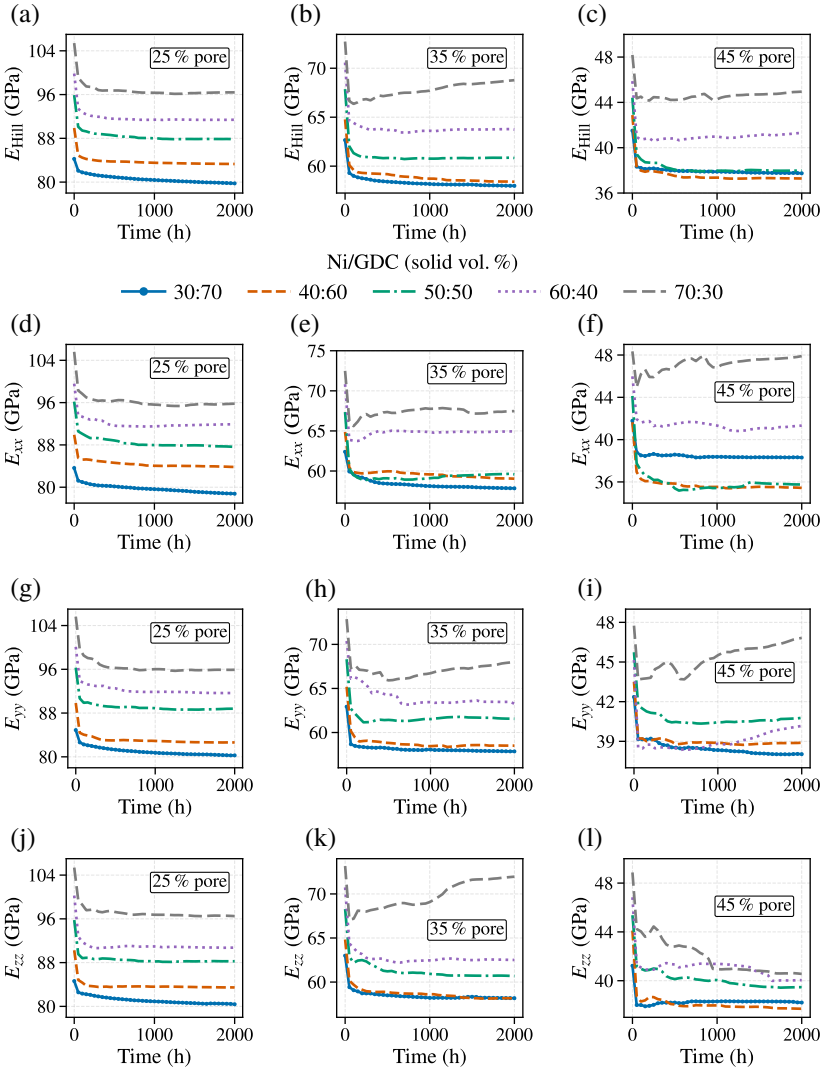


Figure 6.8: Evolution of elastic properties over 2000h of aging from multiphase-field simulations. (a-c) Hill average elastic modulus (E_{Hill}), and effective directional elastic moduli (d-f) E_{xx}, (g-i) E_{yy}, (j-l) E_{zz} for porosity groups of 25 %, 35 %, and 45 %, respectively, across solid volume fractions (solid vol.%) of Ni/GDC.

Figure 6.8(d-l) shows the evolution of the effective directional elastic moduli (E_{xx}, E_{yy}, E_{zz}) for porosity groups A, B, and C. The moduli show a sharp initial decline, followed by a slower decline or near stabilization at later stages, except for configurations B5 and C5, consistent with the trends in the Hill average elastic modulus. The correlation between the increase in mean pore diameter and the reduction in effective directional elastic moduli is weaker for configurations B5 and C5. Although the pore size increases monotonically in these structures, the discontinuous evolution of pore tortuosity in B5 and Ni tortuosity in C5, arising from local particle rearrangements, might strongly influence the evolution of the directional moduli. Overall, the effective directional elastic moduli decrease between 0.9 % and 18.9 % for all configurations. Group C, with high porosity, shows the largest relative decrease, while group A shows the lowest. Configurations with higher Ni content, higher porosity, and less inhibition by the GDC network (e.g., B5 and C5) also display increased anisotropy during aging. In configuration C5, for example, the effective directional elastic moduli decrease by 0.9 %, 1.9 %, and 17 % along the x, y, and z directions, respectively, after 2000h of aging. In the work of Brus et al. [236], it was shown that long-term SOFC operation of a Ni-YSZ anode resulted in strong anisotropy in the anode microstructure. An initially isotropic anode, after prolonged operation of 3800 hours, exhibited strong anisotropy, particularly in the nickel and pore phases of the investigated Ni-YSZ anode. As possible causes for the anisotropies, nickel migration, growth, and coarsening were mentioned. Also, they highlighted the importance of credible numerical simulations of SOFCs accounting for these anisotropies. Liu et al. [115] reported an increase in elastic properties during the sintering stage of Ni-YSZ anode fabrication, as progressive densification resulting in reduced porosity enhances elastic properties with sintering time. The current work demonstrates that during long-term aging of Ni-GDC anodes, microstructural coarsening and pore evolution result in a decrease in elastic properties. Overall, the elastic properties and the evolution of these properties over time are determined by the combined effects of porosity, Ni/GDC volume fractions, pore size and shape, as well as the connectivity of the phases.

Evolution of average von Mises stress and critical volume fraction

Figure 6.9(a-f) shows the evolution of the average von Mises stress and the CVF under the applied stack boundary conditions. As microstructure coarsening progresses, the internal load distribution also changes: Stress concentrations are reduced in areas where sharp curvatures and small features vanish, while other regions carry a larger proportion of the load. These redistributions are also influenced by initial Ni/GDC solid volume fractions, porosity, and the evolution of particle sizes and shapes, and directly affect both overall stress and localized stress concentrations. As shown in Figure 6.9(a-f), the coarsening of the microstructure over aging results in a significant redistribution of local stress fields and large changes in global loading conditions. Consequently, both the average von Mises stress and CVF exhibit similar qualitative trends across configurations.

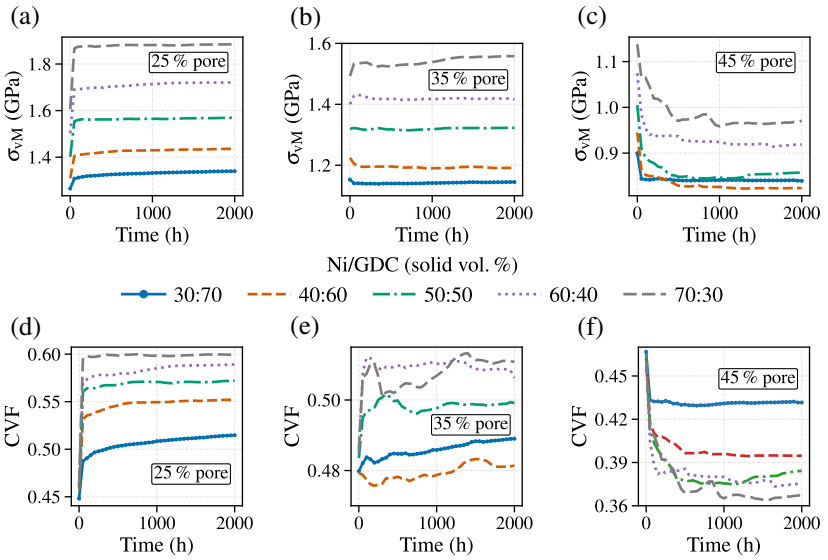


Figure 6.9: Evolution of mechanical response over 2000h of aging from multiphase-field simulations. (a-c) Average von Mises stress, and (d-f) critical volume fraction (CVF) for porosity groups of 25 %, 35 %, and 45 %, respectively, across solid volume fractions (solid vol.%) of Ni/GDC.

In group A (low porosity), both the average von Mises stress and the CVF increase with aging across all Ni/GDC solid volume fractions, indicating an enhancement of thermally induced stresses resulting from the coefficient of thermal expansion (CTE) mismatch between Ni and GDC. These results suggest that high-density Ni-GDC anodes experience elevated stress levels during long-term operation. From a mechanical integrity standpoint, an increase in average von Mises stress, particularly when coupled with an increase in CVF, indicates an overall elevation of the internal stress state and stress concentration within the microstructure. This behavior might be attributed to the high effective stiffness (E_{Hill}) and low porosity of the structures, which strongly constrain the thermal-expansion mismatch and limit stress reduction through pores. In the absence of external mechanical loading, stresses resulting solely from thermal expansion might be determined by competing effects of porosity, stiffness, phase connectivity, and local heterogeneity at the interfaces between Ni/GDC and solid/pores, in addition to the primary CTE mismatch. An increase in the Ni volume fraction further increases the stress levels, as the more rigid Ni phase increasingly restricts GDC deformation. For example, in configuration A5, the average von Mises stress increases from 1.61 to 1.88 GPa over aging. The CVF increases from 46.4 % to 60.0 %, indicating that substantially larger volumes of the microstructure exceed their initial stress threshold. This stress amplification and redistribution caused by coarsening suggest an increased mechanical loading state within the microstructure. Similarly, Xiang et al. [237] simulated thermomechanical stresses arising from the CTE mismatch between Ni and YSZ under operating conditions and external loading. Their results demonstrated that the YSZ volume fraction plays a dominant role in controlling the mechanical strength of the anode, and optimizing the YSZ skeleton during fabrication could significantly improve the resistance to mechanical failure in Ni-YSZ composite anodes.

In the highly porous Ni-GDC anodes of group C, aging enhances stress reduction, as reflected in a systematic reduction in both the average von Mises stress and the CVF across all Ni/GDC compositions. High porosity may promote stress reduction through the pores, allowing the Ni or GDC phase to expand without restriction, and coarsening of the particles under reduced phase constraint might

smooth local stress gradients. As a result, a smaller portion of the microstructure is exposed to stresses above the pristine average. For example, in configuration C5, aging resulted in a decrease in the average von Mises stress from 1.14 to 0.97 GPa, and the corresponding critical volume fraction decreases from 46.0 % to 36.8 %. The decrease in average von Mises stress and CVF over the aging indicates improved tolerance to thermal mismatch strains. However, this improved mechanical stability is achieved at the expense of reduced stiffness (see Figure 6.8) and possibly lower electrochemical performance (see Figure 6.5). Previous studies have highlighted the strong influence of anode composition and porosity on the thermomechanical behavior in SOFC anodes. Celik et al. [238] numerically investigated the stress distributions in porous Ni-YSZ anodes at the microstructural level and demonstrated that increasing the volume fraction of a particular solid phase (Ni or YSZ) stabilizes thermal expansion and reduces thermo-mechanical stress. They further reported that the lowest stress levels occur at high porosity due to stress reduction through the pores.

To further illustrate the local stress redistribution during aging, Figure 6.10 shows representative 3D contour maps of the von Mises stress together with the histograms for configurations A5 and C5 in the initial and 2000h aged states. In all cases, the stress field is strongly heterogeneous, with elevated stresses confined to small localized regions, whereas the majority of the microstructural volume remains at comparatively low stress levels. The histograms are strongly right-skewed, showing that very high stress values occur only with very low probability and therefore contribute only weakly to the volume-averaged stress. Aging shifts the stress distribution differently depending on the volume composition. In the A5 configuration, the distribution shifts toward higher stresses and the maximum local stress increases (from 7.76 GPa to 10.30 GPa), while in C5, the distribution shifts toward lower stresses and the maximum stress increases slightly (from 11.55 GPa to 12.57 GPa). The color scale of the stress contour plots is limited to the range of 0 to 4 GPa to enhance the representation of the dominant stress regime, at which the majority of the distribution density is concentrated. These local stress maps and the histograms show that aging is accompanied by a redistribution of stress within the microstructure, as reflected by the change in the probability distribution

from the initial to the aged state. A few isolated extreme stress values are also observed, likely associated with very thin neck regions, but these occur with very low probability.

Each microstructure exhibits distinct stiffness, phase connectivity, constraint, and thermal load sharing, resulting in different distributions of thermal stresses depending on the Ni/GDC/porosity balance. In group B (intermediate porosity with 35 %), both the average von Mises stress and the CVF remain relatively stable during aging, with only a slight increase observed in the Ni-rich configuration B5 (CVF: 48.6 % to 51.1 %; average von Mises stress: 1.49 to 1.56 GPa). These results suggest that a Ni-GDC anode with intermediate porosity offers a mechanically favorable balance: relatively better stiffness values compared to the high porous group (Figure 6.8) to sustain load-bearing requirements while limiting stress localization and CVF growth. These results provide an understanding of the possible mechanical degradation in the initial configurations of porous Ni-GDC electrode structures over the aging process as a result of thermal expansion-related stresses and the resulting performance losses, degradation of the SOFC. The current work investigates the overall behavior of the mechanical properties and their deterioration resulting from aging-induced complex morphological evolutions of the 3D Ni-GDC SOFC anode. A detailed analysis of the relevant mechanisms and trends with regard to porosity and evolution within specific groups is beyond the scope of the current work. Nevertheless, these findings provide a basis for future research focusing on more comprehensive investigations.

6.5 Interim conclusion

In this Chapter, systematic investigations of fifteen synthetic anode microstructures in the pristine and aged states revealed strong, correlated dependencies of TPB and DPB densities, phase tortuosities, elastic moduli, and stress distributions on Ni and GDC volume fractions and porosity. Considering the initial TPB density and its long-term stability as primary design criteria, configurations A2 (29.77 vol.% Ni, 45.33 vol.% GDC) and A3 (37.60 vol.% Ni, 37.99 vol.% GDC) emerge as the

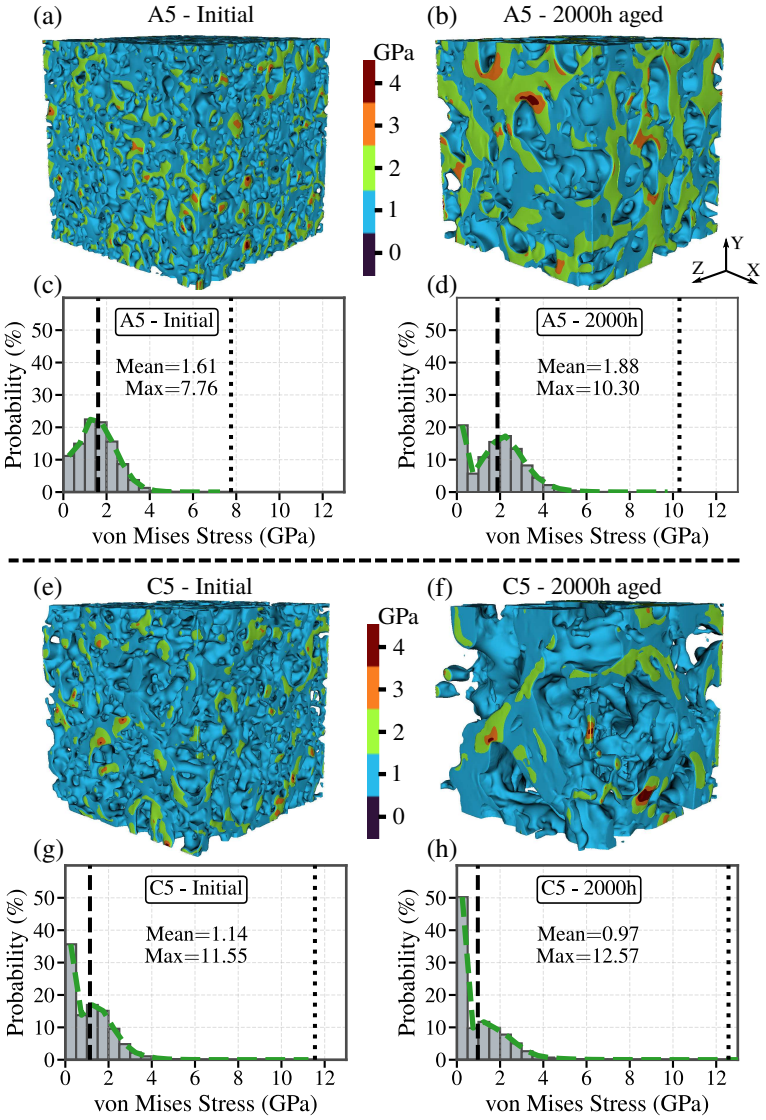


Figure 6.10: Local stress distributions in the initial and 2000h aged microstructures. Contour maps of von Mises stress and stress distributions for the (a-d) A5 and (e-h) C5 configurations.

most promising, exhibiting high initial TPB density accompanied by relatively low degradation after 2000 hours of aging. A3 additionally demonstrated better nickel percolation compared to A2. Given the MIEC nature of GDC and its role in electrochemical activity and transport, configurations with reduced or even non-percolating Ni content may remain viable depending on the cell design. In this context, B1 (19.67 vol.% Ni, 45.28 vol.% GDC), B2 (25.71 vol.% Ni, 39.13 vol.% GDC), and C1 (16.78 vol.% Ni, 38.34 vol.% GDC) configurations offer favorable trade-offs, exhibiting high initial DPB density, relatively low degradation rates, and stable GDC transport pathways. Among these, the B2 configuration provided the best overall performance whilst prioritizing Ni-related metrics, as it incorporated Ni-percolation along with a relatively high TPB density, and reduced degradation.

The effective elastic properties and average von Mises stress decreased linearly with increasing porosity. For all configurations, the effective elastic properties exhibited a pronounced initial decline corresponding to rapid Ni coarsening in the early stages, followed by a gradual decline or near-constant behavior at longer aging times. The coarsening of the microstructure during aging led to a significant redistribution of local stress fields and substantial changes in global stress conditions resulting from thermal eigenstrains. Microstructures with medium porosity (35 %) offered the most balanced mechanical performance by limiting stress localization and critical stress volume fractions during aging. In contrast, anodes with low porosity exhibited increased stress concentrations, while anodes with high porosity showed improved stress tolerance at the expense of lower stiffness and reaction site density values.

Overall, these findings demonstrate that optimal SOFC anode design requires an integrated electrochemical-mechanical performance consideration based on multiple microstructural descriptors rather than a single-metric optimization. The quantitative results presented here provide guidance for selecting Ni and GDC volume fractions tailored to specific cell designs, while the extracted microstructural parameters serve as necessary inputs for transmission line modeling of Ni-GDC-SOFC anodes for cell performance as a function of microstructural composition, as well as for modeling at the cell and stack levels.«

7 Conclusion

7.1 Summary

The current work provides detailed insights into the microstructural degradation and optimization of Ni-GDC anodes under SOFC operating conditions, with the objective of improving the electrochemical performance and mechanical integrity. Furthermore, novel state-of-the-art approaches are presented, including the employment of a Bayesian active learning framework for the identification of unknown physical parameters associated with operating conditions, and a sintering-like morphological coalescence mechanism integrated into the structure generator workflow, enabling the creation of realistic digital twins of Ni-GDC anodes. Three-dimensional multiphase-field simulations are successfully conducted over realistic timescales exceeding a few thousand operating hours, covering the expected lifetime of SOFCs and incorporating various microstructural configurations of the Ni-GDC anode. Both the simulation results and the generated synthetic microstructures are validated against FIB-SEM reconstructed 3D experimental data, demonstrating a high level of morphological detail and the predictive capability of the frameworks.

First, a novel framework was developed to identify the physical parameters required for simulating the aging of Ni-GDC anodes under given operating conditions, employing a multiphase-field method. This framework combines Bayesian active learning with pristine and aged FIB-SEM reconstructed 3D microstructures, coupled with phase-field coarsening simulations. The active learning framework was initially validated using two-dimensional reference structures and corresponding phase-field coarsening simulations, demonstrating its reliability and

effectiveness. Following this validation, the framework was extended to 3D FIB-SEM reconstructed Ni-GDC anode microstructures. The results showed that single-objective optimization, targeting an individual microstructural descriptor, is insufficient to accurately capture the overall morphology, as significant deviations arise in other critical descriptive parameters. In contrast, a multi-objective optimization technique based on a weighted sum scalarization approach provided significantly improved results, achieving an overall error of approximately 7 %–8 %. Through comparison with available physical parameters and data from the literature, consistent and representative parameters were obtained for the aging simulations of the Ni-GDC anode under the given operating conditions. Although the current work focuses on the Ni-GDC anode system, the framework can be readily transferable to other SOFC material systems, such as the widely used Ni-YSZ anodes.

In the subsequent analysis, quantitative simulations of nickel and GDC coarsening in SOFC anodes were conducted using both pristine and pre-aged reference microstructures to evaluate the predictive capability of the phase-field model under varying initial conditions. This multi-faceted approach enabled robust validation of the phase-field model, essential for the reliable prediction and optimization of long-term SOFC performance. Validation against experimental data showed good agreement for most microstructural properties. Commercial viability of SOFCs requires operating lifetimes of more than 40,000h (up to 80,000h), and conducting experimental aging studies over such a long duration is extremely resource-intensive and time-consuming. Large-scale simulations were performed using an optimized, vectorized solver for up to 60,000h, enabling an efficient analysis of time-dependent microstructural evolution and property changes. Furthermore, investigations on the influence of surface and interfacial energies under different thermodynamic equilibrium conditions showed the wettability as a decisive factor in the degradation processes: Low nickel contact angles suppress nickel coarsening, while low GDC contact angles enhance long-term nickel stability. The predictive capabilities and limitations of the model were also discussed.

Accurately reproducing the complex sintered microstructures of SOFC anodes remains a challenge. In this study, an extended structure generator workflow was employed, which includes a computationally efficient, sintering-like morphological coalescence step based on a modified Allen-Cahn formulation, along with a correction term controlling curvature minimization, to create realistic digital twins of Ni-GDC anodes. The generated synthetic structure was rigorously validated against a FIB-SEM 3D reconstruction using seventeen quantitative descriptors, which resulted in a low global error (mean absolute percentage error of 4.92 %) and demonstrated high accuracy across geometric, transport, and mechanical properties. Furthermore, statistical analysis of ten microstructures generated independently under identical conditions (as in the validation case) showed low variability (coefficient of variation of about 1 %–3 %), confirming the robustness and reproducibility of the structure generation method. The strong agreement established the synthetic structures as reliable digital twins, enabling subsequent sensitivity analyses and correlations between microstructure and properties for electrode optimization.

Initial phase volume fractions and particle sizes play a key role in governing the electrochemical and mechanical performance of Ni-GDC anodes. In this work, comprehensive degradation investigations were performed by combining realistic synthetic microstructure generation with large-scale aging simulations, enabling an integrated analysis of electrochemical descriptors and mechanical properties. The results provide detailed insights into the design of anode microstructures by highlighting trade-offs between initial and aging-induced electrochemical and mechanical behavior. Based on the initial TPB density and its long-term stability, a configuration containing approximately 37.6 vol.% Ni and 38.0 vol.% GDC exhibited high initial performance with a relatively low degradation rate. Given the MIEC nature of GDC, the configuration with approximately 25.7 vol.% Ni and 39.1 vol.% GDC offered the best overall performance, with Ni-related metrics in the foreground. Furthermore, microstructures with intermediate porosity (about 35 %) exhibited the most balanced mechanical behavior, while lower and higher porosities led to increased stress concentrations and reduced functional performance, respectively. Overall, these results demonstrate that an optimal design

of the Ni-GDC SOFC anode requires an integrated electrochemical-mechanical approach based on multiple microstructural descriptors, rather than single-metric optimization. The results provide quantitative guidelines for selecting Ni and GDC volume fractions tailored to specific cell designs, as well as for modeling at the cell and stack levels.

7.2 Outlook

This Section outlines potential directions for future work, focusing on the open questions and challenges that have emerged from this research, as well as on how future studies might further advance the contributions presented in this dissertation.

Beyond the scalarization-based approach adopted in this work, alternative multi-objective optimization methods could be investigated further. Although the multi-objective weighted sum scalarization approach employed in this work provided an optimized parameter set consistent with the available literature, further refinement through Pareto-based multi-objective approaches (e.g., evolutionary algorithms) could improve the accuracy of the parameters. Such approaches might better account for the cases of interdependent or inversely related material properties.

Future work could further extend the phase-field model framework by incorporating additional degradation mechanisms relevant to the long-term operation of the electrode, such as evaporation-condensation processes and GDC migration under polarization conditions. Incorporating these mechanisms, together with experimentally determined input parameters and validation data, would further improve the model's predictions across a wider range of operating conditions. Furthermore, spatial variations in wettability due to oxygen partial pressure gradients, particularly in thicker electrodes, would be an interesting direction for further investigation. With the availability of experimental data on wettability distributions in Ni-GDC anodes, the current framework can be extended to account

for spatially dependent wettability behavior and provide a more comprehensive understanding of Ni-GDC redistribution and degradation.

At the microstructural level, extending the framework to incorporate anisotropic interfacial properties and grain boundary effects could be an interesting direction for further research. Incorporating crystallographic orientation information and orientation-dependent parameters, such as grain boundary energies and diffusion coefficients, supported by detailed reconstructed microstructures and experimental measurements could enable a more comprehensive modeling of microstructural evolution. In conjunction with large-scale simulations, these developments could provide further insights into the influence of grain boundaries in the anode degradation process.

From an optimization standpoint, extending the framework to include particle size effects and evaluating their impact on both the initial performance and the long-term degradation of SOFC electrodes can provide further insights into structure-property relations. Additionally, further detailed investigation into the evolution of mechanical behavior, including the modeling of crack formation and delamination at the anode-electrolyte interface, particularly in relation to porosity and aging-induced morphological changes in Ni-GDC anodes, would provide new insights into the mechanical failures of SOFCs.

Bibliography

[1] UN Climate Change, "UN climate change conferences - United Arab Emirates." https://unfccc.int/sites/default/files/resource/cma2023_L17_adv.pdf. Accessed: 2026-07-22.

[2] Federal Ministry for Economic Affairs and Climate Action (BMWK), "Federal Climate Action Act." https://www.gesetze-im-internet.de/englisch_ksg/englisch_ksg.html. Accessed: 2026-07-22.

[3] A. B. Stambouli and E. Traversa, "Solid oxide fuel cells (SOFCs): a review of an environmentally clean and efficient source of energy," *Renewable and sustainable energy reviews*, vol. 6, no. 5, pp. 433–455, 2002.

[4] A. Hauch, S. D. Ebbesen, S. H. Jensen, and M. Mogensen, "Highly efficient high temperature electrolysis," *Journal of Materials Chemistry*, vol. 18, no. 20, pp. 2331–2340, 2008.

[5] S. C. Singhal, "Advances in solid oxide fuel cell technology," *Solid State Ionics*, vol. 135, no. 1-4, pp. 305–313, 2000.

[6] Federal Ministry for Economic Affairs and Climate Action (BMWK), "National Hydrogen Strategy." https://www.bmwk.de/Redaktion/EN/Publikationen/Energie/the-national-hydrogen-strategy.pdf?__blob=publicationFile&v=6. Accessed: 2026-07-22.

[7] S. Dorregaray-Oyaregui, C. Martín-Gómez, and M. Aguado, "Installation of fuel cells in building in use: Technical, regulatory, and economic

feasibility," *Energy Conversion and Management: X*, vol. 22, p. 100536, 2024.

[8] D. Manzo, R. Thai, H. T. Le, and G. K. Venayagamoorthy, "Fuel cell technology review: Types, economy, applications, and vehicle-to-grid scheme," *Sustainable Energy Technologies and Assessments*, vol. 75, p. 104229, 2025.

[9] Z. Zhang, H. Du, K. Xu, X. Zhang, X. Ma, and S. Shuai, "Review of the Application of Metal-Supported Solid Oxide Fuel Cell in the Transportation Field," *Automotive Innovation*, vol. 8, no. 2, pp. 443–471, 2025.

[10] K. Huang and S. C. Singhal, "Cathode-supported tubular solid oxide fuel cell technology: A critical review," *Journal of Power Sources*, vol. 237, pp. 84–97, 2013.

[11] T. Nakao, S. Inoue, S. Uenoyama, Y. Takuwa, and M. Suzuki, "Progress of SOFC residential CHP system: Over 50,000 units market experience of Osaka Gas," *Electrochemical Society Transactions*, vol. 91, no. 1, pp. 43–49, 2019.

[12] Y. Wang, J. Shi, X. Gu, O. Deutschmann, Y. Shi, and N. Cai, "Toward mobility of solid oxide fuel cells," *Progress in Energy and Combustion Science*, vol. 102, p. 101141, 2024.

[13] U.S. Department of Energy - Energy Efficiency & Renewable Energy: Fuel Cell Technologies Office, "Comparison of fuel cell technologies," 2016.

[14] S. Dierickx, *Charakterisierung, Modellentwicklung und Simulation von mehrschichtigen Brenngaselektroden in Festoxid-Brennstoffzellen*, vol. 38. KIT Scientific Publishing, 2019.

[15] D. Dees, T. D. Claar, T. Easler, D. Fee, and F. Mrazek, "Conductivity of Porous Ni/ZrO2-Y2O3 Cermets," *Journal of the Electrochemical Society*, vol. 134, no. 9, pp. 2141–2146, 1987.

[16] J.-H. Lee, H. Moon, H.-W. Lee, J. Kim, J.-D. Kim, and K.-H. Yoon, "Quantitative analysis of microstructure and its related electrical property of SOFC anode, Ni–YSZ cermet," *Solid State Ionics*, vol. 148, no. 1-2, pp. 15–26, 2002.

[17] B. C. H. Steele and A. Heinzel, "Materials for Fuel-Cell Technologies," *Nature*, vol. 414, no. 6861, pp. 345–352, 2001.

[18] A. J. Samson, M. Søgaard, and P. V. Hendriksen, "Model for solid oxide fuel cell cathodes prepared by infiltration," *Electrochimica Acta*, vol. 229, pp. 73–95, 2017.

[19] J. Zhang, C. Lenser, N. H. Menzler, and O. Guillon, "Comparison of solid oxide fuel cell (SOFC) electrolyte materials for operation at 500 °C," *Solid State Ionics*, vol. 344, p. 115138, 2020.

[20] N. Jaiswal, K. Tanwar, R. Suman, D. Kumar, S. Upadhyay, and O. Parkash, "A brief review on ceria based solid electrolytes for solid oxide fuel cells," *Journal of Alloys and Compounds*, vol. 781, pp. 984–1005, 2019.

[21] C. Zhang, M. E. Grass, A. H. McDaniel, S. C. DeCaluwe, F. E. Gabaly, Z. Liu, K. F. McCarty, R. L. Farrow, M. A. Linne, Z. Hussain, G. S. Jackson, H. Bluhm, and B. W. Eichhorn, "Measuring fundamental properties in operating solid oxide electrochemical cells by using in situ X-ray photoelectron spectroscopy," *Nature Materials*, vol. 9, no. 11, pp. 944–949, 2010.

[22] W. C. Chueh, Y. Hao, W. Jung, and S. M. Haile, "High electrochemical activity of the oxide phase in model ceria-Pt and ceria-Ni composite anodes," *Nature Materials*, vol. 11, no. 2, pp. 155–161, 2012.

[23] W. C. Chueh and S. M. Haile, "Electrochemical studies of capacitance in cerium oxide thin films and its relationship to anionic and electronic defect densities," *Physical Chemistry Chemical Physics*, vol. 11, no. 37, pp. 8144–8148, 2009.

[24] N. Q. Minh, "Ceramic fuel cells," *Journal of the American Ceramic Society*, vol. 76, no. 3, pp. 563–588, 1993.

[25] S. Uhlenbruck, N. Jordan, D. Sebold, H. Buchkremer, V. Haanappel, and D. Stöver, "Thin film coating technologies of (Ce, Gd) O2-δ interlayers for application in ceramic high-temperature fuel cells," *Thin Solid Films*, vol. 515, no. 7-8, pp. 4053–4060, 2007.

[26] A. Mai, V. A. Haanappel, F. Tietz, and D. Stöver, "Ferrite-based perovskites as cathode materials for anode-supported solid oxide fuel cells: Part II. Influence of the CGO interlayer," *Solid State Ionics*, vol. 177, no. 19-25, pp. 2103–2107, 2006.

[27] K. N. Grew and W. K. Chiu, "A review of modeling and simulation techniques across the length scales for the solid oxide fuel cell," *Journal of Power Sources*, vol. 199, pp. 1–13, 2012.

[28] M. E. Khan and F. Khan, "A comparative study of white box, black box and grey box testing techniques," *International Journal of Advanced Computer Science and Applications*, vol. 3, no. 6, 2012.

[29] J. P. Stempien, Q. Sun, and S. H. Chan, "Solid Oxide Electrolyzer Cell Modeling: A Review.," *Journal of Power Technologies*, vol. 93, no. 4, 2013.

[30] Z. Li, H. Zhang, H. Xu, and J. Xuan, "Advancing the multiscale understanding on solid oxide electrolysis cells via modelling approaches: A review," *Renewable and Sustainable Energy Reviews*, vol. 141, p. 110863, 2021.

[31] A. J. Cohen, P. Mori-Sánchez, and W. Yang, "Challenges for density functional theory," *Chemical Reviews*, vol. 112, no. 1, pp. 289–320, 2012.

[32] X. Zhao and Y. Liu, "Unveiling the active structure of single nickel atom catalysis: critical roles of charge capacity and hydrogen bonding," *Journal of the American chemical society*, vol. 142, no. 12, pp. 5773–5777, 2020.

[33] J. Morin and J. M. Pelletier, *Density functional theory: Principles, applications and analysis*. Nova Science Publishers, Incorporated, 2013.

[34] D. Marx and J. Hutter, *Ab initio molecular dynamics: basic theory and advanced methods*. Cambridge University Press, 2009.

[35] H. Brinkman, W. J. Briels, and H. Verweij, "Molecular dynamics simulations of yttria-stabilized zirconia," *Chemical physics letters*, vol. 247, no. 4-6, pp. 386–390, 1995.

[36] H. Inaba, R. Sagawa, H. Hayashi, and K. Kawamura, "Molecular dynamics simulation of gadolinia-doped ceria," *Solid State Ionics*, vol. 122, no. 1-4, pp. 95–103, 1999.

[37] Y. Sun, C. Wang, and Y. Chen, "Molecular dynamics simulations of the deformation behavior of gadolinia-doped ceria solid electrolytes under tensile loading," *Journal of Power Sources*, vol. 233, pp. 131–138, 2013.

[38] P. K. Schelling and S. R. Phillpot, "Mechanism of thermal transport in zirconia and yttria-stabilized zirconia by molecular-dynamics simulation," *Journal of the American Ceramic Society*, vol. 84, no. 12, pp. 2997–3007, 2001.

[39] M. Ni and T. S. Zhao, *Solid oxide fuel cells: from materials to system modeling*, vol. 7. Royal society of chemistry, 2013.

[40] A. Satoh, *Introduction to practice of molecular simulation: molecular dynamics, Monte Carlo, Brownian dynamics, Lattice Boltzmann and dissipative particle dynamics*. Elsevier, 2010.

[41] D. S. Gunn, J. A. Purton, and S. Metz, "Monte carlo simulations of gadolinium doped ceria surfaces," *Solid State Ionics*, vol. 324, pp. 128–137, 2018.

[42] R. Krishnamurthy, Y.-G. Yoon, D. Srolovitz, and R. Car, "Oxygen diffusion in yttria-stabilized zirconia: a new simulation model," *Journal of the American Ceramic Society*, vol. 87, no. 10, pp. 1821–1830, 2004.

[43] X. Yang, G. Yang, S. Li, Q. Shen, H. Miao, and J. Yuan, "Application and development of the Lattice Boltzmann modeling in pore-scale electrodes of solid oxide fuel cells," *Journal of Power Sources*, vol. 599, p. 234071, 2024.

[44] M. Rahimi Takami, D. Domiri Ganji, M. Aghajani Delavar, and S. Bozorgmehri, "A parametric study of the heat and mass diffusion dimensionless parameter in SOFC with DIR by lattice Boltzmann method," *Journal of Thermal Analysis and Calorimetry*, vol. 146, no. 6, pp. 2639–2653, 2021.

[45] W. Chiu, A. Joshi, and K. Grew, "Lattice boltzmann model for multi-component mass transfer in a solid oxide fuel cell anode with heterogeneous internal reformation and electrochemistry," *The European Physical Journal Special Topics*, vol. 171, no. 1, pp. 159–165, 2009.

[46] T. Nagasawa and K. Hanamura, "Prediction of overpotential and effective thickness of Ni/YSZ anode for solid oxide fuel cell by improved species territory adsorption model," *Journal of Power Sources*, vol. 353, pp. 115–122, 2017.

[47] N. Shikazono, D. Kanno, K. Matsuzaki, H. Teshima, S. Sumino, and N. Kasagi, "Numerical assessment of SOFC anode polarization based on three-dimensional model microstructure reconstructed from FIB-SEM images," *Journal of The Electrochemical Society*, vol. 157, no. 5, pp. B665–B672, 2010.

[48] S. Liu, S. Liu, L. C. Saha, A. M. Iskandarov, Z. Jiao, S. Hara, T. Ishimoto, T. Tada, Y. Umeno, N. Shikazono, *et al.*, "Multi-scale, multi-physics approach for solid oxide fuel cell anode reaction," *Electrochemical Society Transactions sofc2017*, vol. 78, no. 1, pp. 2835–2844, 2017.

[49] P. A. Cundall and O. D. Strack, "A discrete numerical model for granular assemblies," *Geotechnique*, vol. 29, no. 1, pp. 47–65, 1979.

[50] A. Bezrukov, M. Bargieł, and D. Stoyan, "Statistical analysis of simulated random packings of spheres," *Particle & Particle Systems Characterization: Measurement and Description of Particle Properties and Behavior in Powders and Other Disperse Systems*, vol. 19, no. 2, pp. 111–118, 2002.

[51] X. Liu, C. L. Martin, G. Delette, J. Laurencin, D. Bouvard, and T. Delahaye, "Microstructure of porous composite electrodes generated by the discrete element method," *Journal of Power Sources*, vol. 196, no. 4, pp. 2046–2054, 2011.

[52] L. C. R. Schneider, C. L. Martin, Y. Bultel, D. Bouvard, and E. Siebert, "Discrete modelling of the electrochemical performance of SOFC electrodes," *Electrochimica acta*, vol. 52, no. 1, pp. 314–324, 2006.

[53] X. Liu, C. L. Martin, G. Delette, and D. Bouvard, "Elasticity and strength of partially sintered ceramics," *Journal of the Mechanics and Physics of Solids*, vol. 58, no. 6, pp. 829–842, 2010.

[54] Q. Li, L. Liang, K. Gerdes, and L.-Q. Chen, "Phase-field modeling of three-phase electrode microstructures in solid oxide fuel cells," *Applied Physics Letters*, vol. 101, no. 3, p. 33909, 2012.

[55] Z. Jiao and N. Shikazono, "Simulation of nickel morphological and crystal structures evolution in solid oxide fuel cell anode using phase field method," *Journal of The Electrochemical Society*, vol. 161, no. 5, pp. F577–F582, 2014.

[56] Z. Jiao and N. Shikazono, "Simulation of the reduction process of solid oxide fuel cell composite anode based on phase field method," *Journal of Power Sources*, vol. 305, pp. 10–16, 2016.

[57] L.-Q. Chen, "Phase-field models for microstructure evolution," *Annual review of materials research*, vol. 32, no. 1, pp. 113–140, 2002.

[58] Z. Hong and V. Viswanathan, "Open-sourcing phase-field simulations for accelerating energy materials design and optimization," *ACS Energy Letters*, vol. 5, no. 10, pp. 3254–3259, 2020.

[59] E. Johnson and S. Haussener, "Contrasting views of the electric double layer in electrochemical CO2 reduction: continuum models vs molecular dynamics," *The Journal of Physical Chemistry C*, vol. 128, no. 25, pp. 10450–10464, 2024.

[60] M. S. Kilic, M. Z. Bazant, and A. Ajdari, "Steric effects in the dynamics of electrolytes at large applied voltages. II. Modified Poisson-Nernst-Planck equations," *Physical Review E—Statistical, Nonlinear, and Soft Matter Physics*, vol. 75, no. 2, p. 021503, 2007.

[61] K. Hu, B. Li, Z. Tian, and L. Chen, "Multiscale Simulation in Fuel Cell and Electrolyzer Systems: a Review of Methods, Applications, and Future Prospects," *Sustainable Engineering Novit*, vol. 1, p. 5, 2025.

[62] Z. Wu, P. Zhu, Y. Huang, J. Yao, F. Yang, Z. Zhang, and M. Ni, "A comprehensive review of modeling of solid oxide fuel cells: from large systems to fine electrodes," *Chemical Reviews*, vol. 125, no. 4, pp. 2184–2268, 2025.

[63] C. Bao, Y. Shi, E. Croiset, C. Li, and N. Cai, "A multi-level simulation platform of natural gas internal reforming solid oxide fuel cell–gas turbine hybrid generation system: Part I. Solid oxide fuel cell model library," *Journal of Power Sources*, vol. 195, no. 15, pp. 4871–4892, 2010.

[64] S. Kang and K.-Y. Ahn, "Dynamic modeling of solid oxide fuel cell and engine hybrid system for distributed power generation," *Applied energy*, vol. 195, pp. 1086–1099, 2017.

[65] L. Ma, X. Ru, and Z. Lin, "Theoretical model and control-parameter classification analysis for solid oxide fuel cell systems with cooling air bypass into burner," *Journal of Power Sources*, vol. 606, p. 234572, 2024.

[66] T. Takahashi, T. Ikeda, K. Murata, O. Hotaka, S. Hasegawa, Y. Tachikawa, M. Nishihara, J. Matsuda, T. Kitahara, S. M. Lyth, *et al.*, "Accelerated durability testing of fuel cell stacks for commercial automotive applications: a case study," *Journal of the electrochemical Society*, vol. 169, no. 4, p. 044523, 2022.

[67] T. Mou, H. S. Pillai, S. Wang, M. Wan, X. Han, N. M. Schweitzer, F. Che, and H. Xin, "Bridging the complexity gap in computational heterogeneous catalysis with machine learning," *Nature Catalysis*, vol. 6, no. 2, pp. 122–136, 2023.

[68] D. Su, J. Zheng, J. Ma, Z. Dong, Z. Chen, and Y. Qin, "Application of machine learning in fuel cell research," *Energies*, vol. 16, no. 11, p. 4390, 2023.

[69] L. Duan, Z. Yan, Z. Pan, and Z. Zhong, "Microstructure-informed performance boost in solid oxide fuel cells through multiphysical modeling and machine learning," *Journal of Materials Chemistry A*, vol. 13, no. 34, pp. 28471–28482, 2025.

[70] D. W. Joh, M. K. Rath, J. W. Park, J. H. Park, K. H. Cho, S. Lee, K. J. Yoon, J.-H. Lee, and K. T. Lee, "Sintering behavior and electrochemical performances of nano-sized gadolinium-doped ceria via ammonium carbonate assisted co-precipitation for solid oxide fuel cells," *Journal of Alloys and Compounds*, vol. 682, pp. 188–195, 2016.

[71] J. R. Wilson, W. Kobsiriphat, R. Mendoza, H.-Y. Chen, J. M. Hiller, D. J. Miller, K. Thornton, P. W. Voorhees, S. B. Adler, and S. A. Barnett, "Three-dimensional reconstruction of a solid-oxide fuel-cell anode," *Nature materials*, vol. 5, no. 7, pp. 541–544, 2006.

[72] S. Jang, Y. Kang, K. T. Bae, S. H. Park, Y. J. Park, D. Kim, H. Yu, H. Kim, S. Yu, and K. T. Lee, "Digital Twin of Solid Oxide Electrochemical Cells: From 3D Microstructure Reconstruction to Multiphysics Modeling," *Advanced Energy Materials*, vol. 15, no. 47, p. e03842, 2025.

[73] T. Kanit, S. Forest, I. Galliet, V. Mounoury, and D. Jeulin, “Determination of the size of the representative volume element for random composites: statistical and numerical approach,” *International Journal of solids and structures*, vol. 40, no. 13-14, pp. 3647–3679, 2003.

[74] R. K. Jeela, M. Ahmad, M. Wieler, Y. Liu, M. Juckel, D. Schneider, A. Weber, N. H. Menzler, and B. Nestler, “Multiphase-Field Simulation Studies of Coarsening in Ni-GDC SOFC Anode Microstructures and the Effect of Interfacial Energies,” *ACS Applied Energy Materials*, vol. 8, no. 24, pp. 17670–17687, 2025.

[75] K. Haga, S. Adachi, Y. Shiratori, K. Itoh, and K. Sasaki, “Poisoning of SOFC anodes by various fuel impurities,” *Solid State Ionics*, vol. 179, no. 27-32, pp. 1427–1431, 2008.

[76] J.-M. Klein, S. Georges, and Y. Bultel, “Modeling of a SOFC fueled by methane: anode barrier to allow gradual internal reforming without coking,” *Journal of The Electrochemical Society*, vol. 155, no. 4, p. B333, 2008.

[77] B. Iwanschitz, J. Sfeir, A. Mai, and M. Schütze, “Degradation of SOFC anodes upon redox cycling: a comparison between Ni/YSZ and Ni/CGO,” *Journal of The Electrochemical Society*, vol. 157, no. 2, p. B269– B278, 2010.

[78] T. Klemensø and M. Mogensen, “Ni–YSZ solid oxide fuel cell anode behavior upon redox cycling based on electrical characterization,” *Journal of the American Ceramic Society*, vol. 90, no. 11, pp. 3582–3588, 2007.

[79] D. Sarantaridis and A. Atkinson, “Redox cycling of Ni-based solid oxide fuel cell anodes: a review,” *Fuel cells*, vol. 7, no. 3, pp. 246–258, 2007.

[80] A. Faes, A. Hessler-Wyser, D. Presvytes, C. Vayenas, and J. Van Herle, “Nickel–zirconia anode degradation and triple phase boundary quantification from microstructural analysis,” *Fuel cells*, vol. 9, no. 6, pp. 841–851, 2009.

[81] B. Iwanschitz, L. Holzer, A. Mai, and M. Schütze, "Nickel agglomeration in solid oxide fuel cells: The influence of temperature," *Solid State Ionics*, vol. 211, pp. 69–73, 2012.

[82] Z. Jiao and N. Shikazono, "Study on the effects of polarization on local morphological change of nickel at active three-phase-boundary using patterned nickel-film electrode in solid oxide fuel cell anode," *Acta Materialia*, vol. 135, pp. 124–131, 2017.

[83] A. Zekri, M. Knipper, J. Parisi, and T. Plaggenborg, "Microstructure degradation of Ni/CGO anodes for solid oxide fuel cells after long operation time using 3D reconstructions by FIB tomography," *Physical Chemistry Chemical Physics*, vol. 19, no. 21, pp. 13767–13777, 2017.

[84] Q. Fang, C. E. Frey, N. H. Menzler, and L. Blum, "Electrochemical performance and preliminary post-mortem analysis of a solid oxide cell stack with 20,000 h of operation," *Journal of The Electrochemical Society*, vol. 165, no. 2, p. F38– F45, 2018.

[85] M. Trini, A. Hauch, S. De Angelis, X. Tong, P. V. Hendriksen, and M. Chen, "Comparison of microstructural evolution of fuel electrodes in solid oxide fuel cells and electrolysis cells," *Journal of Power Sources*, vol. 450, p. 227599, 2020.

[86] L. Holzer, B. Iwanschitz, T. Hocker, B. Münch, M. Prestat, D. Wiedenmann, U. Vogt, P. Holtappels, J. Sfeir, A. Mai, and T. Graule, "Microstructure degradation of cermet anodes for solid oxide fuel cells: Quantification of nickel grain growth in dry and in humid atmospheres," *Journal of Power Sources*, vol. 196, no. 3, pp. 1279–1294, 2011.

[87] Z. Ouyang, Y. Komatsu, A. Sciazko, J. Onishi, K. Nishimura, and N. Shikazono, "Operando observations of active three phase boundary of patterned nickel-yttria stabilized zirconia electrode in solid oxide cell," *Journal of Power Sources*, vol. 529, p. 231228, 2022.

[88] Y. Komatsu, A. Sciazko, Y. Suzuki, Z. Ouyang, Z. Jiao, and N. Shikazono, "Operando observation of patterned nickel-gadolinium doped ceria solid oxide fuel cell anode," *Journal of Power Sources*, vol. 516, p. 230670, 2021.

[89] Y. Liu, F. Wankmüller, T. P. Lehnert, M. Juckel, N. H. Menzler, and A. Weber, "Microstructural changes in nickel-ceria fuel electrodes at elevated temperature," *Fuel Cells*, vol. 23, no. 6, pp. 430–441, 2023.

[90] R. K. Jeela, A. Elmoghazy, L. Schöller, M. Wieler, A. Prahs, D. Schneider, and B. Nestler, "Effect of volume fractions and aging on Ni-GDC SOFC anode degradation and performance: multiphase-field simulations," *npj Materials Degradation*, 2026.

[91] H.-Y. Chen, H.-C. Yu, J. S. Cronin, J. R. Wilson, S. A. Barnett, and K. Thornton, "Simulation of coarsening in three-phase solid oxide fuel cell anodes," *Journal of Power Sources*, vol. 196, no. 3, pp. 1333–1337, 2011.

[92] R. Davis, F. Abdeljawad, J. Lillibridge, and M. Haataja, "Phase wettability and microstructural evolution in solid oxide fuel cell anode materials," *Acta Materialia*, vol. 78, pp. 271–281, 2014.

[93] F. Abdeljawad, B. Völker, R. Davis, R. M. McMeeking, and M. Haataja, "Connecting microstructural coarsening processes to electrochemical performance in solid oxide fuel cells: An integrated modeling approach," *Journal of Power Sources*, vol. 250, pp. 319–331, 2014.

[94] Z. Jiao and N. Shikazono, "Prediction of nickel morphological evolution in composite solid oxide fuel cell anode using modified phase field model," *Journal of The Electrochemical Society*, vol. 165, no. 2, p. F55– F63, 2018.

[95] Y. Lei, T.-L. Cheng, H. Abernathy, W. Epting, T. Kalapos, G. Hackett, and Y. Wen, "Phase field simulation of anode microstructure evolution of solid oxide fuel cell through Ni (OH) 2 diffusion," *Journal of Power Sources*, vol. 482, p. 228971, 2021.

[96] M. Trini, S. De Angelis, P. S. Jørgensen, P. V. Hendriksen, K. Thornton, and M. Chen, "Towards the validation of a phase field model for Ni coarsening in solid oxide cells," *Acta Materialia*, vol. 212, p. 116887, 2021.

[97] Y. Lei, Y.-L. Lee, W. K. Epting, J. H. Mason, T.-L. Cheng, H. Abernathy, G. Hackett, and Y.-H. Wen, "Modeling Ni redistribution in the hydrogen electrode of solid oxide cells through $Ni(OH)_2$ diffusion and Ni-YSZ wettability change," *Journal of Power Sources*, vol. 545, p. 231924, 2022.

[98] P. W. Hoffrogge, D. Schneider, F. Wankmüller, M. Meffert, D. Gerthsen, A. Weber, B. Nestler, and M. Wieler, "Performance estimation by multiphase-field simulations and transmission-line modeling of nickel coarsening in FIB-SEM reconstructed Ni-YSZ SOFC anodes I: Influence of wetting angle," *Journal of Power Sources*, vol. 570, p. 233031, 2023.

[99] S. Yang, J. Gao, M. Trini, S. De Angelis, P. S. Jørgensen, J. R. Bowen, L. Zhang, and M. Chen, "Ni coarsening in Ni-yttria stabilized zirconia electrodes: Three-dimensional quantitative phase-field simulations supported by ex-situ ptychographic nano-tomography," *Acta Materialia*, vol. 246, p. 118708, 2023.

[100] M. Sun, A. Li, X. Zhang, Y. Fei, L. Zhu, and Z. Huang, "Influence of operating conditions on the fuel electrode degradation of solid oxide electrolysis cell investigated by phase field model with wettability analysis," *Journal of Power Sources*, vol. 587, p. 233700, 2023.

[101] Y. Lei, Y. A. Mantz, W. A. Saidi, H. W. Abernathy, and Y. Wen, "Ni coarsening under humid atmosphere in the electrode of solid oxide cells: A combined study of density-functional theory and phase-field modeling," *Journal of Power Sources*, vol. 613, p. 234778, 2024.

[102] D. Seol, S. Hu, Z. Liu, L. Chen, S. Kim, and K. Oh, "Phase-field modeling of stress-induced surface instabilities in heteroepitaxial thin films," *Journal of Applied Physics*, vol. 98, no. 4, p. 44910, 2005.

[103] S. M. Allen and J. W. Cahn, “A microscopic theory for antiphase boundary motion and its application to antiphase domain coarsening,” *Acta Metallurgica*, vol. 27, no. 6, pp. 1085–1095, 1979.

[104] J. W. Cahn and J. E. Hilliard, “Free energy of a nonuniform system. I. Interfacial free energy,” *The Journal of Chemical Physics*, vol. 28, no. 2, pp. 258–267, 1958.

[105] Y. Lei, T.-L. Cheng, and Y.-H. Wen, “Phase field modeling of microstructure evolution and concomitant effective conductivity change in solid oxide fuel cell electrodes,” *Journal of Power Sources*, vol. 345, pp. 275–289, 2017.

[106] L.-Q. Chen and D. Fan, “Computer Simulation Model for Coupled Grain Growth and Ostwald Ripening—Application to Al2O3-ZrO2 Two-Phase Systems,” *Journal of the American Ceramic Society*, vol. 79, no. 5, pp. 1163–1168, 1996.

[107] A. Choudhury and B. Nestler, “Grand-potential formulation for multicomponent phase transformations combined with thin-interface asymptotics of the double-obstacle potential,” *Physical Review E*, vol. 85, no. 2, p. 021602, 2012.

[108] P. W. Hoffrogge, A. Mukherjee, E. Nani, P. K. Amos, F. Wang, D. Schneider, and B. Nestler, “Multiphase-field model for surface diffusion and attachment kinetics in the grand-potential framework,” *Physical Review E*, vol. 103, no. 3, p. 033307, 2021.

[109] M. Sun, A. Li, X. Zhang, Y. Fei, L. Zhu, and Z. Huang, “Microstructure Evolution and Performance Evaluation of Nickel/Gadolinium-Doped Ceria Fuel Electrode for Solid Oxide Fuel Cell Investigated by Integrated Meso-Scale Modeling.” Preprint at SSRN, 2024.

[110] Z. Chang, C. Bao, X. Lu, and S. Mi, “Numerical reconstruction and evolution of nickel and gadolinium doped ceria anode microstructure based

on phase-field method," *International Journal of Hydrogen Energy*, vol. 172, p. 151141, 2025.

[111] A. Selcuk and A. Atkinson, "Elastic properties of ceramic oxides used in solid oxide fuel cells (SOFC)," *Journal of the European Ceramic Society*, vol. 17, no. 12, pp. 1523–1532, 1997.

[112] M. Radovic and E. Lara-Curzio, "Mechanical properties of tape cast nickel-based anode materials for solid oxide fuel cells before and after reduction in hydrogen," *Acta materialia*, vol. 52, no. 20, pp. 5747–5756, 2004.

[113] A. Nakajo, J. Kuebler, A. Faes, U. F. Vogt, H. J. Schindler, L.-K. Chiang, S. Modena, T. Hocker, *et al.*, "Compilation of mechanical properties for the structural analysis of solid oxide fuel cell stacks. Constitutive materials of anode-supported cells," *Ceramics International*, vol. 38, no. 5, pp. 3907–3927, 2012.

[114] R. Basu, S. S. Kumar, A. K. Mukhopadhyay, and H. S. Maiti, "Improvement in Mechanical Properties of Anode-Supported Planar SOFC," *ECS Transactions*, vol. 7, no. 1, pp. 533–541, 2007-05.

[115] X. Liu, S. Zhou, Z. Yan, Z. Zhong, N. Shikazono, and S. Hara, "Correlation between microstructures and macroscopic properties of nickel/yttria-stabilized zirconia (Ni-YSZ) anodes: Meso-scale modeling and deep learning with convolutional neural networks," *Energy and AI*, vol. 7, p. 100122, 2022.

[116] A. Elmoghazy, S. Weber, R. K. Jeela, A. Prahs, B. Prifling, D. Schneider, V. Schmidt, and B. Nestler, "Investigations on the microstructural degradation and mechanical response of Ni–CGO anodes using phase-field method and stochastic modeling," *Materials & Design*, vol. 269, p. 116665, 2026.

[117] Y. J. Kim and M. C. Lee, "Numerical investigation of flow/heat transfer and structural stress in a planar solid oxide fuel cell," *International Journal of Hydrogen Energy*, vol. 42, no. 29, pp. 18504–18513, 2017.

[118] N. Provatas and K. Elder, *Phase-field methods in materials science and engineering*. John Wiley & Sons, 2011.

[119] S. B. Biner *et al.*, *Programming phase-field modeling*. Springer, 2017.

[120] J. D. Van der Waals, "The thermodynamic theory of capillarity under the hypothesis of a continuous variation of density," *Journal of Statistical Physics*, vol. 20, no. 2, pp. 200–244, 1979.

[121] V. L. Ginzburg and L. D. Landau, "On the theory of superconductivity," in *On superconductivity and superfluidity: a scientific autobiography*, pp. 113–137, Springer, 2009.

[122] J. W. Cahn, "On spinodal decomposition," *Acta metallurgica*, vol. 9, no. 9, pp. 795–801, 1961.

[123] S. M. Allen and J. W. Cahn, "Ground state structures in ordered binary alloys with second neighbor interactions," *Acta Metallurgica*, vol. 20, no. 3, pp. 423–433, 1972.

[124] S. M. Allen and J. W. Cahn, "A correction to the ground state of FCC binary ordered alloys with first and second neighbor pairwise interactions," *Scripta Metallurgica*, vol. 7, no. 12, pp. 1261–1264, 1973.

[125] L. D. Landau and I. M. Khalatikov, "The selected works of L. D. Landau," *(Oxford: Pergamon) (Engl. transl.)*, 1963.

[126] I. Steinbach, F. Pezzolla, B. Nestler, M. Seeßelberg, R. Prieler, G. J. Schmitz, and J. L. Rezende, "A phase field concept for multiphase systems," *Physica D: Nonlinear Phenomena*, vol. 94, no. 3, pp. 135–147, 1996.

[127] S. Daubner, P. W. Hoffrogge, M. Minar, and B. Nestler, "Triple junction benchmark for multiphase-field and multi-order parameter models," *Computational Materials Science*, vol. 219, p. 111995, 2023.

[128] B. Nestler, H. Garcke, and B. Stinner, "Multicomponent alloy solidification: phase-field modeling and simulations," *Physical Review E—Statistical, Nonlinear, and Soft Matter Physics*, vol. 71, no. 4, p. 041609, 2005.

[129] I. Steinbach and F. Pezzolla, "A generalized field method for multiphase transformations using interface fields," *Physica D: Nonlinear Phenomena*, vol. 134, no. 4, pp. 385–393, 1999.

[130] P. W. Hoffrogge, *Understanding degradation phenomena in solid-oxide fuel-cell anodes by phase-field modeling and analytics*. KIT Scientific Publishing, 2024.

[131] S. Enugala, *Some refinements in the phase-field and sharp interface treatments of eutectic growth*. PhD thesis, Karlsruhe, Karlsruher Institut für Technologie (KIT), 2021.

[132] A. A. Wheeler, W. J. Boettinger, and G. B. McFadden, "Phase-field model for isothermal phase transitions in binary alloys," *Physical Review A*, vol. 45, no. 10, p. 7424, 1992.

[133] J. Tiaden, B. Nestler, H.-J. Diepers, and I. Steinbach, "The multiphase-field model with an integrated concept for modelling solute diffusion," *Physica D: Nonlinear Phenomena*, vol. 115, no. 1-2, pp. 73–86, 1998.

[134] S. G. Kim, W. T. Kim, and T. Suzuki, "Phase-field model for binary alloys," *Physical Review E*, vol. 60, no. 6, p. 7186, 1999.

[135] J. Eiken, B. Böttger, and I. Steinbach, "Multiphase-field approach for multicomponent alloys with extrapolation scheme for numerical application," *Physical Review E—Statistical, Nonlinear, and Soft Matter Physics*, vol. 73, no. 6, p. 066122, 2006.

[136] M. Plapp, "Unified derivation of phase-field models for alloy solidification from a grand-potential functional," *Physical Review E—Statistical, Nonlinear, and Soft Matter Physics*, vol. 84, no. 3, p. 031601, 2011.

[137] W. W. Mullins, “Theory of thermal grooving,” *Journal of Applied Physics*, vol. 28, no. 3, pp. 333–339, 1957.

[138] D. Turnbull, “Theory of grain boundary migration rates,” *Journal of Metals*, vol. 3, no. 8, pp. 661–665, 1951.

[139] J. W. Cahn and J. E. Taylor, “surface motion by surface diffusion,” *Acta metallurgica et materialia*, vol. 42, no. 4, pp. 1045–1063, 1994.

[140] A. Rätz, A. Ribalta, and A. Voigt, “Surface evolution of elastically stressed films under deposition by a diffuse interface model,” *Journal of Computational Physics*, vol. 214, no. 1, pp. 187–208, 2006.

[141] P. C. Fife and O. Penrose, “Interfacial dynamics for thermodynamically consistent phase-field models with nonconserved order parameter,” *Electronic Journal of Differential Equations*, pp. 1–49, 1995.

[142] R. F. Almgren, “Second-order phase field asymptotics for unequal conductivities,” *SIAM Journal on Applied Mathematics*, vol. 59, no. 6, pp. 2086–2107, 1999.

[143] M. Ohno, T. Takaki, and Y. Shibuta, “Variational formulation and numerical accuracy of a quantitative phase-field model for binary alloy solidification with two-sided diffusion,” *Physical Review E*, vol. 93, no. 1, p. 012802, 2016.

[144] “Pace3D (Phase-field Algorithms for Computational Engineering in 3D).” `https://www.iam.kit.edu/mms/pace3d.php`. Accessed: 2026-07-22.

[145] J. Hötzer, A. Reiter, H. Hierl, P. Steinmetz, M. Selzer, and B. Nestler, “The parallel multi-physics phase-field framework Pace3D,” *Journal of computational science*, vol. 26, pp. 1–12, 2018.

[146] M. Seiz, P. Hoffrogge, H. Hierl, A. Reiter, D. Schneider, and B. Nestler, “Phase-field simulations with the grand potential approach,” in *High Performance Computing in Science and Engineering ’20: Transactions of*

the High Performance Computing Center, Stuttgart (HLRS), pp. 561–577, Stuttgart, Germany: Springer, 2022.

[147] M. Irshad, K. Siraj, R. Raza, A. Ali, P. Tiwari, B. Zhu, A. Rafique, A. Ali, M. Kaleem Ullah, and A. Usman, "A brief description of high temperature solid oxide fuel cell's operation, materials, design, fabrication technologies and performance," *Applied Sciences*, vol. 6, no. 3, p. 75, 2016.

[148] J. Blakely and H. Mykura, "Surface self diffusion measurements on nickel by the mass transfer method," *Acta Metallurgica*, vol. 9, no. 1, pp. 23–31, 1961.

[149] P. Hoffrogge, S. Daubner, D. Schneider, B. Nestler, B. Zhou, and J. Eiken, "Triple junction benchmark for multiphase-field models combining capillary and bulk driving forces," *Modelling and Simulation in Materials Science and Engineering*, vol. 33, no. 1, p. 015001, 2025.

[150] Y. Sun and C. Beckermann, "Sharp interface tracking using the phase-field equation," *Journal of Computational Physics*, vol. 220, no. 2, pp. 626–653, 2007.

[151] L. Schöller, L. Wehner, D. Schneider, R. Schwaiger, and B. Nestler, "Virtual design of multilayered SOFC microstructures based on particle packing and spherical harmonics," *Modelling and Simulation in Materials Science and Engineering*, vol. 34, no. 4, p. 045013, 2026.

[152] B. Nestler, F. Wendler, M. Selzer, B. Stinner, and H. Garcke, "Phase-field model for multiphase systems with preserved volume fractions," *Physical Review E—Statistical, Nonlinear, and Soft Matter Physics*, vol. 78, no. 1, p. 011604, 2008.

[153] E. Schoof, D. Schneider, N. Streichhan, T. Mittnacht, M. Selzer, and B. Nestler, "Multiphase-field modeling of martensitic phase transformation in a dual-phase microstructure," *International journal of solids and structures*, vol. 134, pp. 181–194, 2018.

[154] C. Chen, H. Lin, and C. Lan, "Phase field modeling with large interface thickness and undercooling," *Journal of crystal growth*, vol. 385, pp. 121–126, 2014.

[155] D. Schneider, O. Tschukin, A. Choudhury, M. Selzer, T. Böhlke, and B. Nestler, "Phase-field elasticity model based on mechanical jump conditions," *Computational Mechanics*, vol. 55, no. 5, pp. 887–901, 2015.

[156] A. Durga, P. Wollants, and N. Moelans, "Evaluation of interfacial excess contributions in different phase-field models for elastically inhomogeneous systems," *Modelling and simulation in materials science and engineering*, vol. 21, no. 5, p. 055018, 2013.

[157] J. Mosler, O. Shchyglo, and H. M. Hojjat, "A novel homogenization method for phase field approaches based on partial rank-one relaxation," *Journal of the Mechanics and Physics of Solids*, vol. 68, pp. 251–266, 2014.

[158] D. Schneider, F. Schwab, E. Schoof, A. Reiter, C. Herrmann, M. Selzer, T. Böhlke, and B. Nestler, "On the stress calculation within phase-field approaches: a model for finite deformations," *Computational Mechanics*, vol. 60, no. 2, pp. 203–217, 2017.

[159] B. Münch and L. Holzer, "Contradicting geometrical concepts in pore size analysis attained with electron microscopy and mercury intrusion," *Journal of the American Ceramic Society*, vol. 91, no. 12, pp. 4059–4067, 2008.

[160] J. Joos, T. Carraro, A. Weber, and E. Ivers-Tiffée, "Reconstruction of porous electrodes by FIB/SEM for detailed microstructure modeling," *Journal of Power Sources*, vol. 196, no. 17, pp. 7302–7307, 2011.

[161] K. Palágyi and A. Kuba, "A 3D 6-subiteration thinning algorithm for extracting medial lines," *Pattern Recognition Letters*, vol. 19, no. 7, pp. 613–627, 1998.

[162] A. Bertram, *Elasticity and plasticity of large deformations: including gradient materials*. Springer Nature, 2021.

[163] T. Böhlke and C. Brüggemann, "Graphical representation of the generalized Hooke's law," *Technische Mechanik*, vol. 21, no. 2, pp. 145–158, 2001.

[164] R. Hill, "The elastic behaviour of a crystalline aggregate," *Proceedings of the Physical Society. Section A*, vol. 65, no. 5, p. 349, 1952.

[165] D. Klotz, A. Weber, and E. Ivers-Tiffée, "Practical guidelines for reliable electrochemical characterization of solid oxide fuel cells," *Electrochimica Acta*, vol. 227, pp. 110–126, 2017.

[166] R. K. Jeela, G. Tosato, M. Ahmad, M. Wieler, A. Koeppe, B. Nestler, and D. Schneider, "Enhancing solid oxide fuel cells development through Bayesian active learning," *Advanced Energy Materials*, vol. 15, no. 34, p. 2501216, 2025.

[167] J. Joos, *Microstructural characterisation, modelling and simulation of solid oxide fuel cell cathodes*, vol. 30. KIT Scientific Publishing, 2017.

[168] P. Haremski, L. Epple, M. Wieler, P. Lupetin, R. Thelen, and M. J. Hoffmann, "A thermal grooving study of relative grain boundary energies of nickel in polycrystalline Ni and in a Ni/YSZ anode measured by atomic force microscopy," *Acta Materialia*, vol. 214, p. 116936, 2021.

[169] P. Haremski, L. Epple, M. Wieler, P. Lupetin, L. Klinger, E. Rabkin, and M. J. Hoffmann, "Grain boundary grooving by surface diffusion in nickel bicrystals," *Acta Materialia*, vol. 241, p. 118334, 2022.

[170] B. Settles, *Active learning literature survey*. University of Wisconsin-Madison Department of Computer Sciences, 2009.

[171] P. I. Frazier, "A tutorial on Bayesian optimization," *arXiv preprint arXiv:1807.02811*, 2018.

[172] Q. Liang, A. E. Gongora, Z. Ren, A. Tiihonen, Z. Liu, S. Sun, J. R. Deneault, D. Bash, F. Mekki-Berrada, S. A. Khan, *et al.*, "Benchmarking the performance of Bayesian optimization across multiple experimental

materials science domains," *npj Computational Materials*, vol. 7, no. 1, p. 188, 2021.

[173] G. Tosato, A. Koeppe, M. Selzer, and B. Nestler, "Bayesian optimization framework for data-driven materials design," *Tage 2023*, p. 306, 2023.

[174] N. Brandt, L. Griem, C. Herrmann, E. Schoof, G. Tosato, Y. Zhao, P. Zschumme, and M. Selzer, "Kadi4Mat: A research data infrastructure for materials science," *Data Science Journal*, vol. 20, p. 8, 2021.

[175] L. Griem, P. Zschumme, M. Laqua, N. Brandt, E. Schoof, P. Altschuh, and M. Selzer, "KadiStudio: FAIR modelling of scientific research processes," *Data Science Journal*, vol. 21, p. 16, 2022.

[176] F. Chollet *et al.*, "Keras." `https://github.com/fchollet/keras`, 2015.

[177] F. Pedregosa, G. Varoquaux, A. Gramfort, V. Michel, B. Thirion, O. Grisel, M. Blondel, P. Prettenhofer, R. Weiss, V. Dubourg, J. Vanderplas, A. Passos, D. Cournapeau, M. Brucher, M. Perrot, and E. Duchesnay, "Scikit-learn: Machine Learning in Python," *Journal of Machine Learning Research*, vol. 12, pp. 2825–2830, 2011.

[178] C. E. Rasmussen and C. K. I. Williams, *Gaussian Processes for Machine Learning*. The MIT Press, 2006.

[179] J. Snoek, H. Larochelle, and R. P. Adams, "Practical bayesian optimization of machine learning algorithms," *Advances in neural information processing systems*, vol. 25, 2012.

[180] C. Hvarfner, E. O. Hellsten, and L. Nardi, "Vanilla bayesian optimization performs great in high dimensions," *arXiv preprint arXiv:2402.02229*, 2024.

[181] P. Maiya and J. Blakely, "Surface self-diffusion and surface energy of nickel," *Journal of Applied Physics*, vol. 38, no. 2, pp. 698–704, 1967.

[182] J. R. Wolfe, *Surface self-diffusion on nickel (111) by radioactive tracers*. University of Missouri–Rolla, 1968.

[183] E. Latta and H. Bonzel, "Anisotropy of Surface Self-Diffusion on Ni (110)," *Physical Review Letters*, vol. 38, no. 15, p. 839, 1977.

[184] T. Roth, "The surface and grain boundary energies of iron, cobalt and nickel," *Materials Science and Engineering*, vol. 18, no. 2, pp. 183–192, 1975.

[185] E. Hayward and A. Greenough, "The surface energy of solid nickel," *J Inst Met*, vol. 88, pp. 217–220, 1959.

[186] R. Digilov, S. Zadumkin, V. Kumykov, and K. B. Khokonov, "Measurement of surface tension of refractory metals in solid state," *Fiz. Met. Metalloved.;(USSR)*, vol. 41, no. 5, pp. 979–982, 1976.

[187] E. Clark, R. Yeske, and H. Birnbaum, "The effect of hydrogen on the surface energy of nickel," *Metallurgical Transactions A*, vol. 11, pp. 1903–1908, 1980.

[188] D. Stickle, J. Hirth, G. Meyrick, and R. Speiser, "A new technique for measuring the effects of oxygen activity on surface energies: application to nickel," *Metallurgical Transactions A*, vol. 7, pp. 71–74, 1976.

[189] R. Tran, Z. Xu, B. Radhakrishnan, D. Winston, W. Sun, K. A. Persson, and S. P. Ong, "Surface energies of elemental crystals," *Scientific data*, vol. 3, no. 1, pp. 1–13, 2016.

[190] M. Kappeler, A. Marusczyk, and B. Ziebarth, "Simulation of nickel surfaces using ab-initio and empirical methods," *Materialia*, vol. 12, p. 100675, 2020.

[191] R. Fujimatsu, T. Oda, M. Kobayashi, H. Ohka, and M. Izumi, "Measurement of oxygen partial pressure in fuel electrode of sofc," *ECS Transactions*, vol. 71, no. 1, p. 113, 2016.

[192] A. T. Hasouna, K. Nogi, and K. Ogino, "Influence of oxygen partial pressure on the wettability of solid Fe by liquid Bi," *Materials Transactions, JIM*, vol. 31, no. 4, pp. 302–306, 1990.

[193] K. Mukai, Z. Yuan, K. Nogi, and T. Hibiya, "Effect of the oxygen partial pressure on the surface tension of molten silicon and its temperature coefficient," *Isij International*, vol. 40, no. Suppl, pp. S148–S152, 2000.

[194] N. Zouvelou, X. Mantzouris, and P. Nikolopoulos, "Surface and grain-boundary energies as well as surface mass transport in polycrystalline CeO_2," *Materials Science and Engineering: A*, vol. 495, no. 1-2, pp. 54–59, 2008.

[195] M. Jin, E. Shimada, and Y. Ikuma, "Atomic force microscopy study of surface diffusion in polycrystalline CeO2 via grain boundary grooving," *Journal of the ceramic society of Japan*, vol. 108, no. 1257, pp. 456–461, 2000.

[196] A. R. Symington, M. Molinari, S. Moxon, J. M. Flitcroft, D. C. Sayle, and S. C. Parker, "Strongly bound surface water affects the shape evolution of cerium oxide nanoparticles," *The Journal of Physical Chemistry C*, vol. 124, no. 6, pp. 3577–3588, 2020.

[197] N. Skorodumova, M. Baudin, and K. Hermansson, "Surface properties of CeO2 from first principles," *Physical Review B*, vol. 69, no. 7, p. 075401, 2004.

[198] M. Nolan, S. C. Parker, and G. W. Watson, "The electronic structure of oxygen vacancy defects at the low index surfaces of ceria," *Surface Science*, vol. 595, no. 1-3, pp. 223–232, 2005.

[199] H. Nahor, H. Meltzman, and W. D. Kaplan, "Ni–YSZ (111) solid–solid interfacial energy," *Journal of materials science*, vol. 49, pp. 3943–3950, 2014.

[200] H. Nahor and W. D. Kaplan, "Ni-YSZ (001) solid-solid interfacial energy and orientation relationships," *Journal of the American Ceramic Society*, vol. 102, no. 5, pp. 2987–2998, 2019.

[201] X. Lin, Z. Yang, X. Zhang, and Q. Zhang, "Pareto set learning for expensive multi-objective optimization," *Advances in neural information processing systems*, vol. 35, pp. 19231–19247, 2022.

[202] A. Messac, G. J. Sundararaj, R. V. Tappeta, and J. E. Renaud, "Ability of objective functions to generate points on nonconvex pareto frontiers," *AIAA journal*, vol. 38, no. 6, pp. 1084–1091, 2000.

[203] M. Ehrgott, *Multicriteria optimization*, vol. 491. Springer Science & Business Media, 2005.

[204] C. Bazgan, S. Ruzika, C. Thielen, and D. Vanderpooten, "The power of the weighted sum scalarization for approximating multiobjective optimization problems," *Theory of Computing Systems*, pp. 1–21, 2022.

[205] Z. Jiao, E. P. Busso, and N. Shikazono, "Influence of polarization on the morphological changes of nickel in fuel electrodes of solid oxide cells," *Journal of The Electrochemical Society*, vol. 167, no. 2, p. 024516, 2020.

[206] L. Murr, O. Inal, and G. Wong, "Applications of the SEM, TEM, and FIM in the analysis of structure and energy of metal interfaces," *Electron microscopy and structure of materials. University of California Press, Berkeley*, pp. 417–426, 1972.

[207] T. Nakamura, T. Kobayashi, K. Yashiro, A. Kaimai, T. Otake, K. Sato, J. Mizusaki, and T. Kawada, "Electrochemical behaviors of mixed conducting oxide anodes for solid oxide fuel cell," *Journal of The Electrochemical Society*, vol. 155, no. 6, p. B563– B569, 2008.

[208] A. Sciazko, Y. Komatsu, T. Shimura, and N. Shikazono, "Multiscale microstructural evolutions of nickel-gadolinium doped ceria in solid oxide fuel cell anode," *Journal of Power Sources*, vol. 478, p. 228710, 2020.

[209] H. Tu and U. Stimming, "Advances, aging mechanisms and lifetime in solid-oxide fuel cells," *Journal of Power Sources*, vol. 127, no. 1-2, pp. 284–293, 2004.

[210] K. Miyawaki, M. Kishimoto, H. Iwai, M. Saito, and H. Yoshida, "Comprehensive understanding of the active thickness in solid oxide fuel cell anodes using experimental, numerical and semi-analytical approach," *Journal of Power Sources*, vol. 267, pp. 503–514, 2014.

[211] S. Ihara, S. Naruse, H. Muroyama, and T. Matsui, "Wettability analysis of Ni/YSZ interface under operating conditions of solid oxide cells," *Journal of Power Sources*, vol. 654, p. 237867, 2025.

[212] C. L. Yeong and S. Torquato, "Reconstructing random media," *Physical Review E*, vol. 57, no. 1, p. 495, 1998.

[213] D. Westhoff, I. Manke, and V. Schmidt, "Generation of virtual lithium-ion battery electrode microstructures based on spatial stochastic modeling," *Computational Materials Science*, vol. 151, pp. 53–64, 2018.

[214] A. Gayon-Lombardo, L. Mosser, N. P. Brandon, and S. J. Cooper, "Pores for thought: generative adversarial networks for stochastic reconstruction of 3D multi-phase electrode microstructures with periodic boundaries," *npj Computational Materials*, vol. 6, no. 1, p. 82, 2020.

[215] A. Abbaspour, J.-L. Luo, and K. Nandakumar, "Three-dimensional random resistor-network model for solid oxide fuel cell composite electrodes," *Electrochimica Acta*, vol. 55, no. 12, pp. 3944–3950, 2010.

[216] K. Zheng and M. Ni, "Reconstruction of solid oxide fuel cell electrode microstructure and analysis of its effective conductivity," *Science bulletin*, vol. 61, no. 1, pp. 78–85, 2016.

[217] B. Timurkutluk, Y. Ciflik, T. Altan, and O. Genc, "Synthetical designing of solid oxide fuel cell electrodes: Effect of particle size and volume fraction," *International Journal of Hydrogen Energy*, vol. 47, no. 73, pp. 31446–31458, 2022.

[218] M. Prioux, E. da Rosa Silva, M. Hubert, J. Vulliet, J. Debayle, P. Cloetens, and J. Laurencin, "Numerical microstructural optimization for the hydrogen electrode of solid oxide cells," *Fuel Cells*, vol. 23, no. 6, pp. 408–419, 2023.

[219] F. Muetter, C. Berger, B. Koenigshofer, M. Höber, C. Hochenauer, and V. Subotić, "Artificial intelligence for solid oxide fuel cells: Combining automated high accuracy artificial neural network model generation and genetic algorithm for time-efficient performance prediction and optimization," *Energy Conversion and Management*, vol. 291, p. 117263, 2023.

[220] J. Peng, D. Zhao, Y. Xu, X. Wu, and X. Li, "Comprehensive analysis of solid oxide fuel cell performance degradation mechanism, prediction, and optimization studies," *Energies*, vol. 16, no. 2, p. 788, 2023.

[221] R. Farraro and R. B. Mclellan, "Temperature dependence of the Young's modulus and shear modulus of pure nickel, platinum, and molybdenum," *Metallurgical Transactions A*, vol. 8, no. 10, pp. 1563–1565, 1977.

[222] P. Hidnert, "Thermal expansion of some nickel alloys," *J. Res. Natl. Bur. Stand*, vol. 58, no. 1934, p. 89, 1957.

[223] X. Fan, E. D. Case, Q. Yang, and J. D. Nicholas, "Room temperature elastic properties of gadolinia-doped ceria as a function of porosity," *Ceramics International*, vol. 39, no. 6, pp. 6877–6886, 2013.

[224] K. B. Andersen, B. Charlas, E. Stamate, and K. K. Hansen, "Permeability, strength and electrochemical studies on ceramic multilayers for solid-state electrochemical cells," *Heliyon*, vol. 3, no. 8, 2017.

[225] D. Chen, Z. Lin, H. Zhu, and R. J. Kee, "Percolation theory to predict effective properties of solid oxide fuel-cell composite electrodes," *Journal of Power Sources*, vol. 191, no. 2, pp. 240–252, 2009.

[226] B. Kenney, M. Valdmanis, C. Baker, J. Pharoah, and K. Karan, "Computation of TPB length, surface area and pore size from numerical

reconstruction of composite solid oxide fuel cell electrodes," *Journal of Power Sources*, vol. 189, no. 2, pp. 1051–1059, 2009.

[227] A. Bertei and C. Nicolella, "Percolation theory in SOFC composite electrodes: Effects of porosity and particle size distribution on effective properties," *Journal of Power Sources*, vol. 196, no. 22, pp. 9429–9436, 2011.

[228] S. Wang, T. Kobayashi, M. Dokiya, and T. Hashimoto, "Electrical and ionic conductivity of Gd-doped ceria," *Journal of the Electrochemical Society*, vol. 147, no. 10, p. 3606, 2000.

[229] L. J. Gibson and M. F. Ashby, *Cellular Solids: Structure and Properties*. Cambridge University Press, 1997.

[230] M. Pihlatie, A. Kaiser, and M. Mogensen, "Mechanical properties of NiO/Ni–YSZ composites depending on temperature, porosity and redox cycling," *Journal of the European Ceramic Society*, vol. 29, no. 9, pp. 1657–1664, 2009.

[231] W. Pabst, E. Gregorová, and G. Tichá, "Elasticity of porous ceramics—A critical study of modulus- porosity relations," *Journal of the European Ceramic Society*, vol. 26, no. 7, pp. 1085–1097, 2006.

[232] M. Kishimoto, M. Lomberg, E. Ruiz-Trejo, and N. P. Brandon, "Numerical modeling of nickel-infiltrated gadolinium-doped ceria electrodes reconstructed with focused ion beam tomography," *Electrochimica Acta*, vol. 190, pp. 178–185, 2016.

[233] Y. Xiang, Y. Da, N. Shikazono, and Z. Jiao, "Quantitative study on solid oxide fuel cell anode microstructure stability based on 3D microstructure reconstructions," *Journal of Power Sources*, vol. 477, p. 228653, 2020.

[234] N. Vivet, S. Chupin, E. Estrade, A. Richard, S. Bonnamy, D. Rochais, and E. Bruneton, "Effect of Ni content in SOFC Ni-YSZ cermets: A three-dimensional study by FIB-SEM tomography," *Journal of Power Sources*, vol. 196, no. 23, pp. 9989–9997, 2011.

[235] T. Nakamura, K. Yashiro, A. Kaimai, T. Otake, K. Sato, T. Kawada, and J. Mizusaki, "Determination of the reaction zone in gadolinia-doped ceria anode for solid oxide fuel cell," *Journal of the Electrochemical Society*, vol. 155, no. 12, pp. B1244–B1250, 2008.

[236] G. Brus, H. Iwai, and J. S. Szmyd, "An anisotropic microstructure evolution in a solid oxide fuel cell anode," *Nanoscale Research Letters*, vol. 15, no. 1, p. 3, 2020.

[237] Y. Xiang, Y. Da, Z. Zhong, N. Shikazono, and Z. Jiao, "Thermo-mechanical stress analyses of solid oxide fuel cell anode based on three-dimensional microstructure reconstruction," *International Journal of Hydrogen Energy*, vol. 45, no. 38, pp. 19791–19800, 2020.

[238] S. Celik, B. Ibrahimoglu, S. Toros, and M. D. Mat, "Three dimensional stress analysis of solid oxide fuel cell anode micro structure," *International journal of hydrogen energy*, vol. 39, no. 33, pp. 19119–19131, 2014.

List of the author's publications

- **R. K. Jeela**, G. Tosato, M. Ahmad, M. Wieler, A. Koeppe, B. Nestler, and D. Schneider, "Enhancing solid oxide fuel cells development through Bayesian active learning," *Advanced Energy Materials*, vol. 15, no. 34, p. 2501216, 2025.
- **R. K. Jeela**, M. Ahmad, M. Wieler, Y. Liu, M. Juckel, D. Schneider, A. Weber, N. H. Menzler, and B. Nestler, "Multiphase-Field Simulation Studies of Coarsening in Ni-GDC SOFC Anode Microstructures and the Effect of Interfacial Energies," *ACS Applied Energy Materials*, vol. 8, no. 24, pp. 17670–17687, 2025.
- **R. K. Jeela**, A. Elmoghazy, L. Schöller, M. Wieler, A. Prahs, D. Schneider, and B. Nestler, "Effect of volume fractions and aging on Ni-GDC SOFC anode degradation and performance: multiphase-field simulations," *npj materials degradation*, 2026.
- S. Weber, B. Prifling, **R. K. Jeela**, A. Prahs, D. Schneider, B. Nestler, and V. Schmidt, "A time-continuous approach to analyzing anode aging in solid-oxide fuel cells via stochastic 3D microstructure modeling and physics-based simulations," *Computational Materials Science*, vol. 264, p. 114491, 2026.
- A. Kumar, N. Prajapati, M. Reder, **R. K. Jeela**, D. Schneider, and B. Nestler, "A grand-potential phase-field approach for modeling pitting corrosion and pressure-driven cracking in multiphase alloys," *Journal of Materials Research and Technology*, vol. 42, pp. 8726–8747, 2026.

- A. Elmoghazy, S. Weber, **R. K. Jeela**, A. Prahs, B. Prifling, D. Schneider, V. Schmidt, and B. Nestler, "Investigations on the microstructural degradation and mechanical response of Ni-CGO anodes using phase-field method and stochastic modeling," *Materials & Design*, vol. 269, p. 116665, 2026.
- L. Schöller, L. Wehner, D. Ramler, I. Kogut, S. Kucharski, C. Lenser, **R. K. Jeela**, D. Schneider, A. Weber, R. Schwaiger, and B. Nestler, "Understanding electro-chemo-mechanical stresses in ceria-based solid oxide electrolysis cells using virtual microstructures," *Journal of Power Sources*, vol. 696, p. 241459, 2026.

List of Figures

Figure 1.1 Schematic of an operating SOFC showing two porous electrodes (anode and cathode) separated by a dense electrolyte (adapted from ref [14]). 8
Figure 1.2 An overview of the characteristic time and length scales of functional and degradation processes in heterogeneous SOFC electrode structures, including common modeling and simulation approaches across these scales (adapted from ref [27]). 16
Figure 1.3 Different modeling levels for solid oxide fuel cells, spanning from stack-level to atomic-scale reaction kinetics. 21
Figure 1.4 Representative Volume Element (RVE) of an SOFC anode microstructure, along with key microstructural characterization metrics related to structural features, electrochemical performance, and mechanical integrity. . . 26
Figure 1.5 Schematic representation of the current-voltage characteristic curve of an SOFC, indicating three major losses contributing to the cell voltage drop: activation loss, ohmic loss, and concentration loss. 27
Figure 2.1 Schematic representation of the extended microstructure generation workflow, emphasizing the extended sintering-like morphological coalescence step and resulting enhancements to synthetic SOFC Ni-GDC anode microstructures. The figure has been adjusted to the format of this dissertation. 59

Figure 2.2 Sub-regions extracted from a pristine FIB-SEM reconstructed 3D real microstructure. Sub-regions representing 1/4th, 1/9th, and 1/16th of the total volume were extracted from the Central region of the real microstructure. Given that the microstructure's thickness in the z-direction is only 6.4 µm, it was kept consistent for all sub-regions, with only the x- and y-dimensions being reduced accordingly. The figure has been adjusted to the format of this dissertation. 71

Figure 2.3 Comparison of normalized microstructural properties variations over different subdomain sizes against the real domain. (a) Normalised property values and error bars for the nine subdomains of size 1/9. (b) Normalised property values and error bars for the four subdomains of size 1/2. Each bar represents the mean value across the subdomains, with the error bars indicating the standard deviation. The values of the real domain are used as a normalisation reference. The figure has been adjusted to the format of this dissertation. 74

Figure 3.1 Visualization of the KadiStudio workflow for automated parameter identification of Ni-GDC anode aging in SOFCs. The workflow consists of: (a) user input nodes for configuring environment settings, working directories, and KadiWeb communication tokens; (b) a Bayesian Optimization Oracle node; (c) preprocessing nodes that convert the Oracle outputs into input data for PACE3D simulations; (d) nodes for job submission and monitoring on the computing cluster; (e) postprocessing nodes for analyzing the simulation results; and (f) a Scorer node that evaluates each simulation output against the defined objective. All nodes continuously update the corresponding records in Kadi4Mat, thereby ensuring synchronized data management across the entire workflow (based on joint work presented in [166]). 81

Figure 3.2 Microstructural evolution in Ni-GDC anodes. Experimental conditions (temperature, environment) drive microstructure changes, while precise parameter settings in physical modeling simulations aim to reproduce these outcomes accurately. This precision is crucial for quantitatively simulating microstructural aging. Note: Size variations between pristine and aged samples reflect different FIB-SEM volume segments, not aging effects. The figure has been adjusted to the format of this dissertation. 83

Figure 3.3 AL framework validation for a 1D, single-objective optimization problem. Tuned parameter: γ_{NiGDC}. The figure shows (a) an overview of the search and (b) a visualization of the error at four different iteration steps. The error is measured as a voxel-by-voxel difference between the resulting and target microstructure (*framedifference*). The first 3 data points are randomly sampled to produce a sufficient baseline for the BO Oracle search. The figure has been adjusted to the format of this dissertation. 90

Figure 3.4 Framework validation for a 6-dimensional, single-objective optimization problem. The figure shows the overview of the search (a) and a visualization of the error at four different iteration steps (b). The error is measured as a voxel-by-voxel difference between the resulting and target microstructure (*framedifference*). The best result is found at iteration 22, with a *framedifference* error of 0.0097. The figure has been adjusted to the format of this dissertation. 92

Figure 3.5 (a) Search overview of a 5D, single objective optimization, with total TPB density used as scoring value. Target value for total TPB density found at iteration 11. (b) A comparison is presented between the target values for the nine considered microstructure properties and those obtained from the Oracle-guided simulation at iteration 11. The plot demonstrates that the parameter considered for scoring closely matches the target, while others mostly deviate from their respective target values. The figure has been adjusted to the format of this dissertation. 96

Figure 3.6 (a) Optimization convergence over time: The blue line shows the cumulative minimum error at each iteration, reflecting continual improvement in solution quality and evidence of plateauing around iteration 27. The grey line displays the RMSE for each iteration, providing insight into the overall search dynamics. (b) Agreement with target microstructural properties: Comparison of nine key descriptors – highlighting the Oracle-guided simulation at iteration 27, which delivered the best fit at 7 % total error. The two tortuosity metrics (left) were assigned a lower weight during scalarization, while the remaining seven parameters (right) received higher weights to guide the optimization. The figure has been adjusted to the format of this dissertation. 100

Figure 3.7 The figure shows the evolution of the 3D microstructure and its 2D cross-section at distinct iterations of the AL framework. (a) Initial 3D microstructure for simulation and a 2D cross-sectional view of it, (b) 240h evolved 3D microstructure and 2D cross-section obtained from the AL framework at iteration 6 with a poor overall error percentage of 16.6, and (c) 240h evolved 3D microstructure and 2D cross-section obtained from the AL framework at iteration 38 with a best overall error percentage of 7.8. The figure has been adjusted to the format of this dissertation. 103

Figure 4.1 FIB-SEM 3D reconstructed pristine Ni-GDC anode microstructure alongside experimentally aged samples from the same batch after 240 and 1100 hours. 113

Figure 4.2 Phase-field simulation of the (a) 3D microstructure and (b) 2D cross sections at different aging times of 0h, 240h, and 1100h using the pristine microstructure as initial input. 116

Figure 4.3 Phase-field simulation of the (a) 3D microstructure and (b) 2D cross sections at different aging times of 240h, 670h, and 1100h using the pre-aged (240h) microstructure as initial input. 118
Figure 4.4 Phase-field simulation of the (a) 3D Ni-GDC SOFC anode microstructure and (b) 2D cross sections at different aging times of 0h, 30,000h, and 60,000h using the pristine microstructure as initial input. 121
Figure 4.5 Phase-field simulation of the (a) Ni phase 3D morphology and (b) 2D cross sections at different aging times of 0h, 30,000h, and 60,000h using the pristine microstructure as initial input. 122
Figure 4.6 (a) Continuous particle size distributions of the nickel phase at selected aging times up to 60,000h; (b) Evolution of the mean nickel particle diameter over the same duration. 123
Figure 4.7 Phase-field simulation of the (a) GDC phase 3D morphology and (b) 2D cross sections at different aging times of 0h, 30,000h, and 60,000h using the pristine microstructure as initial input. 124
Figure 4.8 (a) Continuous particle size distributions of the GDC phase at selected aging times up to 60,000h; (b) Evolution of the GDC particle diameter over the same duration. 125
Figure 4.9 Phase-field simulation of the (a) Pore phase 3D morphology and (b) 2D cross sections at different aging times of 0h, 30,000h, and 60,000h using the pristine microstructure as initial input. 126
Figure 4.10 (a) Continuous PSD of the Pore phase at selected aging times up to 60,000h; (b) Evolution of the mean Pore diameter over the same duration. 127
Figure 4.11 Distribution of TPBs within the 3D Ni-GDC anode microstructure at the pristine state and after 60,000h of aging, obtained from MPF simulations, with color-coded TPB segments. 127

Figure 4.12 Evolution of (a) TPB density and (b) DPB density in Ni-GDC SOFC anode microstructure over an aging period of 60,000h, estimated using MPF simulations. 128
Figure 4.13 Evolution of the mean tortuosities of (a) GDC and (b) Pore in the microstructure of the Ni-GDC SOFC anode over an aging period of 60,000h, estimated using MPF simulations. 130
Figure 4.14 Morphological evolution of (a) the initial two adjoining nickel and GDC particles contacting a common interface at right angles. (b–d) Morphological evolution at equilibrium by the phase-field simulations using the same kinetic coefficients and paths, but with different sets of thermodynamic equilibrium contact angles $\theta_{Ni} - \theta_{GDC} - \theta_{Pore}$ as $144° - 121° - 95°$, $60° - 152° - 148°$, and $144° - 60° - 156°$ respectively. . . . 135
Figure 4.15 Morphological evolution of the (a) initial pristine 3D Ni-GDC anode microstructure and constituent phases over 2000h of aging, simulated for (b-d) three distinct contact angle configurations using the MPF method. 137
Figure 4.16 Microstructural properties evolution over the aging period of 2000h for three distinct configurations of contact angles in the MPF simulations: (a,b) mean diameter of nickel and GDC, (c) Total TPB density, (d) DPB density, (e,f) mean tortuosities of GDC and pore. . 140
Figure 5.1 Comparison of the FIB-SEM reconstructed 3D SOFC anode microstructure and the individual phase morphologies with a digital twin created by a structure generator. 152
Figure 5.2 Comparison of continuous particle size distributions for the synthetic microstructure and the FIB-SEM reconstruction for (a) nickel phase, (b) GDC phase, and (c) pore phase. 153

Figure 6.1 Variations in microstructural properties depending on porosity and solid volume fractions of Ni/GDC phases. (a) total TPB density, (b) DPB density, and mean tortuosities of (c) nickel, (d) GDC, and (e) pore. . . . 165
Figure 6.2 Effect of porosity and Ni/GDC solid volume fractions on effective mechanical properties and stresses: directional elastic moduli (E_{xx}, E_{yy}, E_{zz}) for pore volume fractions of (a) 25 %, (b) 35 %, and (c) 45 %, (d) Hill average elastic modulus (E_{Hill}), and (e) average von Mises stress. 169
Figure 6.3 Morphological evolution of the pristine synthetic 3D Ni-GDC anode microstructures after 1000 and 2000 hours of aging for selected initial configurations (A1, A5, B1, B5, C1, C5) predicted from multiphase-field simulations. 171
Figure 6.4 Evolution of the mean diameter over 2000 hours of aging from multiphase-field simulations. (a-c) nickel, (d-f) GDC, and (g-i) pore phases at porosity groups of 25 %, 35 %, and 45 %, respectively, across solid volume fractions (solid vol.%) of Ni/GDC. 173
Figure 6.5 Evolution of electrochemical reaction sites over 2000 hours of aging from multiphase-field simulations. (a-c) Total TPB density, (d-f) DPB density at porosity groups of 25 %, 35 %, and 45 %, respectively, across solid volume fractions (solid vol.%) of Ni/GDC. 175
Figure 6.6 Total triple-phase boundary in the initial state and after 2000h of aging for porosity groups of 25 % (A3), 35 % (B3), and 45 % (C3), respectively, from multiphase-field simulations, with color-coded TPB segments. 176
Figure 6.7 Evolution of mean tortuosity over 2000 hours of aging from multiphase-field simulations. (a-c) nickel, (d-f) GDC, and (g-i) pore phases at porosity groups of 25 %, 35 %, and 45 %, respectively, across solid volume fractions (solid vol.%) of Ni/GDC. 178

Figure 6.8 Evolution of elastic properties over 2000h of aging from multiphase-field simulations. (a-c) Hill average elastic modulus (E_{Hill}), and effective directional elastic moduli (d-f) E_{xx}, (g-i) E_{yy}, (j-l) E_{zz} for porosity groups of 25 %, 35 %, and 45 %, respectively, across solid volume fractions (solid vol.%) of Ni/GDC. . . . 183
Figure 6.9 Evolution of mechanical response over 2000h of aging from multiphase-field simulations. (a-c) Average von Mises stress, and (d-f) critical volume fraction (CVF) for porosity groups of 25 %, 35 %, and 45 %, respectively, across solid volume fractions (solid vol.%) of Ni/GDC. 185
Figure 6.10 Local stress distributions in the initial and 2000h aged microstructures. Contour maps of von Mises stress and stress distributions for the (a-d) A5 and (e-h) C5 configurations. 189

List of Tables

Table 1.1 Comparison of major fuel cell technologies (based on ref [13]). 6
Table 2.1 Microstructural characteristic properties of pristine and subdomains of various volumes. 72
Table 2.2 Evaluation of statistical fluctuations in microstructural properties over 1/9th of real domains. 75
Table 2.3 Evaluation of statistical fluctuations in microstructural properties over 1/2 of real domains. 75
Table 3.1 Phase-field parameters used in simulations of Ni-GDC anode ($u_l = 50\,\mathrm{nm}, u_E = 6.25\times10^{-15}\,\mathrm{J}, u_t = 1.45\times10^{-2}\,\mathrm{s}$). . 88
Table 3.2 Overview of the values chosen by the Bayesian Oracle at iteration 22, which gave the best result. The oracle explored the parameter space within predefined constraints, alongside the specified ranges of validity. For the interface energy parameters (γ_{NiGDC}, $\gamma_{GDCPore}$), values were sampled as floats with 0.01 increment. For the diffusion coefficients related parameters (M_{Ni}^{NiPore}, M_{Ni}^{NiGDC}, $M_{\mathrm{GDC}}^{GDCPore}$, M_{GDC}^{NiGDC}), where only changes in the order of magnitude have significant impact on the outcome, the oracle selected integer values for the exponent, effectively adjusting the parameters by powers of ten. The comprehensive error, used as a score for the oracle, was computed with *framedifference* according to eq (3.4) and gave a result of 0.0097. 91
Table 3.3 Microstructural characteristic properties of pristine and 240h aged Ni-GDC anodes. 93

Table 3.4 Overview of the 5 iterations with the best score. The top part of the table shows the values suggested by the Bayesian Oracle for each of the 7 input parameters that we asked to tune (for ranges of validity, refer to Table 3.1). The bottom part of the table shows the error obtained for each of the 9 considered microstructure properties in relation to the reference microstructure and the overall score. 104

Table 4.1 The phase-field model parameters employed in the coarsening simulations of the Ni-GDC anode. These parameters are derived from the physical properties of the material system and represented in a model-specific system of units. The model units are stated as $u_l = 50\,\text{nm}, u_E = 5.25 \times 10^{-15}\,\text{J}, u_t = 1.72\,\text{s}$. Physical parameter values for both surface and interfacial diffusion coefficients and energies at a temperature of 900 °C with a gas composition of 50 % H_2/50 % H_2O were adopted from earlier Chapter 3 and converted into the corresponding model parameters. 110

Table 4.2 Structural properties of pristine, 240h aged, and 1100h aged FIB-SEM 3D reconstructed experimental microstructures of the Ni-GDC anode. 112

Table 4.3 Microstructural characteristic properties of pristine and aged Ni-GDC anodes: comparative analysis of experimental aging with simulations 114

Table 4.4 Equilibrium contact angles at triple junctions corresponding to three different sets of specified interfacial energies. The values in the first row γ_{NiGDC}, γ_{NiPore} and $\gamma_{GDCPore}$ (2.43 J m^{-2}, 2.10 J m^{-2} and 1.43 J m^{-2}) correspond to the results of previous Chapter 3, whereas second- and third-row values represent the assumed and modified surface energy of GDC and interfacial energy of Ni/GDC to obtain a target contact angle of 60° for both Ni and GDC. 133

Table 4.5 Microstructural characteristic properties over the aging of three simulations with distinct configurations of contact angles. 136
Table 5.1 Input parameters given to the structure generator for creating a synthetic microstructure. 150
Table 5.2 Comparison of microstructural and mechanical properties: Digital Twin vs. Experimental. 151
Table 5.3 Evaluation of statistical variations in microstructural properties across 10 synthetic structures (S1 to S10 samples) generated independently under identical conditions from the structure generator. 154
Table 6.1 Properties of the materials used in the mechanical simulations. 160
Table 6.2 Microstructural parameters of the generated synthetic structures. The bold values denote the target (reference) parameters used in the design of the fifteen synthetic microstructures, while the remaining values represent the corresponding realized parameters obtained from the generated structures. 162